# The Science and Technology of Undulators and Wigglers

JAMES A. CLARKE

OXFORD SERIES ON SYNCHROTRON RADIATION

Series Editors

J. CHIKAWA   J. R. HELLIWELL
S. W. LOVESEY

OXFORD SERIES ON SYNCHROTRON RADIATION

The Science and Technology of Undulators and Wigglers

James A. Clarke
Daresbury Laboratory

OXFORD

UNIVERSITY PRESS

OXFORD
UNIVERSITY PRESS

For Gill with Love

This page intentionally left blank

Preface

The purpose of this book is to provide the wider synchrotron radiation community with a comprehensive study of all aspects of insertion devices. Scientists and engineers who use synchrotron radiation to perform experiments should find the answers to all of their questions relating to the production and properties of the light from all of the key types of undulators and wigglers as well as answers to more practical questions regarding the realization of actual devices. However, this book is aimed at not just the users but also the providers of synchrotron radiation and so although it takes the reader step by step through the fundamental issues it should be of sufficient depth so as to be of interest to light source designers, accelerator physicists, and even insertion device specialists. The approach taken is to provide the reader with all of the essential information and to back this up with practical examples and illustrations wherever possible.

The layout of the book is in two main parts; the 'science' of the radiation properties and the 'technology' of the magnetic design. First, synchrotron radiation basics are covered, including the emission from bending magnets, and then there is a detailed study of the output from wigglers and then undulators. The radiation emission in terms of flux, brightness, angular distribution, power levels, polarization properties, and so on are all covered. Also described are the practical details of how to actually compute the properties, including several examples.

Next, the magnetic design of undulators and wigglers is described, explaining how these periodic fields are generated in practice. The possible magnet technologies; permanent magnet, normal conducting and superconducting electromagnets, are all discussed from a practical point of view with the advantages and disadvantages of each being highlighted. Following this is an explanation of how and why magnet measurements are performed, and also a discussion of the possible methods that can be used to improve the magnetic quality of the final device produced by using sophisticated sorting and shimming techniques.

In the final chapters a few specialized stand-alone topics are covered. First, the special requirements of undulators for free electron lasers are discussed. Then the effect these periodic magnets have on the electron beam quality, especially in storage rings, is analysed and finally the last chapter looks at some of the more exotic examples that have been produced and also looks to the future to see what new devices may become available in the years to come.

Acknowledgements

I would like to thank Christopher Gerth, Fay Hannon, Duncan Scott, Ben Shepherd, and Neil Thompson from the Accelerator Science and Technology Centre for reading over the text and providing me with useful comments. I would also like to acknowledge Clive Hill for kindly providing Fig. 7.33. Finally, I would like to express my gratitude to Mike Poole for his support and encouragement throughout my career in accelerator physics and synchrotron radiation.

James A. Clarke,
Accelerator Science and Technology Centre
Daresbury Laboratory,
January, 2004

Contents

1

Introduction

More than fifty years ago a bluish-white light was observed through the glass vacuum chamber of a 70 MeV electron synchrotron at the General Electric Company Research Laboratory in Schenectady, New York State. The light, which was seen to change to a red colour at lower electron energies, was found to agree with theoretical predictions that had been made years earlier regarding relativistic electrons and, has since become known as *Synchrotron Radiation* (SR). This radiation was at first considered a curiosity but soon became an irritation as the energy loss associated with it limited the maximum energies that could be reached by electron accelerators. It was not until several years later that scientists considered using this radiation parasitically to perform experiments in solid-state spectroscopy and then later in atomic physics, surface physics, microscopy, and so on.

Interest in SR as a research tool quickly spread around the world. Initially, radiation produced by the electrons as they travelled through the bending magnets was the primary source used, but within a short time of dedicated electron storage ring facilities coming on stream a new type of photon source started to be installed. Special magnets were built and inserted into the available straight sections of the accelerators, these *Insertion Devices* produced unprecedented levels of flux in narrow angular cones and were soon regarded as the premier light sources in the world over the UV to X-ray region.

Insertion Devices (IDs) have become so important now that complete synchrotron radiation facilities are designed and built around them. These IDs fall into two main categories, *Undulators* and *Wigglers*. The undulator is a device that causes the electron beam to follow a gentle, periodic, undulating trajectory with the consequence that the radiation wavefronts emitted overlap with each other and so interference effects occur. At some wavelengths the interference is constructive and significant enhancement in the intensity is observed, while at others the interference is destructive and consequently there are dark regions in the spectrum. The wiggler has a stronger effect upon the electron beam trajectory, causing it to wiggle from side to side by a greater amount. This prevents the wavefronts from overlapping and so no interference effects are apparent. The advantage of this type of ID over a bending magnet source is that each wiggle produces the same number of photons as a bending magnet and so if tens of wiggles are produced in a straight section then the observer will see an intensity enhancement of the same order.

1.1   The Early History of Synchrotron Radiation

The foundations of SR stretch back to the late nineteenth century when Maxwell put forward his ideas on electromagnetic radiation. Following this, Liénard, in 1898 before relativity was established, derived the radiation due to moving charges and in fact calculated the energy loss of an electron moving on a circular path. This result still stands today, even for our highly relativistic electrons, since radiated power is a Lorentz invariant. Liénard's results were confirmed by Schott in 1908 who also derived the angular distribution of the radiation, the polarization characteristics, and the spectrum itself. At this time it was not possible to generate electrons of high enough energies for these ideas to be tested and so there was a period during which little of significance occurred.

It was in 1940 that a betatron was first operated with an electron energy of 2.3 MeV. The following year 20 MeV electrons were produced and in 1945, 100 MeV was achieved. At this energy, it was realized by Blewett that electromagnetic radiation should be emitted by the electrons. Unfortunately he tried to detect it at very long wavelengths as he was unaware of the relativistic effects that shifted the emitted spectrum to shorter, infrared, and visible wavelengths. He was doubly unlucky since the glass vacuum chamber was opaque and so no SR was observed accidentally either. Without these quirks of fate we would probably be discussing 'Betatron Radiation' instead! Despite no direct observation of SR being made at this time, Blewett was able to indirectly observe the effect of the energy loss in the electrons due to the radiation [1], although this was not universally accepted within the team as the definite cause [2].

The synchrotron was invented in 1945 and by 1947 a 70 MeV version was in operation. This time the chamber was transparent and visible light was soon detected [3]. Fears that this light was caused by sparking within the chamber were soon allayed by showing that it was linearly polarized, as predicted for this type of emission [4].

During this time Schwinger was carrying out theoretical predictions on the radiation and advising the General Electric team on its properties. He published a brief report in 1946 [5], but he is best remembered in this area for his 1949 paper [6] which confirmed much of the work that Schott had carried out years earlier. However, Schwinger made an important breakthrough by simplifying the obscure SR equations to a series of Bessel functions that were available numerically in published tables. From this point on, quantified calculations of SR emission became far more easier to be carried out.

Remarkably, it was only two years after this that Motz proposed the 'undulator' as a source of quasi-monochromatic SR [7]. Shortly afterwards, in 1953, he made an experimental demonstration of the first undulator, producing radiation in both visible and millimetre wavelengths [8].

In parallel with the work taking place in the United States, there were a number of interested researchers in the Soviet Union carrying out similar studies. These workers were deriving similar theoretical results independently of those in the West [9]. This interest continued and much of the early experimental

measurements as well as the first complete theoretical description of the radiation properties of undulator radiation took place in the Soviet Union in the 1970s [10].

1.2 Overview of Undulators and Wigglers

Synchrotron radiation is a relativistic effect for which many of the features can be understood in terms of two basic processes — Lorentz contraction and relativistic Doppler shift. First, in the Lorentz contraction, a rod of length, L, travelling with constant velocity, v, towards a stationary observer appears to the observer to be of length

$$L\sqrt{1 - v^2/c^2} = \frac{L}{\gamma} \ ,$$

where c is the speed of light and γ is known as the relativistic Lorentz factor. So, in the frame of reference where the electron is at rest it appears as if the magnetic fields of the undulator are rushing towards it at high speed. If, in the laboratory, we see the period of the magnetic fields of the undulator as λ_u, then the electron sees it as λ_u/γ and so emits radiation with this wavelength.

Second, the relativistic Doppler effect is just a modification of the effect which causes sound waves, for example, to change frequency depending on the relative velocity of the source to the listener. In the relativistic version, the frequency of light seen by an observer at rest, f, is [11]

$$f = \gamma f'(1 - \beta \cos \theta') \ ,$$

where f' is the frequency emitted by the moving source, θ' is the angle at which the source emits the light, and $\beta = v/c$. When the source is travelling towards the observer, $\theta' = \pi$, and so

$$f = \gamma f'(1 + \beta)$$

or, in terms of wavelength,

$$\lambda = \frac{\lambda'}{\gamma(1 + \beta)} \sim \frac{\lambda'}{2\gamma}$$

assuming a relativistic source for which $\beta \sim 1$.

Combining these two effects then gives us an electron, which emits light of wavelength λ_u/γ and since it is travelling towards us we see this wavelength further reduced by 2γ. So, the wavelengths observed will be of the order of $\lambda_u/2\gamma^2$. In modern storage rings, which have energies of a few GeV and therefore γ values of several thousands we can see that undulators with magnet periods of a few centimetres will typically produce radiation with wavelengths of nanometres.

In the moving reference frame of the electron, the electron is oscillating with simple harmonic motion and so emitting in the familiar dipole pattern (see Fig. 1.1) that has a $\sin^2 \theta'$ distribution [12]. However, a second consequence of the
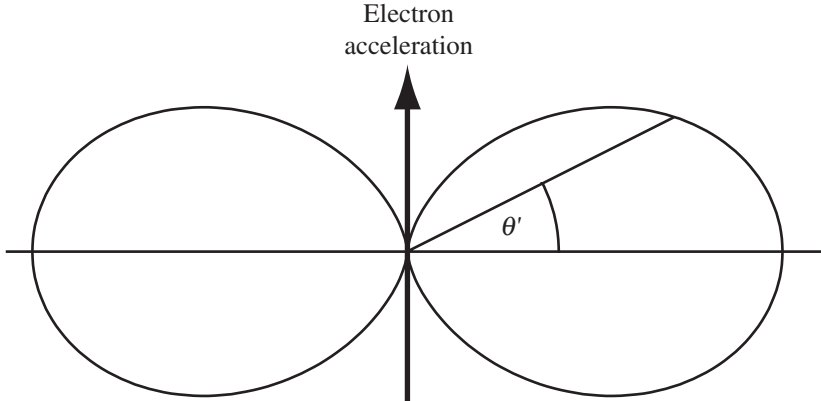
FIG. 1.1. Sketch of the electric dipole field pattern emitted by an oscillating non-relativistic electron.

relativistic Doppler effect is that the angle with which the observer views the source, θ, will also be affected such that [11]

$$\tan \theta = \frac{\sin \theta'}{\gamma(\cos \theta' - \beta)} \quad .$$

Therefore, the point at which the electric dipole has zero amplitude ($\theta' = \pi$) appears at the angle $\theta \sim 1/\gamma$ when $\beta \sim 1$. Again, since γ is of the order of thousands, typically, the radiation is seen by the observer to be emitted into a very narrow cone (less than a milliradian). Also, the peak of the emission is orthogonal to the direction of the electron's acceleration and so the cone is emitted tangential to the (instantaneous) circular path of the electron. A sketch of the radiation emitted by electrons in bending magnets and IDs is given in Fig. 1.2. A consequence of the undulator being an interference device is that the cone of radiation is even narrower by a factor $\sqrt{N}$, where N is the number of periods in the device. Similar effects are observed in other interference devices, such as diffraction gratings, for instance.

If we consider the electron trajectory inside of a bending magnet, as seen by an observer, it is possible to deduce the general form of the spectrum observed. The observer looks at a tangent to the circular path (of radius ρ) and only radiation that is emitted over a short arc of the path can reach him (Fig. 1.3). In particular, given that the radiation is emitted into a cone of angle $\pm \sim 1/\gamma$, it is only over this angular range that the observer experiences any electric field. From simple geometrical arguments we can say that the electric field pulse experienced will have a duration, Δt, given by the difference in time it takes the electron to travel from A to B around the arc and the light along the chord.
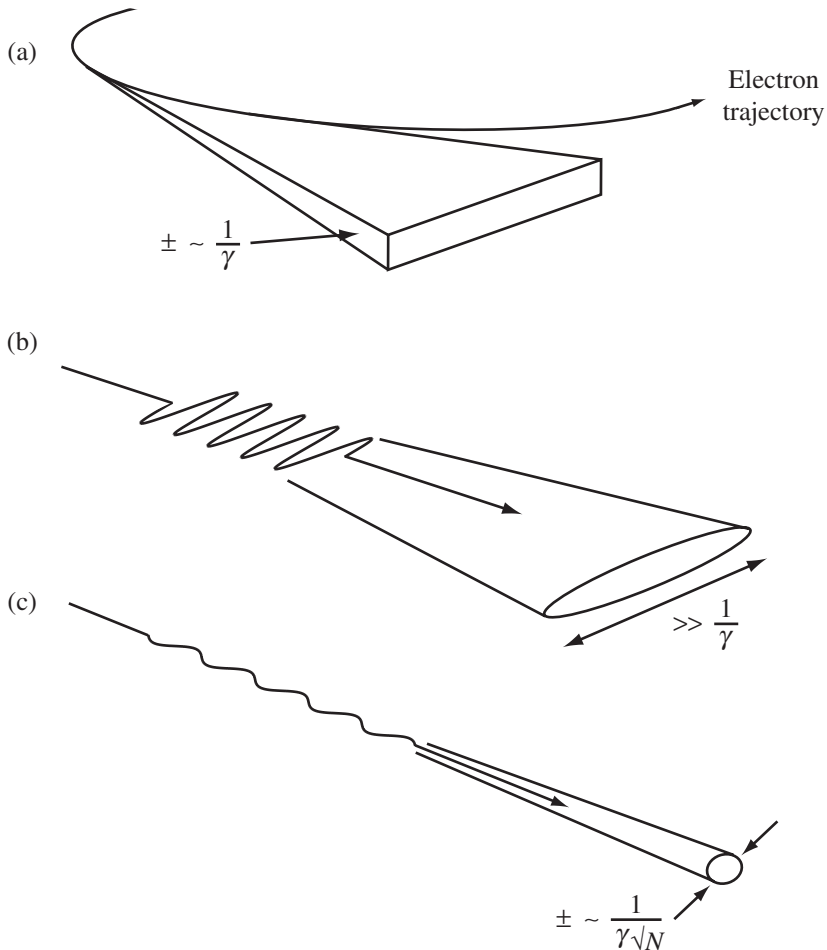
FIG. 1.2. Sketch of the three main types of SR sources, (a) a bending magnet, (b) a multipole wiggler, and (c) an undulator.

$$\Delta t = \frac{2\rho}{v\gamma} - \frac{2\rho}{c\gamma} \sin 1/\gamma$$

$$\sim \frac{2\rho}{\gamma}\left(\frac{1}{v} - \frac{1}{c}\right)$$

$$\sim \frac{2\rho}{\beta c\gamma}(1 - \beta)$$

$$\sim \frac{\rho}{c\gamma^3} \ .$$

Fourier analysis shows that the pulse contains harmonics of the circular orbit
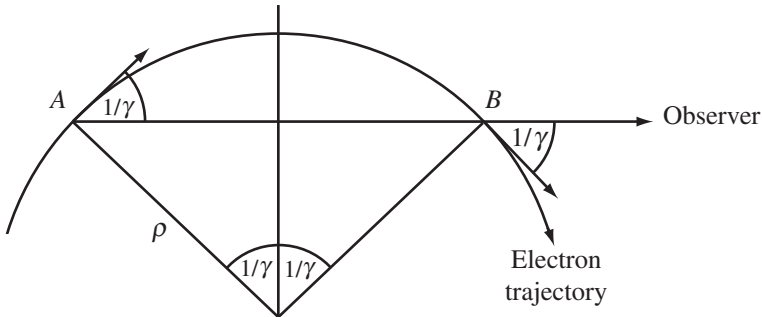
FIG. 1.3. Sketch of the geometry for an observer of bending magnet radiation.
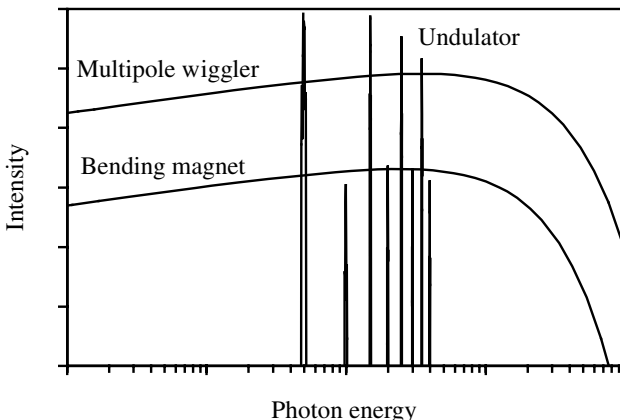
FIG. 1.4. Illustration of the SR spectrum from bending magnets, multipole wigglers, and undulators (on a log-log scale).

frequency up to $\sim c\gamma^3/\rho$. Again, in a typical storage ring, this represents frequencies of $\sim 10^{18}$ Hz or wavelengths of ~ 0.1 nm. In practice the harmonics smear together to form a continuous spectrum. The general form of the radiation spectrum for bending magnets, multipole wigglers, and undulators is presented in Fig. 1.4.

Fundamentals of Synchrotron Radiation Emission

Although this book is primarily concerned with the subject of Insertion Devices (IDs) it is important that we cover the basics first before rushing into the exact output characteristics from undulators and wigglers.

The concept involved in the production of Synchrotron Radiation (SR) is essentially straightforward. The radiation is produced when a relativistic charged particle is accelerated, usually in a magnetic field. Any charged particle will produce SR but the electron is the particle most usually associated with the phenomenon since, as will become apparent, the low rest mass of the electron means that it emits by far the most radiation for a given particle energy ($\sim 10^{13}$ times more than a proton). It is only in the very latest generation of proton accelerators (such as the Large Hadron Collider at CERN) that the emission of SR from protons is of any consequence. The vast majority of synchrotron light sources around the world use electrons as their emitter of SR. The remainder rely on the positron which, although it does have some subtle accelerator physics advantages over the electron, produces exactly the same SR output. Throughout this book I have consistently referred to the electron as the emitting particle but I could equally well have used a positron instead without any loss of accuracy.

This chapter covers the very basics of SR from first principles. An arbitrary electron trajectory is studied to give us some fundamental relationships linking the emitting particle to the observer. The general electric field due to the electron at the observer is then derived and this is applied to the scenario of an electron travelling on a circular path through a uniform magnetic field. This is the extremely important case of *bending magnet* or *dipole* radiation. Finally, equations are derived for the actual number of photons arriving at the observer at particular photon wavelengths and also the exact angular distribution of these photons.

2.1 Emission and Observation

First we consider an electron moving with relativistic velocity (i.e., close to the velocity of light) on an arbitrary path (Fig. 2.1). If the electron emits a photon in the direction of an observer then by the time it arrives at the observer the electron will no longer be in the same position. So, if we want to consider the light that is arriving at the observer now we must appreciate that this was emitted by the moving electron some time ago.
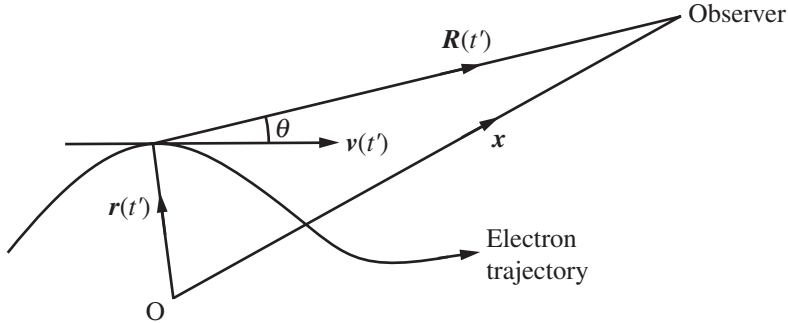
FIG. 2.1. Geometry of the electron and the observer.

The electron emits a photon at a time t', which arrives at the observer at the later time of t. The time t' generally goes by the peculiar name of the *retarded time* but perhaps a better, more intuitive, description is the *emission time*. The time t will be referred to as the *observation time*. The photon travels at the speed of light, c, towards the observer along the path $\boldsymbol{R}(t')$ (note that vector quantities are shown in bold font) and so the observation time is related to the emission time by

$$t = t' + \frac{R(t')}{c} \ . \tag{2.1}$$

The relationship between the emission and observation times is important and so we will explore how one changes with respect to the other

$$\frac{dt}{dt'} = 1 + \frac{1}{c}\frac{dR(t')}{dt'} \ . \tag{2.2}$$

And since

$$\boldsymbol{R}(t') = \boldsymbol{x} - \boldsymbol{r}(t') \ , \tag{2.3}$$

it is clear that

$$\frac{d\boldsymbol{R}(t')}{dt'} = -\frac{d\boldsymbol{r}(t')}{dt'} = -\boldsymbol{v}(t') \ , \tag{2.4}$$

where $\boldsymbol{v}$ is the velocity of the electron, as $\boldsymbol{x}$ does not vary with time.

Recall the standard result that by differentiating the dot product $\boldsymbol{a}(t) \cdot \boldsymbol{a}(t)$ with respect to time we get

$$\boldsymbol{a}(t) \cdot \frac{d\boldsymbol{a}(t)}{dt} = a(t)\frac{da(t)}{dt} \ .$$

Hence

$$R(t')\frac{dR(t')}{dt'} = \boldsymbol{R}(t') \cdot \frac{d\boldsymbol{R}(t')}{dt'}$$
$$= -\boldsymbol{R}(t') \cdot \boldsymbol{v}(t')$$

and so

$$\frac{dR(t')}{dt'} = -\frac{\boldsymbol{R}(t')}{R(t')} \cdot \boldsymbol{v}(t')$$
$$= -\boldsymbol{n}(t') \cdot \boldsymbol{v}(t') \ , \tag{2.5}$$

where $\boldsymbol{n}(t')$ is the unit vector pointing towards the observer along $\boldsymbol{R}(t')$. Substituting this result into (2.2) gives the important result

$$\frac{dt}{dt'} = 1 - \boldsymbol{n}(t') \cdot \boldsymbol{\beta}(t') \ , \tag{2.6}$$

where $\boldsymbol{\beta} = \boldsymbol{v}/c$, is the electron velocity relative to the speed of light. At this point it is also worth noting that

$$\beta = \sqrt{1 - \frac{1}{\gamma^2}} \ ,$$

where γ is the relativistic Lorentz factor that is the ratio of the electron's energy, E, to its rest mass energy, E_0

$$\gamma = \frac{E}{E_0} \ .$$

Since E_0 for an electron is 0.511 MeV and the energy of the electrons in typical synchrotron light sources is a few GeV, the factor γ is usually of the order of several thousands.

2.2 Electric Field at the Observer

A widely used approach to reducing the number of unknowns in Maxwell's equations is to introduce auxiliary variables, which are known as *vector and scalar potentials* [12]. From the standard vector analysis result [13] $\boldsymbol{\nabla} \cdot (\boldsymbol{\nabla} \times \boldsymbol{a}) = 0$ it is clear that for Maxwell's first equation, $\boldsymbol{\nabla} \cdot \boldsymbol{B} = 0$, to hold, it is sufficient to have

$$\boldsymbol{B} = \boldsymbol{\nabla} \times \boldsymbol{A} \ , \tag{2.7}$$

where $\boldsymbol{A}(t)$ is termed the *vector potential*. Similarly, by differentiating (2.7), Maxwell's second equation (Faraday's law)

$$\boldsymbol{\nabla} \times \boldsymbol{E} = -\frac{\partial \boldsymbol{B}}{\partial t}$$

can be rewritten as

$$\boldsymbol{\nabla} \times \boldsymbol{E} = -\boldsymbol{\nabla} \times \left(\frac{\partial \boldsymbol{A}}{\partial t}\right)$$

and so inspection of another vector analysis result [13], $\boldsymbol{\nabla} \times (\boldsymbol{\nabla} U) = 0$, implies that a *scalar potential*, $\Phi(t)$, can be introduced such that

$$\boldsymbol{\nabla} \times \boldsymbol{E} = -\boldsymbol{\nabla} \times \left(\frac{\partial \boldsymbol{A}}{\partial t} + \boldsymbol{\nabla}\Phi\right)$$

and so

$$\boldsymbol{E} = -\boldsymbol{\nabla}\Phi - \frac{\partial \boldsymbol{A}}{\partial t} \quad . \tag{2.8}$$

Clearly there is some arbitrariness in the choice of $\boldsymbol{A}$ and Φ so far. By applying a third condition to this pair of equations it is possible to produce a consistent set of potentials. In particular, if the *Lorentz condition* is applied [12],

$$\boldsymbol{\nabla} \cdot \boldsymbol{A} + \frac{1}{c^2}\frac{\partial \Phi}{\partial t} = 0$$

then the resulting potentials are termed the *Liénard–Wiechert potentials*. We will now use these to derive the electric and magnetic fields received by the observer. The scalar potential in this case is given by

$$\begin{aligned}\Phi(t) &= \frac{e}{4\pi\epsilon_0}\left(\frac{1}{R(t')(1 - \boldsymbol{n}(t') \cdot \boldsymbol{\beta}(t'))}\right) \\ &= \frac{e}{4\pi\epsilon_0}\left(\frac{1}{R(1 - \boldsymbol{n} \cdot \boldsymbol{\beta})}\right)_{t'} \quad , \end{aligned} \tag{2.9}$$

where the t' subscript implies that the variables are all calculated at the emission time. Also note that e is the electronic charge and ϵ_0 is the permittivity of free space. The vector potential is given by

$$\boldsymbol{A}(t) = \frac{e}{4\pi c\epsilon_0}\left(\frac{\boldsymbol{\beta}}{R(1 - \boldsymbol{n} \cdot \boldsymbol{\beta})}\right)_{t'} \quad . \tag{2.10}$$

The derivation of the electric field, $\boldsymbol{E}$, from $\boldsymbol{A}$ and Φ is somewhat longwinded but it is such an important quantity in synchrotron radiation emission that it is worth the effort. Further background on this derivation can be found in [14, 15].

The first term in eqn (2.8) is the gradient of Φ,
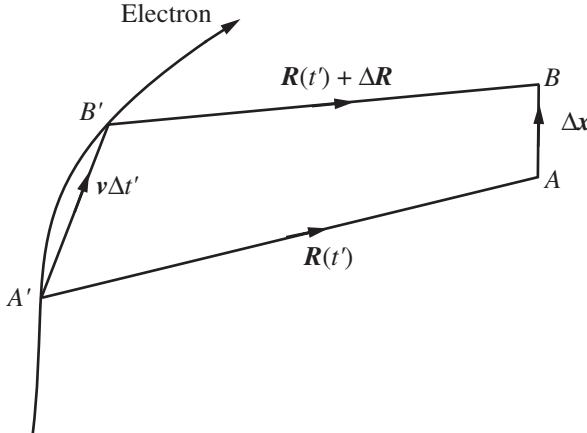
Fig. 2.2. Geometry of the electron as seen by two observers.

$$\boldsymbol{\nabla}\Phi = \frac{e}{4\pi\epsilon_0}\boldsymbol{\nabla}\left(\frac{1}{R - \boldsymbol{R}\cdot\boldsymbol{\beta}}\right)_{t'} \ ,$$

which, using the standard result for the differential of a fraction, gives

$$\begin{aligned}\boldsymbol{\nabla}\Phi &= \frac{e}{4\pi\epsilon_0}\left(\frac{-\boldsymbol{\nabla}(R - \boldsymbol{R}\cdot\boldsymbol{\beta})}{(R - \boldsymbol{R}\cdot\boldsymbol{\beta})^2}\right)_{t'}\\ &= -\frac{e}{4\pi\epsilon_0}\left(\frac{\boldsymbol{\nabla}(R - \boldsymbol{R}\cdot\boldsymbol{\beta})}{R^2(1 - \boldsymbol{n}\cdot\boldsymbol{\beta})^2}\right)_{t'} \ .\end{aligned} \tag{2.11}$$

So, to find $\boldsymbol{\nabla}\Phi$ we will need to calculate $\boldsymbol{\nabla}R(1 - \boldsymbol{n}\cdot\boldsymbol{\beta})$. Consider two observers A and B that are separated by a small amount $\boldsymbol{\Delta x}$ (Fig. 2.2), two photons emitted from A' and B' arrive at the observers at exactly the same time t. The emission times must differ by an amount $\Delta t'$. It is clear then that

$$\boldsymbol{v}\Delta t' + \boldsymbol{R} + \boldsymbol{\Delta R} = \boldsymbol{R} + \boldsymbol{\Delta x}$$

and so

$$\boldsymbol{\Delta R} = \boldsymbol{\Delta x} - c\Delta t'\boldsymbol{\beta} \ ,$$

hence

$$\begin{aligned}\Delta R &= \boldsymbol{n}\cdot\boldsymbol{\Delta R}\\ &= \boldsymbol{n}\cdot\boldsymbol{\Delta x} - c\Delta t'\boldsymbol{n}\cdot\boldsymbol{\beta} \ .\end{aligned} \tag{2.12}$$

Since both photons arrive at the same time at both observers we have

$$t = t' + \frac{R}{c} = (t' + \Delta t') + \frac{(R + \Delta R)}{c}$$

and so

$$\Delta R = -c\Delta t' \ .$$

Equating this result with (2.12) gives

$$\Delta t' = -\frac{\boldsymbol{n} \cdot \boldsymbol{\Delta x}}{c(1 - \boldsymbol{n} \cdot \boldsymbol{\beta})} \ . \tag{2.13}$$

Furthermore

$$\Delta(R(1 - \boldsymbol{n} \cdot \boldsymbol{\beta})) = \Delta(R - \boldsymbol{R} \cdot \boldsymbol{\beta}) = \Delta R - \boldsymbol{\Delta R} \cdot \boldsymbol{\beta} - \boldsymbol{R} \cdot \boldsymbol{\Delta \beta} \ .$$

Substituting for ΔR and $\boldsymbol{\Delta R}$ gives

$$\Delta(R - \boldsymbol{R} \cdot \boldsymbol{\beta}) = -c\Delta t' - (\boldsymbol{\Delta x} - c\Delta t' \boldsymbol{\beta}) \cdot \boldsymbol{\beta} - \boldsymbol{R} \cdot \frac{\partial \boldsymbol{\beta}}{\partial t'} \Delta t' \ .$$

Substituting $\Delta t'$ from (2.13) and using the standard notation of $\dot{\boldsymbol{\beta}} = \partial \boldsymbol{\beta}/\partial t'$, gives

$$\Delta(R - \boldsymbol{R} \cdot \boldsymbol{\beta}) = \boldsymbol{\Delta x} \left(\frac{\boldsymbol{n}}{(1 - \boldsymbol{n} \cdot \boldsymbol{\beta})} - \boldsymbol{\beta} - \frac{\beta^2 \boldsymbol{n}}{(1 - \boldsymbol{n} \cdot \boldsymbol{\beta})} + \frac{(\boldsymbol{R} \cdot \dot{\boldsymbol{\beta}})\boldsymbol{n}}{c(1 - \boldsymbol{n} \cdot \boldsymbol{\beta})} \right) \ .$$

Since

$$\boldsymbol{\nabla} R(1 - \boldsymbol{n} \cdot \boldsymbol{\beta}) = \frac{\Delta(R - \boldsymbol{R} \cdot \boldsymbol{\beta})}{\boldsymbol{\Delta x}}$$

in the limit as $\boldsymbol{\Delta x} \to \boldsymbol{0}$, we have

$$\boldsymbol{\nabla} R(1 - \boldsymbol{n} \cdot \boldsymbol{\beta}) = \frac{\boldsymbol{n}}{(1 - \boldsymbol{n} \cdot \boldsymbol{\beta})} - \boldsymbol{\beta} - \frac{\beta^2 \boldsymbol{n}}{(1 - \boldsymbol{n} \cdot \boldsymbol{\beta})} + \frac{(\boldsymbol{R} \cdot \dot{\boldsymbol{\beta}})\boldsymbol{n}}{c(1 - \boldsymbol{n} \cdot \boldsymbol{\beta})}$$
$$= \frac{c(1 - \beta^2)\boldsymbol{n} - c(1 - \boldsymbol{n} \cdot \boldsymbol{\beta})\boldsymbol{\beta} + R(\boldsymbol{n} \cdot \dot{\boldsymbol{\beta}})\boldsymbol{n}}{c(1 - \boldsymbol{n} \cdot \boldsymbol{\beta})} \ .$$

Substituting this result into (2.11) gives

$$\boldsymbol{\nabla} \Phi = -\frac{e}{4\pi\epsilon_0} \left(\frac{c(1 - \beta^2)\boldsymbol{n} - c(1 - \boldsymbol{n} \cdot \boldsymbol{\beta})\boldsymbol{\beta} + R(\boldsymbol{n} \cdot \dot{\boldsymbol{\beta}})\boldsymbol{n}}{cR^2(1 - \boldsymbol{n} \cdot \boldsymbol{\beta})^3} \right)_{t'} \ . \tag{2.14}$$

The second term in (2.8) contains the differential of the magnetic vector potential with respect to the observer time, t,

$$\frac{\partial \boldsymbol{A}}{\partial t} = \frac{dt'}{dt}\frac{\partial \boldsymbol{A}}{\partial t'}$$

$$= \frac{1}{(1 - \boldsymbol{n}\cdot\boldsymbol{\beta})_{t'}}\frac{\partial \boldsymbol{A}}{\partial t'} \ , \tag{2.15}$$

where we have used the result of (2.6). Differentiating the magnetic vector potential with respect to the emission time, t', we get

$$\frac{\partial \boldsymbol{A}}{\partial t'} = \frac{e}{4\pi c\epsilon_0}\left(\frac{R(1 - \boldsymbol{n}\cdot\boldsymbol{\beta})\dot{\boldsymbol{\beta}} - \boldsymbol{\beta}\frac{\partial(R(1-\boldsymbol{n}\cdot\boldsymbol{\beta}))}{\partial t'}}{R^2(1 - \boldsymbol{n}\cdot\boldsymbol{\beta})^2}\right)_{t'} \ .$$

Note that the derivative in the second term of the numerator is

$$\frac{\partial(R(1 - \boldsymbol{n}\cdot\boldsymbol{\beta}))}{\partial t'} = \frac{\partial(R - \boldsymbol{R}\cdot\boldsymbol{\beta})}{\partial t'} = \frac{\partial R}{\partial t'} - \frac{\partial \boldsymbol{R}}{\partial t'}\cdot\boldsymbol{\beta} - \boldsymbol{R}\cdot\dot{\boldsymbol{\beta}}$$

$$= -\boldsymbol{n}\cdot\boldsymbol{v} + \boldsymbol{v}\cdot\boldsymbol{\beta} - \boldsymbol{R}\cdot\dot{\boldsymbol{\beta}}$$

$$= -c(\boldsymbol{n}\cdot\boldsymbol{\beta}) + c\beta^2 - \boldsymbol{R}\cdot\dot{\boldsymbol{\beta}} \ ,$$

where we have used the results of (2.4) and (2.5). Therefore,

$$\frac{\partial \boldsymbol{A}}{\partial t'} = \frac{e}{4\pi c\epsilon_0}\left(\frac{R(1 - \boldsymbol{n}\cdot\boldsymbol{\beta})\dot{\boldsymbol{\beta}} - \boldsymbol{\beta}(-c(\boldsymbol{n}\cdot\boldsymbol{\beta}) + c\beta^2 - \boldsymbol{R}\cdot\dot{\boldsymbol{\beta}})}{R^2(1 - \boldsymbol{n}\cdot\boldsymbol{\beta})^2}\right)_{t'}$$

$$= \frac{e}{4\pi c\epsilon_0}\left(\frac{\dot{\boldsymbol{\beta}}}{R(1 - \boldsymbol{n}\cdot\boldsymbol{\beta})} - \frac{\boldsymbol{\beta}(-c(\boldsymbol{n}\cdot\boldsymbol{\beta}) + c\beta^2 - \boldsymbol{R}\cdot\dot{\boldsymbol{\beta}})}{R^2(1 - \boldsymbol{n}\cdot\boldsymbol{\beta})^2}\right)_{t'} \ .$$

Putting this result into (2.15) gives

$$\frac{\partial \boldsymbol{A}}{\partial t} = \frac{e}{4\pi c\epsilon_0}\left(\frac{1}{(1 - \boldsymbol{n}\cdot\boldsymbol{\beta})}\left(\frac{\dot{\boldsymbol{\beta}}}{R(1 - \boldsymbol{n}\cdot\boldsymbol{\beta})} - \frac{\boldsymbol{\beta}(-c(\boldsymbol{n}\cdot\boldsymbol{\beta}) + c\beta^2 - \boldsymbol{R}\cdot\dot{\boldsymbol{\beta}})}{R^2(1 - \boldsymbol{n}\cdot\boldsymbol{\beta})^2}\right)\right)_{t'}$$

$$= \frac{e}{4\pi c\epsilon_0}\left(\frac{1}{(1 - \boldsymbol{n}\cdot\boldsymbol{\beta})^3}\left(\frac{\dot{\boldsymbol{\beta}}(1 - \boldsymbol{n}\cdot\boldsymbol{\beta}) + \boldsymbol{\beta}(\boldsymbol{n}\cdot\dot{\boldsymbol{\beta}})}{R} + \frac{c(\boldsymbol{\beta}(\boldsymbol{n}\cdot\boldsymbol{\beta}) - \boldsymbol{\beta}\beta^2)}{R^2}\right)\right)_{t'} \ .$$

Finally, this result can be combined with that from (2.14) to solve (2.8),

$$\boldsymbol{E}(t) = \frac{e}{4\pi\epsilon_0}\left(\frac{c(1-\beta^2)\boldsymbol{n} - c(1-\boldsymbol{n}\cdot\boldsymbol{\beta})\boldsymbol{\beta} + R(\boldsymbol{n}\cdot\dot{\boldsymbol{\beta}})\boldsymbol{n}}{cR^2(1-\boldsymbol{n}\cdot\boldsymbol{\beta})^3}\right)_{t'}$$

$$-\frac{e}{4\pi c\epsilon_0}\left(\frac{1}{(1-\boldsymbol{n}\cdot\boldsymbol{\beta})^3}\left(\frac{\dot{\boldsymbol{\beta}}(1-\boldsymbol{n}\cdot\boldsymbol{\beta}) + \boldsymbol{\beta}(\boldsymbol{n}\cdot\dot{\boldsymbol{\beta}})}{R}\right.\right.$$

$$\left.\left. + \frac{c(\boldsymbol{\beta}(\boldsymbol{n}\cdot\boldsymbol{\beta}) - \boldsymbol{\beta}\beta^2)}{R^2}\right)\right)_{t'} .$$

Gathering terms together with denominators of order R and R^2 gives

$$\boldsymbol{E}(t) = \frac{e}{4\pi c\epsilon_0}\left(\frac{c(1-\beta^2)\boldsymbol{n} - c(1-\beta^2)\boldsymbol{\beta}}{R^2(1-\boldsymbol{n}\cdot\boldsymbol{\beta})^3} + \frac{(\boldsymbol{n}\cdot\dot{\boldsymbol{\beta}})(\boldsymbol{n}-\boldsymbol{\beta}) - (1-\boldsymbol{n}\cdot\boldsymbol{\beta})\dot{\boldsymbol{\beta}}}{R(1-\boldsymbol{n}\cdot\boldsymbol{\beta})^3}\right)_{t'}$$

$$= \frac{e}{4\pi c\epsilon_0}\left(\frac{c(1-\beta^2)(\boldsymbol{n}-\boldsymbol{\beta})}{R^2(1-\boldsymbol{n}\cdot\boldsymbol{\beta})^3} + \frac{\boldsymbol{n}\times((\boldsymbol{n}-\boldsymbol{\beta})\times\dot{\boldsymbol{\beta}})}{R(1-\boldsymbol{n}\cdot\boldsymbol{\beta})^3}\right)_{t'} , \qquad (2.16)$$

where we have used the triple vector product result

$$\boldsymbol{A}\times(\boldsymbol{B}\times\boldsymbol{C}) = (\boldsymbol{A}\cdot\boldsymbol{C})\boldsymbol{B} - (\boldsymbol{A}\cdot\boldsymbol{B})\boldsymbol{C} .$$

In a similar manner, we can derive the result for the magnetic field experienced by the observer as

$$\boldsymbol{B}(t) = \frac{\boldsymbol{n}\times\boldsymbol{E}(t)}{c} . \qquad (2.17)$$

Now that we have derived the electric and magnetic field experienced by the observer we can make several remarks. First, the magnetic field, $\boldsymbol{B}$, must be perpendicular to both the electric field, $\boldsymbol{E}$, and the unit vector pointing towards the observer, $\boldsymbol{n}$ since by definition the result $\boldsymbol{a}\times\boldsymbol{b}$ is perpendicular to both $\boldsymbol{a}$ and $\boldsymbol{b}$. Second, if the electron is stationary ($\boldsymbol{\beta} = \dot{\boldsymbol{\beta}} = \boldsymbol{0}$), then the electric field is given by

$$\boldsymbol{E} = \frac{e\boldsymbol{n}}{4\pi\epsilon_0 R^2} ,$$

which is simply Coulomb's law. Note also that the electric field has two terms, the first is proportional to $1/R^2$ and the second to $1/R$. As R increases the first term becomes less and less significant and it is very common for (2.16) to be written in the simplified form of

$$\boldsymbol{E}(t) = \frac{e}{4\pi c\epsilon_0}\left(\frac{\boldsymbol{n}\times((\boldsymbol{n}-\boldsymbol{\beta})\times\dot{\boldsymbol{\beta}})}{R(1-\boldsymbol{n}\cdot\boldsymbol{\beta})^3}\right)_{t'} . \qquad (2.18)$$

It is very important to remember, however, that this equation only holds in the so-called *far field* when R is large. Exactly how large R needs to be for this

approximation to be valid will be covered later. It will be sufficient to state now that for most situations of interest encountered in a synchrotron light source the far field approximation is valid. A simple consequence of this far field case is that, by virtue of the cross product, the electric field is also perpendicular to $\boldsymbol{n}$.

2.3 Fourier Transform of the Electric Field

Although we now have a means of calculating the electric field as a function of time experienced by an observer due to an electron on an arbitrary path, it is not altogether clear how to interpret this result. It would be much nicer if we could analyse the electric field to determine what frequency content, and so what electromagnetic radiation, it represented. Of course we can convert from time to frequency with a Fourier Transform and this is the next step. We will assume the far field case is valid as this simplifies things somewhat. The Fourier Transform is given by

$$\boldsymbol{E}(\omega) = \frac{1}{\sqrt{2\pi}} \int_{-\infty}^{\infty} \boldsymbol{E}(t) e^{i\omega t} \, dt \; .$$

Obviously the integral is performed with respect to t because we are interested in the frequency content experienced by the observer. However, the integral is actually more straightforward if we transform the integration variable to t' using (2.1) and (2.6)

$$\boldsymbol{E}(\omega) = \frac{1}{\sqrt{2\pi}} \int_{-\infty}^{\infty} \boldsymbol{E}(t) e^{i\omega(t' + \frac{R(t')}{c})} (1 - \boldsymbol{n} \cdot \boldsymbol{\beta})_{t'} \, dt'$$

$$= \frac{e}{4\pi\sqrt{2\pi} \, c\epsilon_0} \int_{-\infty}^{\infty} \left(\frac{\boldsymbol{n} \times ((\boldsymbol{n} - \boldsymbol{\beta}) \times \dot{\boldsymbol{\beta}})}{R(1 - \boldsymbol{n} \cdot \boldsymbol{\beta})^2} \right)_{t'} e^{i\omega(t' + \frac{R(t')}{c})} \, dt' \; .$$

The integral can be simplified if the assumption is made that $\boldsymbol{R}$ does not vary with time $(d\boldsymbol{n}/dt = 0)$, which is reasonable for the relativistic far field case. After integrating by parts (one part being the exponential term and the other being the cross product terms) the expression then becomes

$$\boldsymbol{E}(\omega) = \frac{e}{4\pi\sqrt{2\pi} \, c\epsilon_0 R} \left[\left[\frac{(\boldsymbol{n} \times (\boldsymbol{n} \times \boldsymbol{\beta}))}{(1 - \boldsymbol{n} \cdot \boldsymbol{\beta})} e^{i\omega(t' + \frac{R(t')}{c})} \right]_{-\infty}^{\infty} \right.$$
$$\left. + i\omega \int_{-\infty}^{\infty} (\boldsymbol{n} \times (\boldsymbol{n} \times \boldsymbol{\beta})) e^{i\omega(t' + \frac{R(t')}{c})} \, dt' \right] \; .$$

The first term on the right-hand side can be conveniently dropped since it should be evaluated at $t' = \pm\infty$ and so will not therefore be observed. This gives us the final expression for the far field case of an electron moving on an arbitrary path of
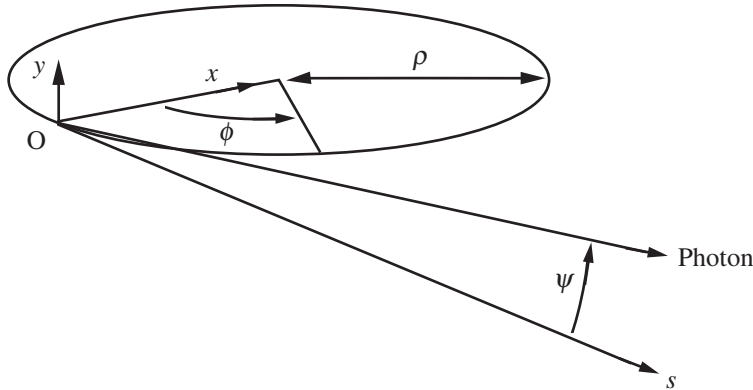
FIG. 2.3. Coordinate frame of an electron on a circular orbit.

$$\boldsymbol{E}(\omega) = \frac{ie\omega}{4\pi\sqrt{2\pi}\,c\epsilon_0 R} \int_{-\infty}^{\infty} (\boldsymbol{n} \times (\boldsymbol{n} \times \boldsymbol{\beta}))e^{i\omega(t' + \frac{R(t')}{c})}\,dt' \quad . \tag{2.19}$$

Again, the magnetic field is related to the electric field by

$$\boldsymbol{B}(\omega) = \frac{\boldsymbol{n} \times \boldsymbol{E}(\omega)}{c} \quad . \tag{2.20}$$

2.4   Synchrotron Radiation in a Bending Magnet

We will use the equations that we have just derived to look at the special case of a single relativistic electron moving on a circular orbit. Passing electrons through a uniform magnetic field (commonly referred to as a bending magnet or more correctly, dipole magnet) is the most basic method of generating synchrotron radiation in particle accelerators.

The angular velocity, ω_0, of the electron is given by

$$\omega_0 = \frac{\beta c}{\rho} \quad ,$$

where ρ is the bending radius of the electron. Assuming the geometry of Fig. 2.3 and with the time coordinate chosen so that $t' = 0$ occurs at the origin, we can determine the position, normalized velocity, and normalized acceleration of the electron to be [14]

$$\boldsymbol{r}(t') = (\rho(1 - \cos(\omega_0 t')), 0, \rho\sin(\omega_0 t'))$$
$$\boldsymbol{\beta}(t') = (\beta\sin(\omega_0 t'), 0, \beta\cos(\omega_0 t'))$$

$$\dot{\boldsymbol{\beta}}(t') = (\beta\omega_0\cos(\omega_0 t'), 0, -\beta\omega_0\sin(\omega_0 t')) \ .$$

Again we assume the far field condition so R is large and we can consider $\boldsymbol{R}$ to be constant over the short time during which the emitted radiation can be received by the observer. The unit vector is given by

$$\boldsymbol{n} = (0, \sin\psi, \cos\psi)$$

and the vector triple product from (2.19) is

$$
\begin{aligned}
(\boldsymbol{n}\times(\boldsymbol{n}\times\boldsymbol{\beta})) &= (\boldsymbol{n}\cdot\boldsymbol{\beta})\boldsymbol{n} - \boldsymbol{\beta} \\
&= \beta\cos\psi\cos(\omega_0 t')\boldsymbol{n} - \boldsymbol{\beta} \\
&= (-\beta\sin(\omega_0 t'), \beta\sin\psi\cos\psi\cos(\omega_0 t'), -\beta\sin^2\psi\cos(\omega_0 t')) \ .
\end{aligned}
$$

Since we are only considering relativistic particles, with the relativistic Lorentz factor $\gamma = (1-\beta^2)^{-1/2} \gg 1$, the vertical opening angle of the radiation is very small , $\psi \sim 1/\gamma$, and only a small part of the trajectory contributes to the radiation seen by our observer ($\Delta\phi = \omega_0 t' \ll 1$). We can therefore approximate the vector product to

$$(\boldsymbol{n}\times(\boldsymbol{n}\times\boldsymbol{\beta})) \approx \beta(-\omega_0 t', \psi, 0) \ . \tag{2.21}$$

Also, the term in the exponent of (2.19) can be expressed as follows

$$t' + \frac{R(t')}{c} = t' + \frac{\boldsymbol{n}\cdot\boldsymbol{x}}{c} - \frac{\boldsymbol{n}\cdot\boldsymbol{r}}{c} \tag{2.22}$$

from (2.3), and so, using small angle approximations again we get

$$
\begin{aligned}
t' + \frac{R(t')}{c} &\approx t' + \frac{x}{c} - \frac{\rho}{c}\sin(\omega_0 t')\cos\psi \\
&\approx t' + \frac{x}{c} - \frac{\rho}{c}\left(\omega_0 t' - \frac{\omega_0^3 t'^3}{6}\right)\left(1 - \frac{\psi^2}{2}\right) \\
&\approx \frac{x}{c} + t'\left(1 - \frac{\rho\omega_0}{c} + \frac{\rho\omega_0\psi^2}{2c}\right) + \frac{t'^3\omega_0^3\rho}{6c}\left(1 - \frac{\psi^2}{2}\right)
\end{aligned}
$$

substituting $\omega_0 = \beta c/\rho$ and noting that $\beta = \sqrt{1-1/\gamma^2} \approx 1 - 1/2\gamma^2$ we get

$$
\begin{aligned}
t' + \frac{R(t')}{c} &\approx \frac{x}{c} + t'\left(1 - \beta + \frac{\beta\psi^2}{2}\right) + \frac{c^2\beta^3 t'^3}{6\rho^2}\left(1 - \frac{\psi^2}{2}\right) \\
&\approx \frac{x}{c} + t'\left(\frac{1}{2\gamma^2} + \frac{\beta\psi^2}{2}\right) + \frac{c^2\beta^3 t'^3}{6\rho^2}\left(1 - \frac{\psi^2}{2}\right)
\end{aligned}
$$

$$\approx \frac{x}{c} + \frac{t'}{2\gamma^2}(1 + \gamma^2\psi^2) + \frac{c^2t'^3}{6\rho^2} \quad. \tag{2.23}$$

An alternative but equivalent approach to deriving the above equation is to apply the small angle approximation to dt/dt' (eqn (2.6)) and then to integrate this with respect to dt' [16].

Introducing our results from (2.21) and (2.23) into the electric field as a function of frequency (2.19) we obtain

$$\boldsymbol{E}(\omega) = \frac{ie\omega}{4\pi\sqrt{2\pi}\,c\epsilon_0 R}$$
$$\times \int_{-\infty}^{\infty} \beta(-\omega_0 t', \psi, 0) \exp\left(i\omega\left(\frac{x}{c} + \frac{t'}{2\gamma^2}(1 + \gamma^2\psi^2) + \frac{c^2t'^3}{6\rho^2}\right)\right) dt' \quad.$$

We can now express the exponential part in terms of sine and cosine and again use the approximation that $\beta \approx 1$. We can also remove the term x/c in the exponential as this is a constant (the time taken to travel between the origin and the observer) and so will just give a fixed phase shift, which is of no importance to us. We are then left with

$$\boldsymbol{E}(\omega) = \frac{ie\omega}{4\pi\sqrt{2\pi}\,c\epsilon_0 R} \int_{-\infty}^{\infty} (-\omega_0 t', \psi, 0) \left(\cos U + i\sin U\right) dt' \quad,$$

where

$$U = \omega\left(\frac{t'}{2\gamma^2}(1 + \gamma^2\psi^2) + \frac{c^2t'^3}{6\rho^2}\right) \quad.$$

If we now look at the x, y, and s terms separately we will get an interesting insight into the emitted radiation. The first remark to make is that there is no electric field in the direction of s (i.e. $E_s(\omega) = 0$). In fact, we had already established this earlier when we found that the electric field was perpendicular to $\boldsymbol{n}$ in Section 2.2. We will now look at the electric field seen by the observer that is aligned in the x direction, $E_x(\omega)$.

$$E_x(\omega) = \frac{-ie\omega\omega_0}{4\pi\sqrt{2\pi}\,c\epsilon_0 R} \left[\int_{-\infty}^{\infty} t'\cos U \, dt' + i\int_{-\infty}^{\infty} t'\sin U \, dt'\right] \quad.$$

A function of the form $f(x) = x\cos g(x)$ is a so-called *odd function*, which means that $f(x) = -f(-x)$. The significance of this is that the integral of such a function between $-\infty$ and ∞ will always equal zero. Hence, the above equation can be reduced to

$$E_x(\omega) = \frac{e\omega\omega_0}{4\pi\sqrt{2\pi}\,c\epsilon_0 R} \int_{-\infty}^{\infty} t'\sin\left(\omega\left(\frac{t'}{2\gamma^2}(1 + \gamma^2\psi^2) + \frac{c^2t'^3}{6\rho^2}\right)\right) dt' \quad.$$

This can be made a little more easy to digest by substituting the variable $u = t'(\omega c^2/2\rho^2)^{1/3}$ and also by introducing the *critical frequency*, $\omega_c = 3c\gamma^3/2\rho$.

$$E_x(\omega) = \frac{e\omega\omega_0}{4\pi\sqrt{2\pi}\,c\epsilon_0 R}$$

$$\times \int_{-\infty}^{\infty} \left(\frac{2\rho^2}{\omega c^2}\right)^{2/3} u \sin\left(\frac{\omega}{2\gamma^2}\left(\frac{2\rho^2}{\omega c^2}\right)^{1/3}(1+\gamma^2\psi^2)u + \frac{u^3}{3}\right) du$$

$$= \frac{e\omega\omega_0}{4\pi\sqrt{2\pi}\,c\epsilon_0 R}\left(\frac{2\rho^2}{\omega c^2}\right)^{2/3}$$

$$\times \int_{-\infty}^{\infty} u \sin\left(\left(\frac{3\omega}{4\omega_c}\right)^{2/3}(1+\gamma^2\psi^2)u + \frac{u^3}{3}\right) du \quad . \quad (2.24)$$

Similarly for the electric field in the vertical plane

$$E_y(\omega) = \frac{ie\omega\psi}{4\pi\sqrt{2\pi}\,c\epsilon_0 R}\left[\int_{-\infty}^{\infty}\cos U\,dt' + i\int_{-\infty}^{\infty}\sin U\,dt'\right] \quad .$$

Note again that $f(x) = \sin x$ is an odd function and so the second integral in the above equation can be neglected, leaving us with

$$E_y(\omega) = \frac{ie\omega\psi}{4\pi\sqrt{2\pi}\,c\epsilon_0 R}\int_{-\infty}^{\infty}\cos\left(\omega\left(\frac{t'}{2\gamma^2}(1+\gamma^2\psi^2) + \frac{c^2 t'^3}{6\rho^2}\right)\right) dt'$$

$$= \frac{ie\omega\psi}{4\pi\sqrt{2\pi}\,c\epsilon_0 R}\left(\frac{2\rho^2}{\omega c^2}\right)^{1/3}$$

$$\times \int_{-\infty}^{\infty}\cos\left(\left(\frac{3\omega}{4\omega_c}\right)^{2/3}(1+\gamma^2\psi^2)u + \frac{u^3}{3}\right) du \quad . \quad (2.25)$$

We can present (2.24) and (2.25) in a more useful form but first we need to make a brief diversion into Airy functions and modified Bessel functions. A standard result from math texts for the Airy function, $Ai(x)$, is [17]

$$Ai(x) = \frac{1}{\pi}\int_0^{\infty}\cos\left(xt + \frac{t^3}{3}\right) dt$$

and so the differential of this with respect to x would be

$$\frac{dAi(x)}{dx} = Ai'(x) = -\frac{1}{\pi}\int_0^{\infty} t\sin\left(xt + \frac{t^3}{3}\right) dt \quad .$$

Two more standard results express the Airy functions in terms of modified Bessel functions [17], $K_{1/3}$ and $K_{2/3}$

$$Ai(x) = \frac{1}{\pi}\sqrt{\frac{x}{3}}K_{1/3}\left(\frac{2x^{3/2}}{3}\right)$$

$$Ai'(x) = -\frac{1}{\pi}\frac{x}{\sqrt{3}}K_{2/3}\left(\frac{2x^{3/2}}{3}\right) \quad .$$

We will now use these functions to express our results for $E_x(\omega)$ and $E_y(\omega)$ in terms of either Airy functions or modified Bessel functions. First, expressed as Airy functions we have

$$E_x(\omega) = -\frac{e\gamma}{\sqrt{2\pi}\,c\epsilon_0 R}\left(\frac{3\omega}{4\omega_c}\right)^{1/3} Ai'\left(\left(\frac{3\omega}{4\omega_c}\right)^{2/3}(1+\gamma^2\psi^2)\right)$$

$$E_y(\omega) = \frac{ie\psi\gamma^2}{\sqrt{2\pi}\,c\epsilon_0 R}\left(\frac{3\omega}{4\omega_c}\right)^{2/3} Ai\left(\left(\frac{3\omega}{4\omega_c}\right)^{2/3}(1+\gamma^2\psi^2)\right) \quad ,$$

and then expressed as Bessel functions this becomes

$$E_x(\omega) = \frac{\sqrt{3}\,e\gamma}{4\pi\sqrt{2\pi}\,c\epsilon_0 R}\left(\frac{\omega}{\omega_c}\right)(1+\gamma^2\psi^2)K_{2/3}(G) \tag{2.26}$$

$$E_y(\omega) = \frac{i\sqrt{3}\,e\psi\gamma^2}{4\pi\sqrt{2\pi}\,c\epsilon_0 R}\left(\frac{\omega}{\omega_c}\right)(1+\gamma^2\psi^2)^{1/2}K_{1/3}(G) \quad , \tag{2.27}$$

where

$$G = \left(\frac{\omega}{2\omega_c}\right)(1+\gamma^2\psi^2)^{3/2} \quad .$$

Some example graphs of $E_x(\omega)$ and $E_y(\omega)$ are given in Figs. 2.4 and 2.5. The result for $E_x(\omega)$ looks very much like the classic bending magnet spectrum, as we shall see later in this section. Note that the lower frequencies become more and more important in both the planes as the vertical angle $(\gamma\psi)$ increases. This is also a standard bending magnet behaviour where long wavelength radiation extends much further out in vertical angle than shorter wavelength radiation. It is also important to note that the vertical electric field vanishes when $\psi = 0$, or in other words, the radiation is polarized entirely in the horizontal plane when observed on-axis.

Whether one chooses to work with either the Airy functions or the Bessel functions is purely a matter of personal preference. In the literature, the Bessel function form appears more often though some find the Airy function easier to work with analytically. I have found the Bessel function to be more readily available in commercial software such as spreadsheets and programming libraries and so I generally prefer this form. Table 2.1 gives the value of $K_{1/3}(u)$ and $K_{2/3}(u)$ for a wide range of u, as well as two other useful Bessel functions that we will meet in the following section.

We will need the expressions for the electric fields in the next part where we will look at how the synchrotron radiation power emitted by the electron is distributed in angle.
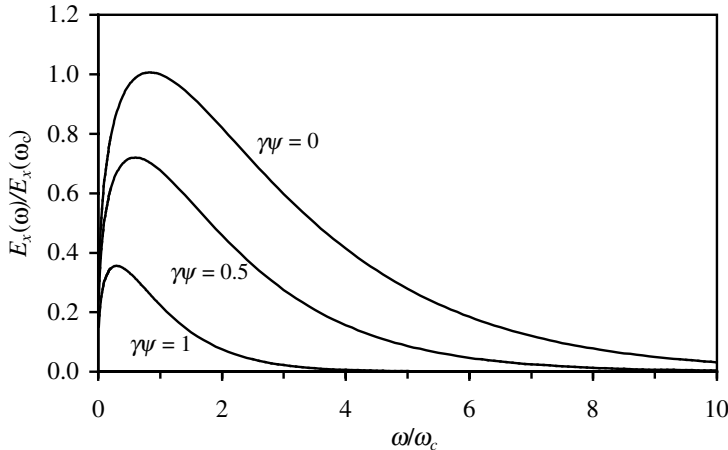
FIG. 2.4. Horizontal electric field as a function of frequency for different vertical angles.
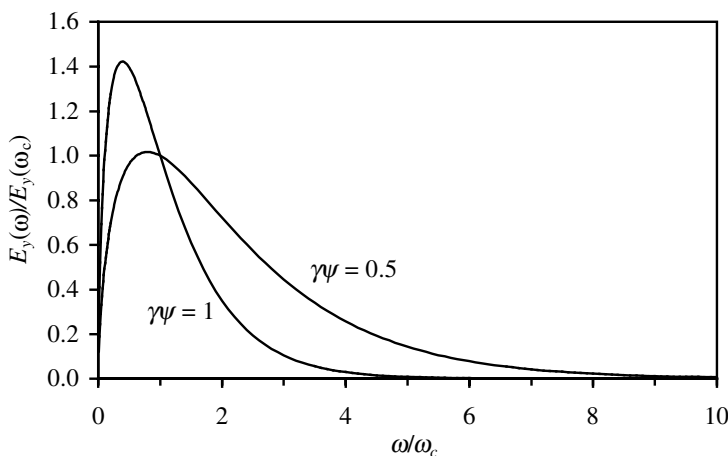
FIG. 2.5. Vertical electric field as a function of frequency for different vertical angles.

2.4.1 *Angular Power Distribution*

A standard result in electromagnetic theory is that the Poynting vector, $\boldsymbol{S}$, gives the energy flow per unit area per unit time [18].

$$\boldsymbol{S} = \frac{1}{\mu_0}(\boldsymbol{E} \times \boldsymbol{B}) = \epsilon_0 c^2 (\boldsymbol{E} \times \boldsymbol{B}) \ ,$$

TABLE 2.1 Numerical values for modified Bessel functions that are encountered in synchrotron radiation calculations

u	$K_{1/3}(u)$	$K_{2/3}(u)$	$K_{5/3}(u)$	$\int_u^\infty K_{5/3}(u)du$
0.0001	36.28	498.9	6.651E+06	995.9
0.0002	28.76	314.3	2.095E+06	626.7
0.0004	22.79	198.0	6.599E+05	394.1
0.0005	21.13	170.6	4.550E+05	339.4
0.0007	18.86	136.3	2.597E+05	270.8
0.0008	18.03	124.7	2.079E+05	247.6
0.001	16.72	107.5	1.433E+05	213.1
0.002	13.19	67.69	4.514E+04	133.6
0.004	10.38	42.62	1.422E+04	83.49
0.005	9.594	36.72	9.802E+03	71.70
0.007	8.514	29.33	5.594E+03	56.93
0.008	8.116	26.82	4.478E+03	51.93
0.01	7.486	23.10	3.087E+03	44.50
0.02	5.781	14.50	972.3	27.36
0.04	4.386	9.052	306.1	16.57
0.05	3.991	7.762	211.0	14.03
0.07	3.437	6.136	120.3	10.85
0.08	3.231	5.581	96.25	9.777
0.1	2.900	4.753	66.27	8.182
0.2	1.979	2.802	20.66	4.517
0.4	1.206	1.517	6.263	2.255
0.5	0.9890	1.206	4.205	1.742
0.7	0.6965	0.8148	2.248	1.126
0.8	0.5932	0.6839	1.733	0.9280
1	0.4384	0.4945	1.098	0.6514
2	0.1165	0.1248	0.1998	0.1508
4	0.01130	0.01173	0.01521	0.01321
5	0.003729	0.003844	0.004754	0.004250
7	4.280E-04	4.376E-04	5.113E-04	4.725E-04
8	1.474E-04	1.504E-04	1.725E-04	1.611E-04
10	1.787E-05	1.816E-05	2.030E-05	1.922E-05

where μ_0 is the permeability of free space. Using our result for $\boldsymbol{B}$ found earlier (2.17) we have that

$$\boldsymbol{S} = \epsilon_0 c(\boldsymbol{E} \times (\boldsymbol{n} \times \boldsymbol{E})) = \epsilon_0 c(E^2\boldsymbol{n} - (\boldsymbol{n} \cdot \boldsymbol{E})\boldsymbol{E})$$

but $\boldsymbol{n} \cdot \boldsymbol{E} = 0$ since they are orthogonal from (2.18) and so

$$\boldsymbol{S} = \epsilon_0 c E^2 \boldsymbol{n} \ .$$

If we define an area at the observer in terms of a solid angle $\Delta\Omega$ then we can say that the energy radiated by the electron through this area ($R^2\Delta\Omega$) in the time Δt is

$$W = (\boldsymbol{n} \cdot \boldsymbol{S})\Delta t R^2 \Delta\Omega = \epsilon_0 c E^2 R^2 \Delta t \Delta\Omega \ .$$

The power observed will be

$$P = \frac{dW}{dt} = \int \epsilon_0 c E^2 R^2 \, d\Omega \ ,$$

and the power observed per solid angle will be

$$\frac{dP}{d\Omega} = \frac{d^2 W}{dt \, d\Omega} = \epsilon_0 c E^2 R^2 \ .$$

The total energy received by the observer in a single turn of the electron is

$$W = \int_0^{4\pi} \int_{-\infty}^{\infty} \epsilon_0 c E^2(t) R^2 \, dt \, d\Omega$$

and the energy received per unit solid angle is

$$\frac{dW}{d\Omega} = \int_{-\infty}^{\infty} \epsilon_0 c E^2(t) R^2 \, dt$$

We now express $E(t)$ in terms of its Fourier Transform

$$E(t) = \frac{1}{\sqrt{2\pi}} \int_{-\infty}^{\infty} E(\omega) e^{-i\omega t} \, d\omega \ ,$$

and we get

$$\frac{dW}{d\Omega} = \frac{\epsilon_0 c R^2}{2\pi} \int_{-\infty}^{\infty} \int_{-\infty}^{\infty} \int_{-\infty}^{\infty} E(\omega) e^{-i\omega t} E(\omega') e^{-i\omega' t} \, d\omega \, d\omega' \, dt \ .$$

Noting at this point that the Dirac delta function has integral form [19]

$$\delta(x) = \frac{1}{2\pi} \int_{-\infty}^{\infty} e^{ixt} \, dt$$

and so

$$\frac{dW}{d\Omega} = \epsilon_0 c R^2 \int_{-\infty}^{\infty} \int_{-\infty}^{\infty} E(\omega) E(\omega') \delta(-\omega - \omega') \, d\omega \, d\omega' \ .$$

Since $E(t)$ is a real function, its conjugate $E^*(t) = E(t)$ (this is easy to see if one expresses the exponential term in trigonometric form). This then has the

consequence that $E^*(\omega) = E(-\omega)$. Remembering that, by definition, the integral of the delta function is equal to unity, the energy per solid angle then becomes

$$
\begin{aligned}
\frac{dW}{d\Omega} &= \epsilon_0 c R^2 \int_{-\infty}^{\infty} E(\omega) E^*(\omega) \, d\omega \\
&= \epsilon_0 c R^2 \int_{-\infty}^{\infty} E(\omega) E(-\omega) \, d\omega \\
&= \epsilon_0 c R^2 \int_{-\infty}^{\infty} |E(\omega)|^2 \, d\omega \\
&= 2\epsilon_0 c R^2 \int_{0}^{\infty} |E(\omega)|^2 \, d\omega \ ,
\end{aligned}
$$

and the *spectral* angular distribution radiated by an electron on a single revolution is

$$
\frac{d^2 W}{d\Omega \, d\omega} = 2\epsilon_0 c R^2 |E(\omega)|^2 \ , \tag{2.28}
$$

where 'spectral' implies that it is into a particular frequency band. Since the electron is on a circular path it will make $c/2\pi\rho$ revolutions per second. And so the spectral power angular density will be

$$
\frac{d^2 P}{d\Omega \, d\omega} = \frac{c}{2\pi\rho} \frac{d^2 W}{d\Omega \, d\omega} = \frac{R^2}{\pi\mu_0\rho} |E(\omega)|^2 \ .
$$

We can insert $|E(\omega)|^2 = E_x^2(\omega) + E_y^2(\omega)$ into the above equation and use our results from (2.26) and (2.27)

$$
\frac{d^2 P}{d\Omega \, d\omega} = \frac{3e^2\gamma^2}{32\pi^4\epsilon_0\rho} \left(\frac{\omega}{\omega_c}\right)^2 (1+\gamma^2\psi^2)^2 \left[K_{2/3}^2(G) + \frac{\gamma^2\psi^2}{(1+\gamma^2\psi^2)} K_{1/3}^2(G) \right]. \tag{2.29}
$$

Integrating this over all angles will give the spectral power, remembering that Ω is the solid angle [14].

$$
\begin{aligned}
\frac{dP}{d\omega} &= \int \frac{d^2 P}{d\Omega \, d\omega} \, d\Omega = 2\pi \int \frac{d^2 P}{d\psi \, d\omega} \, d\psi \\
&= \frac{P_0}{\omega_c} S\left(\frac{\omega}{\omega_c}\right) = \frac{P_0}{\omega_c} \left(S_x\left(\frac{\omega}{\omega_c}\right) + S_y\left(\frac{\omega}{\omega_c}\right) \right) \ , \tag{2.30}
\end{aligned}
$$

where P_0 is the total power radiated by one electron [12]

$$
P_0 = \frac{ce^2\gamma^4}{6\pi\epsilon_0\rho^2}
$$

and

$$S_x\left(\frac{\omega}{\omega_c}\right) = \frac{9\sqrt{3}\,\omega}{16\pi\omega_c}\left[\int_{\omega/\omega_c}^{\infty} K_{5/3}(u)\,du + K_{2/3}\left(\frac{\omega}{\omega_c}\right)\right]$$

$$S_y\left(\frac{\omega}{\omega_c}\right) = \frac{9\sqrt{3}\,\omega}{16\pi\omega_c}\left[\int_{\omega/\omega_c}^{\infty} K_{5/3}(u)\,du - K_{2/3}\left(\frac{\omega}{\omega_c}\right)\right]$$

$$S\left(\frac{\omega}{\omega_c}\right) = \frac{9\sqrt{3}\,\omega}{8\pi\omega_c}\int_{\omega/\omega_c}^{\infty} K_{5/3}(u)\,du \ .$$

The functions S, S_x, and S_y are plotted in Fig. 2.6 and values for the integral of $K_{5/3}$ are given in Table 2.1. It is clear from this graph that the majority of the power is horizontally polarized. We can integrate $dP/d\omega$ over frequency to find some remarkable results. First if we consider all frequencies then

$$\int_0^{\infty} S\left(\frac{\omega}{\omega_c}\right)\,d(\omega/\omega_c) = 1$$

$$\int_0^{\infty} S_x\left(\frac{\omega}{\omega_c}\right)\,d(\omega/\omega_c) = \frac{7}{8}$$

$$\int_0^{\infty} S_y\left(\frac{\omega}{\omega_c}\right)\,d(\omega/\omega_c) = \frac{1}{8} \ .$$

Therefore, of all of the power radiated, exactly 7/8 is horizontally polarized and exactly 1/8 is vertically polarized. If we only integrate the frequencies up to $\omega = \omega_c$ then we find

$$\int_0^1 S\left(\frac{\omega}{\omega_c}\right)\,d(\omega/\omega_c) = \frac{1}{2} \ ,$$

which demonstrates that the critical frequency, ω_c, actually divides the power spectrum into two equal parts. This fact is often used in the literature to *define* the critical frequency.

Having integrated (2.29) over all angles to examine the power emitted as a function of frequency, we will now do the reverse and integrate over frequency to determine how the power varies with angle [14].

$$\frac{dP}{d\Omega} = \int \frac{d^2P}{d\Omega\,d\omega}\,d\omega = 2\pi\int\frac{d^2P}{d\psi\,d\omega}\,d\omega$$

$$\frac{dP}{d\psi} = \frac{21P_0\gamma}{32(1+\gamma^2\psi^2)^{5/2}}\left[1+\frac{5\gamma^2\psi^2}{7(1+\gamma^2\psi^2)}\right] \ . \tag{2.31}$$

The first and second terms in the square brackets again correspond to the horizontal and vertical polarizations, respectively. This function is plotted in
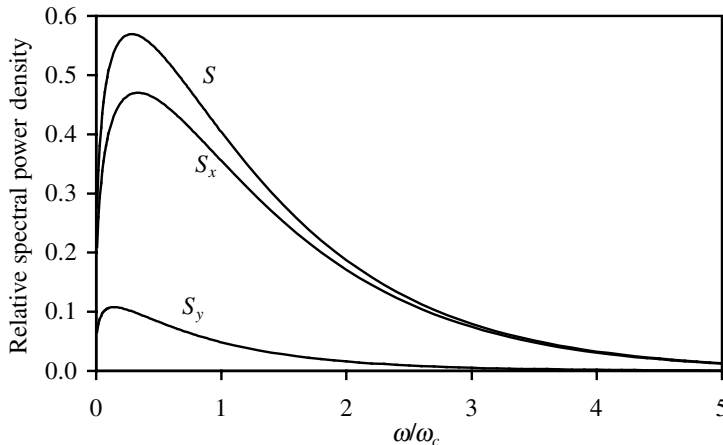
FIG. 2.6. The power spectral density and the horizontal and vertical polarization
components.
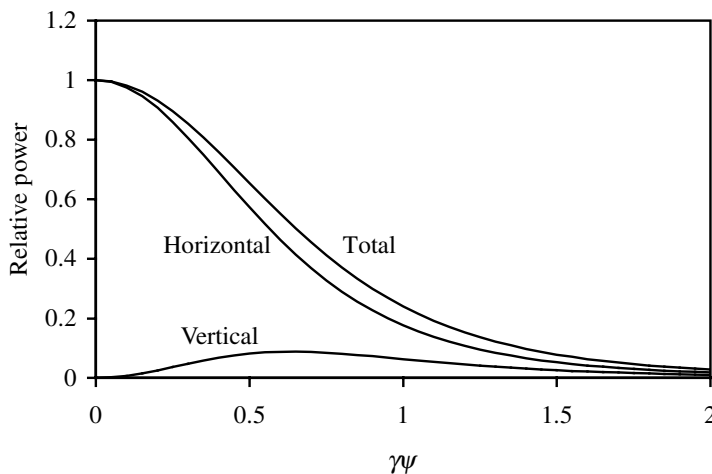
FIG. 2.7. The angular power distribution and the horizontal and vertical polar-
ization components.

Fig.2.7, again demonstrating that there is no vertical power on-axis. We could
integrate this result further over ψ to show that of the total power emitted 7/8
is horizontally polarized and 1/8 vertically as seen earlier.

2.4.2   *Photon Flux*

It is quite straightforward to convert the power results from the previous section
into a more commonly used result in terms of the number of photons. The energy

TABLE 2.2 Example values for the critical photon energy and angular frequency for three light sources

Ring	Energy (GeV)	γ	B (T)	ρ (m)	ω_c ($\times 10^{18}\text{s}^{-1}$)	ϵ_c (keV)	λ_c (nm)
SRS	2	3914	1.2	5.56	4.9	3.19	0.39
DIAMOND	3	5871	1.4	7.15	13	8.38	0.15
ESRF	6	11742	0.8	25.0	29	19.2	0.06

of each photon comes from the well known result $\epsilon = h\omega/2\pi = \hbar\omega$, where h is the Planck constant. Note at this point that the *critical photon energy* is, as expected, given by $\epsilon_c = \hbar\omega_c$. Similarly the *critical wavelength* is given by $\lambda_c = 2\pi c/\omega_c$. Typical values for ω_c, ϵ_c, and other common parameters are given in Table 2.2.

If the number of photons emitted per second with energy ϵ is $\dot{N}$ then the power emitted at that photon energy is simply $\dot{N}\epsilon$. The number of photons emitted per second per solid angle by one electron into a relative photon energy bandwidth $\Delta\epsilon/\epsilon$ is

$$\frac{d^2\dot{N}}{d\Omega\,d\epsilon/\epsilon} = \frac{\epsilon d^2\dot{N}}{d\Omega\,d\epsilon}$$

$$= \frac{d^2P}{d\Omega\,d\epsilon} = \frac{d^2P}{\hbar\,d\Omega\,d\omega}$$

$$= \frac{3e^2\gamma^2}{32\pi^4\hbar\epsilon_0\rho}\left(\frac{\omega}{\omega_c}\right)^2(1+\gamma^2\psi^2)^2\left[K_{2/3}^2(G) + \frac{\gamma^2\psi^2}{(1+\gamma^2\psi^2)}K_{1/3}^2(G)\right] \ .$$

Remembering that the fine structure constant, α, is given by

$$\alpha = \frac{e^2}{2ch\epsilon_0} \approx \frac{1}{137}$$

this becomes

$$\frac{d\dot{N}}{d\Omega} = \frac{3\alpha\gamma^2}{4\pi^2}\frac{c}{2\pi\rho}\left(\frac{\Delta\epsilon}{\epsilon}\right)\left(\frac{\omega}{\omega_c}\right)^2$$

$$\times(1+\gamma^2\psi^2)^2\left[K_{2/3}^2(G) + \frac{\gamma^2\psi^2}{(1+\gamma^2\psi^2)}K_{1/3}^2(G)\right] \ . \qquad (2.32)$$

Let us consider for a moment how many electrons, N_e, are passing a given point per second for a given beam current of electrons, I_b. The electron beam current, measured in amperes, is simply the amount of charge flowing in unit time. For a beam of electrons this is simple to calculate as the charge carried by each electron, e, is well known. However, we must remember that as the electrons

are travelling on a circular path they will pass the same point many times in one second. Putting all this together we find that the beam current is given by the product of the number of electrons, the charge per electron, and the number of revolutions per second

$$I_b = N_e e \frac{c}{2\pi\rho} \quad. \tag{2.33}$$

Rearranging this we find that the number of electrons is given by

$$N_e = \frac{I_b}{e} \frac{2\pi\rho}{c} \quad.$$

So the number of photons emitted per second per solid angle into a bandwidth $\Delta\epsilon/\epsilon$ by a beam current, I_b, is

$$\frac{d\dot{N}}{d\Omega} = \frac{3\alpha\gamma^2}{4\pi^2} \frac{I_b}{e} \left(\frac{\Delta\epsilon}{\epsilon}\right) \left(\frac{\omega}{\omega_c}\right)^2 (1 + \gamma^2\psi^2)^2$$
$$\times \left[K_{2/3}^2(G) + \frac{\gamma^2\psi^2}{(1 + \gamma^2\psi^2)} K_{1/3}^2(G) \right] \quad. \tag{2.34}$$

The quantity $d\dot{N}/d\Omega$ is referred to as the *spectral angular flux density* or more correctly the *spectral intensity*. We can write this quantity in more useful terms, with units of photons per second per milliradian^2 per 0.1% bandwidth

$$\frac{d\dot{N}}{d\Omega} = 1.33 \times 10^{13} \, E^2 I_b \left(\frac{\omega}{\omega_c}\right)^2$$
$$\times (1 + \gamma^2\psi^2)^2 \left[K_{2/3}^2(G) + \frac{\gamma^2\psi^2}{(1 + \gamma^2\psi^2)} K_{1/3}^2(G) \right] \quad, \tag{2.35}$$

where E is the electron energy in GeV and I_b is given in A. If we consider only the radiation that is *on-axis* ($\psi = 0$) then this simplifies to

$$\left.\frac{d\dot{N}}{d\Omega}\right|_{\psi=0} = 1.33 \times 10^{13} \, E^2 I_b \left(\frac{\omega}{\omega_c}\right)^2 K_{2/3}^2 \left(\frac{\omega}{2\omega_c}\right) \quad. \tag{2.36}$$

Three examples for the spectral intensity are given in Fig. 2.8, each for a different photon angular frequency. Note that at lower frequency and longer wavelength, the radiation extends further out in the vertical angle and also that the vertical polarization contribution becomes quite significant. Since the vertical electric field is 90° out of phase with the horizontal component (by inspection of (2.26) and (2.27)), the result is circular polarization. We can also see that at frequencies close to ω_c the approximation that the radiation is emitted with a
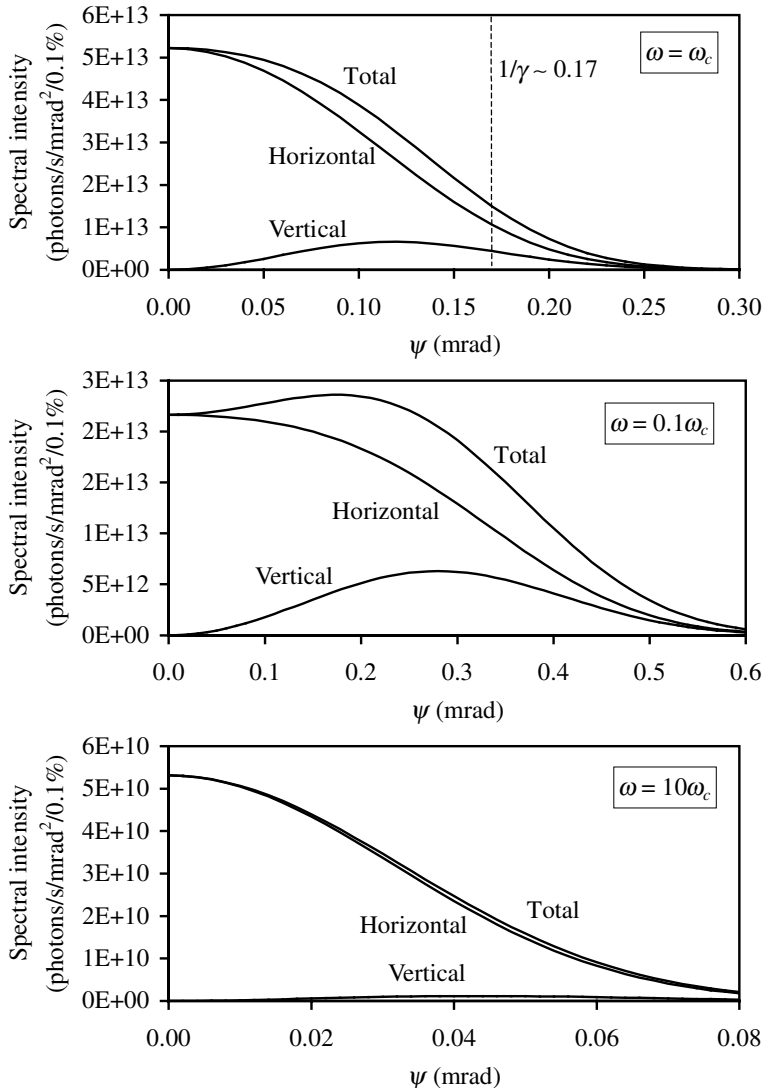
FIG. 2.8. Spectral intensity at ω_c, $0.1\omega_c$, and $10\omega_c$ for a 300 mA, 3 GeV electron beam passing through a 1.4 T bending magnet.

vertical angle of $\pm 1/\gamma$ is a good one. Finally we can see that at high frequencies the angular distribution is significantly less and the beam is more tightly collimated.

We can use the same approach to look at the number of photons emitted per electron per second into all angles

$$\frac{d\dot{N}}{d\epsilon/\epsilon} = \frac{dP}{\hbar\,d\omega} = \frac{P_0}{\hbar\omega_c}S\left(\frac{\omega}{\omega_c}\right)$$
$$= \frac{ce^2\gamma^4}{6\pi\epsilon_0\rho^2\epsilon_c}\frac{9\sqrt{3}\,\omega}{8\pi\omega_c}\int_{\omega/\omega_c}^{\infty}K_{5/3}(u)\,du \ .$$

Substituting in for the critical photon energy

$$\epsilon_c = \hbar\omega_c = \frac{3hc\gamma^3}{4\pi\rho} \tag{2.37}$$

and noting that $\omega/\omega_c = \epsilon/\epsilon_c$ we get

$$\frac{d\dot{N}}{d\epsilon/\epsilon} = \sqrt{3}\,\gamma\frac{e^2}{2ch\epsilon_0}\frac{c}{2\pi\rho}\left(\frac{\epsilon}{\epsilon_c}\right)\int_{\epsilon/\epsilon_c}^{\infty}K_{5/3}(u)\,du$$
$$= \sqrt{3}\,\alpha\gamma\frac{c}{2\pi\rho}\left(\frac{\epsilon}{\epsilon_c}\right)\int_{\epsilon/\epsilon_c}^{\infty}K_{5/3}(u)\,du \ .$$

Again, multiplying this result by the number of electrons will give us the number of photons emitted per second into all angles for a beam current, I_b, into a relative energy bandwidth $\Delta\epsilon/\epsilon$

$$\dot{N} = \sqrt{3}\,\alpha\gamma\frac{I_b}{e}\left(\frac{\Delta\epsilon}{\epsilon}\right)\left(\frac{\epsilon}{\epsilon_c}\right)\int_{\epsilon/\epsilon_c}^{\infty}K_{5/3}(u)\,du \ . \tag{2.38}$$

The parameter $\dot{N}$ is referred to as the *spectral photon flux* or the *vertically integrated spectral flux*, this latter name conveys the message that the photon emission has been summed over all angles (as the electron travels on a circle of 2π radians it is automatically integrated horizontally). Again, in practical units this reduces to

$$\dot{N} = 2.46 \times 10^{13}\,EI_b\left(\frac{\epsilon}{\epsilon_c}\right)\int_{\epsilon/\epsilon_c}^{\infty}K_{5/3}(u)\,du \tag{2.39}$$

in units of photons per second per milliradian horizontally per 0.1% bandwidth.

A plot of $\dot{N}$ versus ϵ/ϵ_c is known as the *universal curve* (Fig. 2.9). Absolute flux levels for a particular electron energy and beam current can be quickly scaled off the curve for any photon energy once the critical photon energy is calculated. It should be clear from this that all bending magnet sources have the same characteristic spectrum. The spectral flux always increases slowly from the low photon energies, peaking at approximately $\epsilon/\epsilon_c = 0.25$. The spectrum then falls off sharply, with a typical consideration being that the flux is useful up to about $\epsilon/\epsilon_c \approx 5$. The low photon energies extend down until the emitted radiation reaches a wavelength of the order of the vacuum chamber dimensions
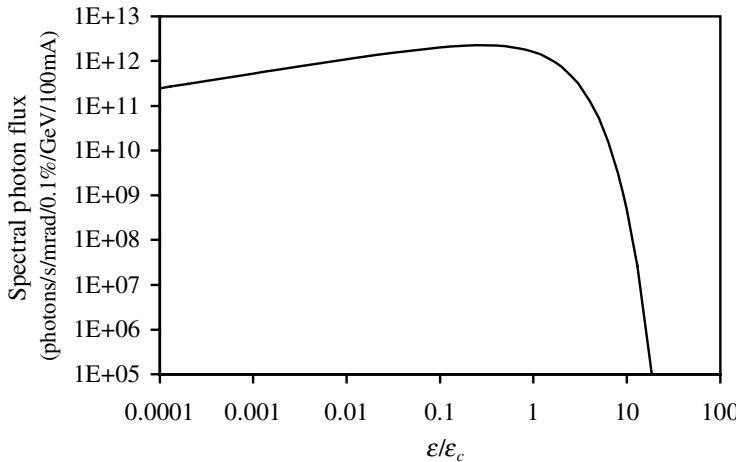
FIG. 2.9. The universal flux curve. Note that both axes have a logarithmic scale.
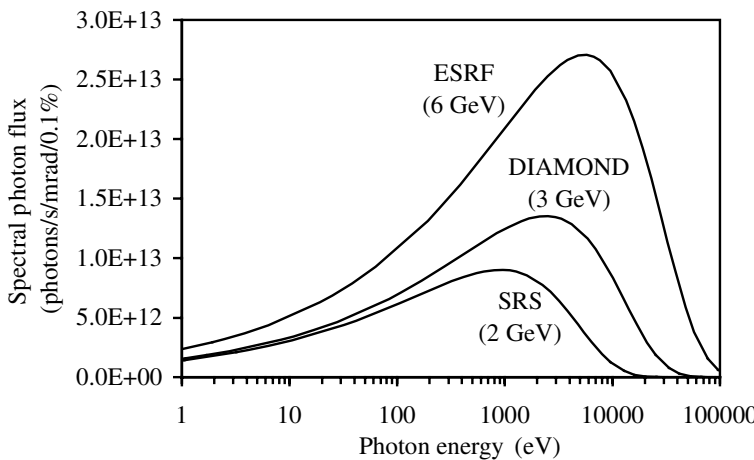

FIG. 2.10. Spectral output from the bending magnets of three well known electron storage rings. A beam current of 200 mA has been assumed. Note the logarithmic scale along the *x*-axis.

(usually tens of mm) and so becomes cut-off from the observer. Typical bending magnet spectral curves are shown in Fig. 2.10 for the three storage rings whose parameters are given in Table 2.2.

In summary then, the spectral range covered by a bending magnet is fixed by the critical photon energy, which is a function of the electron energy and the bending radius (2.37). The bending radius itself depends upon the electron

energy and the magnetic field, B

$$\rho = \frac{E}{0.3B} \quad,$$

where E is expressed in GeV and B is in Tesla and so in more practical units the critical energy is given (in eV) by

$$\epsilon_c = 665E^2B$$

In an electron storage ring with a fixed energy the SR spectrum can be shifted sideways along the photon energy axis if a different ϵ_c can be generated locally. It is possible to change ϵ_c in this way by having a different magnetic field in a local part of the storage ring. The insertion devices which can produce this local change in ϵ_c and so shift the SR spectrum, go by the name of *wavelength shifters* and these are the subject of Section 2.6.

2.4.3 *Vertical Opening Angle*

We have already seen that different photon energies emit SR over quite different vertical angular distributions. It is useful to be able to estimate what a 'typical' angle might be for each particular photon energy. This 'typical' angle is the so-called *vertical opening angle* of the radiation, denoted as $\sigma_{r'}$. The most common method for estimating this opening angle is to assume that the angular distribution follows a Gaussian or Normal distribution. This is not a particularly good assumption, especially when $\epsilon \ll \epsilon_c$ where the vertical polarization component can become quite significant (see Fig. 2.8, for example) so the results should always be treated with some caution.

Let's just remind ourselves of the main features of a Gaussian distribution. First it has a functional form

$$f(x) = \frac{1}{\sqrt{2\pi}\,\sigma} \exp\left(-\frac{(x-\mu)^2}{2\sigma^2}\right) \quad,$$

where μ is the *mean* and σ is the *standard deviation*. Second, the integral of $f(x)$ over all x is equal to unity and finally, the full width at half maximum (FWHM) for a Gaussian distribution is equal to $2.355\,\sigma$.

Now, we are assuming that the vertical angular distribution is of Gaussian form and symmetric about $\psi = 0$, so

$$\frac{d\dot{N}}{d\Omega} = \left.\frac{d\dot{N}}{d\Omega}\right|_{\psi=0} \exp\left(-\frac{\psi^2}{2\sigma_{r'}^2}\right) \quad. \tag{2.40}$$

Integrating this over all vertical angles we get

$$\frac{\dot{N}}{2\pi} = \sqrt{2\pi}\,\sigma_{r'} \left.\frac{d\dot{N}}{d\Omega}\right|_{\psi=0}$$

therefore

$$\sigma_{r'} = \frac{\dot{N}}{2\pi\sqrt{2\pi}\ \left.\frac{d\dot{N}}{d\Omega}\right|_{\psi=0}}$$

Substituting our results from (2.38) and (2.34) gives

$$\sigma_{r'} = \frac{\sqrt{3}\,\alpha\gamma(I_b/e)(\Delta\epsilon/\epsilon)(\epsilon/\epsilon_c)\int_{\epsilon/\epsilon_c}^{\infty}K_{5/3}(u)\,du}{2\pi\sqrt{2\pi}(3\alpha\gamma^2/4\pi^2)(I_b/e)(\Delta\epsilon/\epsilon)(\epsilon/\epsilon_c)^2K_{2/3}^2(\epsilon/2\epsilon_c)}$$

$$= \sqrt{\frac{2\pi}{3}}\,\frac{1}{\gamma}\left(\frac{\epsilon_c}{\epsilon}\right)\frac{\int_{\epsilon/\epsilon_c}^{\infty}K_{5/3}(u)\,du}{K_{2/3}^2(\epsilon/2\epsilon_c)} \qquad (2.41)$$

So, for instance, at $\epsilon = \epsilon_c$ we find that

$$\sigma_{r'} = \frac{0.65}{\gamma}$$

A plot of the output from the above result for $\sigma_{r'}$ is given in Fig. 2.11 for a 3 GeV electron beam. Note that the vertical opening angle changes by two orders of magnitude between low and high photon energies. The examples that were used for Fig. 2.8 are plotted again in Fig. 2.12 but this time with the superimposed ideal Gaussian distribution using the calculated value of $\sigma_{r'}$ as well. It is clear from this that the Gaussian assumption is only correct at the highest photon energies, the approximation is already struggling at $\epsilon = \epsilon_c$. Since this treatment is only an approximation, if the exact vertical angular distribution is of particular interest the distribution $d\dot{N}/d\Omega$ should be examined directly.

2.4.4 *Bending Magnet Brightness*

If we take a perpendicular slice through the SR travelling towards the observer then we will intercept millions of photons. Each of these photons in this slice will have a particular position and angular direction. Some will have a position close to the axis but a relatively large divergence and others will be far from the axis but have a very shallow trajectory. This concept of particles having a position and an angle that evolves with time as they travel towards the observer is known as the *phase space*. It is an important concept that also crops up in many other areas of physics. In particular, it is often used in accelerator physics to describe the distribution of the charged particles travelling around an accelerator.

The *brightness* of a source is the phase space density of the photon flux (i.e. the photons per unit solid angle per unit solid area) and it is a figure of merit that takes into account not only the number of photons emitted but also their concentration. It is often encountered in geometric optics where it is widely used because it is a quantity which is *invariant* in an ideal optical beam transport system (a result from thermodynamics known as *Liouville's theorem* [20]), unlike angular flux density, for instance.
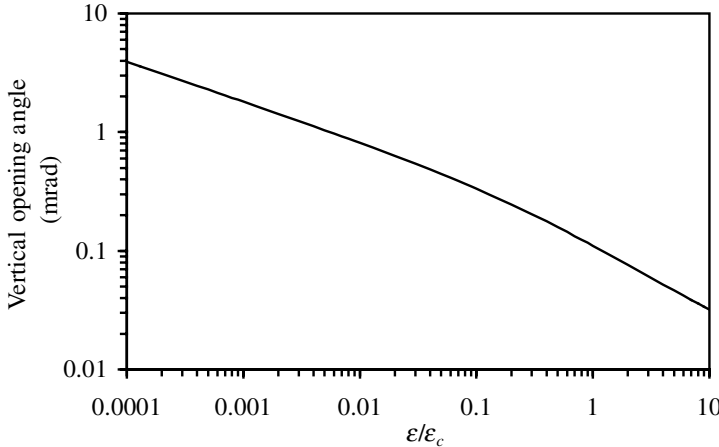
FIG. 2.11. A plot of $\sigma_{r'}$ vs. ϵ/ϵ_c for a 3 GeV electron beam.

To calculate the bending magnet brightness we need to consider the effective phase space area from which the photon flux is being emitted taking account of both the finite electron and photon beam sizes and divergences. First, there is no need to consider any horizontal angle effects as the light is emitted smoothly over the full horizontal 2π radians. The effective vertical angle, $\Sigma_{y'}$, will be a combination of the electron vertical beam divergence, $\sigma_{y'}$, and the photon beam opening angle, $\sigma_{r'}$. Since these are both from Gaussian distributions they are added in quadrature

$$\Sigma_{y'} = \sqrt{\sigma_{y'}^2 + \sigma_{r'}^2} \ .$$

For the effective source sizes we have to combine the electron beam sizes, σ_x and σ_y, with the photon beam size, σ_r, in a similar manner

$$\Sigma_x = \sqrt{\sigma_x^2 + \sigma_r^2}$$
$$\Sigma_y = \sqrt{\sigma_y^2 + \sigma_r^2} \ .$$

The photon beam size is found by approximating the single electron photon source to the fundamental mode of an optical resonator (see Section 4.4)

$$\sigma_r = \frac{\lambda}{4\pi\sigma_{r'}} \ .$$

The bending magnet brightness, B, is then given by

$$B = \frac{\dot{N}}{(2\pi)^{3/2}\Sigma_x\Sigma_y\Sigma_{y'}} \ ,$$
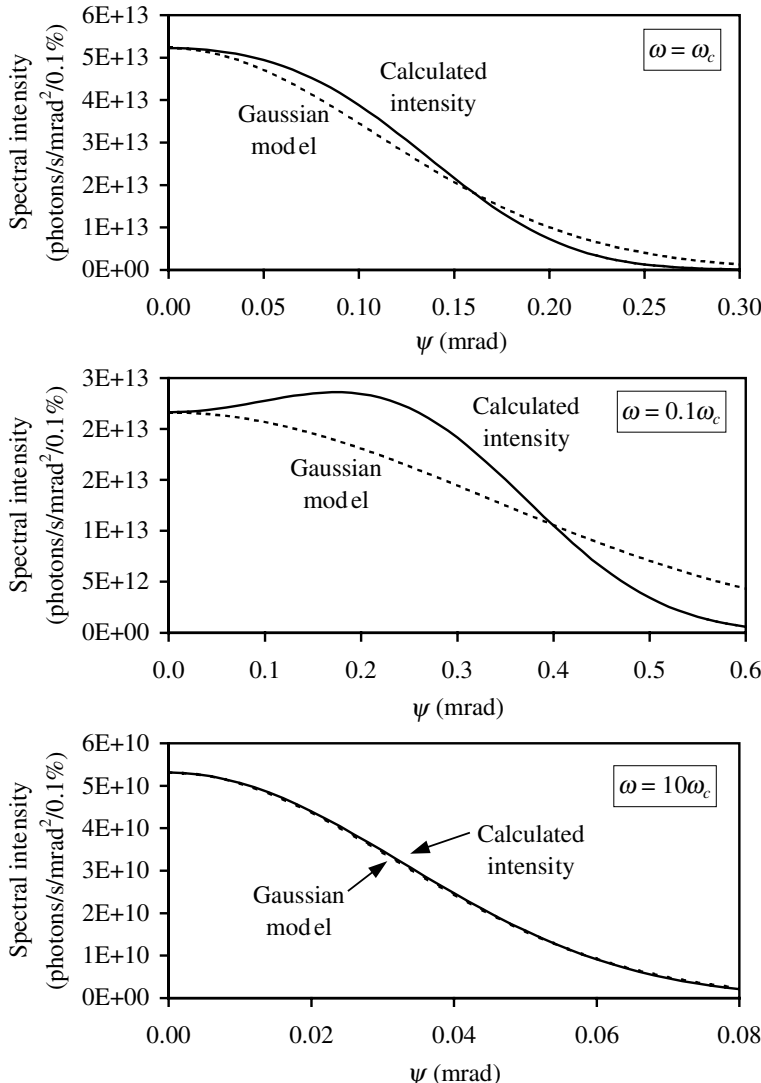
FIG. 2.12. Spectral intensity at ω_c, $0.1\omega_c$, and $10\omega_c$ for a 300 mA, 3 GeV electron beam passing through a 1.4 T bending magnet. Also plotted is the Gaussian distribution for the appropriate vertical opening angle $\sigma_{r'}$.

where $\dot{N}$ is the photon flux per unit horizontal angle (2.38). Note that each Σ term introduces a $\sqrt{2\pi}$ because the rectangular function of equal area to a Gaussian has a width of $\sqrt{2\pi}\sigma$ (see Section 2.4.3).

In general, $\sigma_r \ll \sigma_{x,y}$ and the brightness equation can be simplified to

$$B = \frac{\dot{N}}{(2\pi)^{3/2}\sigma_x\sigma_y(\sigma_{y'}^2 + \sigma_{r'}^2)^{1/2}} \ .$$

The bending magnet brightness has units of photons per second per solid area per solid angle per spectral bandwidth.

2.5 Power and Power Density from a Bending Magnet

A considerable amount of power can be generated in the form of synchrotron radiation in a storage ring. This is not only important for the users of the radiation but also those who have to design and operate the accelerator. The power and power density levels are often high enough in a synchrotron light source to cause damage to the accelerator itself. A number of accelerators around the world have melted components inside the vacuum chamber and the vacuum chamber itself in some cases! For this reason all light sources have to water cool many items inside the vacuum system that the synchrotron radiation impinges upon. In some accelerators sophisticated monitoring of the electron beam position is necessary to ensure that it is operating safely and if the beam moves outside of certain prescribed limits it is quickly dumped to prevent any possible thermal damage.

2.5.1 *Total Power*

The instantaneous total power emitted by a single relativistic electron is [12]

$$P_0 = \frac{ce^2\gamma^4}{6\pi\epsilon_0\rho^2} \ ,$$

where ρ is the radius of curvature of the electron path. So, in a storage ring of circumference, C, with fixed bending radius in the dipoles, ρ_0, the energy radiated by each electron per turn is

$$\Delta E = \frac{e^2\gamma^4}{6\pi\epsilon_0} \int_0^C \frac{ds}{\rho_0^2} \tag{2.42}$$

(the c is cancelled because the integral is expressed with respect to s and not t). And since the integral equals $2\pi/\rho_0$ (there is no emission in the straight sections) this becomes

$$\Delta E = \frac{e^2\gamma^4}{3\epsilon_0\rho_0} \ .$$

So, the total power emitted by a beam of electrons of current, I_b, using (2.33) is

$$P_{\text{total}} = \frac{e\gamma^4 I_b}{3\epsilon_0\rho_0} \ ,$$

which in practical units is

$$P_{\text{total}} = 88.46 \frac{E^4 I_b}{\rho_0} \ , \tag{2.43}$$

where the power is in kW and the electron energy, E, is in GeV.

TABLE 2.3 Example values for the power, power per horizontal angle and power density on-axis for three light sources

Ring	Energy (GeV)	ρ (m)	I_b (mA)	P_{total} (kW)	$dP/d\theta$ (W/mrad)	$dP/d\Omega$ (W/mrad^2)
SRS	2	5.56	200	50.9	8.1	20.8
DIAMOND	3	7.15	300	300.7	47.9	184.4
ESRF	6	25.0	200	916.5	145.9	1124.0

Another useful number to know is the power per horizontal angle. Again, expressed in practical units this is given by

$$\frac{dP}{d\theta} = 14.08 \, \frac{E^4 I_b}{\rho_0} \;,$$

where the result is in W/mrad.

2.5.2 *Power Density*

The bending magnet power distribution in the vertical plane has already been derived (2.31) and plotted in Fig. 2.7. We can use this result to find the power density. In particular, the power density on-axis ($\psi = 0$) is given by

$$\left.\frac{dP}{d\Omega}\right|_{\psi=0} = \frac{21\gamma}{64\pi} P_{\text{total}} \;,$$

which in practical units of W/mrad^2 is

$$\left.\frac{dP}{d\Omega}\right|_{\psi=0} = 18.08 \, \frac{E^5 I_b}{\rho_0} \;. \tag{2.44}$$

Some actual values for the power levels that are experienced in modern light sources are given in Table 2.3.

2.6 Wavelength Shifters

Wavelength shifters are a type of insertion device, which essentially produces bending magnet style radiation. The advantage that they have over the storage ring bend magnets is that their magnetic field, and so the critical photon energy, can be tailored to a specific beamline requirement. Generally, wavelength shifters are used to shift the spectrum towards the higher photon energy end. In the SRS, for instance, the 6.0 T magnetic field in one of the wavelength shifters produces a critical photon energy five times higher than the 1.2 T bending magnets [21]. This gives a larger flux at the high photon energy end of the spectrum than is normally available (Fig. 2.13). From this plot it becomes apparent why the term *wavelength shifter* is used since the spectrum literally *shifts* along the photon energy x-axis.
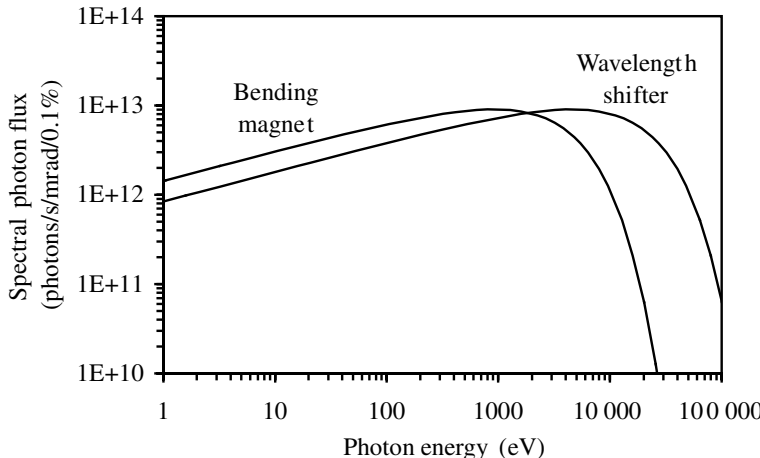
FIG. 2.13. A comparison between the spectral photon flux emitted by a 1.2 T
    SRS bending magnet and the 6.0 T wavelength shifter. The beam current is
    200 mA and the electron energy is 2 GeV.

There is no *absolute* change to the *total* number of photons emitted, just the
wavelength at which they are emitted changes.

A wavelength shifter usually consists of one high magnetic field central pole
surrounded by two weaker side poles of opposite polarity. A typical magnetic
field profile along a wavelength shifter and the electron trajectory through such
a magnet is shown in Fig. 2.14. The magnetic field strengths are arranged so
that the total integrated field strength along the longitudinal axis is equal to
zero. This ensures that the overall angular deflection to the electron is zero and
that the electron exits the insertion device on the same axis that it entered on.

Since the magnetic field along the length of the wavelength shifter is not
constant, the critical photon energy also varies along its length (see Fig. 2.14).
This means that although the SR produced has the same characteristics of bend-
ing magnet radiation, the exact characteristics observed depend on which part
of the electron trajectory the observer is looking at. Furthermore, the observer
may simultaneously also see SR produced by the side poles, which may enhance
the flux but also give a light source with more than one source point.

A wavelength shifter will typically deflect the electron beam by the order
of 10 mm at the peak of the bump, which is of course the optimum source
point (highest magnetic field strength). Clearly if the magnetic field strength
of the wavelength shifter is altered the size of this deflection will alter, in turn
changing the source point position. It is possible to produce a wavelength shifter,
which always has the main source point on-axis by the inclusion of two further
side poles. Examples of this are the 7 T wavelength shifters at CAMD [23] and
BESSY II [24].
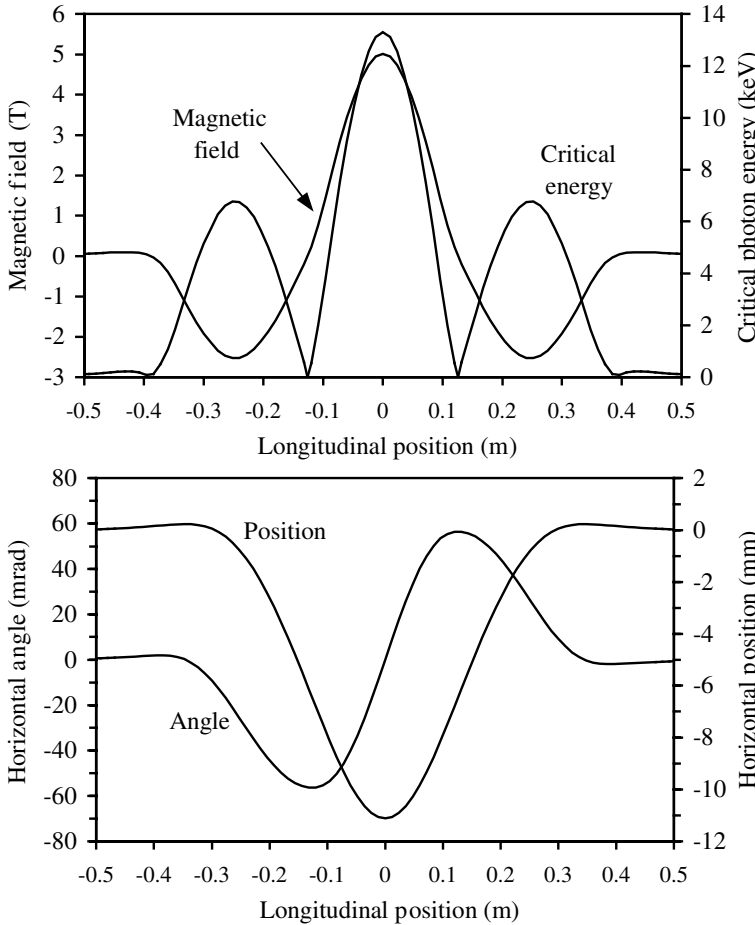
FIG. 2.14. The magnetic field profile for the SRS 5 T wavelength shifter [22], the critical energy and the position and angle of a 2 GeV electron through the magnet.

2.7   Extension to Multipole Wigglers

We have just seen that a wavelength shifter, which is simply a single, large bump on the electron trajectory can produce synchrotron radiation that is essentially bending magnet radiation. Imagine putting several identical wavelength shifters one after the other in a straight section of a storage ring. The electron would simply travel through each wavelength shifter in turn emitting synchrotron radiation in the forward direction. Each wavelength shifter is independent of the other and the electron returns back to the beam axis after passing through each one. Although there is no fundamental relationship between each wavelength shifter
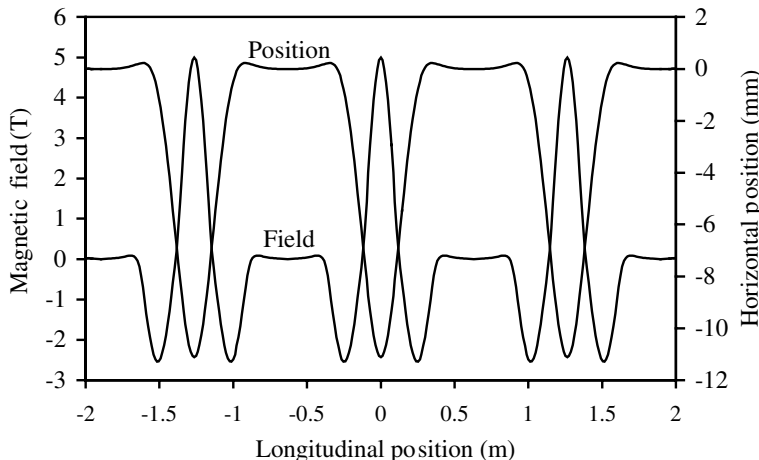
FIG. 2.15. Magnetic field and electron trajectory for three consecutive wavelength shifters in a straight section. The observer will receive three times more flux than from one wavelength shifter.

in terms of the emission of light, an observer will see an enhancement in the flux received simply because there are now several sources emitting radiation in his direction. This point is illustrated in Fig. 2.15. This concept of multiple sources, separated longitudinally and each emitting independently, forms the basis for the *multipole wiggler*. Note that the term *wiggler* on its own is used somewhat carelessly in the literature and refers sometimes to a *wavelength shifter* and sometimes to a *multipole wiggler*.

Of course, putting several wavelength shifters in a straight section is not the most efficient way of creating a multiple source. A better arrangement of alternating magnetic fields is shown in Fig. 2.16. In fact a typical multipole wiggler has a magnetic field, which closely resembles a sinusoidal profile. A detailed derivation of the synchrotron radiation emission from a multipole wiggler is given in Chapter 3 and the design of magnets to create the desired magnetic field is covered in Chapter 7 for permanent magnet based solutions and Chapter 8 for electromagnet based solutions.
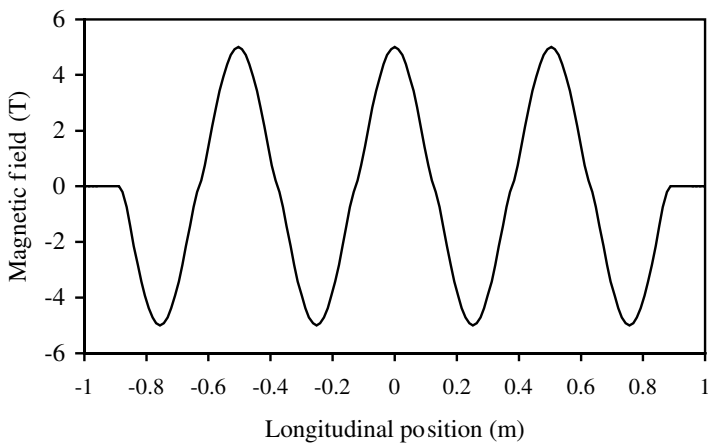
FIG. 2.16. Magnetic field arrangement that utilizes the available straight space more economically. This concept of alternating magnetic fields to generate a flux enhancement is the basis of the *multipole wiggler*.

Synchrotron Radiation Output from Multipole Wigglers

3.1 Electron Trajectory

In the coordinate frame where the electron is travelling in the s direction and it only experiences small angular deflections ($\dot{x} \ll 1, \dot{y} \ll 1$) the equations of motion for the electron are [25]

$$\ddot{x} = \frac{d^2x}{ds^2} = \frac{e}{\gamma m_0 c}(B_y - \dot{y}B_s)$$

$$\ddot{y} = \frac{d^2y}{ds^2} = \frac{e}{\gamma m_0 c}(\dot{x}B_s - B_x)$$

where m_0 is the rest mass of the electron.

In a multipole wiggler or undulator, which only deflects in the horizontal plane and so only has vertical magnetic field on the mid plane ($B_x = B_s = 0$), we have

$$\ddot{x} = \frac{eB_y}{\gamma m_0 c}$$

$$\ddot{y} = 0 \ .$$

Furthermore, if the magnetic field is sinusoidal, with period λ_u, then

$$B_y(s) = -B_0 \sin\left(\frac{2\pi s}{\lambda_u}\right)$$

and we can integrate $\ddot{x}$ to find $\dot{x}$

$$\dot{x}(s) = -\int \frac{B_0 e}{\gamma m_0 c} \sin\left(\frac{2\pi s}{\lambda_u}\right) ds$$

$$= \frac{B_0 e}{\gamma m_0 c} \frac{\lambda_u}{2\pi} \cos\left(\frac{2\pi s}{\lambda_u}\right) \ .$$

Since $\dot{x}(s)$ is the horizontal deflection angle from the s-axis we can conclude from the result above that the *maximum deflection angle* experienced by the electron is

$$\frac{B_0 e}{\gamma m_0 c} \frac{\lambda_u}{2\pi} \ .$$

We will now define a very important parameter for insertion devices, the so-called *deflection parameter*, K,

$$K = \frac{B_0 e}{m_0 c} \frac{\lambda_u}{2\pi} = 93.36 \, B_0 \lambda_u \ , \tag{3.1}$$

where B_0 is expressed in T and λ_u in m. Note that K does not have any units. We can now rewrite the angular deflection as

$$\dot{x}(s) = \frac{K}{\gamma} \cos\left(\frac{2\pi s}{\lambda_u}\right) \tag{3.2}$$

and one more integration gives $x(s)$,

$$x(s) = \frac{K}{\gamma} \int \cos\left(\frac{2\pi s}{\lambda_u}\right) ds$$
$$= \frac{K}{\gamma} \frac{\lambda_u}{2\pi} \sin\left(\frac{2\pi s}{\lambda_u}\right) \ . \tag{3.3}$$

We have now shown that the peak angular deflection caused by the sinusoidal vertical magnetic field is K/γ. This is the case for undulators and multipole wigglers, both of which have sinusoidal magnetic field variation. Remembering that the typical opening angle for the emitted synchrotron radiation (SR) is $\sim 1/\gamma$ it is intuitive that if $K < 1$ then the electron trajectory will overlap with the emitted radiation fan and that interference effects can occur. This is the case for an *undulator*. On the other hand, if $K \gg 1$ there will be little overlap and the source points can be treated as independent and bending magnet-like. This is the case for a *multipole wiggler*. There is a grey area in the distinction between undulators and wigglers when K is in the range of between 1 and 10, say. Some authors define the boundary between undulators and multipole wigglers as $K \leq 1$ and $K > 1$, respectively, others at $K \leq 5$ and $K > 5$. In fact there is no clear boundary and interference effects can still be observed at K values considerably larger than 5. Perhaps the best distinction to make between undulators and multipole wigglers is to say that undulators exhibit interference effects and multipole wigglers do not. However, some devices are built to exhibit interference effects at low photon energies and bending magnet-like output at high photon energies, leading this class of devices to be occasionally referred to as *wundulators*!

As an example of the typical electron amplitudes associated with insertion devices, if we have a magnet with a period of 50 mm and K of 3 then the peak horizontal displacement and angular deflection will be approximately 4 μm and 0.5 mrad, respectively, for a 3 GeV electron.

3.2   Multipole Wiggler Critical Energy

We found in Chapter 2 that synchrotron radiation from dipoles can be characterized by a *critical photon energy*, ϵ_c (2.37). This critical energy is used as a representative or 'typical' value for a particular dipole spectrum and the shape of the whole spectrum can be derived once the critical energy is known. The multipole wiggler, like the wavelength shifter will produce a spectrum of the same characteristic shape as a bending magnet spectrum but, as the magnetic field varies along the s axis, the critical photon energy also varies. In other words, the spectrum that the observer sees depends upon the horizontal observation angle, θ, unlike in a dipole where it has no such dependence. We will now examine how ϵ_c varies in a multipole wiggler.

From (2.37) we have that the critical energy is given by

$$\epsilon_c = \frac{3hc\gamma^3}{4\pi\rho} \ ,$$

which in more practical units is

$$\epsilon_c = 665\, E^2 B \ ,$$

where ϵ_c is measured in eV, the electron energy, E, is measured in GeV and the magnetic field, B, is measured in Tesla.

If the observer views the radiation emitted from a multipole wiggler with zero deflection angle (i.e. $\dot{x}(s) = \theta = 0$) then the critical energy of the spectrum observed is

$$\epsilon_{c0} = 665\, E^2 B_0 \ .$$

At any particular value of s and θ the critical energy will be

$$\epsilon_c = 665\, E^2 B_0 \sin\left(\frac{2\pi s}{\lambda_u}\right)$$
$$= \epsilon_{c0} \sin\left(\frac{2\pi s}{\lambda_u}\right) \ .$$

Since, from the electron trajectory calculations (3.2), we know that

$$\cos\left(\frac{2\pi s}{\lambda_u}\right) = \frac{\theta\gamma}{K}$$

we can rewrite the critical energy for a multipole wiggler as

$$\epsilon_c = \epsilon_{c0}\sqrt{1 - \left(\frac{\theta\gamma}{K}\right)^2} = \epsilon_{c0}\sqrt{1 - \left(\frac{\theta}{\theta_{\max}}\right)^2} \ .$$

Fig. 3.1 shows how the critical photon energy varies along the length of a multipole wiggler. In this case a magnet with a 2.0 T peak field and period of 200 mm has been used with a 2 GeV electron beam.
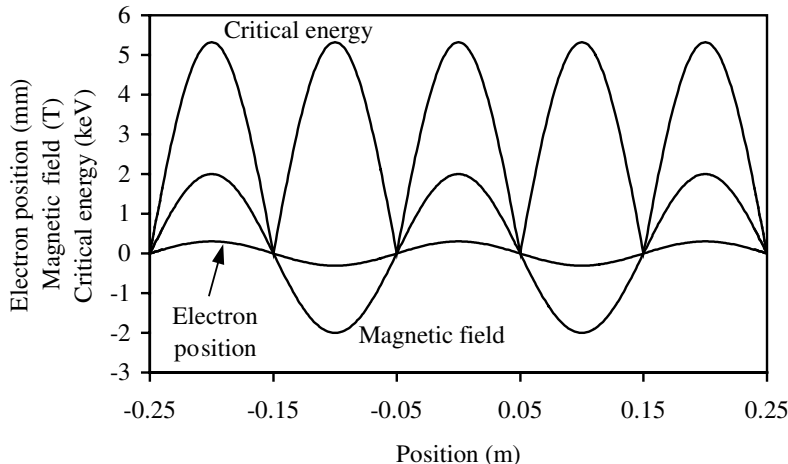
Fig. 3.1. Magnetic field, critical energy, and electron trajectory for a 2.0 T, 200 mm period multipole wiggler. The critical photon energy has been calculated for a 2 GeV electron beam.

3.3 Flux from a Multipole Wiggler

Since the multipole wiggler can, in its simplest form, be considered as a series of bending magnets, one behind the other, the flux that the observer sees is simply the sum of the flux from each apparent bending magnet or source point. As the magnetic field is generally assumed to be sinusoidal there are two source points per period, one for each magnetic dipole. For an observer at a particular angle, the total flux that the observer receives at a specific photon energy is therefore determined by the critical photon energy due to the observation angle, as shown in Section 3.2, and the number of periods in the insertion device. In particular, the flux is given by the product of twice the number of periods and the flux for one bending magnet source at that magnetic field (2.38).

It should now be clear why the multipole wiggler is so advantageous when compared with a bending magnet. Not only can the peak magnetic field be chosen, to some extent, to meet the required spectral range, but also the flux will be enhanced by twice the number of periods. A typical number of periods for a multipole wiggler would be approximately 20 – 30, though this clearly depends upon the actual period chosen and the space available for the magnet length. From this we can see that a flux enhancement over a standard bending magnet source of a factor of 50 is typical. This is one reason why modern synchrotron radiation sources are based upon the use of insertion devices as their primary source of light rather than the bending magnets. An example of the flux output from a multipole wiggler compared with a bending magnet and a wavelength shifter is given in Fig. 3.2.
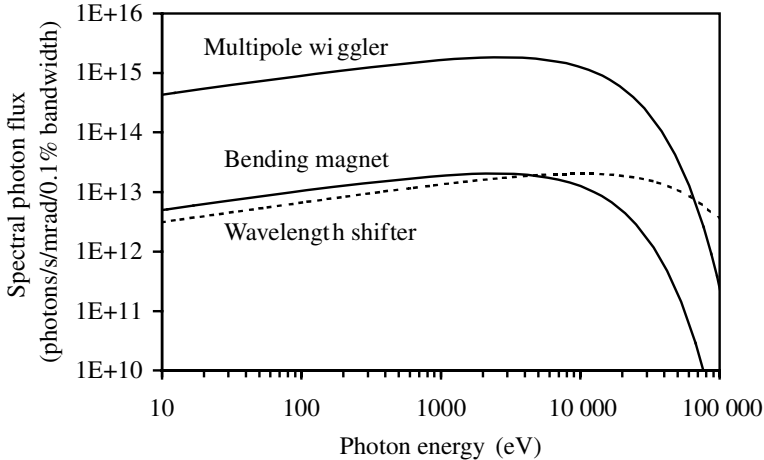
FIG. 3.2. Photon flux generated by a 300 mA, 3 GeV electron beam for a 1.4 T bending magnet, a 6 T wavelength shifter and a 1.6 T multipole wiggler with 45 periods.

3.4 Multipole Wiggler Brightness

The brightness of a multipole wiggler source is not straightforward to derive because of the large source length, L, and the large horizontal angular excursion of the electron beam ($\pm K/\gamma$) being significantly greater than the radiation opening angle ($\sim 1/\gamma$).

An analytical approach has been taken in [26] by first of all tracking all photons back to the intersection with the mid-plane of the multipole wiggler and then examining the probability of finding a photon in a small phase space element on this plane. The derivation assumes that the magnetic field is sinusoidal, the photon emission is uniform in the horizontal plane over the angular excursion of the electron beam and that the emission is concentrated at the poles of the device. The resulting expression for the brightness (with units of photons per second per solid area per solid angle per spectral bandwidth) is a sum over the length of the device at each pole position, z_i,

$$B = F_{\text{pole}} \sum_{i=1}^{N} \frac{\exp(-x_0^2/2(\sigma_x^2 + s_i^2\sigma_{x'}^2))}{(2\pi)^{3/2}(\sigma_x^2 + s_i^2\sigma_{x'}^2)^{1/2}(\sigma_y^2(\sigma_{y'}^2 + \sigma_{r'}^2) + s_i^2\sigma_{y'}^2\sigma_{r'}^2)^{1/2}} \ , \qquad (3.4)$$

where F_{pole} is the flux per unit horizontal angle per magnet pole (from (2.38)), N is the number of poles, $x_0 = K\lambda_u/2\pi\gamma$ is the maximum horizontal deflection of the electron beam (3.3), $\sigma_{r'}$ is the rms photon divergence (2.41) and the electron beam has source sizes of σ_x and σ_y and divergences of $\sigma_{x'}$ and $\sigma_{y'}$. Figure 3.3 plots the brightness for a 'typical' multipole wiggler and a bending magnet.
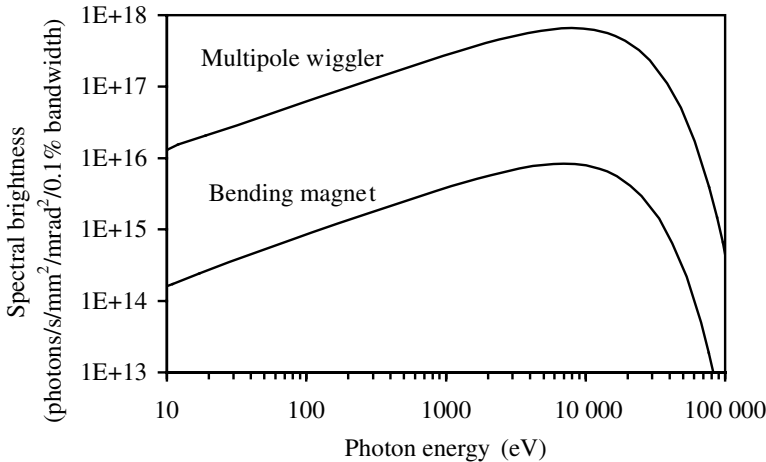
FIG. 3.3. The brightness generated by a 300 mA, 3 GeV electron beam for a 1.4 T bending magnet and a 1.6 T multipole wiggler with 45 periods. The electron beam dimensions are $\sigma_x = 100 \ \mu$m, $\sigma_y = 10 \ \mu$m, $\sigma_{x'} = 20 \ \mu$rad, and $\sigma_{y'} = 2 \ \mu$rad.

3.5   Power and Power Density from an Insertion Device

3.5.1   *Total Power*

To find the total power emitted by an insertion device we follow the same principal as that applied to bending magnets in Section 2.5. Starting with the instantaneous power emitted by a single relativistic electron

$$P_0 = \frac{ce^2\gamma^4}{6\pi\epsilon_0\rho^2}$$

we want to convert this to the energy loss per pass through the insertion device. The energy radiated by one electron passing through a device of length, L, is

$$\Delta E = \frac{e^2\gamma^4}{6\pi\epsilon_0} \int_0^L \frac{1}{\rho(s)^2}ds \ \ .$$

Since it is much more usual to describe insertion devices in terms of the magnetic field through the magnet, $B(s)$, rather than the varying bending radius, $\rho(s)$, of the electron beam, we will put the equation in terms of B instead. Substituting for B with the relationship, $B = E/ce\rho$, and also expanding γ gives

$$\Delta E = \frac{e^4E^2}{6\pi\epsilon_0m_e^4c^6} \int_0^L B(s)^2ds$$

It is important to keep in mind the difference between the energy lost by the electron, ΔE, and the energy of the electron itself, E. Changing the units of the electron energy to GeV gives the energy loss per pass in eV as

$$\Delta E = 1265.5 \, E^2 \int_0^L B(s)^2 ds \ .$$

So the total power emitted by a beam of electrons of current, I_b, and energy, E, in GeV passing through any insertion device is

$$P_{\text{total}} = 1265.5 \, E^2 I_b \int_0^L B(s)^2 ds \ . \tag{3.5}$$

Notice that nothing so far has been assumed about the insertion device and that this result is quite general. In fact, the bending magnet total power result can be derived by solving the integral for a constant B around a circumference of $2\pi\rho_0$. If we assume that the insertion device has a sinusoidal field, with a whole number of periods along its length, then the integral becomes $B_0^2 L/2$, where B_0 is the peak field of the insertion device, and the total power emitted in Watts is

$$P_{\text{total}} = 632.8 \, E^2 B_0^2 L I_b$$

3.5.2 *Power Density*

The power density that is emitted by an insertion device has been found [27] in a similar manner to the total power. The equation for the instantaneous power radiated per solid angle by an electron [6] has to be integrated along the length of the device. The result for a planar device with a sinusoidal field variation is

$$\frac{dP}{d\Omega} = \frac{21\gamma^2}{16\pi K} P_{\text{total}} G(K) F_K(\gamma\theta, \gamma\psi) \ ,$$

where $G(K)$ is a normalization factor given by

$$G(K) = \frac{K(K^6 + \frac{24}{7}K^4 + 4K^2 + \frac{16}{7})}{(1 + K^2)^{7/2}}$$

and $F_K(\gamma\theta, \gamma\psi)$ is the term which describes the angular dependence

$$F_K(\gamma\theta, \gamma\psi) = \frac{16K}{7\pi G(K)} \int_{-\pi}^{\pi} \left(\frac{1}{D^3} - \frac{4(\gamma\theta - K\cos\alpha)^2}{D^5} \right) \sin^2\alpha \, d\alpha \ ,$$

where θ is the horizontal angle, ψ is the vertical angle and

$$D = 1 + (\gamma\psi)^2 + (\gamma\theta - K\cos\alpha)^2 \ .$$

Since $F_K(0,0) = 1$, the on-axis power density is given by

$$\left. \frac{dP}{d\Omega} \right|_{\psi,\theta=0} = \frac{21\gamma^2}{16\pi K} P_{\text{total}} G(K) \ ,$$

which in practical units of W/mrad^2 is
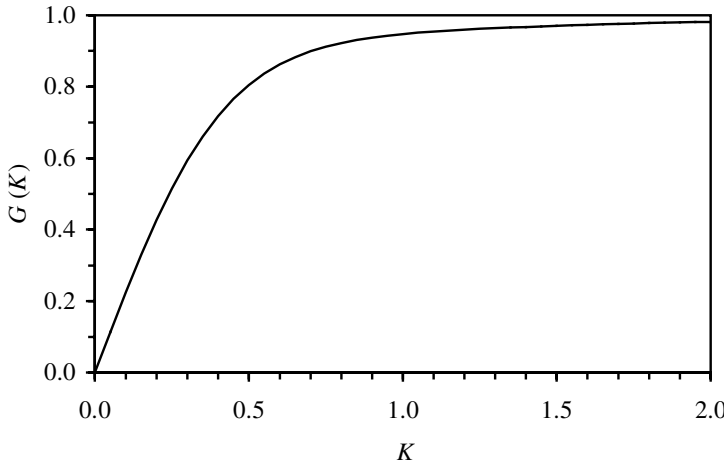
FIG. 3.4. The function $G(K)$ used in power density calculations.

$$\left.\frac{dP}{d\Omega}\right|_{\psi,\theta=0} = 1012.5 \, \frac{E^4 B_0^2}{K} L I_b G(K) \ ,$$

where E is in GeV as usual.

The function $G(K)$ is plotted in Fig. 3.4. It quickly tends towards 1 as K increases. The function $F_K(\gamma\theta, \gamma\psi)$ is difficult to solve analytically but can be evaluated numerically without too much difficulty. $F_K(\gamma\theta, \gamma\psi)$ is plotted as a function of θ for $\psi = 0$ and as a function of ψ for $\theta = 0$ in Fig. 3.5. $F_K(\gamma\theta, 0)$ tends towards a semicircular shape as K increases. In the vertical plane, $F_K(0, \gamma\psi)$ quickly tends towards the $K = \infty$ limit, which is identical to the bending magnet result we saw earlier (Fig. 2.7).

Some example power and power density levels are given in Table 3.1 for some 'typical' undulator and multipole wiggler parameters. Comparing these with the dipole power levels given in Table 2.3 we can see that the insertion devices produce huge power levels, which can be extremely difficult to handle. One of the biggest problems for beamline designers is to cope with these power levels on the beamline optics without the optics becoming damaged or distorted. Interestingly, the total power from the multipole wiggler is much higher than the undulator, but the power density is similar to the undulator case (taking account of the different lengths used) since the beam is spread over a larger solid angle. One further point to note is that the power densities generated by insertion devices on a surface within a few metres of the source are often greater than that needed to weld metal!
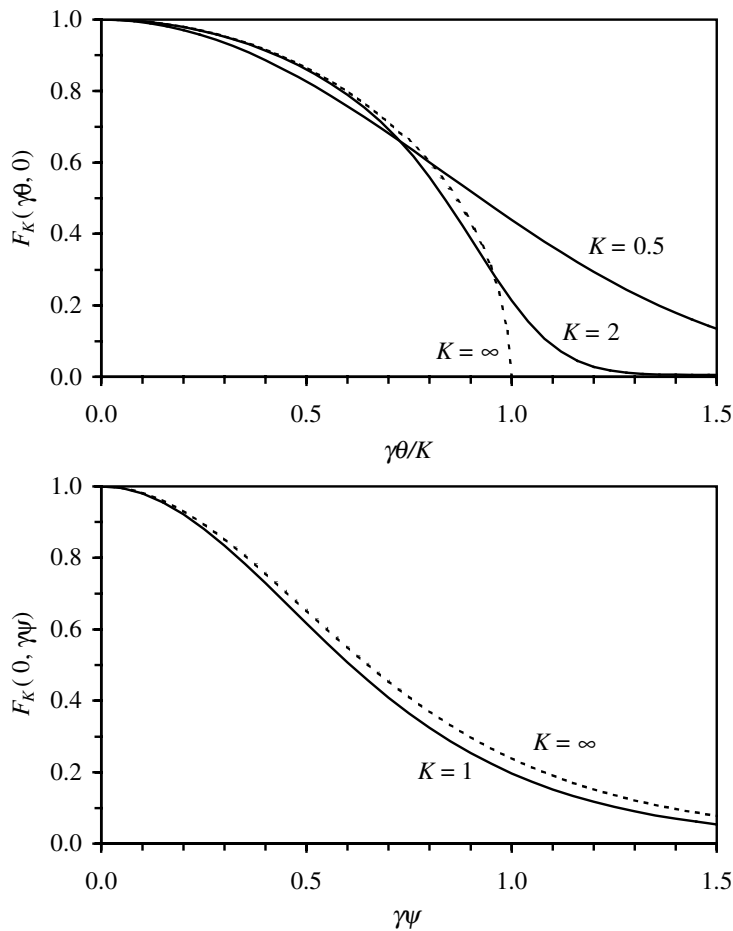
Fɪɢ. 3.5. The functions $F_K(\gamma\theta, 0)$ and $F_K(0, \gamma\psi)$ for different K values.

TABLE 3.1 Example values for the power and power
density on-axis for two insertion devices at three dif-
ferent electron energies

Energy (GeV)	B_0 (T)	K	L (m)	I_b (mA)	P_{total} (kW)	$dP/d\Omega$ (kW/mrad^2)
2	0.64	3	5	200	1.0	2.2
3	0.64	3	5	300	3.5	16.8
6	0.64	3	5	200	9.3	179.1
2	2	40	2	200	4.0	0.6
3	2	40	2	300	13.7	4.9
6	2	40	2	200	36.4	52.5

Synchrotron Radiation Output from Undulators

4.1   The Undulator Equation

From (3.2) we have

$$\dot{x}(s) = \frac{dx}{ds} = \frac{K}{\gamma} \cos\left(\frac{2\pi s}{\lambda_u}\right)$$

and to a good approximation $\Delta s = c\Delta t$ so

$$\frac{\Delta x}{\Delta s} = \frac{\Delta x}{c\Delta t} = \frac{1}{c}\frac{dx}{dt} = \frac{K}{\gamma} \cos\left(\frac{2\pi s}{\lambda_u}\right) \quad .$$

Also, since β_x is defined as the relative transverse velocity, v_x/c, we have

$$\beta_x = \frac{dx/dt}{c} = \frac{K}{\gamma} \cos\left(\frac{2\pi s}{\lambda_u}\right) \quad . \tag{4.1}$$

As the energy of the electron is fixed, β is also fixed and so any variation in β_x must result in a corresponding change in β_s $(\beta^2 = \beta_x^2 + \beta_s^2)$. From this we have

$$\beta_s^2 = \beta^2 - \beta_x^2$$
$$= \beta^2 - \frac{K^2}{\gamma^2} \cos^2\left(\frac{2\pi s}{\lambda_u}\right) \quad .$$

Using the result, $\cos 2A = 2\cos^2 A - 1$, we get

$$\beta_s^2 = \beta^2 - \frac{K^2}{\gamma^2}\left(\frac{1}{2} + \frac{1}{2}\cos\left(\frac{4\pi s}{\lambda_u}\right)\right)$$

and using the approximation, $(1-x)^{1/2} \sim 1 - x/2$, this becomes

$$\beta_s \sim \beta\left(1 - \frac{1}{2}\left(\frac{K^2}{\beta^2\gamma^2}\left(\frac{1}{2} + \frac{1}{2}\cos\left(\frac{4\pi s}{\lambda_u}\right)\right)\right)\right)$$
$$\sim \beta\left(1 - \frac{K^2}{4\beta^2\gamma^2} - \frac{K^2}{4\beta^2\gamma^2}\cos\left(\frac{4\pi s}{\lambda_u}\right)\right) \quad . \tag{4.2}$$

On inspection we can see that this is a constant with an oscillating cosine term and so the average velocity in the forward direction, $\hat{\beta}_s$, is simply
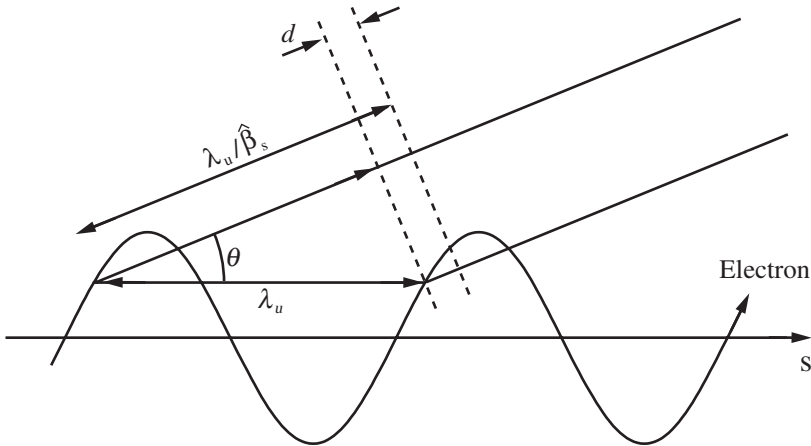
FIG. 4.1. Geometry for an electron travelling through an undulator.

$$\hat{\beta}_s \sim \beta - \frac{K^2}{4\beta\gamma^2}$$

$$\sim 1 - \frac{1}{2\gamma^2} - \frac{K^2}{4\beta\gamma^2} \ .$$

If we now move on to the conditions required for interference we can see from Fig. 4.1 that for interference to occur between wavefronts emitted by the same electron the electron must slip behind the first wavefront by a whole number of wavelengths over one period. The time for the electron to travel one full period is $\lambda_u/c\hat{\beta}_s$ and during this time the first wavefront (moving at velocity c of course) will have travelled a distance $\lambda_u/\hat{\beta}_s$. Assuming the wavefront is emitted with an angle θ then, the separation, d, between the two wavefronts will be

$$d = \frac{\lambda_u}{\hat{\beta}_s} - \lambda_u \cos\theta \ . \tag{4.3}$$

This separation must be a whole number of wavelengths for constructive interference to occur

$$n\lambda = \frac{\lambda_u}{\hat{\beta}_s} - \lambda_u \cos\theta \ .$$

Inserting our value for $\hat{\beta}_s$ and remembering that $(1-x)^{-1} \sim 1 + x$ we find

$$n\lambda \sim \lambda_u \left(1 + \frac{1}{2\gamma^2} + \frac{K^2}{4\beta\gamma^2}\right) - \lambda_u \cos\theta$$

$$\sim \lambda_u (1 - \cos\theta) + \frac{\lambda_u}{2\gamma^2} + \frac{\lambda_u K^2}{4\beta\gamma^2} \quad .$$

Using the identity, $1 - \cos\theta = 2\sin^2(\theta/2)$, and the approximation for small angles that $\sin\theta \sim \theta$ this becomes

$$n\lambda \sim \frac{\lambda_u \theta^2}{2} + \frac{\lambda_u}{2\gamma^2} + \frac{\lambda_u K^2}{4\beta\gamma^2}$$

$$\sim \frac{\lambda_u}{2\gamma^2} \left(1 + \frac{K^2}{2} + \theta^2\gamma^2 \right) \quad ,$$

which leads to the famous undulator equation

$$\lambda = \frac{\lambda_u}{2n\gamma^2} \left(1 + \frac{K^2}{2} + \theta^2\gamma^2 \right) \quad . \tag{4.4}$$

Taking the earlier example from Section 3.1 of a 3 GeV electron passing through an undulator with a period of 50 mm and K of 3 we find that the wavelength of the first harmonic ($n = 1$) on-axis ($\theta = 0$) is ~ 4 nm (a photon energy of ~ 310 eV).

It is worth spending a few minutes pondering over the implications of the undulator equation. The most obvious one is that a magnet with a period of a few 10s of mm produces light with a wavelength on the order of nm because of the huge γ^2 term (remember that γ is typically a few thousand (see Table 2.2)). We can also see from the equation that the harmonic wavelength changes with not only the magnet period and electron energy but also the deflection parameter, K, and the observation angle, θ. K is a function of the peak on-axis magnetic field and the undulator period again, so by changing the amplitude of the magnetic field the output wavelength of the undulator can be varied. For this reason undulators are almost always built with a smoothly adjustable magnetic field amplitude allowing the output wavelength to be varied continuously over the *tuning range* of the undulator. This raises one slightly counter-intuitive element to the undulator output; at the maximum magnetic field value, K is also maximum and so the output wavelength is longer than when K is small. In other words, the output wavelength of an undulator gets *longer* as the magnetic field *increases*. This is different to the synchrotron radiation emitted by a dipole where we saw that *higher* magnetic fields are used, especially in wavelength shifters, to produce *shorter* wavelength radiation.

One final remark concerning the undulator equation is that the wavelength observed changes significantly with observation angle but since there is a θ^2 term the wavelength always lengthens as the observer moves away from the on-axis position ($\theta = 0$). In a practical undulator beamline, therefore, the choice of the aperture through which the radiation has to pass before reaching the observer is crucial as it alters the light source characteristics. An example of how the wavelength changes with both K and θ is given in Fig. 4.2. Note that although
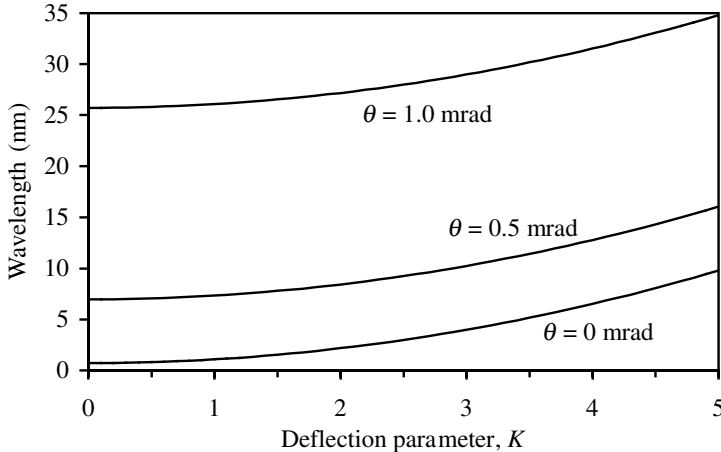
FIG. 4.2. The variation of undulator output first harmonic wavelength with the deflection parameter and the observation angle for a 3 GeV electron passing through a 50 mm period undulator.

very large wavelength variations are possible, especially by going to large θ, this equation makes no comment on the actual *number* of photons that would be observed. In fact the number of photons at large angles is small as we shall see later.

To get an idea of the wavelength spread for each harmonic we can look at the interference effect over the full length of the device. If the undulator has N periods over a length L then the condition for constructive interference over the entire length is

$$Nn\lambda = \frac{N\lambda_u}{\hat{\beta}_s} - N\lambda_u \cos\theta$$

and similarly the condition for destructive interference first occurs when there is one complete extra wavelength advance over the whole device, this occurs at wavelength λ^*

$$Nn\lambda^* + \lambda^* = \frac{N\lambda_u}{\hat{\beta}_s} - N\lambda_u \cos\theta \ .$$

Equating these two interference conditions at a fixed θ we have

$$Nn\lambda = Nn\lambda^* + \lambda^*$$

or

$$\lambda^* = \frac{Nn\lambda}{1 + Nn} \ .$$

The wavelength range over which there is some emission is $\Delta\lambda = \lambda - \lambda^*$ and the bandwidth of the emitted radiation is

$$\frac{\Delta\lambda}{\lambda} = \frac{\lambda - \lambda^*}{\lambda}$$

$$= \frac{1}{1 + Nn}$$

$$\sim \frac{1}{Nn} \quad . \tag{4.5}$$

So a typical undulator with say 100 periods would have a bandwidth of around 1% at the first harmonic and clearly higher order harmonics will have narrower bandwidths.

We can go through a similar process to look at the angular spread over which a particular wavelength will be produced. Destructive interference will first occur at an angle θ^* when

$$Nn\lambda + \lambda = \frac{N\lambda_u}{\hat{\beta}_s} - N\lambda_u \cos\theta^* \quad .$$

Again equating this with the earlier condition for constructive interference we find that

$$\frac{N\lambda_u}{\hat{\beta}_s} - N\lambda_u \cos\theta^* - \lambda = \frac{N\lambda_u}{\hat{\beta}_s} - N\lambda_u \cos\theta$$

and so

$$N\lambda_u \cos\theta^* + \lambda = N\lambda_u \cos\theta \quad .$$

Substituting in the small angle approximation, $\cos\theta \sim 1 - \theta^2/2$, this reduces to

$$\theta^{*2} - \theta^2 = \frac{2\lambda}{N\lambda_u} \quad .$$

Therefore, for the radiation emitted on-axis ($\theta = 0$), the angle at which the intensity falls to zero is

$$\Delta\theta = \sqrt{\frac{2\lambda}{N\lambda_u}} = \frac{1}{\gamma}\sqrt{\frac{1 + K^2/2}{Nn}} \quad .$$

If we approximate the distribution in angle by a Gaussian with standard deviation, $\sigma_{r'}$, then

$$\sigma_{r'} = \sqrt{\frac{\lambda}{N\lambda_u}} = \sqrt{\frac{\lambda}{L}} \quad ,$$

where L is the length of the undulator. For our typical undulator with 100 periods and a K of 3 the angular spread for the first harmonic at 3 GeV is ~ 30 μrad, which is significantly less than the $1/\gamma \sim 170$ μrad, the typical opening angle for a bending magnet or multipole wiggler that we found earlier.

4.2   Odd and Even Harmonics

There is an important distinction in undulators between odd harmonics ($n = 1, 3, 5, ...$) and even harmonics ($n = 2, 4, 6, ...$). In the on-axis direction ($\theta = 0$) *only odd harmonics are observed*. Away from the axis, even harmonics are also present though they generally have inferior spectral properties, as we shall see later. In many undulator designs the even harmonics are completely disregarded but in practice they can still be an extremely useful source of photons. One way of understanding why the even harmonics are not present along the axis is to consider the electric field generated by the electron.

If we consider an electron moving along with an oscillating trajectory with maximum angular excursion of K/γ (as found in Section 3.1) while emitting synchrotron radiation into a cone of $\sim 1/\gamma$ then if the angular excursion of the electron is much less than this (i.e. $K \ll 1$) all of the emitted radiation is seen by the observer and is thus a continuous sinusoidal electric field. If we decompose this electric field (using Fourier analysis) into a frequency spectrum, which is equivalent to the radiation spectrum, then it is clear that the pure sinusoidal field is simply a single, odd, ($n = 1$) harmonic (shown schematically in Fig. 4.3).

Now if we increase K to well beyond 1 the angular excursion of the electron beam is well above $1/\gamma$ and the observer only sees the electric field briefly as the electron passes into this radiation emission angle. However, as we are still on-axis the electric field peaks are still equally spaced in time but of alternating polarity (Fig. 4.4). Since the spikes are equally spaced, the Fourier Transform of the electric field still only contains odd harmonics, though of course it should be noted that as K increases, the sharpness of the electric field spikes also increases and so the radiation spectrum contains increasingly higher numbers of harmonics.

If we now consider the case where the observer is viewing from off-axis, he still sees only the electric field when the electron is within $\sim 1/\gamma$ of his observation angle. However, since he is no longer on-axis the electric field he observes is not equally spaced in time. At larger and larger angles the electric field peaks of opposite polarity tend to move towards each other and the Fourier Transform of such a field has to contain even harmonics (Fig. 4.5) [28].

An important point should be noted here with regard to the total number of harmonics observed. We saw that at larger K values the electric field became much sharper and consequently the radiation spectrum contained far more harmonics. In the extreme case where K is very large the number of harmonics is also so large that the radiation spectrum smoothes out, losing the harmonic structure, and actually takes on the overall shape of the bending magnet spectrum. Of course, the process we are considering here is the undulator (spectrum full of structure) changing into a multipole wiggler (smooth bending magnet type spectrum). The change from one type of insertion device to the other is gradual and there is clearly an intermediate state in between. The intrinsic interference effects still present in large K multipole wigglers near its fundamental and low harmonics are often neglected as they are generally so far away from the spectral
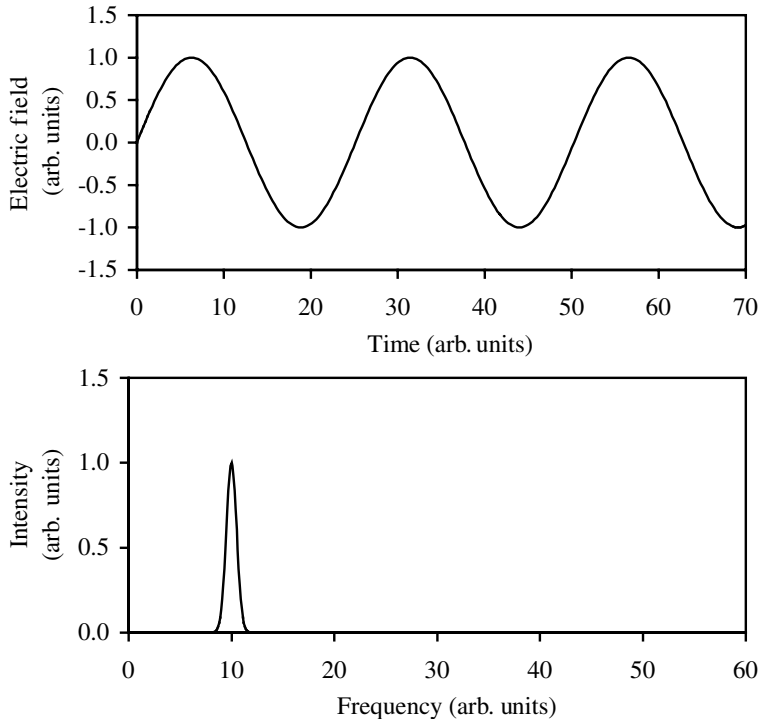
FIG. 4.3. Schematic illustration of the relationship between the electric field experienced by the observer and the radiation spectrum for an undulator with $K \ll 1$.

region of interest but it should be remembered that they are *always* present to some extent.

4.3 Undulator Angular Flux Distribution

We need to return to some earlier results so that we can consider the angular flux density produced by a periodic magnet. If we recall from (2.28) that in the general case the spectral angular distribution of the energy radiated by an electron is

$$\frac{d^2W}{d\Omega\, d\omega} = 2\epsilon_0 cR^2 |E(\omega)|^2$$

and substitute in our earlier expression for $E(\omega)$ from (2.19), remembering that this has already assumed the far-field case that $\boldsymbol{R}$ does not vary with time, then we have
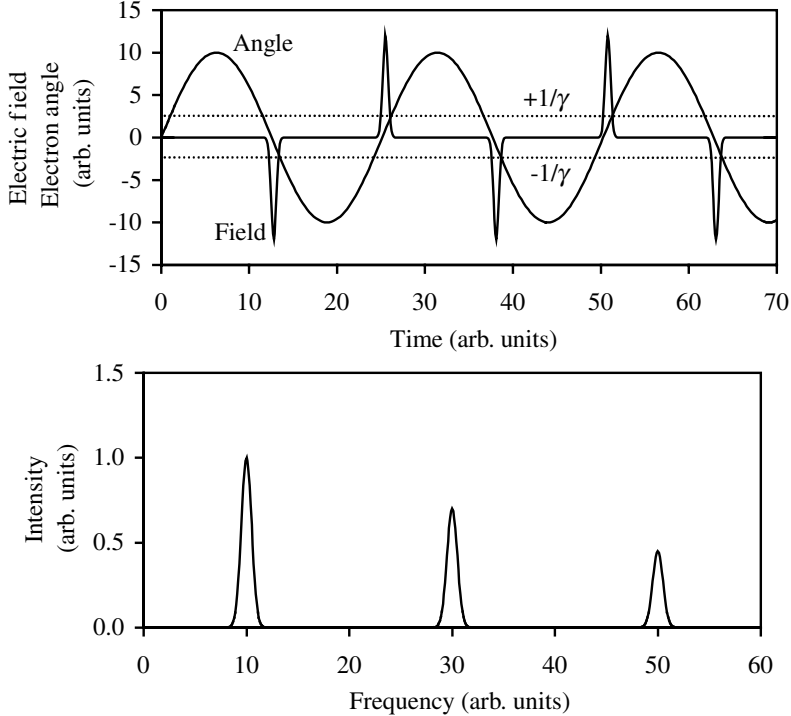
FIG. 4.4. Schematic illustration of the relationship in an undulator between the electron beam angular excursion, the electric field experienced by the observer, and the radiation spectrum for $K \gg 1$ with the observer on-axis.

$$
\frac{d^2W}{d\Omega\,d\omega} = 2\epsilon_0 cR^2 \left| \frac{e\omega}{4\pi\sqrt{2\pi}\,c\epsilon_0 R} \int_{-\infty}^{\infty} (\boldsymbol{n} \times (\boldsymbol{n} \times \boldsymbol{\beta})) e^{i\omega(t' + \frac{R(t')}{c})}\,dt' \right|^2
$$

$$
= \frac{e^2\omega^2}{16\pi^3 c\epsilon_0} \left| \int_{-\infty}^{\infty} (\boldsymbol{n} \times (\boldsymbol{n} \times \boldsymbol{\beta})) e^{i\omega(t' + \frac{R(t')}{c})}\,dt' \right|^2 . \tag{4.6}
$$

We can change the term in the exponential by substituting in eqn (2.22)

$$
t' + \frac{R(t')}{c} = t' + \frac{\boldsymbol{n} \cdot \boldsymbol{x}}{c} - \frac{\boldsymbol{n} \cdot \boldsymbol{r}}{c}
$$

but again we can disregard the $\boldsymbol{n} \cdot \boldsymbol{x}/c$ part as in the far field it represents a fixed phase shift (the time taken to travel between the origin and the observer). This leaves us with

$$
\frac{d^2W}{d\Omega\,d\omega} = \frac{e^2\omega^2}{16\pi^3 c\epsilon_0} \left| \int_{-\infty}^{\infty} (\boldsymbol{n} \times (\boldsymbol{n} \times \boldsymbol{\beta})) e^{i\omega(t' - \frac{\boldsymbol{n} \cdot \boldsymbol{r}}{c})}\,dt' \right|^2 . \tag{4.7}
$$

Now, since we are dealing with a periodic magnet (with N periods) we can split up this integral as follows [29]
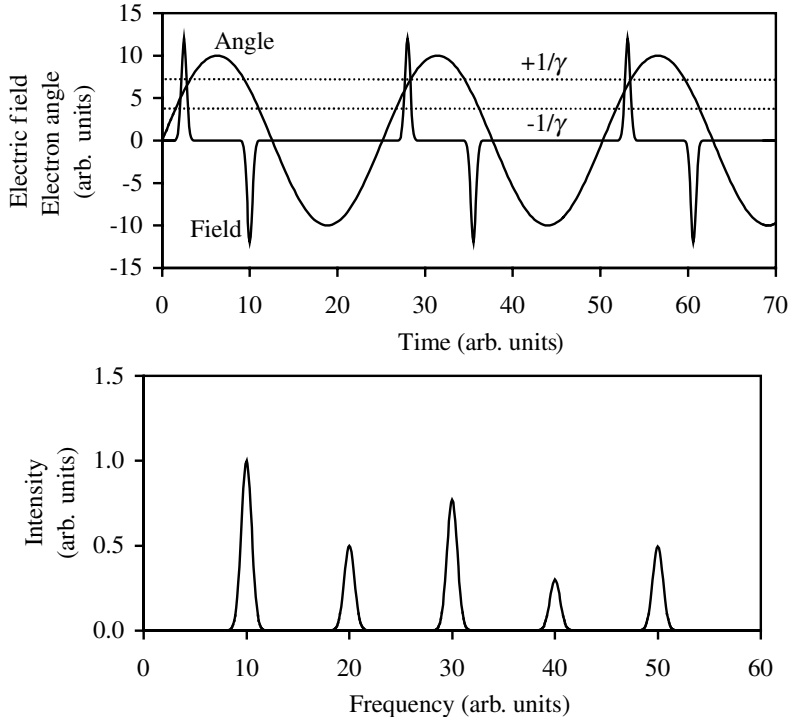
FIG. 4.5. Schematic illustration of the relationship in an undulator between the electron beam angular excursion, the electric field experienced by the observer, and the radiation spectrum for $K \gg 1$ with the observer off-axis.

$$\frac{d^2W}{d\Omega\,d\omega} = \frac{e^2\omega^2}{16\pi^3 c\epsilon_0} \left| \int_{-\frac{\lambda_u}{2c\beta_s}}^{\frac{\lambda_u}{2c\beta_s}} (\boldsymbol{n} \times (\boldsymbol{n} \times \boldsymbol{\beta})) e^{i\omega(t' - \frac{\boldsymbol{n}\cdot\boldsymbol{r}}{c})}\,dt' \right.$$

$$+ \int_{-\frac{\lambda_u}{2c\beta_s}}^{\frac{\lambda_u}{2c\beta_s}} (\boldsymbol{n} \times (\boldsymbol{n} \times \boldsymbol{\beta})) e^{i\omega(t' - \frac{\boldsymbol{n}\cdot\boldsymbol{r}}{c} + \frac{d}{c})}\,dt' + ...$$

$$\left. ... + \int_{-\frac{\lambda_u}{2c\beta_s}}^{\frac{\lambda_u}{2c\beta_s}} (\boldsymbol{n} \times (\boldsymbol{n} \times \boldsymbol{\beta})) e^{i\omega(t' - \frac{\boldsymbol{n}\cdot\boldsymbol{r}}{c} + (N-1)\frac{d}{c})}\,dt' \right|^2 \, ,$$

where d is the time between successive wavefronts (4.3) and so d/c is the time that one wavefront is ahead of the following one (or in other words is the phase difference in time between successive periods) and the integration limits are the time taken for an electron to travel between $-\lambda_u/2$ and $\lambda_u/2$.

Separating out these phase terms gives

$$\frac{d^2W}{d\Omega\,d\omega} = \frac{e^2\omega^2}{16\pi^3 c\epsilon_0} \left| \left(\int_{-\frac{\lambda_u}{2c\beta_s}}^{\frac{\lambda_u}{2c\beta_s}} (\boldsymbol{n} \times (\boldsymbol{n} \times \boldsymbol{\beta})) e^{i\omega(t' - \frac{\boldsymbol{n}\cdot\boldsymbol{r}}{c})}\,dt' \right) \right.$$

$$\times \left. \left(1 + e^{\frac{i\omega d}{c}} + ... + e^{\frac{i(N-1)\omega d}{c}} \right) \right|^2$$

$$= \frac{e^2\omega^2}{16\pi^3 c\epsilon_0} \left| \int_{-\frac{\lambda_u}{2c\beta_s}}^{\frac{\lambda_u}{2c\beta_s}} (\boldsymbol{n} \times (\boldsymbol{n} \times \boldsymbol{\beta})) e^{i\omega(t' - \frac{\boldsymbol{n}\cdot\boldsymbol{r}}{c})}\,dt' \right|^2$$

$$\times \left| 1 + e^{\frac{i\omega d}{c}} + ... + e^{\frac{i(N-1)\omega d}{c}} \right|^2 .$$

The final term in this equation is identical to that found in studies of diffraction gratings [30] as the diffraction effects of a grating with N slits is extremely similar in many respects to emission from a periodic magnet with N periods. This 'grating' function, which represents the interference term for N periods, can be expressed as follows

$$\left| 1 + e^{\frac{i\omega d}{c}} + ... + e^{\frac{i(N-1)\omega d}{c}} \right|^2 = \frac{\sin^2\left(\frac{N\omega d}{2c}\right)}{\sin^2\left(\frac{\omega d}{2c}\right)} = \frac{\sin^2\left(\frac{N\pi\omega}{\omega_1}\right)}{\sin^2\left(\frac{\pi\omega}{\omega_1}\right)} ,$$

where ω_1 is the angular frequency of the first harmonic.

The maximum value for this function is N^2 and this occurs when $\omega/\omega_1 = 1, 2, 3, ...$ (these are known as the *principal maxima* in diffraction optics). For interest we note that there are $N - 1$ *minima* and $N - 2$ *secondary maxima* between successive *principal maxima*. An example of this function is plotted for $N = 5$ in Fig. 4.6.

We will now focus on the shape of this function close to the harmonics. First we will normalize the function by dividing by N^2, then we will consider frequencies near to the harmonic, $\omega = n\omega_1 + \Delta\omega$. This is the so-called *lineshape function* and interestingly, for large (and realistic) values for the number of periods ($N > \sim 10$), it is independent of the number of periods. We will denote this new function as $L(N\Delta\omega/\omega_1)$,

$$L\left(\frac{N\Delta\omega}{\omega_1}\right) = \frac{\sin^2\left(\frac{N\pi\Delta\omega}{\omega_1}\right)}{N^2 \sin^2\left(\frac{\pi\Delta\omega}{\omega_1}\right)} .$$

The lineshape function is plotted in Fig. 4.7. We can see that this function drops to half its maximum value when $N\Delta\omega/\omega_1 \sim 0.5$ and so we can take the (full width half maximum) bandwidth of the nth harmonic at frequency $\omega_n = n\omega_1$ to be
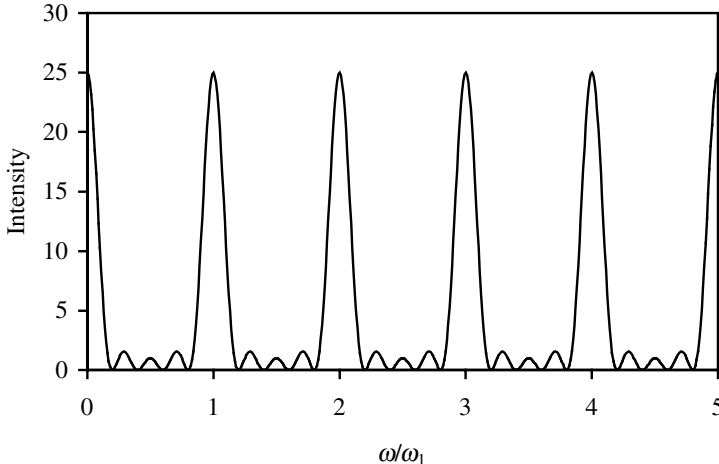
FIG. 4.6. The undulator interference term ('grating function') for $N = 5$.
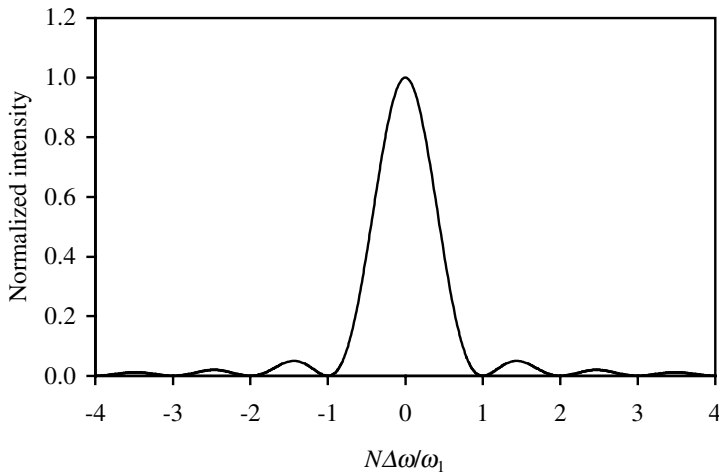
FIG. 4.7. The undulator lineshape function plotted for $N = 20$.

$$\frac{\Delta\omega}{\omega_n} = \frac{1}{nN}$$

in agreement with the result found earlier (4.5) from a simple interference constraint argument.

Getting back to our original expression for the spectral angular distribution of the energy radiated by an electron during one passage through the undulator,
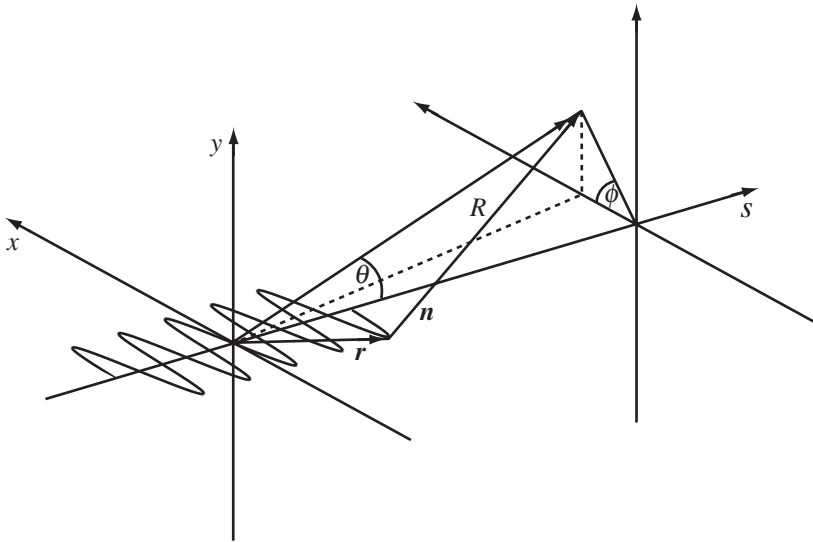
Fig. 4.8. The undulator geometry used for the angular flux analysis.

we now have that

$$\frac{d^2W}{d\Omega\,d\omega} = \frac{e^2\omega^2 N^2}{16\pi^3 c\epsilon_0}L\left(\frac{N\Delta\omega}{\omega_1}\right)\left|\int_{-\frac{\lambda_y}{2c\beta_s}}^{\frac{\lambda_y}{2c\beta_s}}(\boldsymbol{n}\times(\boldsymbol{n}\times\boldsymbol{\beta}))e^{i\omega(t'-\frac{\boldsymbol{n}\cdot\boldsymbol{r}}{c})}\,dt'\right|^2 \qquad (4.8)$$

To solve the integral we will have to spend a little time reducing it into something more manageable. First we will start with the cross product part. From the geometry (Fig. 4.8) we know that the unit vector $\boldsymbol{n}$ is

$$\boldsymbol{n} = (\sin\theta\cos\phi, \sin\theta\sin\phi, \cos\theta)\ ,$$

which we will simplify with the usual small angle approximation to

$$\boldsymbol{n} = (\theta\cos\phi, \theta\sin\phi, \cos\theta)\ .$$

Since we are assuming that the undulator only has a vertical magnetic field on-axis (planar geometry) then there is no vertical component to the electron velocity and $\boldsymbol{\beta}$ is

$$\boldsymbol{\beta} = (\beta_x, 0, \beta_s)\ , \qquad (4.9)$$

where

$$\beta_x = \frac{K}{\gamma}\cos\left(\frac{2\pi s}{\lambda_u}\right)$$

$$\beta_s = \hat{\beta}_s - \frac{K^2}{4\gamma^2} \cos\left(\frac{4\pi s}{\lambda_u}\right)$$

from (4.1) and (4.2).

Or, using the variable

$$W = \frac{2\pi\hat{\beta}_s c}{\lambda_u}$$

we can express them as

$$\beta_x = \frac{K}{\gamma} \cos(Wt)$$

$$\beta_s = \hat{\beta}_s - \frac{K^2}{4\gamma^2} \cos(2Wt) \ .$$

For the triple vector product we will again make use of the identity first encountered in Chapter 2

$$\boldsymbol{n} \times (\boldsymbol{n} \times \boldsymbol{\beta}) = (\boldsymbol{n} \cdot \boldsymbol{\beta})\boldsymbol{n} - \boldsymbol{\beta}$$

and so

$$\boldsymbol{n} \cdot \boldsymbol{\beta} = \beta_x \theta \cos\phi + \beta_s \cos\theta$$
$$(\boldsymbol{n} \cdot \boldsymbol{\beta})\boldsymbol{n} = (\theta \cos\phi, \theta \sin\phi, \beta_s)$$
$$(\boldsymbol{n} \cdot \boldsymbol{\beta})\boldsymbol{n} - \boldsymbol{\beta} = (\theta \cos\phi - \beta_x, \theta \sin\phi, 0) \ ,$$

where terms of order θ^2 and above have been dropped.

To calculate the exponent we will need $\boldsymbol{r}$, the path of the electron

$$\boldsymbol{r} = (x, 0, s)$$
$$= \left(\frac{Kc}{\gamma W} \sin(Wt), 0, c\hat{\beta}_s t - \frac{K^2 c}{8\gamma^2 W} \sin(2Wt)\right)$$

from (3.3) and the integration of (4.2). Now, the dot product is simply

$$\boldsymbol{n} \cdot \boldsymbol{r} = x\theta \cos\phi + s \cos\theta$$

and so the exponent from (4.8) is

$$\omega(t - (\boldsymbol{n} \cdot \boldsymbol{r})/c) = \omega t - \frac{\omega x\theta \cos\phi}{c} - \frac{\omega s \cos\theta}{c}$$
$$= \omega t - \frac{\omega\theta \cos\phi}{c} \frac{Kc}{\gamma W} \sin(Wt) - \frac{\omega \cos\theta}{c} c\hat{\beta}_s t$$

$$+\frac{\omega\cos\theta}{c}\frac{K^2c}{8\gamma^2W}\sin(2Wt)$$

$$=\omega t(1-\hat{\beta}_s\cos\theta)-\frac{\omega\theta\cos\phi}{W}\frac{K}{\gamma}\sin(Wt)+\frac{\omega\cos\theta}{8W}\frac{K^2}{\gamma^2}\sin(2Wt).$$

We saw earlier that for large N it is only the harmonics that contain significant intensity, so the integral only needs to be evaluated at these discrete harmonics, i.e. when $\omega=n\omega_1$

$$n\omega_1=\frac{2\pi nc}{\lambda_1}$$

and inserting the interference condition for λ_1 from (4.1) gives

$$n\omega_1=\frac{2\pi nc}{(\lambda_u/\hat{\beta}_s)-\lambda_u\cos\theta}$$
$$=\frac{nW}{1-\hat{\beta}_s\cos\theta}\ .$$

Alternatively, inserting the undulator equation (4.4) gives the equivalent result

$$n\omega_1=\frac{2nW\gamma^2}{1+K^2/2+\theta^2\gamma^2}=\frac{2nW\gamma^2}{A}\ ,\tag{4.10}$$

where

$$A=1+K^2/2+\theta^2\gamma^2\ .$$

We will now insert these discrete ω values into the exponent term

$$\omega(t-(\boldsymbol{n}\cdot\boldsymbol{r})/c)=nWt-\frac{2nW\gamma^2}{A}\frac{\theta\cos\phi}{W}\frac{K}{\gamma}\sin(Wt)+\frac{2nW\gamma^2}{A}\frac{\cos\theta}{8W}\frac{K^2}{\gamma^2}\sin(2Wt)$$
$$=nWt-X\sin(Wt)+Y\sin(2Wt)\ ,$$

where

$$X=\frac{2n\gamma\theta K\cos\phi}{A}$$
$$Y=\frac{nK^2}{4A}\ .$$

We can reduce the exponential to something more digestible now with the use of the Bessel function relationship

$$e^{ix\sin\phi}=\sum_{p=-\infty}^{+\infty}J_p(x)e^{ip\phi}\ ,$$

and so

$$e^{\omega(t-(\boldsymbol{n}\cdot\boldsymbol{r})/c)} = e^{i(nWt - X\sin(Wt) + Y\sin(2Wt))}$$

$$= e^{inWt}e^{-iX\sin(Wt)}e^{iY\sin(2Wt)}$$

$$= e^{inWt}\sum_{p'=-\infty}^{+\infty} J_{p'}(X)e^{-ip'Wt}\sum_{p=-\infty}^{+\infty} J_p(Y)e^{2ipWt}$$

$$= \sum_{p'=-\infty}^{+\infty} J_{p'}(X)\sum_{p=-\infty}^{+\infty} J_p(Y)e^{iWt(n-p'+2p)} \ .$$

Therefore (4.8) becomes

$$\frac{d^2W}{d\Omega\,d\omega} = \frac{e^2\omega^2N^2}{16\pi^3 c\epsilon_0}\, L\left(\frac{N\Delta\omega}{\omega_1}\right)\left|\sum_{p'=-\infty}^{+\infty} J_{p'}(X)\sum_{p=-\infty}^{+\infty} J_p(Y)\right.$$

$$\left.\times \int_{-\frac{\lambda_u}{2c\hat{\beta}_s}}^{\frac{\lambda_u}{2c\hat{\beta}_s}} (\theta\cos\phi - \beta_x, \theta\sin\phi, 0)e^{iWt(n-p'+2p)}\,dt'\right|^2 \ ,$$

where the two non-zero terms in the integrand represent the amplitudes polarized horizontally and vertically. Since the integral is over one full period it will in general be equal to zero (remembering that the exponential can be expressed in sine and cosine terms). It is non-zero when $n - p' + 2p = 0$ for the terms which are independent of t and equally it is non-zero when $n - p' + 2p = 1$ or $n - p' + 2p = -1$ for the β_x term.

Taking the vertical case first, the exponential term is equal to unity and so

$$\frac{d^2W}{d\Omega\,d\omega} = \frac{e^2\omega^2N^2}{16\pi^3 c\epsilon_0}L\left(\frac{N\Delta\omega}{\omega_1}\right)\left|\frac{\lambda_u}{c\hat{\beta}_s}\theta\sin\phi\sum_{p=-\infty}^{+\infty} J_{n+2p}(X)J_p(Y)\right|^2$$

Using the result from (4.10) and noting that $\lambda_u/c\hat{\beta}_s = 2\pi/W$ we get

$$\frac{d^2W}{d\Omega\,d\omega} = \frac{e^2 n^2 N^2 \gamma^2}{4\pi\epsilon_0 cA^2}L\left(\frac{N\Delta\omega}{\omega_1}\right)\left|2\gamma\theta\sin\phi\sum_{p=-\infty}^{+\infty} J_{n+2p}(X)J_p(Y)\right|^2 \ . \quad (4.11)$$

The horizontal case for the $\theta\cos\phi$ term gives a similar result but we also need to include the β_x term for when $n - p' + 2p = \pm1$. This is fairly straightforward and comes out as

$$\frac{d^2W}{d\Omega\,d\omega} = \frac{e^2n^2N^2\gamma^2}{4\pi\epsilon_0cA^2}L\left(\frac{N\Delta\omega}{\omega_1}\right)\left|2\gamma\theta\cos\phi\sum_{p=-\infty}^{+\infty}J_{n+2p}(X)J_p(Y)\right.$$

$$\left.-K\left(\sum_{p=-\infty}^{+\infty}J_{n+2p-1}(X)J_p(Y) + \sum_{p=-\infty}^{+\infty}J_{n+2p+1}(X)J_p(Y)\right)\right|^2 \quad (4.12)$$

Although the infinite sums in the angular flux density equations (4.11 and 4.12) look rather daunting, in fact they are not too hard to calculate to good accuracy. In most circumstances the first ~ 10 terms about zero are more than enough to give adequate accuracy. The intensity for the first four harmonics is shown in Fig. 4.9. Note that in the horizontal plane there are n peaks and that on-axis there is zero intensity for the even harmonics. Remember when looking at these plots that they are not at a fixed photon energy or wavelength. They illustrate how the flux density for each harmonic varies with observation angle but the wavelength is also changing according to the undulator equation (4.4).

4.3.1 *On-Axis Flux Density and Flux in the Central Cone*

We will now look at the particular case of the on-axis energy density ($\theta = 0$). All of the terms become easier to handle immediately. First there is no vertical contribution and so all of the radiation emitted on-axis is horizontally polarized. We also have that

$$X = 0$$
$$Y = \frac{nK^2}{4A} = \frac{nK^2}{4(1 + K^2/2)} \quad .$$

The Bessel function sum also becomes more straightforward as $J_k(0)$ is only non-zero (and equal to unity) when $k = 0$. As a consequence of this

$$p = \frac{\pm 1 - n}{2}$$

and since we know that p is an integer we can now say that n must be *odd* and thus there are *no even harmonics observed on-axis*. This reinforces the assertion made in Section 4.2 that was based on a purely physical argument.

The spectral angular energy density on-axis is therefore

$$\left.\frac{d^2W}{d\Omega\,d\omega}\right|_{\theta=0} = \frac{e^2n^2N^2\gamma^2}{4\pi\epsilon_0cA^2}L\left(\frac{N\Delta\omega}{\omega_1}\right)\left|-K\left(J_{(1-n)/2}(Y) + J_{(-1-n)/2}(Y)\right)\right|^2 \quad .$$

The Bessel function relationship

$$J_{-k}(x) = (-1)^kJ_k(x)$$

can be used to rewrite this as
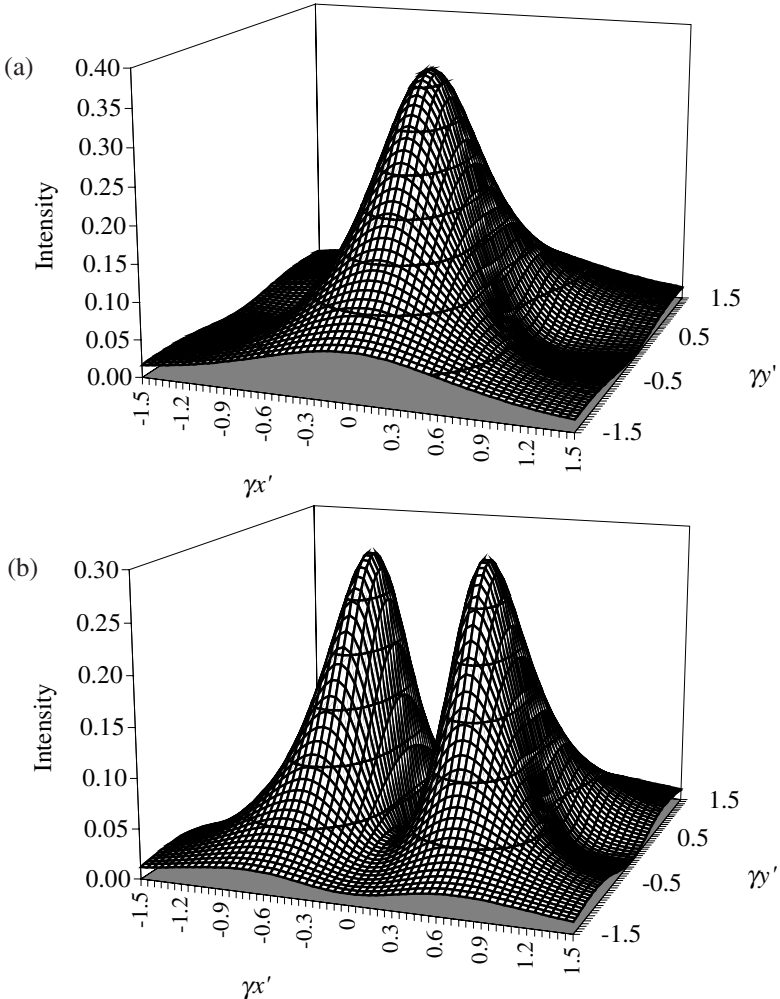
FIG. 4.9. The undulator angular flux density (relative) of the first four harmonics for $K = 1$.

$$\left. \frac{d^2W}{d\Omega\, d\omega} \right|_{\theta=0} = \frac{e^2 n^2 N^2 \gamma^2}{4\pi\epsilon_0 cA^2} L\left(\frac{N\Delta\omega}{\omega_1}\right) \left|K\left(J_{(n+1)/2}(Y) - J_{(n-1)/2}(Y)\right)\right|^2 \ ,$$

where the alternating signs in the modulus have been removed for clarity, without any loss of accuracy. This equation is often written in an alternative form

$$\left. \frac{d^2W}{d\Omega\, d\omega} \right|_{\theta=0} = \frac{e^2 N^2 \gamma^2}{4\pi\epsilon_0 c} L\left(\frac{N\Delta\omega}{\omega_1}\right) F_n(K) \ ,$$
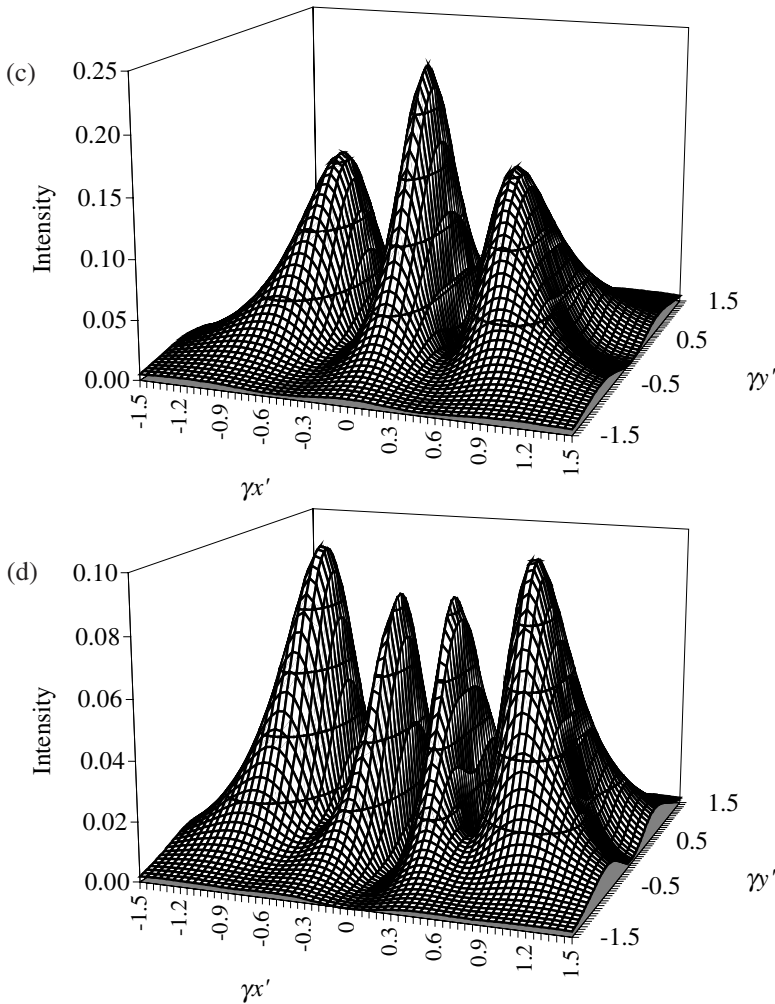
Fɪɢ. 4.9. *Continued.*

where

$$F_n(K) = \frac{n^2 K^2}{(1 + K^2/2)^2} \left(J_{(n+1)/2}(Y) - J_{(n-1)/2}(Y) \right)^2 \quad .$$

The function $F_n(K)$ is plotted in Fig. 4.10 for different n values.

The energy emitted per electron per pass can readily be converted into an on-axis angular power density by multiplying by the number of electrons per second (I_b/e, where I_b is the beam current). This gives
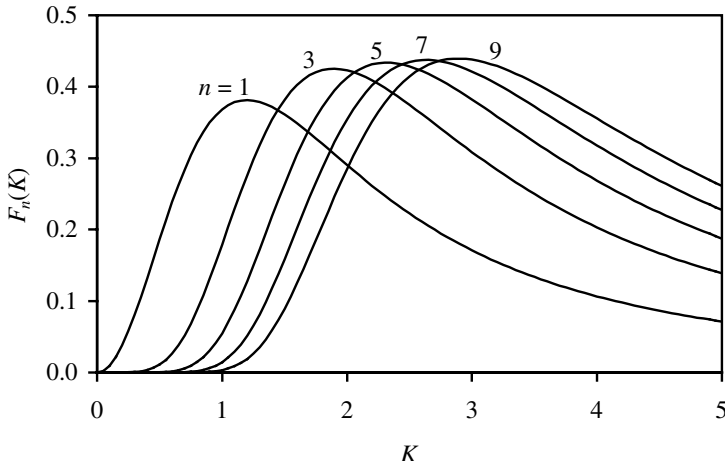
FIG. 4.10. The on-axis angular energy distribution function, $F_n(K)$, plotted for different undulator harmonics.

$$\frac{d^2 P}{d\Omega\, d\omega}\bigg|_{\theta=0} = \frac{e^2 N^2 \gamma^2}{4\pi\epsilon_0 c} \frac{I_b}{e} L\left(\frac{N\Delta\omega}{\omega_1}\right) F_n(K) \ .$$

Again this can be converted into a number of photons per second by dividing by the energy of each photon ($h\omega/2\pi$). The result will be expressed in terms of a relative bandwidth ($d\omega/\omega$) in this case.

$$\frac{d^2 N}{d\Omega\, d\omega/\omega}\bigg|_{\theta=0} = \frac{e^2 N^2 \gamma^2}{4\pi\epsilon_0 c} \frac{I_b}{e} \frac{2\pi}{h} L\left(\frac{N\Delta\omega}{\omega_1}\right) F_n(K) \ .$$

In practical units this gives the number of photons per solid angle per second on-axis for a planar undulator as

$$\frac{d\dot{N}}{d\Omega}\bigg|_{\theta=0} = 1.74 \times 10^{14}\, N^2 E^2 I_b F_n(K) \tag{4.13}$$

in units of photons per second per mrad² per 0.1% bandwidth. For our 50 mm period example undulator with K of 3 and 100 periods we will have an angular flux density on the first harmonic of 8×10^{17} photons/s/mrad²/0.1% bandwidth with a 300 mA electron beam current of energy 3 GeV.

We saw earlier that the flux on-axis was confined to a central cone of angular dimension approximated by a Gaussian of standard deviation, $\sigma_{r'} = \sqrt{\lambda/L}$. We also argued in Chapter 2 for bending magnet radiation (2.40) that the flux per solid angle is related to the flux per solid angle on-axis by

$$\frac{d\dot{N}}{d\Omega} = \frac{d\dot{N}}{d\Omega}\bigg|_{\theta=0} \exp\left(-\frac{\theta^2}{2\sigma_{r'}^2}\right) \ .$$

This also holds true for undulators and so integrating over all angles gives

$$\dot{N} = 2\pi\sigma_{r'}^2 \left.\frac{d\dot{N}}{d\Omega}\right|_{\theta=0}$$

and so

$$\dot{N} = \frac{2\pi\lambda}{L}\frac{e^2 N^2 \gamma^2}{4\pi\epsilon_0 c}\frac{I_b}{e}\frac{2\pi}{h}\frac{\Delta\omega}{\omega}F_n(K) \ .$$

Inserting the undulator wavelength equation and remembering that the fine structure constant, $\alpha = e^2/2ch\epsilon_0$, gives

$$\dot{N} = \alpha\pi N\frac{I_b}{e}\frac{\Delta\omega}{\omega}Q_n(K) \ , \tag{4.14}$$

where

$$Q_n(K) = \frac{1+K^2/2}{n}F_n(K)$$

In practical units of photons per second per 0.1% bandwidth this gives the flux in the central cone as

$$\dot{N} = 1.43 \times 10^{14}\, NI_b Q_n(K)$$

The function $Q_n(K)$ is plotted in Fig. 4.11. For our example 50 mm period undulator with K of 3 and 100 periods we will have a flux on the first harmonic of 4×10^{15} photons/s/0.1% bandwidth, this compares with the typical flux from a bending magnet (2.39) of $\sim 10^{13}$. As the K of an undulator is varied both the photon flux in the central cone and the photon energy changes. A graph of the relationship between the flux and the photon energy for our example undulator is given in Fig. 4.12 for the first three odd harmonics. Plots such as this display the *tuning curve* of the undulator and they are easily misinterpreted. The tuning curve shows how the flux varies with the photon energy but this does not mean that all of this flux is available at the same instant. It is important to remember that the undulator spectrum is in fact made up of discrete harmonics whose photon energies depend upon the K value that is set (or equivalently, the magnetic field value). The tuning curve traces out how the peaks of the harmonics move as the K parameter is varied, so in a sense they show the *potential* of a particular undulator at every energy, so long as the appropriate K value is selected.

Intriguingly this peak flux from an undulator does not occur at an exact harmonic wavelength. In fact the peak flux wavelength, λ_{peak}, must be slightly detuned away from the harmonic by a small amount such that
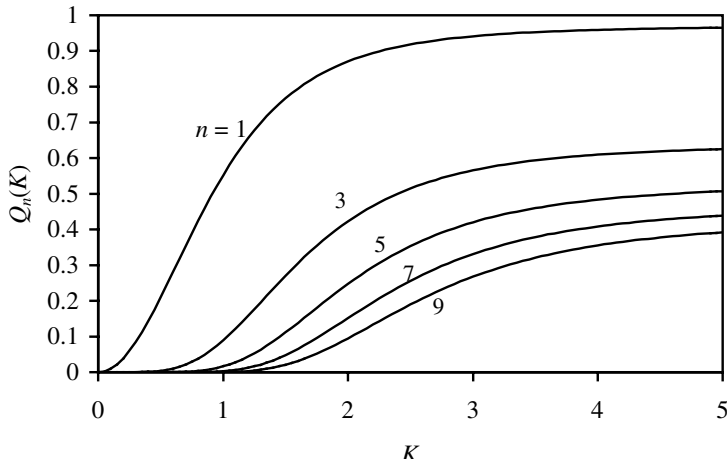
FIG. 4.11. The on-axis flux function, $Q_n(K)$, plotted for different undulator harmonics.
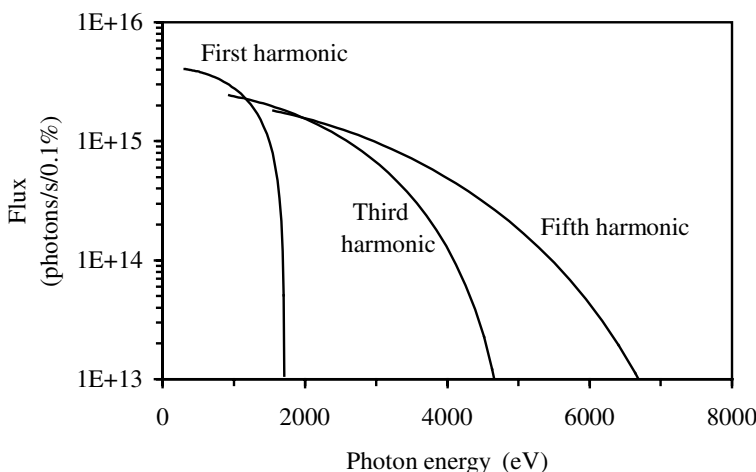

FIG. 4.12. The flux as a function of photon energy for a 50 mm period undulator with 100 periods and K of 3. The electron beam has an energy of 3 GeV and a beam current of 300 mA.

$$\lambda_{\text{peak}} = \frac{\lambda_1}{n(1 - 1/nN)} \ .$$

The detune change is small. Again a 50 mm period undulator with 100 periods, which has a first harmonic wavelength of 3.99 nm, will actually have the peak

flux in the central cone at the slightly longer wavelength of 4.03 nm.

This surprising result is due to the fact that the exact harmonic wavelength on-axis can only receive contributions to the total flux from higher angles, whereas the detuned, longer wavelength has a hollow cone and so can receive contributions from both higher and lower angles. Since the cone is hollow, with a very distinct dip on-axis, the increased flux does not necessarily imply a brighter source. The exact harmonic actually has half the total flux in the central cone when compared with the detuned source [16]. However, it does have a peak of intensity on-axis and an approximately Gaussian shape of reduced angular width, equal to $\sigma_{r'} = \sqrt{\lambda/2L}$. The flux density as a function of angle for our example undulator at the first harmonic and slightly detuned away from it is given in Fig. 4.13.

4.3.2 *Polarization Characteristics of a Planar Undulator*

The horizontal and vertical components of the electric field, (4.11) and (4.12), both have the same phase, implying that the radiation is linearly polarized at all angles in a planar ($B_x = 0$) undulator. However, the angle of the polarization, Ψ (given by the ratio of the electric fields) does depend upon the observation angle [31]

$$\tan \Psi = \frac{2\gamma\theta \sin\phi \sum J_j(X)J_p(Y)}{2\gamma\theta \cos\phi \sum J_j(X)J_p(Y) - K\left(\sum J_{j-1}(X)J_p(Y) + \sum J_{j+1}(X)J_p(Y)\right)} ,$$

where $j = n + 2p$. This is illustrated for the first four harmonics in Fig. 4.14. The polarization is oriented almost entirely in the horizontal plane for the odd harmonics near the central axis. At larger observation angles the plane of the polarization rotates with the azimuthal angle, ϕ, although it is always horizontal on the x- and y-axes. The even harmonics have the interesting feature that the radiation is vertically polarized on the y-axis.

4.4 Undulator Brightness

As discussed in Section 2.4.4 the brightness of a source is the phase space density of the photon flux (i.e. the photons per unit solid angle per unit solid area). It is often encountered in geometric optics where it is widely used because, like the flux, it is a quantity which is invariant in an optical beam transport system (i.e. it does not change with longitudinal position), unlike angular flux density, for instance. The brightness, therefore, is a true measure of the properties of a source and so sensible source to source comparisons can be made. Note that the term *brilliance* is sometimes used, especially within Europe, instead of *brightness*. Indeed the term brightness is occasionally used instead to represent the angular flux density! The best way to be sure of what an author means by these terms is to refer to the units, which should be unambiguous.

The phase space area for the single electron-photon source is the product $2\pi\sigma_r\sigma_{r'}$, where σ_r is the spatial source size. The value of this product has been

(a)

(b)
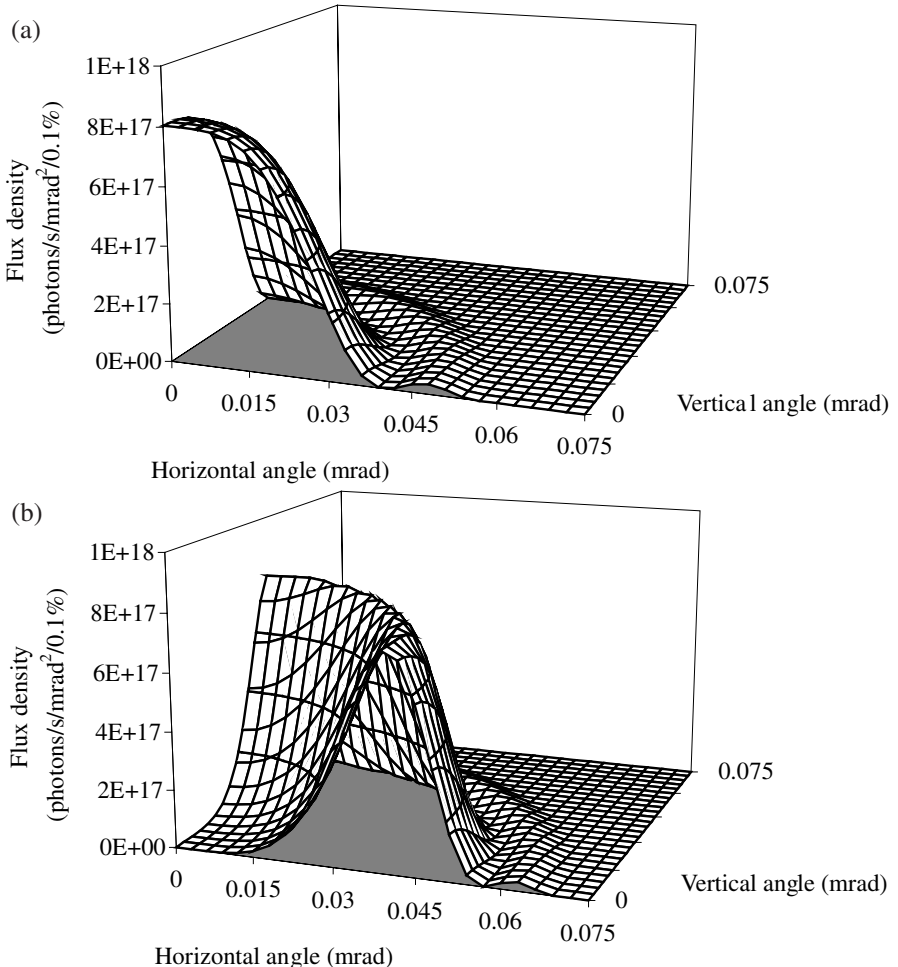
FIG. 4.13. The flux density as a function of angle for the first harmonic at (a) the exact harmonic wavelength (3.99 nm) and (b) slightly detuned away from it (4.03 nm). The undulator has a 50 mm period, 100 periods, and $K = 3$. A 300 mA filament electron beam of energy 3 GeV has been assumed.

found by approximating the undulator source to the fundamental mode of an optical resonator (Gaussian laser mode) [32]. In this case the phase space area is

$$2\pi\sigma_r\sigma_{r'} = \frac{\lambda}{2} \tag{4.15}$$

and so for the peak flux condition
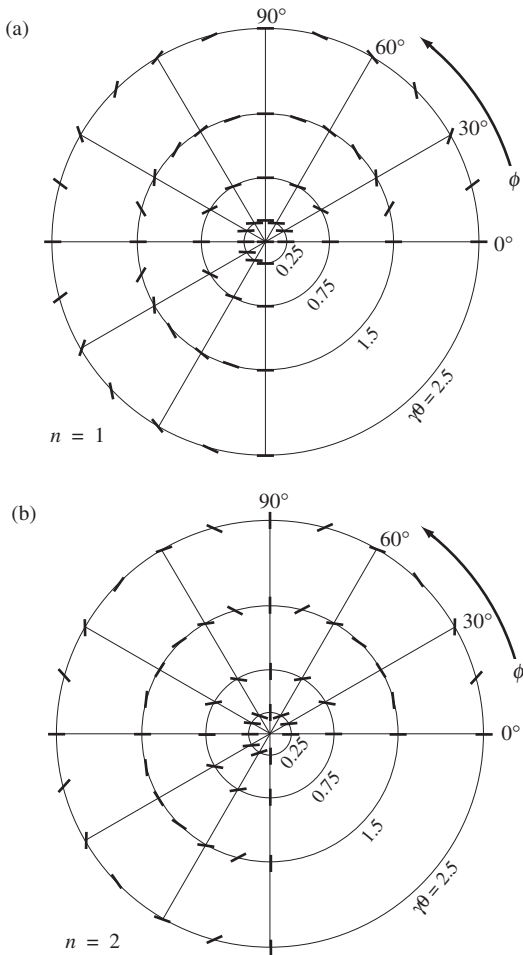
FIG. 4.14. The plane of polarization for the first four harmonics of a planar undulator with $K = 1$ as a function of observation angle. The circles represent contours of $\gamma\theta$ and the direction of each bar represents the angle of the polarization.

$$\sigma_r = \frac{1}{4\pi}\sqrt{\lambda L}$$

$$\sigma_{r'} = \sqrt{\frac{\lambda}{L}} \ .$$

Our example undulator, which has a fundamental wavelength of 4 nm and a total length of 5 m has an approximate source size and divergence of 11 μm and 28 μrad, respectively.

(c)

$n = 3$

(d)

$n = 4$
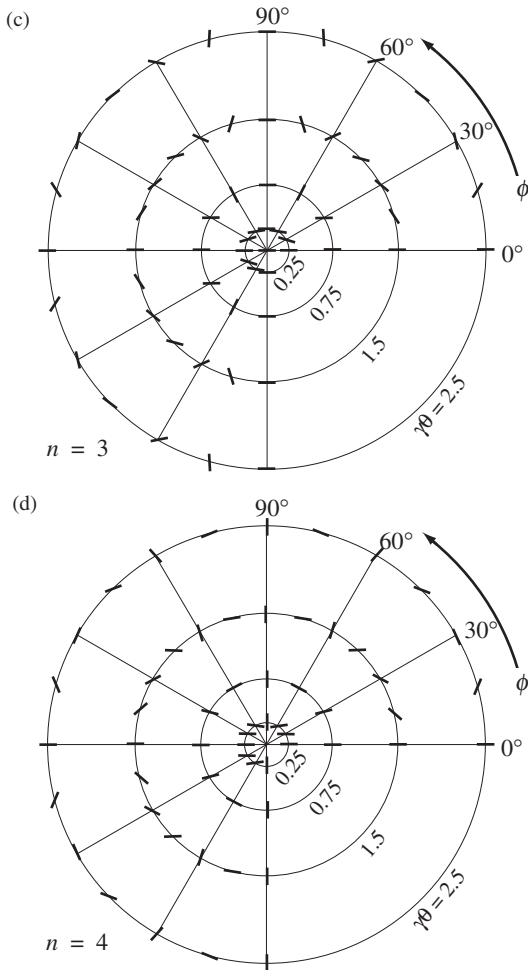
FIG. 4.14. *Continued.*

Since the electron beam is also described by a Gaussian distribution (the electron beam is far closer to a true Gaussian than the photon beam!), with source sizes of σ_x and σ_y and divergences of $\sigma_{x'}$ and $\sigma_{y'}$, it is straightforward to include the electron beam contribution to the overall source brightness. We calculate the *effective* horizontal and vertical source size and divergences to be

$$\Sigma_x = \sqrt{\sigma_x^2 + \sigma_r^2}$$
$$\Sigma_y = \sqrt{\sigma_y^2 + \sigma_r^2}$$
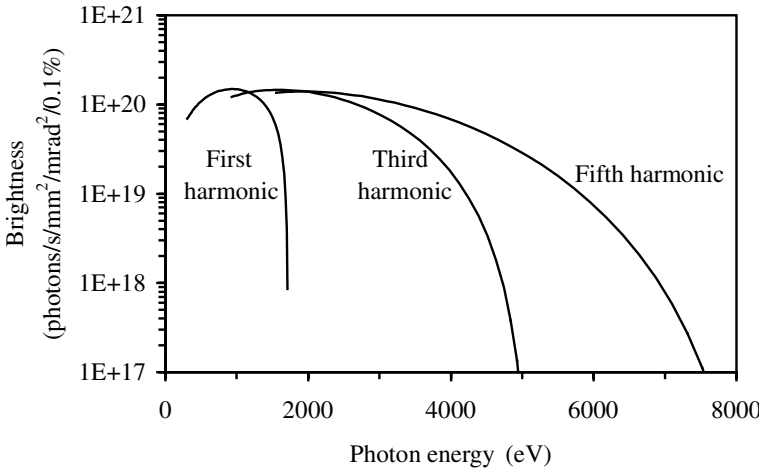
FIG. 4.15. The brightness as a function of photon energy for a 50 mm period undulator with 100 periods and K of 3. The electron beam has an energy of 3 GeV, beam current of 300 mA, and beam dimensions $\sigma_x = 100$ μm, $\sigma_y = 10$ μm, $\sigma_{x'} = 20$ μrad, and $\sigma_{y'} = 2$ μrad.

$$\Sigma_{x'} = \sqrt{\sigma_{x'}^2 + \sigma_{r'}^2}$$

$$\Sigma_{y'} = \sqrt{\sigma_{y'}^2 + \sigma_{r'}^2} \ .$$

The undulator brightness, B, is simply the flux in the central cone divided by the phase space volume described by these effective source dimensions

$$B = \frac{\dot{N}}{4\pi^2 \Sigma_x \Sigma_y \Sigma_{x'} \Sigma_{y'}} \ . \tag{4.16}$$

If we calculate the brightness for our example undulator with electron beam dimensions of $\sigma_x = 100$ μm, $\sigma_y = 10$ μm, $\sigma_{x'} = 20$ μrad, and $\sigma_{y'} = 2$ μrad the brightness is 7×10^{19} photons/s/mrad^2/mm^2/0.1% bandwidth. A graph showing how the brightness varies with photon energy for our example undulator is given in Fig. 4.15.

It should be noted that since the brightness is only an estimation (primarily because the photon beam distribution is non-Gaussian) there are alternative, equally valid, versions of eqn (4.16) in the literature. A nice summary of alternative expressions is given in [33]. The differences are in the exact definitions of σ_r and $\sigma_{r'}$ with alternative coefficients being included. The final difference to the brightness calculations of real undulators is generally small but it does explain why comparisons between alternative light sources can occasionally be confusing! A numerical approach to finding the equivalent Gaussian photon beam source size and divergence has been taken by one author [34]. He has shown that the
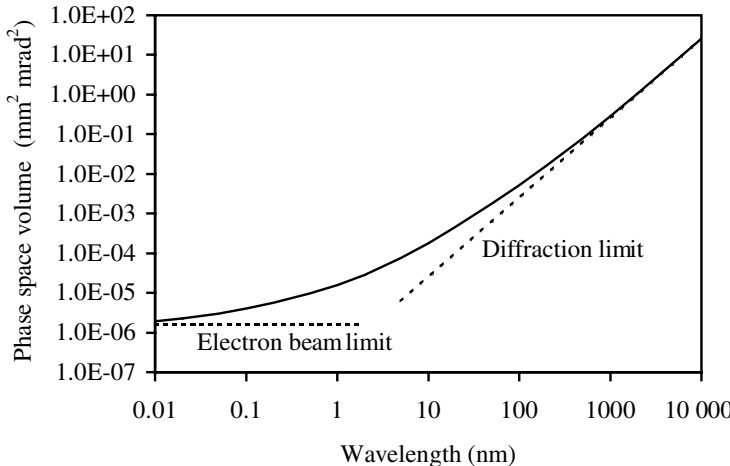
FIG. 4.16. The phase space volume of a light source $(4\pi^2\Sigma_x\Sigma_y\Sigma_{x'}\Sigma_{y'})$ with electron beam dimensions $\sigma_x = 100\ \mu$m, $\sigma_y = 10\ \mu$m, $\sigma_{x'} = 20\ \mu$rad, and $\sigma_{y'} = 2\ \mu$rad, as a function of wavelength. An undulator length of 5 m has been assumed.

amount of detune has a significant effect on these values and that, as expected, the minimum photon beam emittance ($\sigma_r\sigma_{r'}$) is at zero detune.

Modern light sources all strive to reduce the electron beam emittance as it impacts so directly on the undulator source brightness. The only circumstance when there is no advantage to be gained from reducing the electron beam dimensions is when $\sigma_r \gg \sigma_{x,y}$ and $\sigma_{r'} \gg \sigma_{x',y'}$. Since the photon beam dimensions are wavelength related this situation always occurs at some photon energy in any light source. In these circumstances the source is said to be *diffraction limited* and the brightness cannot be increased any further (other than by increasing the electron beam current). In fact, due to the properties of electron beams in storage rings, which always have a far greater horizontal than vertical emittance (typically 100 times greater) the photon source does remain diffraction limited in the vertical plane to shorter wavelengths than in the horizontal plane. Many experiments are designed to take advantage of this reduced source size and divergence in the vertical plane. Fig. 4.16 shows the phase space volume of a high quality third generation light source as a function of wavelength.

It is a common misconception that the flux from undulators scales with N and that the brightness scales with N^2. The first remark is correct (coming directly from (4.14)) but the second is misleading. At first glance it would appear that the brightness scales with N only as it is proportional to flux. However, since the photon divergence is proportional to $1/\sqrt{N}$, if the electron beam divergences are both much smaller than $\sigma_{r'}$ and so $\Sigma_{x',y'} \sim \sigma_{r'}$ then the brightness is indeed proportional to N^2. In other words, the brightness does depend on the number

of periods but the exact dependence changes with the electron beam properties
and the photon wavelength.

4.5   Coherence of Undulator Radiation

Any experiment that involves interference of light beams requires coherence in
these beams. The availability of high brightness synchrotron radiation from the
latest generation of light sources means that there are additional opportunities
for exploiting the coherent properties of the radiation. A simple discussion of
undulator coherence is given here, a more rigorous discussion can be found in [32].

4.5.1   *Temporal Coherence*

For interference effects to occur there must be a definite phase relationship be-
tween two light beams. This phase relationship can be in either time or position.
If we consider a monochromatic wave being emitted by a point source then the
phase difference between two fixed points along this wave will be constant with
time. This is the condition for *perfect temporal (or longitudinal) coherence*. This
property is used when a beam is split into two parts and later recombined to
form interference fringes in a Michelson interferometer, for example.

The *coherent time*, Δt, is simply the reciprocal of the frequency bandwidth,
$\Delta \nu$, of the light

$$\Delta t = \frac{1}{\Delta \nu} \ .$$

The distance light travels in this time is called the *coherence length*, and this can
be expressed in terms of the wavelength of the light

$$c \Delta t = \frac{c}{\Delta \nu} = \frac{\lambda^2}{\Delta \lambda} \ .$$

We can see that the coherence length is dependent upon the monochromaticity
of the light. Although undulators produce light in fairly narrow bandwidths
the output is almost always conditioned by a monochromator to narrow the
bandwidth further. So, the coherence length can be increased if necessary by
narrowing the bandpass of the optical system, but at the expense of flux of
course.

4.5.2   *Spatial Coherence*

If we again consider a monochromatic wave of plane wavefronts passing two
fixed points in a plane normal to the wave direction, then if the phase differ-
ence between the two points is constant with time we have the condition for
perfect spatial (or transverse) coherence. This property is used when we combine
beams from two different points on a wavefront in a Young's slits experiment,
for example.

In the simplest mode of a laser (known as the TEM_{00} mode) the flux density
across the beam is approximately Gaussian, with no phase differences and so
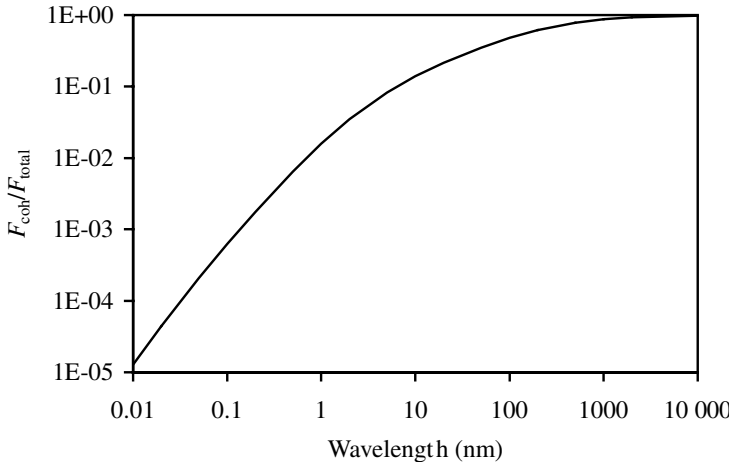
FIG. 4.17. The fraction of the flux that is spatially coherent for an electron beam with dimensions $\sigma_x = 100~\mu$m, $\sigma_y = 10~\mu$m, $\sigma_{x'} = 20~\mu$rad, and $\sigma_{y'} = 2~\mu$rad, as a function of wavelength. An undulator length of 5 m has been assumed.

the beam is fully spatially coherent [30]. In fact, we have already approximated the undulator radiation to this mode when we considered undulator brightness in Section 4.4. The phase space area due to this single electron source (4.15) is $\lambda/2$. To find how much flux from an undulator is spatially coherent, F_{coh}, we need to calculate how much of the flux is emitted from this diffraction limited phase space area. This is simply the product of the undulator brightness, B, and the phase space area squared (squared because there is a horizontal and vertical phase space contribution)

$$ F_{\text{coh}} = B \left(\frac{\lambda}{2} \right)^2 \ . $$

The ratio of the coherent flux to the total flux, F_{total}, is found by using (4.16)

$$ \frac{F_{\text{coh}}}{F_{\text{total}}} = \left(\frac{\lambda}{4\pi} \right)^2 \left(\frac{1}{\Sigma_x \Sigma_y \Sigma_{x'} \Sigma_{y'}} \right) $$

and is obviously closely related to the phase space volume of the light source discussed in Section 4.4 and illustrated in Fig. 4.16. The fraction of the flux that is spatially coherent for the same example is given in Fig. 4.17.

Occasionally the coherence of undulator radiation has caused problems for experiments. Unwanted interference effects can occur, such as 'speckle' for instance. In these cases efforts have been made to decohere the beam with an element in the beamline, such as a rotating piece of wood!

4.6 Near Field Effects

In Chapter 2 the electric field at the observer due to an electron moving on an arbitrary path was derived (2.16)

$$\boldsymbol{E}(t) = \frac{e}{4\pi c\epsilon_0} \left(\frac{c(1-\beta^2)(\boldsymbol{n}-\boldsymbol{\beta})}{R^2(1-\boldsymbol{n}\cdot\boldsymbol{\beta})^3} + \frac{\boldsymbol{n}\times((\boldsymbol{n}-\boldsymbol{\beta})\times\dot{\boldsymbol{\beta}})}{R(1-\boldsymbol{n}\cdot\boldsymbol{\beta})^3} \right)_{t'} .$$

It was then noted that the first term (sometimes called the *velocity* term) varied with $1/R^2$ whereas the second term (sometimes called the *acceleration* term) varied with $1/R$ and since R (the distance to the observer) is in general large we chose to neglect the velocity term from then on. Furthermore, to simplify the Fourier transform of the electric field, we made the assumption that $\boldsymbol{R}$ did not vary with time ($d\boldsymbol{n}/dt = 0$) leading to eqn (2.19). This result was used to derive the synchrotron radiation produced by both bending magnets (Section 2.4) and undulators (Section 4.3). The assumptions used are valid for the *far field* case but when the observer is close to the source then they are no longer valid and *near field* effects can become important.

The near field effects were first considered in undulator calculations in terms of the amplitude of the radiation [35]. A second study also considered the effect of variable path lengths to the observer along the length of the device in terms of phase and interference effects [36]. Given the near field geometry of Fig. 4.18, which differs from our previous assumption, in that the rays travelling towards the observer are no longer parallel (compare with Fig. 4.1), the path length difference introduced by the observer not being at infinity is to the first order

$$PR - PQ \sim TR - TS \sim \frac{L^2\theta^2}{8D} .$$

If we introduce the parameter, W, given by

$$W = \frac{L^2\theta^2}{2\lambda D}$$

then we can see that this path difference is equal to a $\pi/2$ phase change at the output wavelength (i.e. $\lambda/4$) when $W = 1$. The criteria that $W \geq 1$ has been suggested as a criterion for observing near field effects in off-axis radiation [36].

A similar approach to that used in Section 4.1 can be used to find the effect on the spectral width and also the angular spread. The results being

$$\frac{\Delta\lambda}{\lambda} = \frac{W}{Nn}$$

and

$$\Delta\theta^2 = W\frac{2\lambda}{N\lambda_u} .$$

In each case there is a factor W now included that will increase both the spectral width and the angular spread if it is greater than unity. As an example, for an
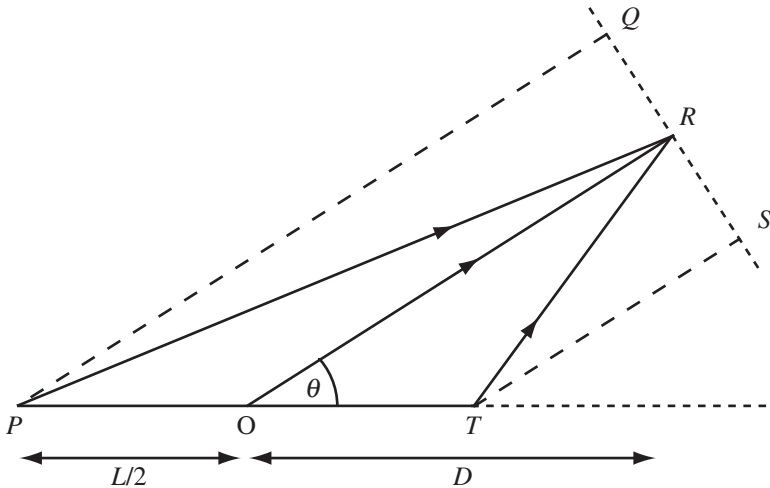
FIG. 4.18. Sketch of the undulator geometry in the near field case.

undulator of length 5 m, with period of 50 mm, K value of 3, electron energy of 3 GeV, and with the observer 25 m from the source the angle at which $W = 1$ is ~ 90 μrad. Although this angle is about three times greater than the angular spread of the first harmonic, it is still a surprisingly small number for which near field effects can become relevant. It also disproves the popular misconception that since the observer is much farther away than the length of the source the near field effects can be neglected.

Detailed analysis has also shown that in most circumstances (when $R \gg \lambda_u$) the velocity term in the electric field can *still be neglected* even when considering near field effects. The principle effect predicted is that as W increases the undulator harmonics broaden and develop an oscillating structure on the peak and this has indeed been observed in practice [37]. Very similar patterns are observed in Fresnel diffraction of light by a slit [30], which is perhaps not too surprising when we remember that this effect is characterized by the source or the observer, or both, being at a finite distance from the slit. The alternative, Fraunhofer diffraction , is equivalent to our far field case. More dramatic effects are predicted off-axis (though still at relatively large angles) when the source to observer distance becomes very short, with the energy spectrum becoming smoother over a wide range and the harmonics standing out less [38]. However, close to the axis it is rarely necessary to include near field effects unless some unusual configuration is being considered. Even the 30 m long undulator in SPring-8, which has the observer only 50 m away, has negligible near field effects on the radiation close to the axis [39].

A number of computer codes have been produced, which correctly calculate the electric field and also include the variation in the angle between the elec-

tron and the observer, and so they are able to accurately account for any near field contributions [40, 41]. Because of the fundamental nature of the equations that they solve they are able to calculate the synchrotron radiation emitted by electrons travelling through arbitrary magnetic fields.

Computation of Synchrotron Radiation

In the preceding chapters we have generated several equations describing the properties of synchrotron radiation from bending magnets, wavelength shifters, multipole wigglers, and undulators. One of the best ways of gaining a real insight into what these equations actually represent is to look at real examples and to vary the input parameters to get a feel for how the output changes. The reader is encouraged to do this whenever possible to reinforce the examples that are given in the text. This chapter explains possible approaches to the numerical calculation of synchrotron radiation emission and also gives some examples of where calculations have been compared with actual measurements.

5.1   Bending Magnets

In Chapter 2 we covered the fundamentals of synchrotron radiation emission and bending magnet radiation in particular (Section 2.4). We derived equations for angular flux density (2.35), vertically integrated flux (2.39), vertical opening angle (2.41), total power emitted (2.43), power density (2.44), and so on.

The only part of these equations that is numerically challenging to calculate is the modified Bessel functions (e.g. $K_{1/3}$, $K_{2/3}$, and $K_{5/3}$) and their integrals. Indeed, some appropriate numerical examples have already been provided in Table 2.1. Calculation of these Bessel functions for any arbitrary value is quite challenging and involves the numerical evaluation of infinite series. However, the advent of modern commercial mathematical software, as well as freely available library routines (which often now have Bessel functions built in), has removed the need for this anymore. Also, modern computer speeds ensure that solving the integral of a modified Bessel function can be done in real time.

One calculation that is sometimes needed by accelerator designers is a representation of the quantum nature of synchrotron radiation. This can be useful when investigating longitudinal electron beam dynamics, when discrete energy changes to the electron need to be considered. Energy loss due to photon emission or energy gain due to the passage of the electron through an accelerating radio-frequency cavity are occasions when the electron experiences step changes in its energy. Studying the quantum nature of the radiation emission is also useful for designers of charged particle colliders as the synchrotron radiation can be a serious source of background noise in the experiments and modelling of the tracks of individual photons through masks and collimators is often required.
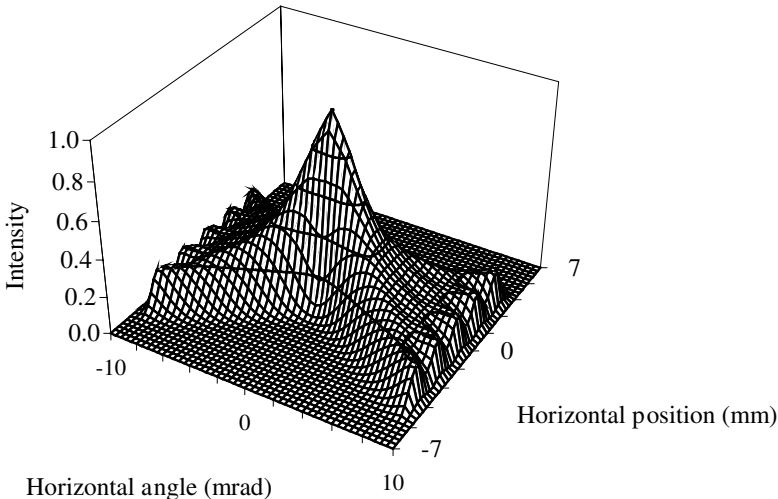
FIG. 5.1. Horizontal phase space plot for a 2 T MPW with a period of 200 mm and 10 poles projected to the central plane of the magnet. The electron energy is 2 GeV with an rms horizontal beam size of 0.5 mm and a divergence of 0.05 mrad. The plot is for a photon energy of 1 keV.

What is needed is an algorithm that randomly selects appropriate photon energies for emission but with the correct probability distribution function to match the bending magnet spectrum. One method that has been used is a Monte Carlo technique [42] though several others are possible.

5.2 Undulators and Multipole Wigglers

Since multipole wigglers are essentially an extension of bending magnet radiation, much of the same calculations apply. One area that is different though is the extended source length and the separation of the individual source points seen by the observer. One approach that has been used to look into how this might affect the source properties has been to trace back to the midplane of the multipole wiggler the position and angle of each emitted photon. A phase space plot of the position and angle for the multipole wiggler source can then be generated which can also include the electron beam dimensions [43]. These phase space plots can later be included in optical ray tracing codes that are used for beamline design (e.g. SHADOW [44]). An example of the horizontal phase space generated by a multipole wiggler is given in Fig. 5.1. The ten distinct poles of the wiggler can be seen in the plot at large angles.

The calculation of undulator radiation is certainly more complicated and hence has been the subject of greater study. Two basic approaches have been used, numerical and analytical. The analytical approach assumes a sinusoidal magnetic field and that the observer is sufficiently distant from the undulator

that the far field case can be assumed. In this instance the equations derived in Chapter 4 for flux density (4.11, 4.12), flux in the central cone (4.14), and so on, are used. The influence of the finite electron beam dimensions and energy spread can also be included. A good example of an analytical code is URGENT [45]. Although the analytical approach makes several basic assumptions, they are generally valid and the software runs faster than numerical techniques. However, with the ever increasing computer power available, numerical codes are becoming more and more popular. These codes either solve the fundamental synchrotron radiation integrals (4.6) [46] or calculate the electric and magnetic fields seen by the observer in the time domain (2.16) and then apply a Fourier transform to calculate the radiation spectrum [28]. The advantage of the numerical approach is that actual measured magnetic fields can be used and that near field effects can be included easily. The main disadvantage, of course, is the time the calculations can take. Since the numerical codes essentially work from first principles they can be used for any arbitrary magnetic fields, not just undulators.

5.2.1 *Example Undulator Results*

We will now look at some illustrative undulator output, calculated using the analytical code URGENT. First, the effect of the electron beam emittance on the flux density as a function of angle is presented in Fig. 5.2, this can be compared directly with the result given earlier in Fig. 4.13 which was for an electron beam with zero emittance. We can see that the finite electron beam size and divergence has the predictable effect of spreading out the undulator flux in angle and smoothing out the structure that was present.

It is also interesting to look at how the flux density varies with photon energy with and without electron beam emittance effects. This is illustrated for the first and ninth harmonics of our example undulator in Fig. 5.3. In general it can be seen that the inclusion of the electron beam size and divergence lowers the photon energies emitted overall (increases the wavelength). This is due to the θ^2 term in the undulator equation (4.4). It is also clear that the effects at the higher harmonic are more dramatic in terms of the reduction in flux density. A wider view of the spectrum of the on-axis flux density is given in Fig. 5.4, this clearly shows some flux not only at the first, third and fifth harmonics but also at the even harmonics as well. If this plot is generated with an electron beam of zero emittance (filament beam) then no even harmonics are present at all, as discussed in Section 4.2. It is only the presence of finite emittance, which implies that not all the electrons are travelling directly along the observer axis and so are effectively emitting light off-axis (and so towards the observer), that creates the even harmonics in this graph.

The effect of restricting the flux through a particular aperture is also useful to calculate as this can simulate photon beam transport lines and experiments. Again this is illustrated for different harmonics in Fig. 5.5. As the aperture size increases the peak flux increases to a maximum and also shifts slightly lower in energy, in line with the detune comments made earlier in Section 4.3.1. It can also

(a)

(b)
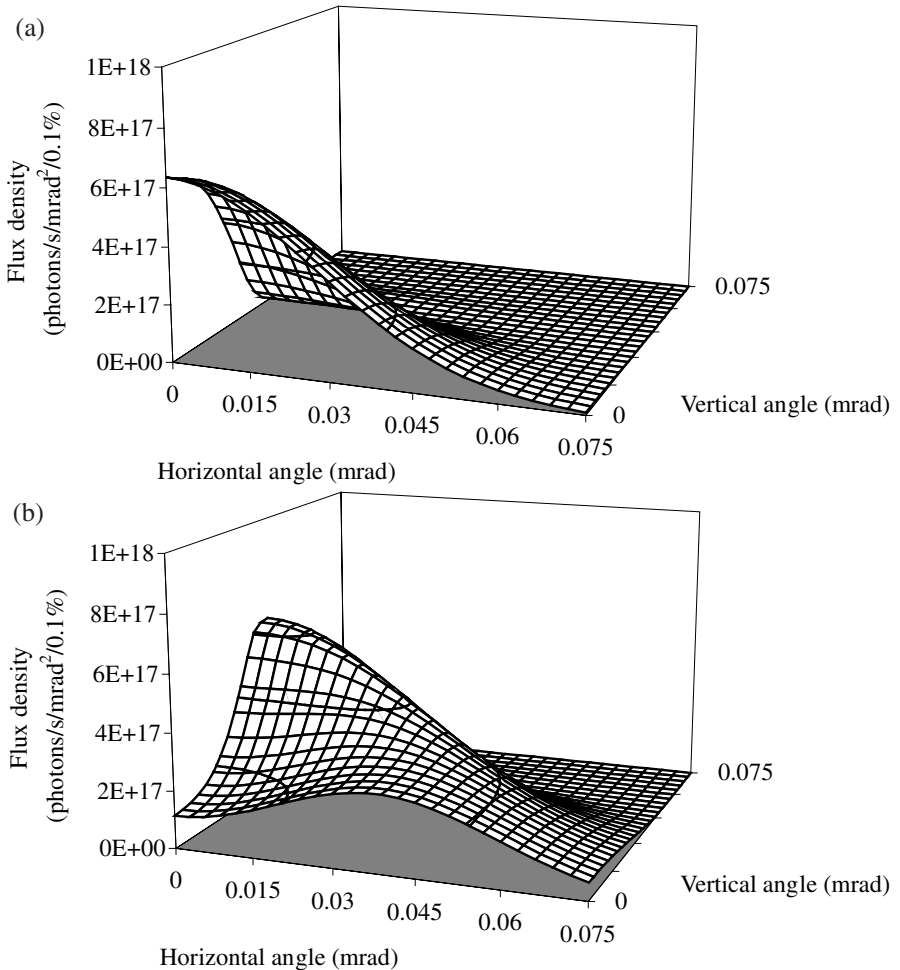
FIG. 5.2. The flux density as a function of angle for the first harmonic at (a) the exact harmonic wavelength (3.99 nm) and (b) slightly detuned away from it (4.03 nm). The undulator has a 50 mm period, 100 periods, and $K = 3$. A 300 mA electron beam of energy 3 GeV with beam dimensions $\sigma_x = 100$ μm, $\sigma_y = 10$ μm, $\sigma_{x'} = 20$ μrad, and $\sigma_{y'} = 2$ μrad has been assumed.

be seen that the higher harmonic must have a narrower divergence since almost all of the flux at the peak energy gets through the smallest aperture illustrated. This is to be expected given that the divergence is proportional to $\sqrt{\lambda}$ (see Section 4.1, for example). A wider view of the spectrum is given in Fig. 5.6. This shows the total flux emitted over all angles and also the flux emitted into a small angular aperture. Note that in this plot all of the harmonics that can contribute

(a)

(b)
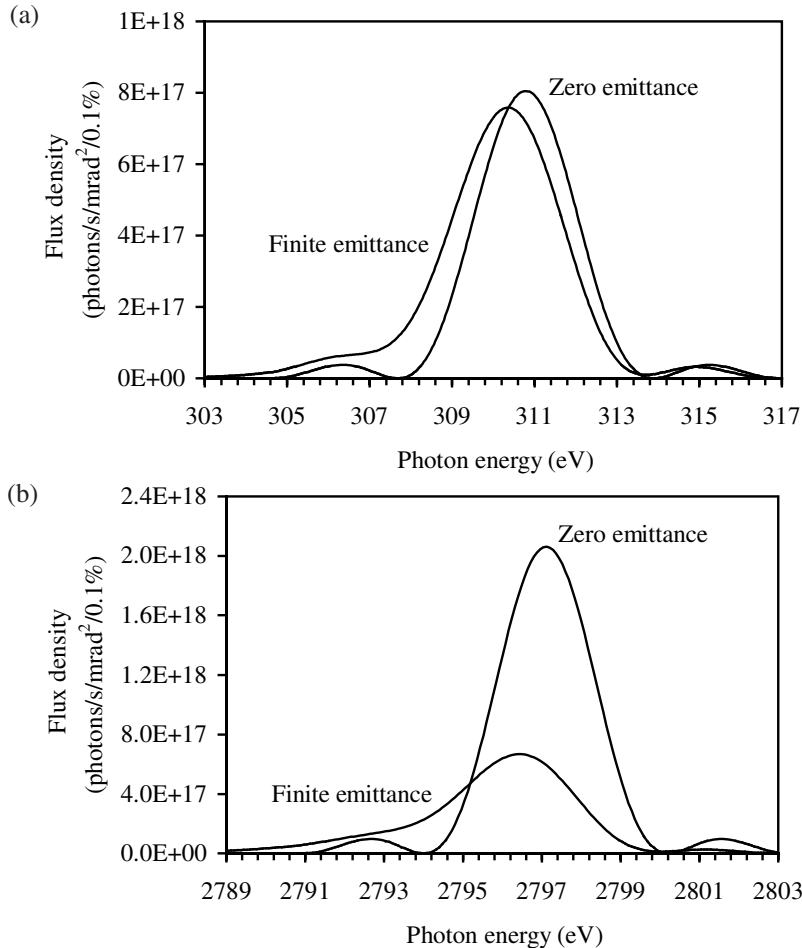
FIG. 5.3. The flux density as a function of photon energy about (a) the first and (b) the ninth harmonics with and without electron beam emittance included. The undulator has a 50 mm period, 100 periods, and $K = 3$.

at a particular energy have been included in the flux calculation. This was not the case for Fig. 5.5 where only the one harmonic contribution was included. This has the consequence that the values for the flux into all angles is significantly greater than the results shown in the previous plot, illustrating the point that many harmonics will contribute to the flux at a particular energy provided that large enough angles are used. This point is emphasized by the result for the 100 x 100 μrad aperture, which is a small enough angular acceptance so as to restrict the flux contributing at each photon energy to a single harmonic. Even with this restricted aperture the even harmonics are clearly present, though at a lower
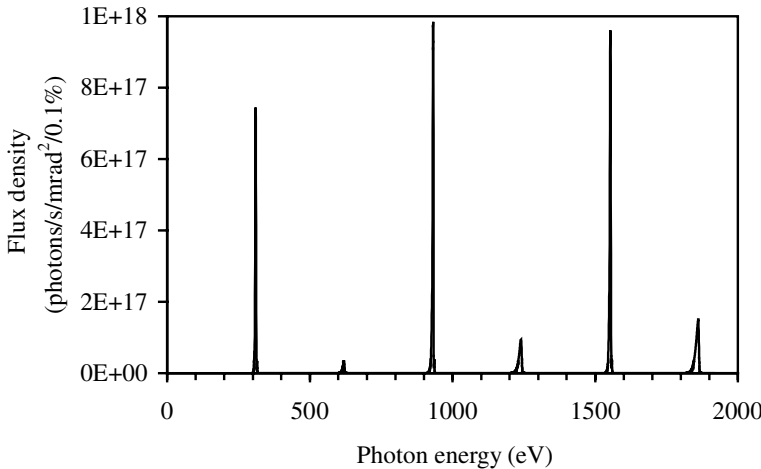
FIG. 5.4. The flux density as a function of photon energy with electron beam emittance included for the same conditions as Fig. 5.3.

overall flux level than the odd harmonics.

Finally, the interference effects that are present in multipole wigglers (where $K \gg 1$) can also be examined. An example of this is given in Fig. 5.7 where the flux into a 200 by 200 μrad aperture has been calculated for a device with $K = 15$. The result given by the analytical code for an undulator is compared with that given by a multipole wiggler spectrum, which is scaled from that of a bending magnet. It can be seen that there are strong interference effects at low energy but that the two calculations converge as the energy increases, this phenomena was discussed in Section 4.2.

5.2.2 *Comparison Between Theory and Experiment*

Accurate absolute measurement of insertion device angular flux density is difficult because of the many components in the photon beamline, which can affect the result or at the least add to the uncertainty in the measurement. Examples of areas which can introduce errors include mirror reflectivity, monochromator transmission, slit width uncertainties, detector calibration, and so on. However, several groups have attempted to compare measurements of actual undulator output with theoretical calculations. In general the relative shape of the flux density as a function of photon energy is as predicted. Agreement in the absolute angular flux density to within about 10% has been achieved at the harmonic peaks [47]. Also the structure between the harmonics predicted by the theory has been reproduced though generally with not such good agreement. Very high order harmonics (beyond 30th) have been observed and good agreement with theoretical predictions again seen [48, 49]. At these very high harmonics the predicted smearing of the spectrum into a smooth wiggler background is also observed.
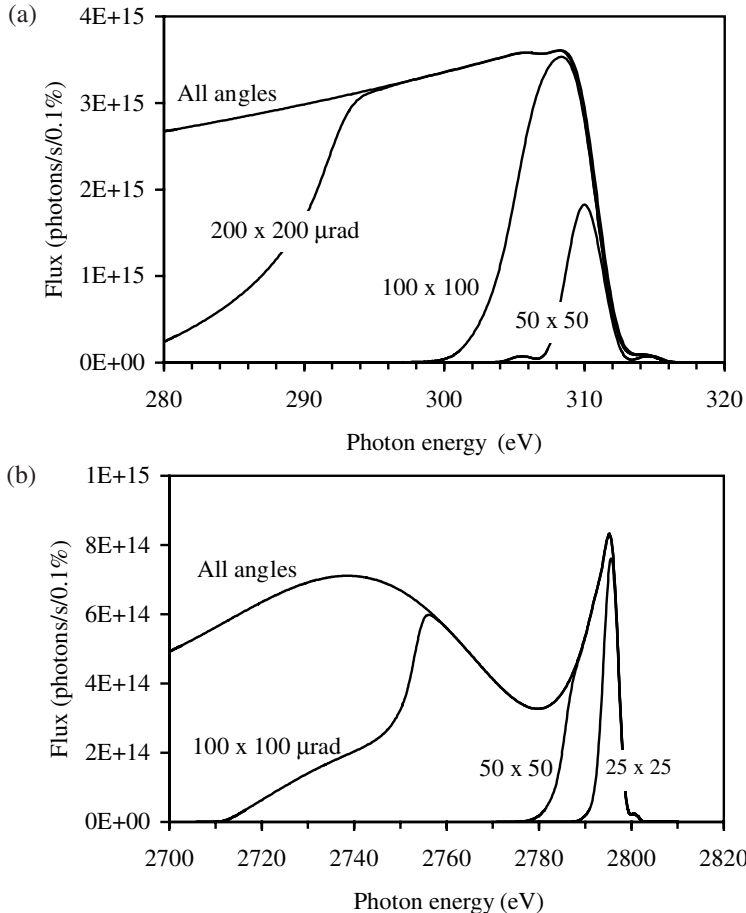
Fig. 5.5. The total flux passing through different aperture sizes as a function of photon energy for (a) the first and (b) the ninth harmonics. The undulator has a 50 mm period, 100 periods, and $K = 3$. A 300 mA filament electron beam of energy 3 GeV has been assumed.

Measurement of angular and spatial distributions have also been made [50]. In all of these measurements the exact electron beam dimensions are never known and so are treated as variables in the theoretical calculations to give the best fit to the experimental data. In this way, undulator spectral measurements have been used as a diagnostic technique for the stored electron beam properties.

Multipole wiggler measurements have also been made. These show the predicted qualitative properties of the smooth spectrum as a function of photon energy but again absolute measurements are difficult and agreement to within a few 10s of % is considered reasonable [51].
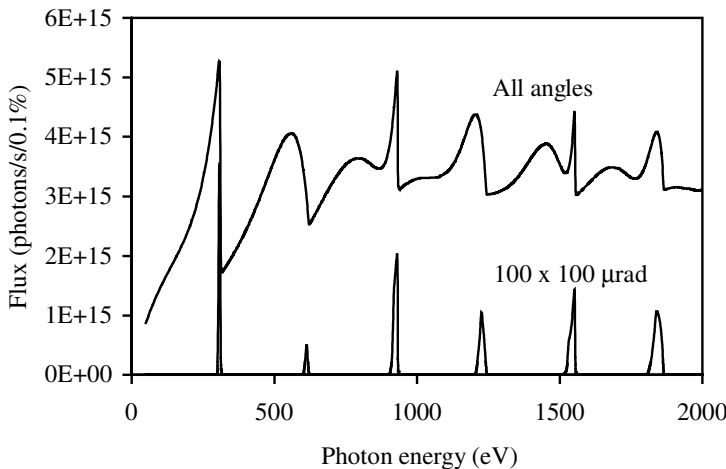
FIG. 5.6. The total flux emitted over all angles and also passing through a 100 x 100 μrad aperture (centred on the axis) as a function of photon energy for the same conditions as Fig. 5.5. A filament electron beam has been assumed.
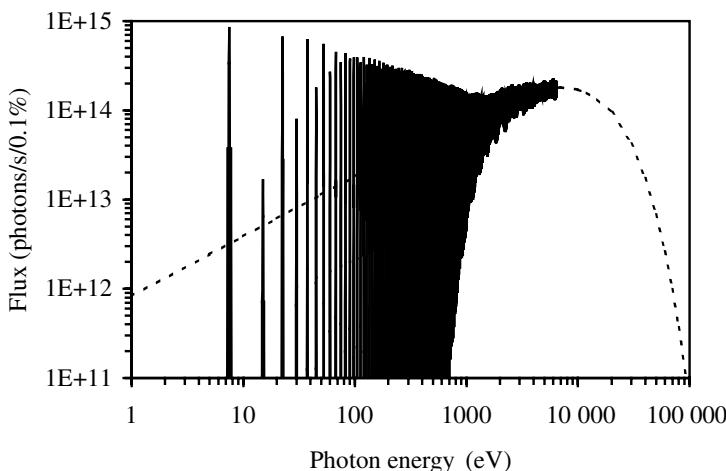
FIG. 5.7. The flux which passes through a 200 x 200 μrad aperture for an *undulator* with a 100 mm period, 45 periods, and $K = 15$. The dotted line is the flux for a *multipole wiggler* based upon the universal curve of a bending magnet. Note that the flux calculation for the undulator mode was deliberately halted at high energy.

Generation of Polarized Light

One of the many attractive features of synchrotron radiation (SR) is the polarization of the light. This chapter will show that the electron beam can be manipulated using magnetic fields in the insertion device (ID) to produce any type of polarization required, from linear horizontal through to linear vertical or from left circular through to right circular. This feature of synchrotron radiation can be very useful for many different types of experiment, from the study of magnetic materials to chiral molecules. The exploitation of insertion devices that produce variable polarization has been one of the fastest growing areas of synchrotron radiation over recent years.

In this chapter, we will first discuss a framework that is used to describe the polarization state, the so-called *Stokes parameters*. We will then explore the polarization properties of various types of insertion device, especially those that have been invented specifically to generate a particular type of polarization state. The actual alternative magnetic designs that have been proposed for each type of insertion device will be described in Chapter 7 for permanent magnet based solutions and Chapter 8 for electromagnet based solutions.

6.1 Characterization of Polarization

There are several formalisms that can be used to describe the polarization state of electromagnetic radiation. Naturally each has its own advocates, though as they are all equivalent it is necessary to only choose one system. Fortunately most of the insertion device literature has converged on the use of the Stokes parameters [52] and these are also used in some common insertion device codes [40, 45].

The polarization of an electromagnetic wave is given by the relationship between two orthogonal components of the electric field. If, as is usual, we describe the electric field by horizontal, E_x, and vertical, E_y, components such that

$$E_x = E_{x_0} \cos(\omega t)$$
$$E_y = E_{y_0} \cos(\omega t + \delta) \ ,$$

then we can see that there are three independent parameters, the amplitudes (E_{x_0} and E_{y_0}), and the phase difference, δ. As mentioned in Section 4.3.2, when

the phase difference is zero the light is linearly polarized with an angle determined by the relative electric field amplitudes. Alternatively, if the phase difference equals $\pi/2$ and $E_{x_0} = E_{y_0}$ then the light will be circularly polarized. However, since these three quantities cannot be measured directly, this particular description of the polarization state is not very practical. The alternative Stokes description, which is based upon measurable quantities, is created with reference to linear erect (I_x and I_y), linear skew ($I_{45°}$ and $I_{135°}$), and circular (I_R and I_L) intensities:

$$
\begin{aligned}
S_0 &= I_x + I_y = I_{45°} + I_{135°} = I_R + I_L \\
S_1 &= I_x - I_y \\
S_2 &= I_{45°} - I_{135°} \\
S_3 &= I_R - I_L \ .
\end{aligned}
$$

Furthermore, these can be expressed in terms of the electric field components (which are complex quantities in general, hence the need for conjugates) [52]

$$
\begin{aligned}
S_0 &= E_x E_x^* + E_y E_y^* \\
S_1 &= E_x E_x^* - E_y E_y^* \\
S_2 &= E_x E_y^* + E_x^* E_y \\
S_3 &= i(E_x^* E_y - E_x E_y^*) \ .
\end{aligned}
$$

The polarization rates, which are dimensionless quantities between -1 and +1, are given by

$$
\begin{aligned}
P_1 &= S_1/S_0 \\
P_2 &= S_2/S_0 \\
P_3 &= S_3/S_0 \ .
\end{aligned}
$$

The total polarization rate is $(P_1^2 + P_2^2 + P_3^2)^{1/2} \leq 1$ and the *natural* or *unpolarized* rate is given by $P_4 = 1 - (P_1^2 + P_2^2 + P_3^2)^{1/2}$.

A figure of merit has been suggested [53] for comparing alternative sources of polarized light. This is the quantity IP^2, which is the product of the total intensity, I, by the square of the desired polarization rate, P. As with many figures of merit, the applicability to a particular experiment should be carefully considered before applying it indiscriminantly.

6.2 Bending Magnets

We have already derived the horizontal and vertical electric field equations for an electron passing through a bending magnet, (2.26) and (2.27), and so we can write down the linear polarization rate as

$$P_1 = \frac{I_x - I_y}{I_x + I_y} = \frac{|E_x^2| - |E_y^2|}{|E_x^2| + |E_y^2|}$$

$$= \frac{K_{2/3}^2(G) - (\gamma^2\psi^2/(1+\gamma^2\psi^2))K_{1/3}^2(G)}{K_{2/3}^2(G) + (\gamma^2\psi^2/(1+\gamma^2\psi^2))K_{1/3}^2(G)} \; .$$

Since E_x is real and E_y is imaginary (implying a $\pi/2$ phase shift between the two) we have the result that $E_x E_y^* = -E_x^* E_y$ and so $S_2 = 0$. For the circular polarization rate we have $S_3 = -2\Re(E_x)\Im(E_y)$ and so

$$P_3 = \frac{-2K_{2/3}(G)(\gamma\psi/(1+\gamma^2\psi^2)^{1/2})K_{1/3}(G)}{K_{2/3}^2(G) + (\gamma^2\psi^2/(1+\gamma^2\psi^2))K_{1/3}^2(G)} \; .$$

In fact the sign of P_3 can be reversed by changing the sign of ψ, which is practically achieved by selecting radiation from below the horizontal axis rather than above it. In other words, both left and right circular radiation is available by changing the angle of observation. In contrast $P_1 \geq 0$ (since $K_{2/3}(G) > K_{1/3}(G)$, see Table 2.1) and so only linear horizontal radiation can be observed, not vertical. Finally, since the skew polarization rate, P_2, is zero no polarization at $45°$ will be observed, this also implies that the polarization ellipse always lies along the horizontal direction. The degree of linear and circular polarization as a function of vertical angle is shown in Fig. 6.1.

It can be seen that the circular polarization rate on the horizontal axis is zero and increases towards 1 at large observation angles. We should remember that the photon intensity has the opposite shape to this, with a maximum on-axis and falling to zero as ψ increases (Fig. 2.8). So, although bending magnets do produce circular polarization, which is certainly utilized at many synchrotron radiation laboratories, the intensity must always be compromised compared to the on-axis one. In fact, many experimenters are willing to accept a poorer circular polarization rate by increasing the beamline acceptance or reducing the observation angle for the advantage of higher intensity on the sample.

The polarization characteristics of a bending magnet can be understood qualitatively by considering the electron trajectory as seen by an observer (Fig. 6.2). First, if the observer is in the plane of the horizontal axis ($\psi = 0$), as the electron passes through the bending magnet he will simply see the electron move across the horizontal axis in a straight line. Hence at this point he will receive only linear horizontal polarization. Now if he observes from above the axis ($\psi > 0$) he will again see the electron pass across his field of view but this time it will have a degree of curvature as well and with an anticlockwise direction, say. Hence he will see a combination of linear and circular polarization. As ψ increases the curvature of the trajectory appears to increase and so does the circular polarization rate. Now, if he observes from below the axis ($\psi < 0$) he will again see the curved trajectory but this time the direction will appear to be reversed (clockwise, say) and so the circular polarization will have changed handedness.
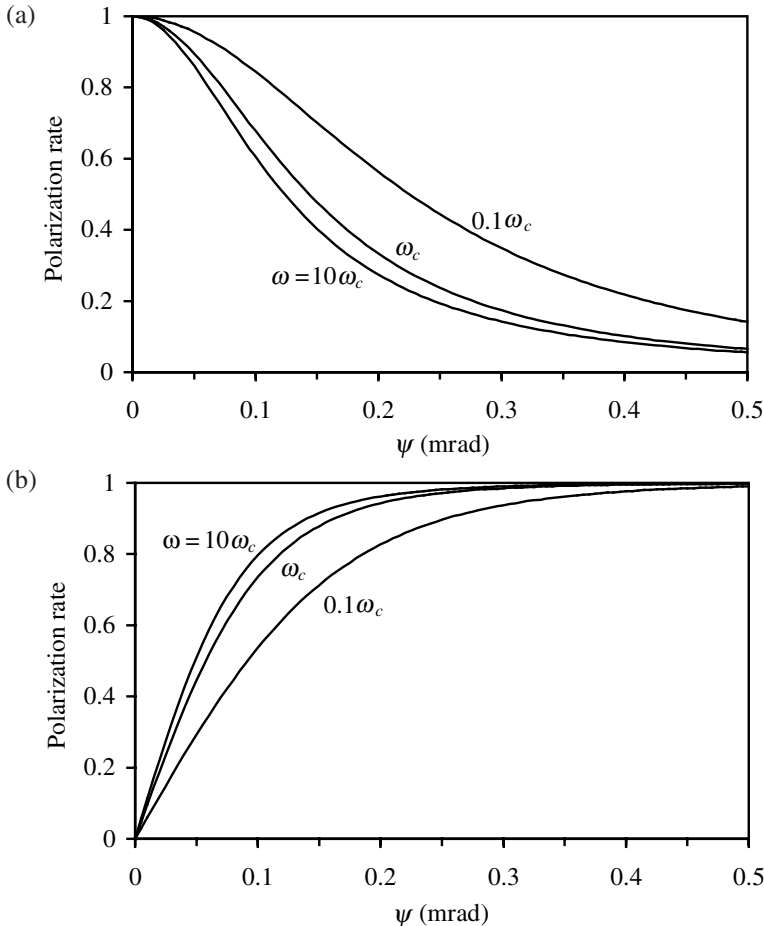
FIG. 6.1. The (a) linear and (b) circular polarization rates for a 1.4 T bending magnet as a function of vertical observation angle at various relative angular frequencies. The electron energy is 3 GeV.

All of these results and explanations assume a zero emittance electron beam and a very small collection angle. In reality, the finite electron beam size, divergence, and realistic beamline apertures will have the effect of diluting the polarization rates observed.

6.3   Conventional Planar Insertion Devices

As conventional undulators and multipole wigglers cause the electrons to oscillate in the horizontal plane the radiation polarization is again linear horizontal when observed on-axis. Away from the axis the undulator and multipole wiggler behave differently. We saw in Chapter 4 that the radiation from a conventional planar
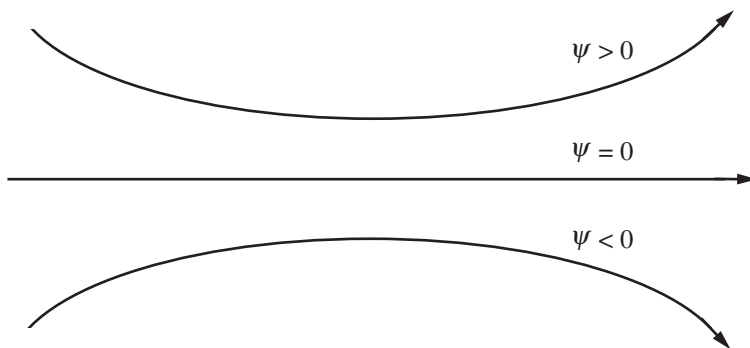
FIG. 6.2. Sketch of the exaggerated electron trajectory seen by an observer as his observation angle changes.

undulator is always linearly polarized no matter what the observation angle but that the inclination of the polarization depended upon the harmonic number and K value as well as the horizontal and vertical observation angles. There are no simple analytical expressions for P_1 and P_2.

For a multipole wiggler, which can be considered as a series of alternating polarity bending magnets, there is no skew linear component ($P_2 = 0$) and so all of the linearly polarized radiation is in the horizontal plane. More importantly though, there is no circular polarization present either ($P_3 = 0$). This can be explained by again considering what an observer would see of an electron trajectory when viewed vertically off-axis. In this case, over one wiggler period, he will not just see an electron make an arc in a clockwise direction but he will also see an equivalent arc in an anticlockwise direction. Therefore, the right circular radiation produced by one sweep will be exactly cancelled by the left circular radiation made in the opposite sweep. In other words, the incoherent sum of the left and right circular radiation will be equal to zero. The radiation generated by a multipole wiggler, which is not linearly polarized will be unpolarized ($P_4 \neq 0$) in contrast to a bending magnet.

6.4 Asymmetric Wigglers

To overcome the problem of multipole wigglers not generating any circularly polarized light two solutions have been employed. The first is the so-called *asymmetric wiggler*. As the name implies, this wiggler no longer has a symmetric magnetic field in the longitudinal direction. Rather it has a large positive field over a short distance followed by a smaller negative field over a longer distance so as to have a net zero integrated field per period. In this case then the circular polarization contributions of the two poles are not equal and so although the cancellation effect still occurs there is a resultant net circular polarization rate off axis.
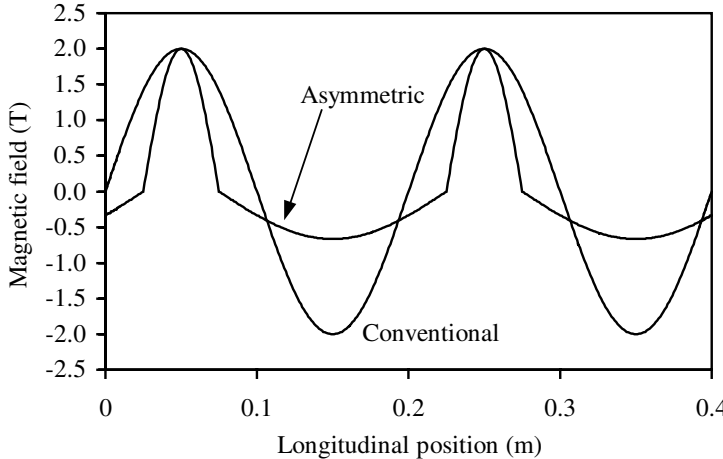
FIG. 6.3. Magnetic field profile of an (idealistic) asymmetric wiggler compared with a conventional multipole wiggler.

As an example we will compare the conventional multipole wiggler that was used in Fig. 3.1 with a modified (idealized) asymmetric version (Fig. 6.3). If we plot the vertical magnetic field as a function of the electron angle through the wigglers then the effect of the asymmetry becomes more obvious (Fig. 6.4). If the observer is at zero horizontal angle then in the conventional magnet he will see contributions from a +2 T pole and a -2 T pole giving perfect cancellation of the circular polarization. However, in our asymmetric example he will see a +2 T pole and a -0.7 T pole whose contributions will not cancel and he will see a net circular polarization when he observes from above or below the vertical axis. The circular polarization rate as a function of photon energy for this wiggler is given in Fig. 6.5. Note that the polarization rate changes sign as the photon energy increases because at low energies the weaker pole makes a larger contribution than the stronger pole with the opposite being true at high photon energies. Also note that as the relative magnetic field strengths change with horizontal angle then so does the circular polarization rate. Of course, the rate will also vary with vertical angle as for the bending magnet. Examples of asymmetric wigglers can be found at HASYLAB [54], ESRF [55], and DELTA [56].

6.5   Elliptical Multipole Wiggler

The second solution to the problem of conventional multipole wigglers not producing circularly polarized light is the *elliptical multipole wiggler*. In this device, a conventional multipole wiggler has a relatively weak horizontal field, B_x, of the same period, λ_u, as the main vertical field but $\pi/2$ out of phase from it. This has the effect of generating an elliptical trajectory in the electron beam (when viewed head on). This will provide a degree of circular polarization on-axis because the
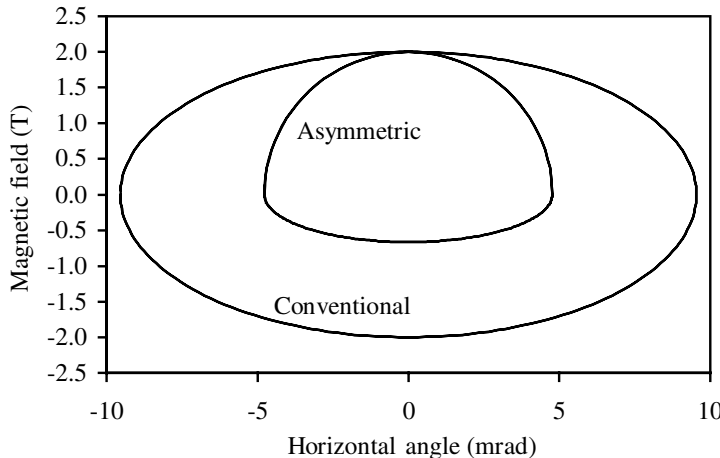
FIG. 6.4. Magnetic field as a function of horizontal angle for an asymmetric and
a conventional wiggler.
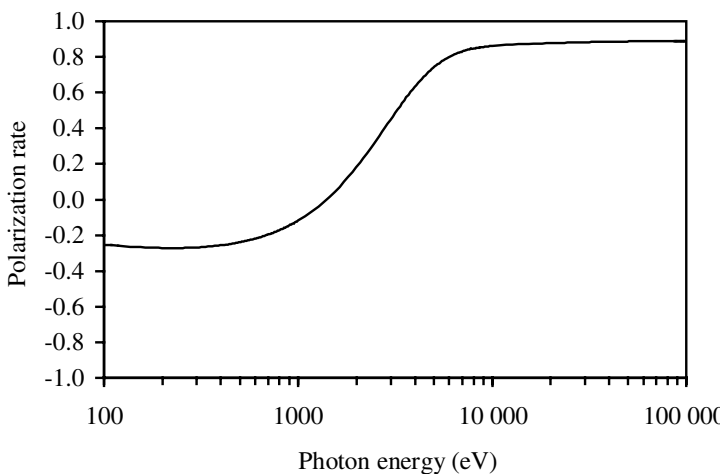
FIG. 6.5. The circular polarization rate for our example asymmetric multipole
wiggler as a function of photon energy at a fixed vertical observation angle
of 0.2 mrad and a beam energy of 2 GeV.

horizontal field has the effect of flipping the apparent vertical observation angle
from one pole to the next. In other words, from on-axis the first pole looks as
if it is being viewed with a positive vertical angle and the second pole, which is
of opposite polarity, looks as if it is being viewed with a negative vertical angle.
So instead of the circular polarizations nullifying each other from one pole to

the next they are reinforced. Since both poles per period work together in this device it will in general yield more useful flux than the asymmetric type where both poles are effectively fighting each other. The *effective* or *apparent* observation angle is equal to K_x/γ where $K_x = 93.4\, B_x \lambda_u$, this angle can be used in conjunction with an appropriate version of Fig. 6.1 to determine the expected circular polarization rate. Examples of elliptical multipole wigglers can be found at Photon Factory [57], ELETTRA [58], and NSLS [59].

6.6 Helical Undulators

The helical (or elliptical) undulator relies upon a similar concept as the elliptical multipole wiggler, in that a periodic horizontal field is introduced on-axis. It is distinguished from the wiggler in that the field values are weaker (low K regime) and so it operates on an interference principal rather than being a broadband, bending magnet-like, source.

We will consider an ideal helical undulator, which has horizontal and vertical fields on-axis with a variable phase difference between them

$$B_x = B_{x_0} \sin\left(\frac{2\pi s}{\lambda_u} - \phi\right)$$

$$B_y = B_{y_0} \sin\left(\frac{2\pi s}{\lambda_u}\right) \ .$$

First we will consider what effect the additional horizontal term has on the undulator wavelength equation. To do this we will build upon the derivation for the planar undulator that was presented in Chapter 4. From the magnetic fields we can write down the electron velocities in the two planes as (4.1),

$$\beta_x = \frac{K_y}{\gamma} \cos\left(\frac{2\pi s}{\lambda_u}\right)$$

$$\beta_y = \frac{K_x}{\gamma} \cos\left(\frac{2\pi s}{\lambda_u} - \phi\right) \ ,$$

where

$$K_x = \frac{B_{x_0} e}{mc} \frac{\lambda_u}{2\pi}$$

$$K_y = \frac{B_{y_0} e}{mc} \frac{\lambda_u}{2\pi} \ .$$

As the energy of the electron is fixed, β is also fixed and so any variation in β_x and β_y must result in a corresponding change in β_s ($\beta^2 = \beta_x^2 + \beta_y^2 + \beta_s^2$). From this we have

$$\beta_s^2 = \beta^2 - \frac{K_y^2}{\gamma^2} \cos^2\left(\frac{2\pi s}{\lambda_u}\right) - \frac{K_x^2}{\gamma^2} \cos^2\left(\frac{2\pi s}{\lambda_u} - \phi\right)$$

$$= \beta^2 - \frac{K_y^2}{2\gamma^2} - \frac{K_y^2}{2\gamma^2} \cos\left(\frac{4\pi s}{\lambda_u}\right) - \frac{K_x^2}{2\gamma^2} - \frac{K_x^2}{2\gamma^2} \cos\left(\frac{4\pi s}{\lambda_u} - 2\phi\right) \quad .$$

Note at this point that for the purely circular case, where $K_x = K_y$ and $\phi = \pi/2$, the longitudinal electron velocity is a constant. This has important consequences for the harmonic content of the on-axis radiation as we shall see later. For the general case, applying the approximation $(1-x)^{1/2} \sim 1 - x/2$, we get

$$\beta_s \sim \beta \left(1 - \frac{K_y^2}{4\beta^2\gamma^2} - \frac{K_x^2}{4\beta^2\gamma^2} - \frac{K_y^2}{4\beta^2\gamma^2} \cos\left(\frac{4\pi s}{\lambda_u}\right) - \frac{K_x^2}{4\beta^2\gamma^2} \cos\left(\frac{4\pi s}{\lambda_u} - 2\phi\right) \right) \quad .$$

For the average value of β_s we can remove the oscillating cosine terms

$$\hat{\beta}_s \sim \beta - \frac{K_y^2}{4\beta\gamma^2} - \frac{K_x^2}{4\beta\gamma^2}$$

$$\sim 1 - \frac{1}{2\gamma^2} - \frac{K_y^2}{4\beta\gamma^2} - \frac{K_x^2}{4\beta\gamma^2} \quad .$$

We can now insert this into the interference condition (4.3) to get

$$\lambda = \frac{\lambda_u}{2n\gamma^2} \left(1 + \frac{K_x^2}{2} + \frac{K_y^2}{2} + \theta^2\gamma^2 \right) \quad . \tag{6.1}$$

The similarity with the result for a planar undulator is clear (4.4). One important and perhaps surprising conclusion from this equation is that the wavelength emitted does not depend upon the phase between the horizontal and vertical fields in an ideal helical undulator.

It has been shown that for the first harmonic and small K_x, K_y the polarization rates can be approximated as [29]

$$P_1 = \frac{B_{y_0}^2 - B_{x_0}^2}{B_{y_0}^2 + B_{x_0}^2}$$

$$P_2 = \frac{2B_{x_0}B_{y_0}\cos\phi}{B_{y_0}^2 + B_{x_0}^2}$$

$$P_3 = \frac{2B_{x_0}B_{y_0}\sin\phi}{B_{y_0}^2 + B_{x_0}^2} \quad .$$

We can see that, as mentioned earlier, only three independent parameters are needed to specify the polarization and so the ideal helical undulator is capable of producing any polarization state.

The derivation for the planar undulator angular flux density that was given in Section 4.3 can be extended to include the contribution from the electron vertical velocity, β_y, in eqn (4.9). The key helical result, when $\phi = \pi/2$, is that the angular flux density on-axis is

$$\left.\frac{d^2N}{d\Omega\,d\omega/\omega}\right|_{\theta=0} = \frac{e^2N^2\gamma^2}{4\pi\epsilon_0 c}\frac{I_b}{e}\frac{2\pi}{h}L\left(\frac{N\Delta\omega}{\omega_1}\right)F_n(K_x, K_y)\ ,$$

where

$$F_n(K_x, K_y) = \frac{n^2}{(1 + K_x^2/2 + K_y^2/2)^2}\left(K_x^2\left(J_{(n+1)/2}(Y) + J_{(n-1)/2}(Y)\right)^2\right.$$
$$\left. + K_y^2\left(J_{(n+1)/2}(Y) - J_{(n-1)/2}(Y)\right)^2\right)$$

and

$$Y = \frac{n(K_y^2 - K_x^2)}{4(1 + K_x^2/2 + K_y^2/2)}\ ,$$

which in practical units of photons per second per mrad^2 per 0.1% bandwidth is

$$\left.\frac{d\dot{N}}{d\Omega}\right|_{\theta=0} = 1.74 \times 10^{14}\,N^2E^2I_bF_n(K_x, K_y)\ .$$

The similarities with the planar result are clear (4.13).

Furthermore the integrated flux is

$$\dot{N} = \alpha\pi N\frac{I_b}{e}\frac{\Delta\omega}{\omega}Q_n(K_x, K_y)\ ,$$

where

$$Q_n(K_x, K_y) = \frac{1 + K_x^2/2 + K_y^2/2}{n}F_n(K_x, K_y)\ ,$$

which in practical units of photons per second per 0.1% bandwidth gives a flux of

$$\dot{N} = 1.43 \times 10^{14}\,NI_bQ_n(K_x, K_y)\ .$$

When $B_{x_0} = B_{y_0}$, the elliptical trajectory of the electron becomes perfectly circular. With $Y = 0$, the only non-zero Bessel term in $F_n(K_x, K_y)$ is J_0 which only occurs when $n = 1$. This implies that only the *first harmonic is present* on-axis in this circular mode. The circular polarization rate, P_3, equals unity in this mode and so the radiation is *purely circularly polarized*. The angular flux density and integrated flux equations simplify to
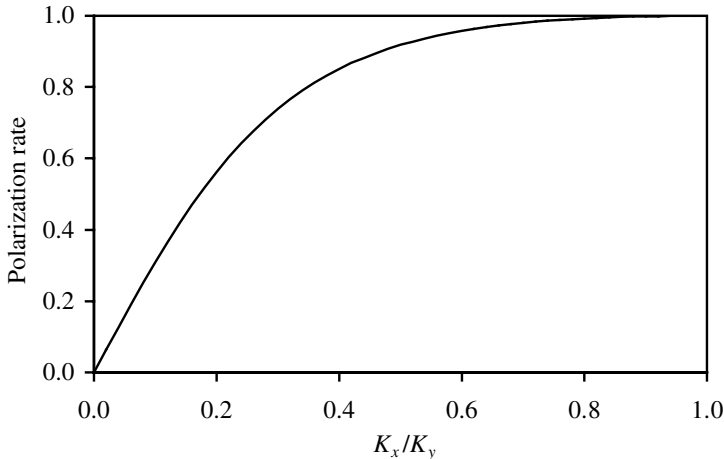
FIG. 6.6. Circular polarization rate as a function of K_x/K_y for an undulator with $K_x = K_y = 3$ in pure circular mode.

$$\frac{d\dot{N}}{d\Omega}\bigg|_{\theta=0} = 3.49 \times 10^{14}\, N^2 E^2 I_b \frac{K^2}{(1+K^2)^2}$$

and

$$\dot{N} = 2.86 \times 10^{14}\, N I_b \frac{K^2}{1+K^2}\ ,$$

where $K = K_x = K_y$. The circular polarization rate for an undulator as it transforms from a planar to a circular device is shown in Fig. 6.6. We can see that in planar mode ($K_x = 0$) there is no circular polarization (pure linear) and in helical mode ($K_x = K_y$) the reverse is true.

There are many helical undulators, of differing magnet designs, in use around the world. Examples include undulators that have been demonstrated on Super-ACO [60], JSR [61], SPEAR [62], and ESRF [63].

6.7   Crossed Undulators

In this scheme two planar undulators, both linearly polarized, are placed in a straight section orthogonal to each other and with a variable phase shifter between them (Fig. 6.7). Polarization ranging from purely helical to purely linear can be generated by varying the phase between the two sections [64].

If the undulators are identical (each with N periods) and the first is polarized in the horizontal plane and the second in the vertical plane then the Stokes polarization rates are given by

Phase shifter

Horizontal undulator

Vertical undulator
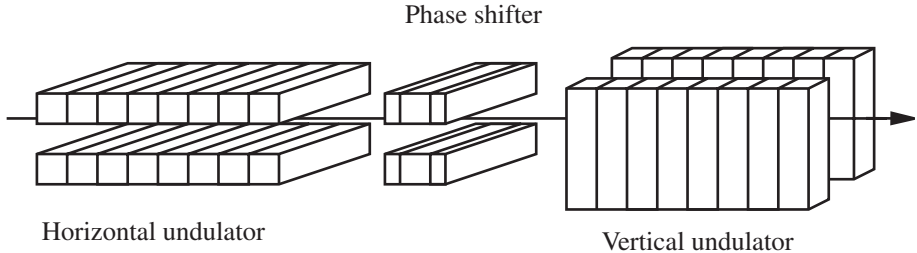
Fig. 6.7. Sketch of the crossed undulator scheme.

$$P_1 = 0$$
$$P_2 = \cos(N\delta + \Psi)$$
$$P_3 = \sin(N\delta + \Psi) \ ,$$

where $\delta = 2\pi\Delta\omega/\omega_1$ (see Section 4.3) is the phase advance per period and Ψ is the additional phase change introduced by the variable phase shifter [65].

At the harmonic frequency (zero detune, $\Delta\omega = 0$) the polarization state depends only on Ψ and smoothly varies between linear at 45° to right handed circular to linear at 135° to left handed circular, and back to linear at 45°. Away from the harmonic frequency the polarization state can change quickly. A narrow range of frequencies must therefore be selected to obtain light of the desired polarization.

Since the crossed undulator will only operate successfully over a narrow bandwidth it follows that it is also sensitive to the angular acceptance that can be used. A narrow acceptance is needed to maintain the polarization. This also places restrictions on the electron beam divergence, which must be small for the same reason.

The sensitivity of the polarization rate to the electron beam quality, monochromator bandpass, and angular acceptance increases with harmonic number. It has been suggested that this sensitivity could be exploited as a method of generating high energy *unpolarized* light, which would be beneficial for some experiments [66].

Interestingly, the crossed undulator will generate circular polarization on-axis at the harmonics of the fundamental, unlike the helical undulator. Also, if horizontal and vertical linear polarization is required then this can be achieved by simply rotating the two undulators by 45° around the electron beam axis. Indeed, this was proposed for the Aladdin crossed undulators [67]. An example of a crossed undulator (using horizontal and vertical undulators) was implemented on the BESSY storage ring [68, 69].

An alternative proposal is to use two helical undulators of opposite helicity instead of linear ones [70]. This combination gives full control of the linear

polarization inclination with zero circular rate. However, since the individual helical undulators only produce one harmonic on-axis, the linear polarization also consists of only the first harmonic as well.

6.8   Power from Helical Undulators

6.8.1   *Total Power*

Following the same approach as used in Section 3.5.1 we can derive the total power emitted by a helical undulator with $K_x = K_y$ and $\phi = \pi/2$. As before, we find that the total power is given by (3.5)

$$P_{\text{total}} = 1265.5 \, E^2 I_b \int_0^L B(s)^2 ds \ .$$

And in the helical case $B(s)$ is constant, since $B^2 = B_x^2 + B_y^2$, and so the total power emitted in Watts is

$$P_{\text{total}} = 1265.5 \, E^2 B_0^2 L I_b$$

exactly double that produced by a planar undulator.

6.8.2   *Power Density*

The angular distribution of the power density from a helical undulator is found by integrating the flux density over all photon energies [71].

$$\frac{dP}{d\Omega} = \frac{4NeK^2\gamma^4 I_b}{\lambda_u \epsilon_0 (1 + K^2 + \gamma^2\theta^2)^3} \sum_{n=1}^{\infty} n^2 \left(J_n'^2(x_n) + \left(\frac{\gamma\theta}{K} - \frac{n}{x_n} \right)^2 J_n^2(x_n) \right) \ ,$$

where $K = K_x = K_y$, n is the harmonic number,

$$x_n = \frac{2Kn\gamma\theta}{1 + K^2 + \gamma^2\theta^2}$$

and

$$J_n'(x) = \frac{J_{n-1}(x) - J_{n+1}(x)}{2} \ .$$

On-axis, $\theta = 0$, all of the Bessel terms are zero for $n > 1$ (since only the first harmonic is present on-axis) and the power density simplifies to

$$\left. \frac{dP}{d\Omega} \right|_{\theta=0} = \frac{2NeK^2\gamma^4 I_b}{\lambda_u \epsilon_0 (1 + K^2)^3} \ ,$$

which in practical units of W/mrad^2 is
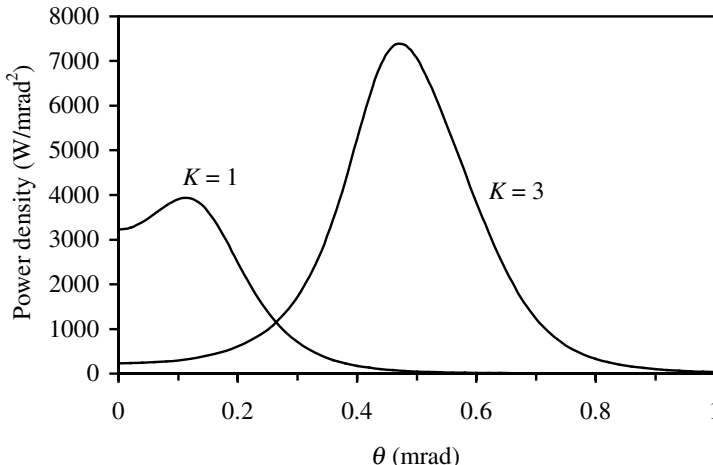
FIG. 6.8. Graph of the power density produced by a helical undulator as a function of angle for two different K values. The undulator period is 50 mm, the length is 5 m, the electron energy is 3 GeV, and the beam current is 300 mA.

$$\left.\frac{dP}{d\Omega}\right|_{\theta=0} = 4625.7\,\frac{B_0^2 E^4 L I_b}{(1+K^2)^3} \quad .$$

A plot of the power density as a function of angle is given in Fig. 6.8 for two different K values. The undulator with a K of 3 produces relatively little power on-axis but has a large power density (and so total power) away from the axis. It is interesting to note that the lower K undulator actually has a larger on-axis power density. This is because it has a higher flux density and also generates higher energy photons on-axis.

Permanent Magnet-Based Design of Insertion Devices

The earlier chapters have discussed in detail the properties of synchrotron radiation (SR) emitted by relativistic particles travelling through various periodic magnetic field configurations generated by alternative types of insertion device (ID). However, so far no means of actually creating these magnetic fields have been discussed. In reality, there are two common methods employed, one based upon electromagnets (which we will cover in Chapter 8) and the other based upon permanent magnets, which is the subject of this chapter.

7.1 Permanent Magnet Basics

The theory that describes permanent magnets is similar to that for soft magnetic materials. However, magnetic properties of materials is a complete topic by itself and so only a brief outline will be presented here. More detailed information and explanation about magnetic theory and permanent magnets in particular can be found in other texts [72, 73].

A magnet is said to be permanent (or 'hard') if it will independently support a useful flux in the air gap of a device. A material is magnetically soft if it can only support such a flux with the aid of an external electrical circuit. A permanent magnet can be considered as a passive device analogous to a spring, which stores mechanical energy.

An electron in a microscopic orbit has a magnetic dipole moment, which can be modelled as a current circulating in a loop. In the case of permanent magnets these 'molecular' currents can be identified with atoms with unfilled inner shells, as present in the 3d metals (Fe, Co, or Ni) or the 4f metals (rare earths, Ce to Yb). Permanent magnet materials are manufactured in a way that enhances their magnetic properties along a preferred axis. This is most readily achieved by taking advantage of crystal lattice structures, which have preferred directions for the magnet moments. The alignment of the moments in the lattice is called *magnetocrystalline anisotropy* or just *magnetic anisotropy*. The direction of alignment is called the *easy magnetization direction* or *easy axis*.

When a magnetic field, $\boldsymbol{B}$, is applied to a magnetic material, each dipole moment tries to align itself with the direction of the field. When $\boldsymbol{B}$ is strong enough (at saturation) all of the moments will align themselves, overcoming

other atomic forces, which resist this change. A permanent magnet must have an internal field to be able to maintain this alignment after $\boldsymbol{B}$ is removed (so-called *spontaneous magnetization*). Magnetization, $\boldsymbol{M}$, is the magnetic dipole moment per unit volume and in the absence of external fields is related to the internal field by $\boldsymbol{B} = \mu_0 \boldsymbol{M}$ (μ_0 is the permeability of free space, $4\pi \times 10^{-7}$ Hm^{-1}).

Ampère's law states that $\boldsymbol{B}$ is related to a current density $\boldsymbol{J}$ in a conductor by

$$\mu_0 \boldsymbol{J} = \nabla \times \boldsymbol{B} \ .$$

If the magnetization is considered to be due to a circulating current of density $\boldsymbol{J_M}$ then

$$\boldsymbol{J_M} = \nabla \times \boldsymbol{M} \ .$$

If we have both a conductor carrying current and a magnet of equivalent current density $\boldsymbol{J_M}$ then the total flux density due to both sources will be

$$\mu_0 (\boldsymbol{J} + \boldsymbol{J_M}) = \nabla \times \boldsymbol{B} \ ,$$

which can be rearranged to give

$$\mu_0 \boldsymbol{J} = \nabla \times (\boldsymbol{B} - \mu_0 \boldsymbol{M}) \ .$$

A new parameter called *magnetizing force*, $\boldsymbol{H}$, is now defined as

$$\mu_0 \boldsymbol{H} = \boldsymbol{B} - \mu_0 \boldsymbol{M}$$

and so

$$\boldsymbol{B} = \mu_0 (\boldsymbol{H} + \boldsymbol{M}) \ . \tag{7.1}$$

This now gives a more general form of Ampère's law

$$\boldsymbol{J} = \nabla \times \boldsymbol{H} \ ,$$

which allows for real currents and material magnetization.

The characteristics of a permanent magnet are broadly determined by its behaviour under an external magnetization force, $\boldsymbol{H}$. When the force is large enough the material is saturated and all of the dipole moments are aligned. The magnetization is now M_{sat} (Fig. 7.1). If $\boldsymbol{H}$ is now reduced the magnetization remains constant, even when $\boldsymbol{H}$ goes negative and tries to demagnetize the material, this is after all a permanent magnet. However, the demagnetizing force will eventually become too strong and the material will no longer be able to resist. Over a relatively short range of $\boldsymbol{H}$ the material flips to the opposite state with a magnetization now of $-M_{\text{sat}}$. The value of $\boldsymbol{H}$, which causes the magnetization to
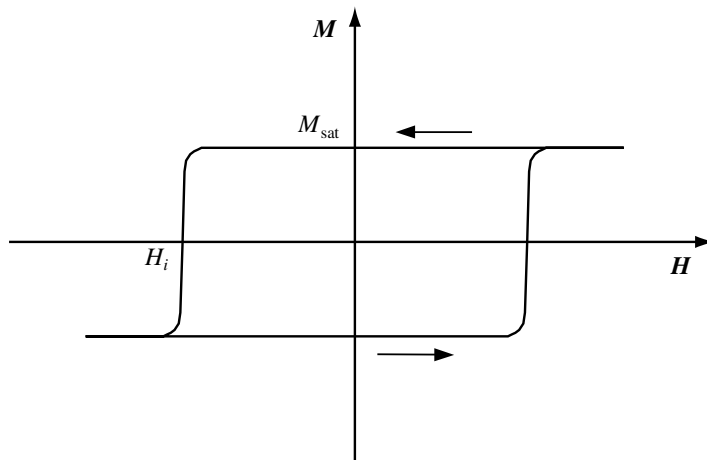
FIG. 7.1. The variation of magnetization as a function of magnetizing force for an ideal permanent magnet.

suddenly flip, or, more precisely, the value at which $M = 0$, is called the *intrinsic coercivity* of the material, H_i.

Another hysteresis loop, this time of $\boldsymbol{B}$ vs. $\boldsymbol{H}$, can be derived from the magnetization curve by using (7.1). Since $\boldsymbol{M}$ has a constant value for most values of $\boldsymbol{H}$, $\boldsymbol{B}$ follows a straight line of gradient μ_0 (Fig. 7.2). The value of $\boldsymbol{B}$ when $\boldsymbol{H}$ is zero is called the *remanent field* or *remanence*, B_r. The value of $\boldsymbol{H}$ that is required to reduce $\boldsymbol{B}$ to zero is called the *coercive force* or *coercivity*, H_c. We can see that for the ideal permanent magnet described, the $\boldsymbol{B}$ vs. $\boldsymbol{H}$ loop in the second quadrant is entirely linear. This is a very important characteristic that is extremely useful in the application of permanent magnets as they are always operated in the second quadrant.

The product of $\boldsymbol{B}$ and $\boldsymbol{H}$ represents the energy density of the material and if we plot this product for the second quadrant we can see that it has a peak value, $BH_{\max}$ (Fig 7.3). This value is another common measure of a permanent magnet that is used to compare alternative materials.

The position on the B-H curve at which the permanent magnet is operated is called the *working point*. When the working point coincides with $BH_{\max}$ then the maximum potential energy available is being utilized and the magnet material is being used efficiently. In a linear material $BH_{\max}$ occurs at $B = B_r/2$, $H = -H_c/2$.

Not all materials exhibit this linear behaviour in the second quadrant. Sometimes the 'knee' of the curve occurs when $B > 0$. This can be a problem in dynamic systems where $\boldsymbol{B}$ is changing (e.g. when opening or closing an undulator or even during assembly of the magnet blocks onto the undulator arrays). If the working point moves into the non-linear region (from point a to point b in
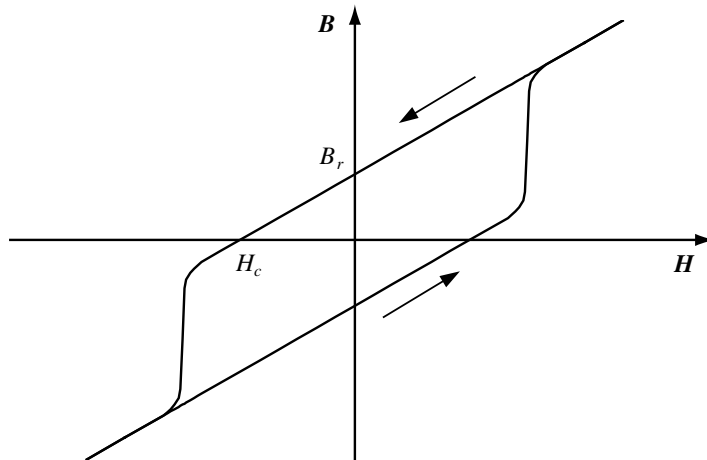
FIG. 7.2. The variation of magnetic field as a function of magnetizing force for an ideal permanent magnet.
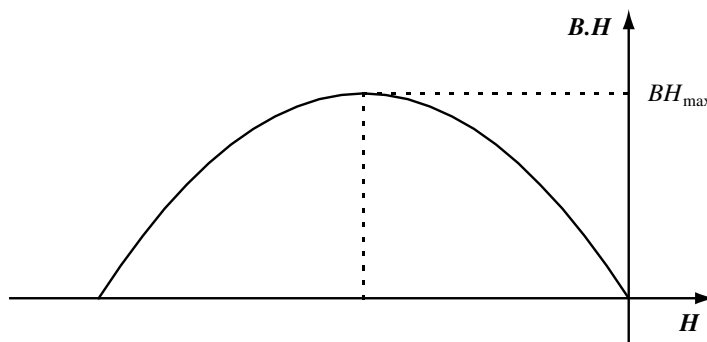
FIG. 7.3. The BH product as a function of magnetizing force for an ideal permanent magnet.

Fig. 7.4) then when B increases again the working point will move to c and not back to a. This loss in the field is *irreversible*.

The B-H curves also change significantly with temperature, becoming increasingly non-linear in the second quadrant as the temperature increases (Fig. 7.5). So long as the working point stays within the linear region of the demagnetization curve the changes in the field are *reversible* and so when the temperature reduces the magnet will fully recover its field level. Fortunately this is not a major problem for most insertion devices as they are usually operated at close to room temperature. However, it does imply that any temperature variation will introduce some unwanted change to the magnetic field of the device and
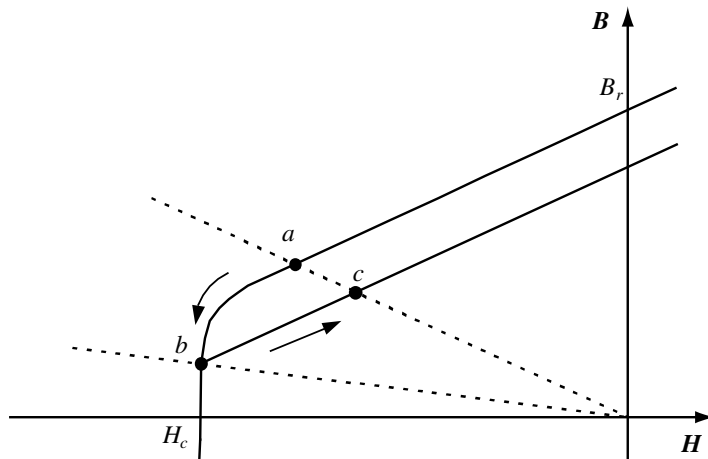
FIG. 7.4. The effect of moving up and down the *B-H* curve in a non-linear region. The dotted lines represent different *load lines*.
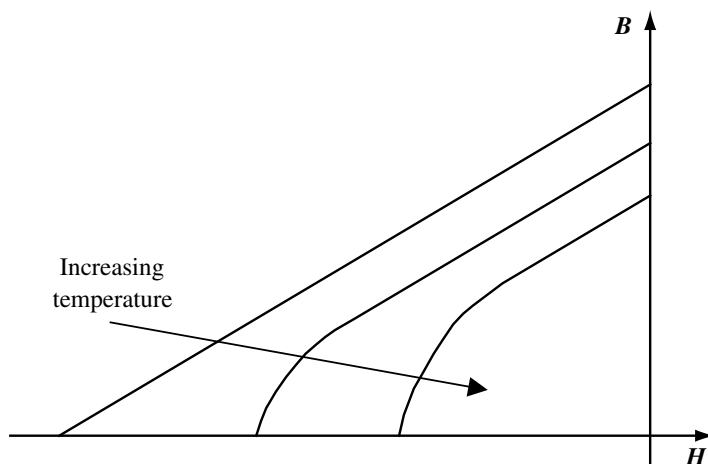
FIG. 7.5. The effect of different temperatures on the *B-H* curve of a permanent magnet.

this is why permanent magnet IDs often have temperature-stabilized enclosures mounted around them.

An ideal permanent magnet will be uniformly magnetized (homogeneous), which implies that the equivalent current model is a current sheet at the block surface with no internal volume currents. To convince yourself of this model consider how a current sheet flowing on the surface of a cylinder (a solenoid) creates a uniform magnetic field within the cylinder. Furthermore, if the relative

permeability of the material is equal to 1 then the bulk material can be treated like vacuum and one only needs to consider the equivalent surface current sheets to accurately model a block of permanent magnet.

Permanent magnets with these properties are called *current sheet equivalent materials*. The implication is that the fields generated by different blocks can be added linearly which makes analytical calculation of permanent magnet systems straightforward so long as there is no soft magnetic material (eg iron) present. In fact, the most popular materials that are used for insertion devices can be treated in this way, which does help considerably with magnet modelling. A permanent magnet block with remanent field of 1 T is equivalent to current sheets of strength ± 8 kA/cm block length, separated by the block width [74]. Figure 7.6 shows the lines of flux generated by a permanent magnet block and also those generated by a current sheet equivalent to this block.

7.2 Available Materials

There are two types of material that are used for insertion devices. The first to be used was *samarium-cobalt* ($SmCo_5$ or Sm_2Co_{17}), which is a member of the *rare earth-cobalt* family of permanent magnets. This intermetallic compound has a remanent field of typically 0.85 - 1.05 T, coercivity of 600 - 800 kA/m, maximum energy density of 150 - 200 kJ/m^3 and relative permeability close to unity. A consequence of the anisotropy of the material is that the relative permeability is different for the directions parallel ($\mu_\parallel$) and transverse ($\mu_\perp$) to the easy axis. For samarium-cobalt they are typically $\mu_\parallel \sim 1.01$ and $\mu_\perp \sim 1.04$. Although the difference between the two directions is small it does have measurable consequences and is often taken into account in detailed computer based magnet modelling.

Samarium-cobalt can be very linear in the second quadrant and also well into the third, implying large values for the intrinsic coercivity. A feature of this material is that it performs well at high temperature. It can be used above 200°C but with a subsequent loss in remanent field of typically 0.04%/°C. The Sm_2Co_{17} grade offers slightly higher remanent field and is also thought to be more resistant to radiation damage, which can be important in a high energy synchrotron light source.

The exact production process and 'additives' for each permanent magnet grade are a closely guarded secret but they do follow the same general sequence. First the alloy is crushed and milled to produce a fine powder, which is then pressed under a magnetic field. It is then sintered and annealed, machined, and finally magnetized. This process produces a ceramic-like material that is quite difficult to work with as it is brittle and has a tendency to chip or crack.

The alternative material, which only became available in the 1980s, is *neodymium-iron-boron* ($Nd_2Fe_{14}B$). This has many advantages over samarium-cobalt and is now the most commonly used of the two materials for insertion devices. It has a higher remanent field of typically 1.1 - 1.4 T, coercivity of 750 - 1000 kA/m and therefore maximum energy density of 200 - 350 kJ/m^3. It can

(a)

(b)
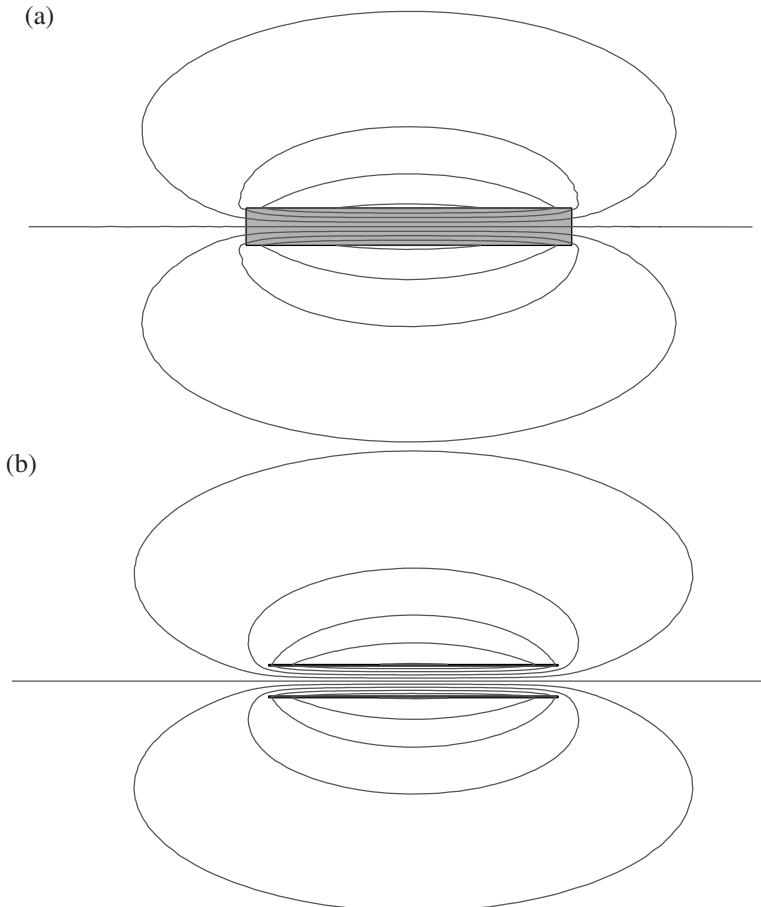
FIG. 7.6. Lines of flux for (a) an ideal permanent magnet block with easy axis directed from left to right and (b) an equivalent current sheet model with currents flowing into and out of the plane of the paper.

also be linear in the second quadrant and part of the third though it does have slightly higher permeabilities of typically $\mu_\parallel \sim 1.05$ and $\mu_\perp \sim 1.15$.

Neodymium-iron-boron does not perform well at high temperatures and generally is kept well below 100°C. It also suffers from a larger temperature coefficient than samarium-cobalt of −0.11%/°C. There is also some evidence that it is not so resistant to radiation damage as both types of samarium-cobalt [75,76].

The material is less brittle than samarium-cobalt and therefore easier to machine though it does still suffer from losing small chips at block edges. Neodymium is more abundant than samarium and this is one reason why neodymium-iron-boron magnets are cheaper than samarium-cobalt ones. Even so, in most
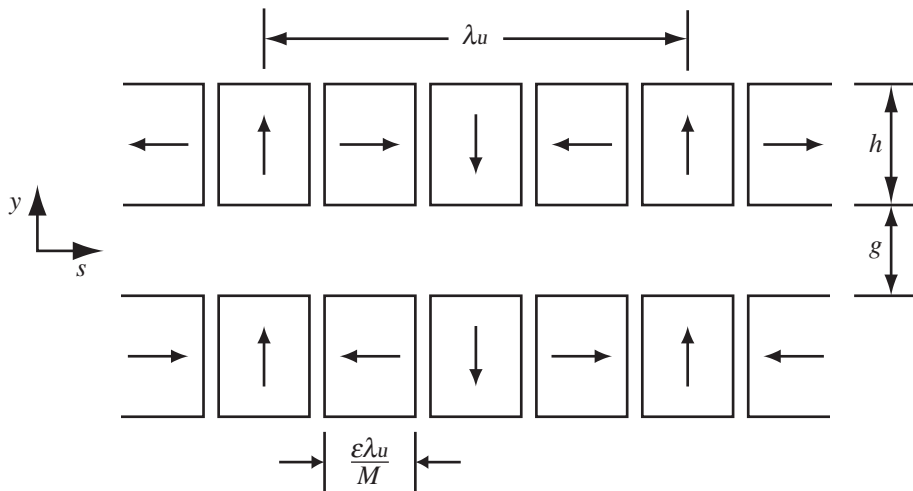
FIG. 7.7. Sketch of the PPM insertion device concept. The arrows indicate the direction of the easy axis in the magnet blocks.

permanent magnet-based insertion devices the magnets themselves form a significant fraction of the total cost.

Although permanent magnets have improved beyond all recognition over the past 100 years it is not expected that there will be any dramatic increase of the maximum energy density in the future. However, there is one tantalising possibility that may transform the field of permanent magnets – superconductivity. 'Permanent' magnets based on high T_c superconductors already exist. Remanent fields of close to 8 T and maximum energy densities of 12 800 kJ/m^3 ($\sim$ 30 times larger than that for neodymium-iron-boron) have been measured [73]. However, as these presently only operate (and survive) at $\sim$77 K it may be some time before we see them used in an insertion device!

7.3 Pure Permanent Magnet Insertion Devices

A magnet which contains no soft magnetic material (e.g. iron poles) or additional current carrying coils is called a *pure permanent magnet* (PPM). An ideal PPM undulator (or multipole wiggler) would consist of two arrays of permanent magnet material with the easy axis of the material smoothly rotating through 360° per undulator period, λ_u, along the direction of the electron beam [77]. In practice this can be approximated by a series of M rectangular homogeneous blocks per period (Fig. 7.7).

The derivation of the magnetic field due to these two arrays can be carried out using the superposition principle. First the field at each point due to a single block is calculated by integrating over each block surface in turn
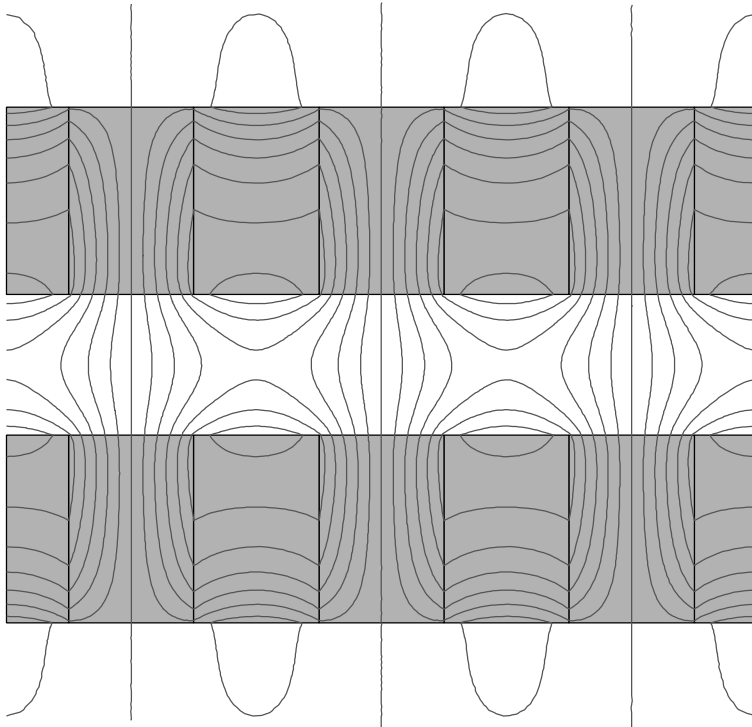
FIG. 7.8. Lines of flux in a PPM insertion device. The direction of the easy axis for each block is as in Fig. 7.7.

$$\boldsymbol{B} = \frac{\mu_0}{4\pi} \int_S \frac{\boldsymbol{M} \times \boldsymbol{n} \times \boldsymbol{r}}{r^3} dS \ ,$$

where $\boldsymbol{n}$ is a unit vector normal to the surface S and $\boldsymbol{r}$ connects the point where $\boldsymbol{B}$ has to be calculated to the point where the integral is being evaluated [78]. Second, the contribution from each block is then added for each point to give the total field due to the two arrays. A plot of the magnetic flux lines in a PPM insertion device, generated by two-dimensional magnet design software, is given in Fig. 7.8.

The field strength between the two arrays, having infinite width in the x direction (i.e. a full two-dimensional approximation), is given by [77]

$$B_y = -2B_r \sum_{i=0}^{\infty} \cos\left(\frac{2n\pi s}{\lambda_u}\right) \cosh\left(\frac{2n\pi y}{\lambda_u}\right) \frac{\sin(n\varepsilon\pi/M)}{n\pi/M} e^{-n\pi g/\lambda_u} \left(1 - e^{-2n\pi h/\lambda_u}\right)$$

$$B_s = 2B_r \sum_{i=0}^{\infty} \sin\left(\frac{2n\pi s}{\lambda_u}\right) \sinh\left(\frac{2n\pi y}{\lambda_u}\right) \frac{\sin(n\varepsilon\pi/M)}{n\pi/M} e^{-n\pi g/\lambda_u} \left(1 - e^{-2n\pi h/\lambda_u}\right) \ ,$$
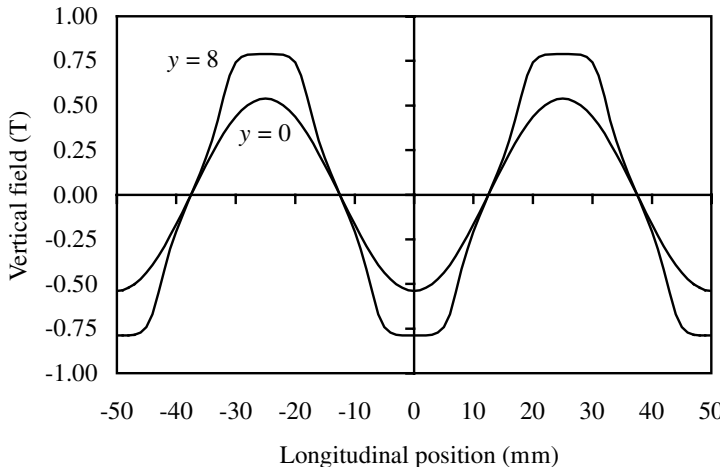
FIG. 7.9. A graph of the vertical field strength at different vertical positions in a PPM insertion device. The insertion device has a period of 50 mm, block height of 25 mm, magnet gap of 20 mm, remanent field of 1.1 T, and 4 blocks per period.

where $n = 1+iM$ and ε is a packing factor that allows for small air gaps between the blocks to be taken into account ($\varepsilon = 1$ if there are no gaps).

We can see that the vertical field on-axis ($y = 0$) is made up of a number of cosine harmonics and that in the limit, $M \longrightarrow \infty$, this reduces to just a single pure cosine. However, if M is chosen to be sufficiently large then the harmonics are of high order and are relatively unimportant. In practice four blocks per period is by far the most popular choice as it is a good compromise between on-axis field strength and quality against engineering complexity. In this case the higher harmonics account for less than $\sim 1\%$ of the field on-axis. Although the vertical field is almost a pure cosine on-axis, it deviates strongly away from this at vertical positions approaching the array surfaces. An example of this is plotted in Fig. 7.9. Also a graph of how the peak vertical on-axis field, B_{y_0}, varies with M is given in Fig. 7.10.

With the approximation that only the first harmonic makes a significant contribution, the on-axis fields reduce to

$$B_y = -2B_r \cos\left(\frac{2\pi s}{\lambda_u}\right) \frac{\sin(\epsilon\pi/M)}{\pi/M} e^{-\pi g/\lambda_u}(1 - e^{-2\pi h/\lambda_u})$$
$$B_s = 0 \ .$$

This equation now makes it clear that so long as all the block dimensions scale together the field levels do not change. This is a general rule for PPM systems but is not true for electromagnets, in their case if the magnet dimensions decrease
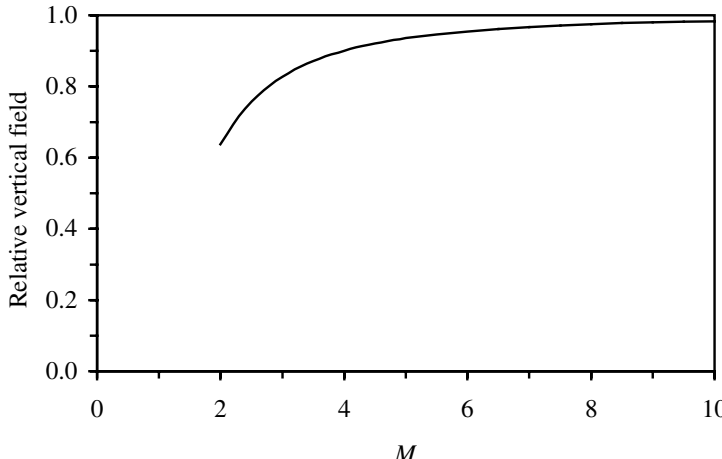
FIG. 7.10. A graph of the relative on-axis field strength as a function of the
number of blocks per period in a PPM insertion device.

then the current density has to increase to maintain the same field levels. This
gives us our first hint that as an insertion device period shrinks a PPM will
at some point outperform an electromagnet. It also demonstrates to us how
important the gap to period ratio is in an insertion device.

A graph of the peak on-axis field against block height to period ratio is given
in Fig. 7.11. Typically the block height is chosen to be half the period length,
which is a loss of $\sim 5\%$ compared to the maximum field that can be reached.
Some designs have even used quarter period height blocks since in a four block
per period magnet this makes all of the blocks identical.

In principle the maximum on-axis field achievable by a PPM insertion device
is $2B_r$, which occurs when $g/\lambda_u \longrightarrow 0$, $M \longrightarrow \infty$, and $h/\lambda_u \longrightarrow \infty$. In practice
however, with four blocks per period and block height of half the period the
on-axis field varies as

$$B_{y_0} = 1.72\, B_r e^{-\pi g/\lambda_u} \quad ,$$

which, for a fairly ambitious ratio of gap to period of 0.1, gives a peak value of
$1.26\, B_r$. We can now see that reaching a peak field of ~ 1.5 T is possible but
requires very high remanent field material and either a small magnet gap or a
relatively long period (or preferably both!).

To reach higher field levels is possible using permanent magnets if ferromag-
netic poles are included in the design. This mixture of hard and soft magnetic
materials is called a *hybrid* insertion device.
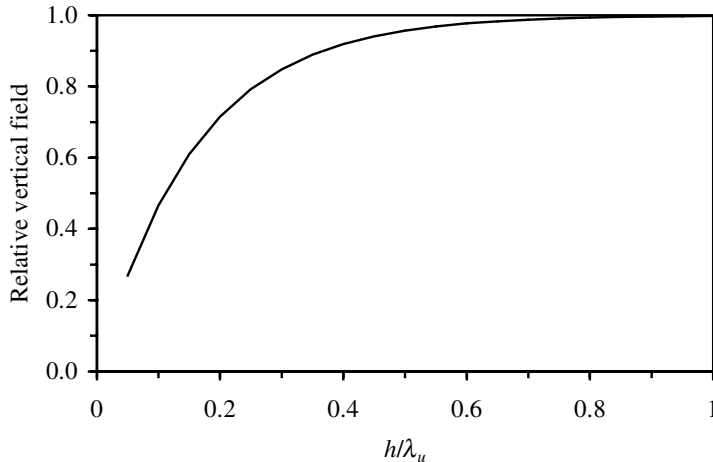
FIG. 7.11. A graph of the relative on-axis field strength as a function of the block height to undulator period ratio in a PPM undulator.

7.4 Hybrid Insertion Devices

The inclusion of magnetic steel poles (shown schematically in Fig. 7.12) means that the fields can no longer be calculated analytically. Accurate predictions of field level, taking into account the non-linear behaviour of the steel, can be made by various computer programs in either two or three dimensions (though this is usually a slow and highly skilled task). A plot of the magnetic flux lines in a hybrid insertion device, generated by a two-dimensional magnet design code, is given in Fig. 7.13. A series of two-dimensional studies were carried out in the 1980s in an attempt to produce an empirical formula for the peak field achievable in a hybrid insertion device using SmCo with a remanent field of 0.9 T [79]. The resulting equation being

$$B_{y_0} = 3.33 \, \exp\left(-5.47 \, \frac{g}{\lambda_u} + 1.8 \, \frac{g^2}{\lambda_u^2}\right) \quad .$$

This was soon updated for NdFeB with a remanent field of 1.1 T [80]

$$B_{y_0} = 3.44 \, \exp\left(-5.08 \, \frac{g}{\lambda_u} + 1.54 \, \frac{g^2}{\lambda_u^2}\right) \quad .$$

Both equations are said to be valid over the range $0.07 < g/\lambda_u < 0.7$. An attempt has been made recently to update the equation for the higher remanent field materials now available and also for the more highly optimized designs that have been developed [81]. The new equation, which assumes a remanent field of 1.3 T, is
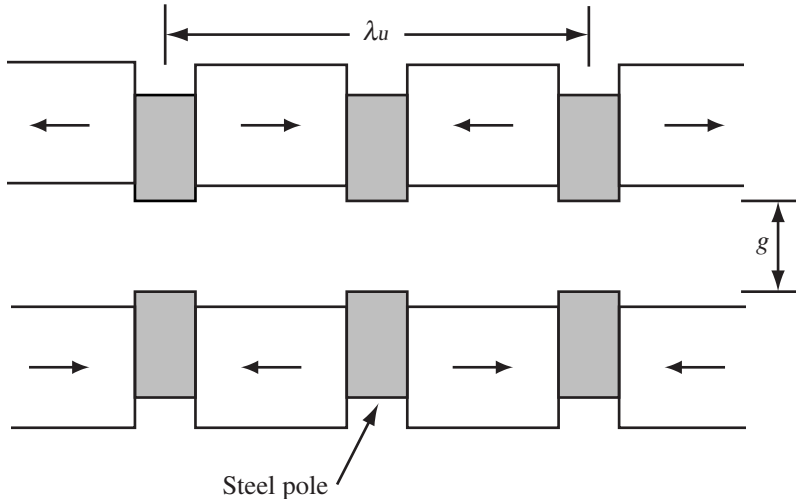
FIG. 7.12. Sketch of the hybrid insertion device concept. The arrows indicate the direction of the easy axis in the magnet blocks.

$$B_{y_0} = 4.3 \exp\left(-6.45 \frac{g}{\lambda_u} + \frac{g^2}{\lambda_u^2}\right)$$

and this is valid over $0.04 < g/\lambda_u < 0.2$. A comparison of the fields achievable in a hybrid magnet compared to a PPM solution is given in Fig. 7.14. At short periods there is little difference between the two designs ($\sim 10\%$ larger for the hybrid) but clearly the hybrid has a significant advantage at longer periods. Fields in excess of 2 T are possible, which are well outside the limits of the PPM design.

7.5   End Design

It is important that when insertion devices are operated they have the least possible net effect on the electron beam. This is because in a storage ring light source, the same electron beam is simultaneously being used by several experiments. Any changes produced by an insertion device may well affect the photon beam quality for the other experiments. One key issue is that the insertion device should have no net effect on the electron beam position or angle. This helps to ensure that if an insertion device field is varied (to change an undulator output wavelength, for example) the experiments on the remainder of the facility see no change to their photon beam at their sample.

The overall effect of the (vertical) magnetic field of an insertion device on the electron beam (horizontal) exit angle, α, is found from the *first field integral* (see Section 3.1)
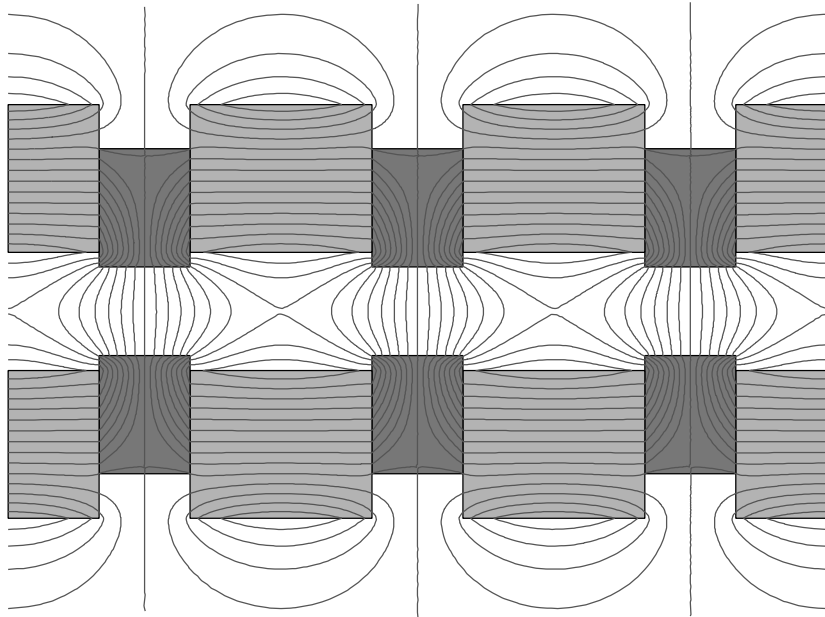
FIG. 7.13. Lines of flux in a hybrid insertion device. The direction of the easy axis for each block is as in Fig. 7.12.

$$I_y = \int_{-\infty}^{\infty} B_y(s)ds$$

such that

$$\alpha = \frac{e}{\gamma m_0 c} I_y \tag{7.2}$$

and the position is found from the *second field integral*

$$II_y = \int_{-\infty}^{\infty} \int_{-\infty}^{s} B_y(s')ds'ds$$

such that

$$x = \frac{e}{\gamma m_0 c} II_y \ . \tag{7.3}$$

The requirement for all insertion devices is that both the first and second field integrals should equal zero under all operating conditions. This is achieved (in theory!) by a suitable selection of the end field terminations for the magnet at the entrance and exit of the device.
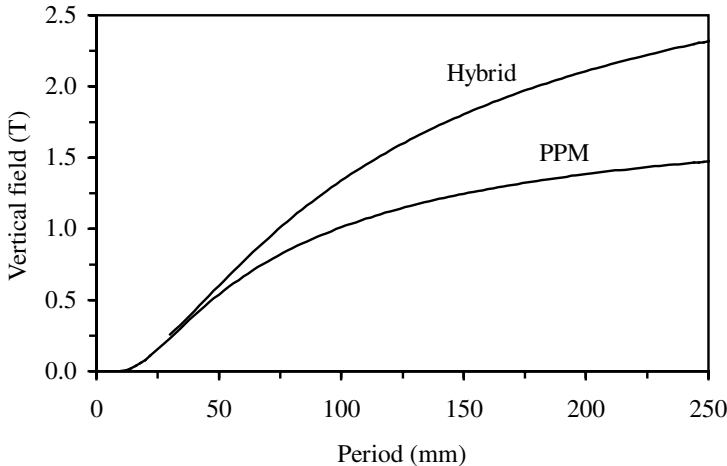
FIG. 7.14. A comparison of the fields achievable in a hybrid and a PPM insertion
device assuming a remanent field of 1.1 T and a magnet gap of 20 mm.

An alternative way of writing down an expression for the final beam position
is to project it back to the centre of the device (see Fig. 7.15). In that case it
can be shown that the distance from the magnet axis, δ, is given by [29]

$$\delta = -\frac{e}{\gamma m_0 c} \int_{-\infty}^{\infty} s B_y(s) ds \ . \tag{7.4}$$

This expression is useful because we can now see by inspection that δ will be
zero whenever the magnetic field is symmetric about $s = 0$ (i.e. when the centre
of the insertion device corresponds to the peak of a pole). This is the so-called
symmetric configuration. The ends of the insertion device are then adjusted to
make sure that the exit angle is zero also.

The alternative arrangement, the *antisymmetric* case, is to have the centre
of the magnet coincide with a zero crossing of B_y (i.e. have an even number of
poles). In this case then the integral of B_y and thus the exit angle is automatically
zero. The ends of the insertion device are then adjusted to set the exit position
to zero also.

The design of end terminations for PPM devices is relatively straightforward
because of the principle of superposition. This is not the case for hybrid structures
where the non-linear effects generally have to be actively compensated for at the
ends as the magnet gap varies.

Of course the field integrals are never truly zero. Material inhomogeneities
and engineering tolerances in block positioning and sizes introduce small errors
to the magnetic fields. A typical target for a first field integral would be to keep
it below $\sim 10^{-5}$ Tm, which corresponds to a net angle offset of ~ 1 μrad for a
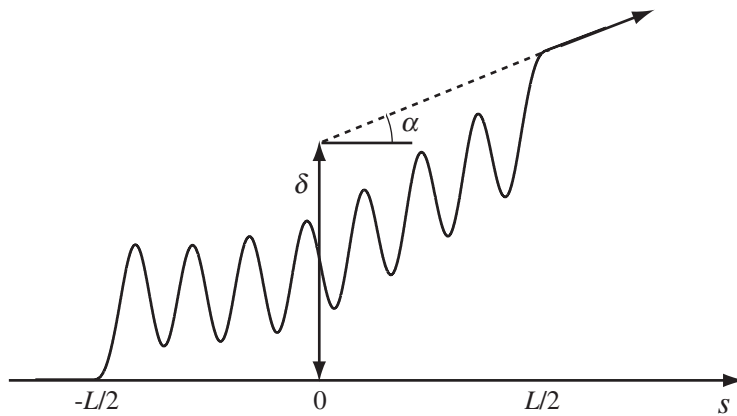
F<small>IG</small>. 7.15. Sketch showing an electron trajectory through a realistic insertion
  device and the back projection of the final position to the centre of the mag-
  net.

3 GeV electron beam. In this instance higher energy electrons are more tolerant
of integral errors.

7.5.1 PPM End Design

For the symmetric designs the ends must be used to ensure that the integral of B_y
is zero. The simplest way of achieving this is to have a vertically magnetized half
length block at each end (see Fig. 7.16(a)). To convince yourself of this remember
that the integrated field of one block can be readily cancelled by another block
through the principle of superposition.

  This half length block end structure is the most common design in use. Al-
though in principle the field integrals are zero for all magnet gaps the non-unit
permeability and anisotropy of the permanent magnets does have a small but
significant effect on the first field integral. A modified end design, which also
includes a short, horizontally magnetized block has been shown to significantly
reduce the field integral variation with magnet gap [82].

  For antisymmetric insertion devices no such common design solutions exist as
a zero beam exit position depends upon the number of poles, N_{poles}. The general
solution is that the strength of the end pole varies with $(N_{\mathrm{poles}}-1/2)/(N_{\mathrm{poles}}-1)$
[29]. An example of an antisymmetric solution is given in Fig. 7.16(b). The
magnetic field for 10-period versions of these end designs are given in Fig. 7.17.

  The electron beam trajectories through these example undulators are given
in Fig. 7.18. Note that in both the symmetric and antisymmetric configurations
the electron beam does not oscillate about the magnetic axis. For the symmetric
case the position offset is small and generally neglected. In the antisymmetric
case there is an angle offset, which can be significant for photon beamlines that

(a)

(b)

(c)
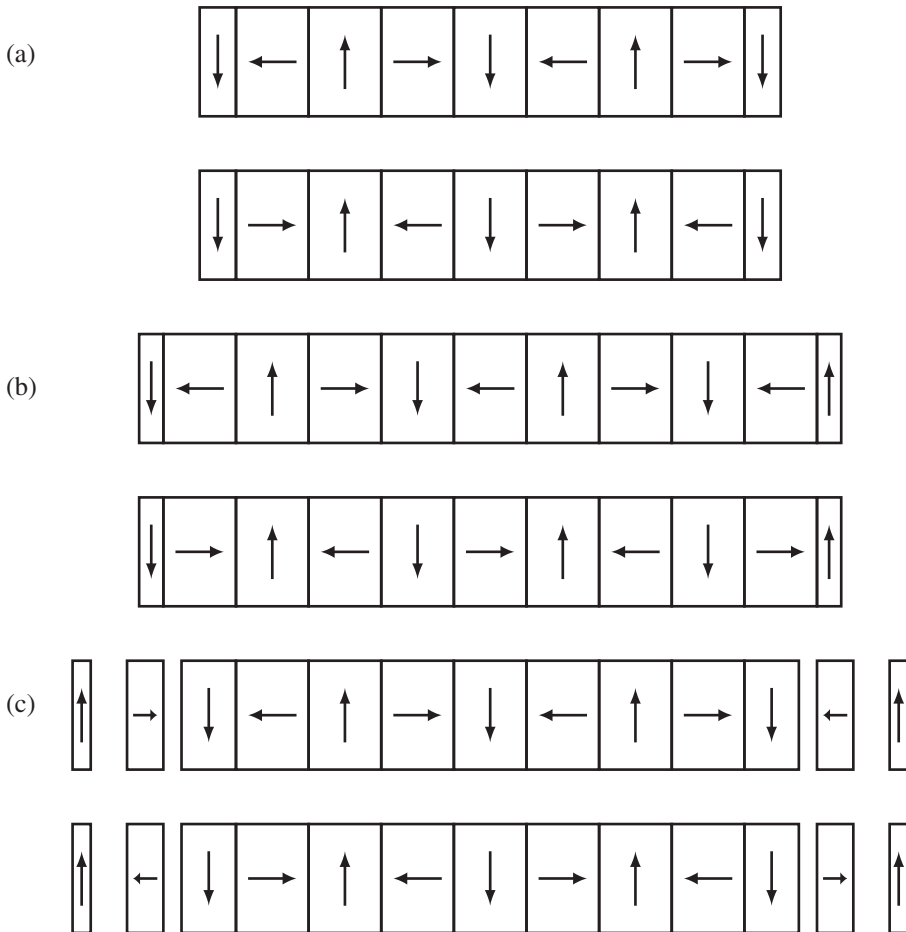
FIG. 7.16. Three alternative PPM undulators used to illustrate the alternative end terminations; (a) a symmetric design with a half length block, (b) an antisymmetric design with an end block whose length depends upon the number of periods and (c) a symmetric design with a longer termination that forces the electron beam to oscillate about the magnetic axis.

are several tens of meters long.

Solutions do exist that force the electron to oscillate about the nominal axis though they have to include more blocks at the end. The simplest solution is a $1/4, -3/4, 1, -1, ...$ end structure which can be used in a symmetric or antisymmetric magnet [83]. The condition for establishing that the oscillation is centred about the magnetic axis for the symmetric case is that the electron beam should have zero angle and position equal to the maximum oscillation amplitude at the
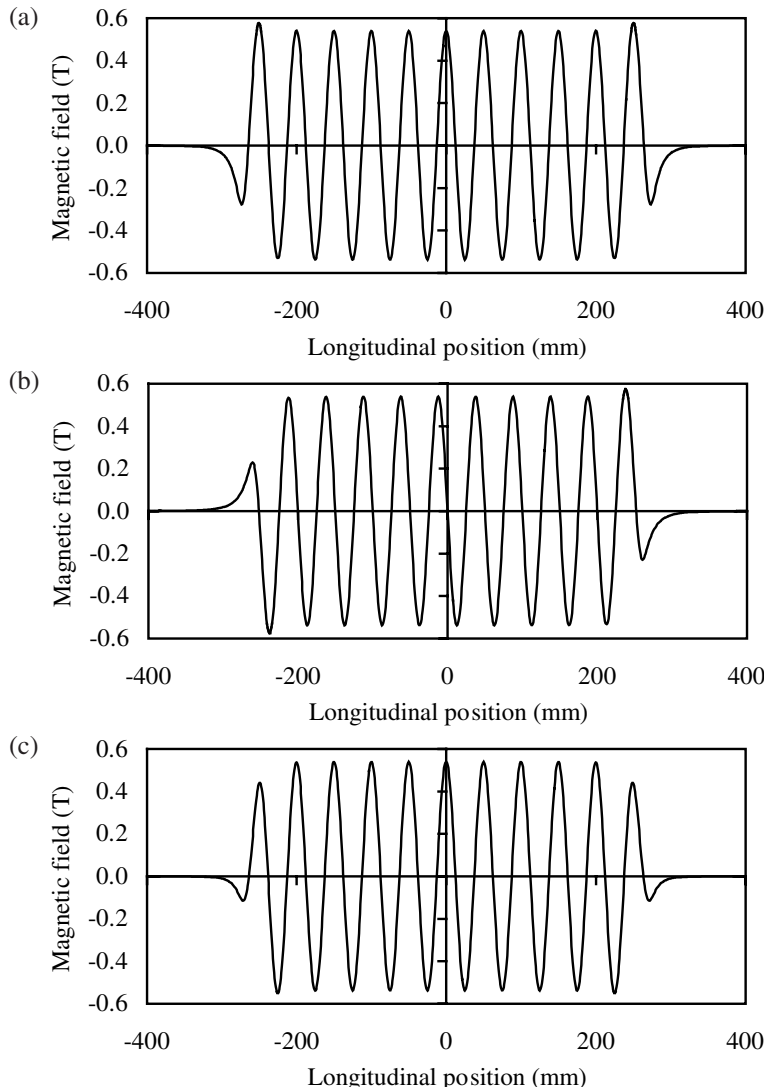
FIG. 7.17. Magnetic fields for 10-period versions of the undulators illustrated
in Fig. 7.16.

longitudinal centre of the undulator (at every full period in fact). This implies
that the first field integral should be zero and that the second should equal

$$\int_{-\infty}^{0} \int_{-\infty}^{s} B_y(s')ds'ds = B_0 \left(\frac{\lambda_u}{2\pi}\right)^2$$

for a sinusoidal field variation. This can easily be shown by equating (7.3) with (3.3) at its peak value. A very similar condition exists for the antisymmetric case where the beam position is zero but the angle is equal to the maximum value after every full period (equate (7.2) and (3.2)). It is easy to demonstrate that a sinusoidal function with the peak amplitudes mentioned above (1/4, −3/4, 1, −1, ...) will meet either the symmetric or antisymmetric conditions. A practical example of an end termination that forces the electron beam to oscillate about the magnetic axis is illustrated in Fig. 7.16 with the magnetic field and subsequent trajectory given in Figs. 7.17 and 7.18 [83, 84].

7.5.2 *Hybrid End Design*

The problem with the hybrid magnets is the non-linear behaviour of the steel. This means that the field integrals are very hard to passively compensate over a wide range of magnet gaps. In almost all designs some form of active compensation is included, such as an electromagnetic coil or even rotating cylinders of permanent magnet material (Fig. 7.19). In general the compensation is applied at the end pole region, though trim coils have been applied around the full magnet length as well [85].

The extensive use of two- and three-dimensional magnet modelling has helped in the generation of hybrid magnets without any active compensation. In one case cylindrical magnet blocks were adjusted and then fixed after the full device was measured to minimize the first field integral over the operating gap range to within $\pm 10^{-4}$ Tm [86]. In another (lower field) example no compensation was included and the field integral was kept within $\pm 1.5 \times 10^{-5}$ Tm [87]. However, it is interesting to note that space was left in the magnet for compensating coils in case they were found to be required at the final measurement stage!

7.6 Helical Designs

7.6.1 *Asymmetric and Elliptical Wigglers*

The first asymmetric multipole wiggler proposed suggested a PPM configuration [88]. A simpler alternative PPM scheme (Fig. 7.20) was built and installed onto the DORIS ring in Germany [54]. The device is effectively a series of PPM wavelength shifters separated by air gaps. If the air gaps are reduced to zero length then the device reverts to a standard four block per period PPM insertion device (see Fig. 7.7). The magnetic field from such an asymmetric MPW is plotted in Fig. 7.21.

The hybrid alternative has also been suggested [89, 90] with the obvious advantage of being able to achieve higher peak fields. A very sophisticated example has been built for the ESRF which, through very careful shaping of the steel poles and permanent magnet blocks, is able to reach fields in excess of 3 T at a magnet gap of 11 mm [55].

Two PPM elliptical wigglers were built and installed in Japan [57]. Magnetically they have a simple configuration (Fig. 7.22), although the mechanical engineering is very demanding. Changing the relative longitudinal position of
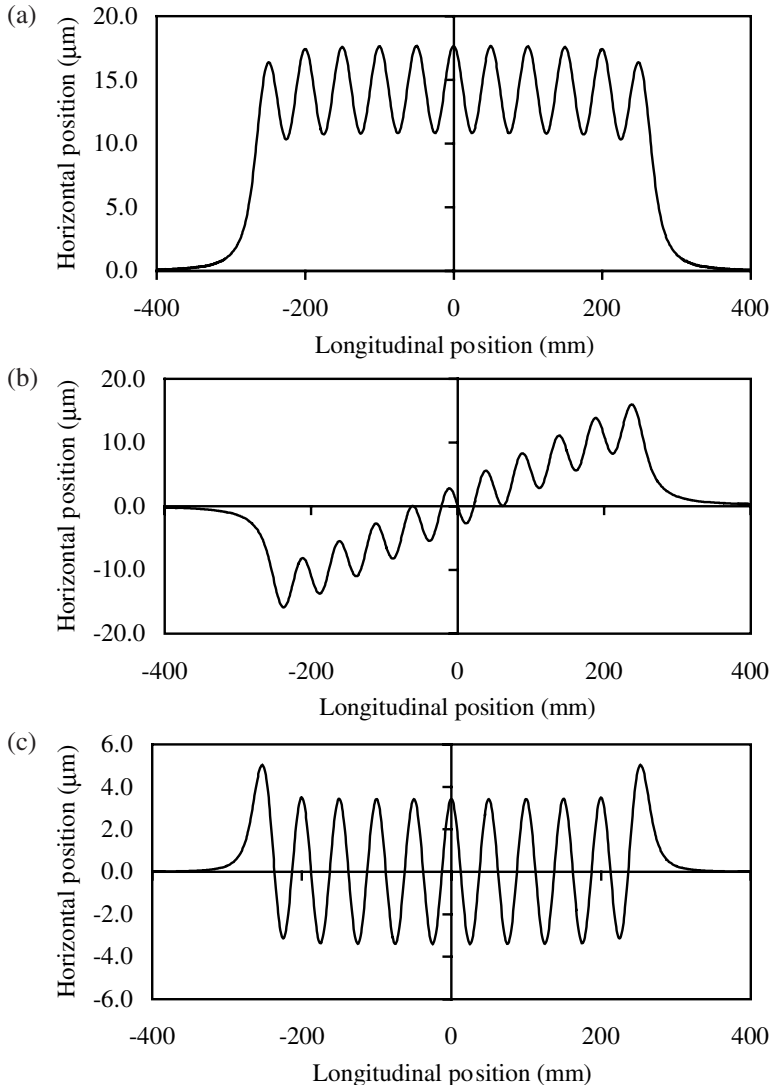
FIG. 7.18. Trajectories for 3 GeV electrons through 10-period versions of the undulators illustrated in Fig. 7.16.

the two pairs of arrays from $+\lambda_u/4$ to $-\lambda_u/4$ switches the electron direction of rotation through the magnet and hence the sense of the circular polarization observed. The horizontal magnet gap is typically five times larger than the vertical one and so the horizontal field is generally very much smaller. In the Japanese example [57], which had a 160 mm period, the horizontal field was 0.2 T compared to the vertical field of 1.0 T.
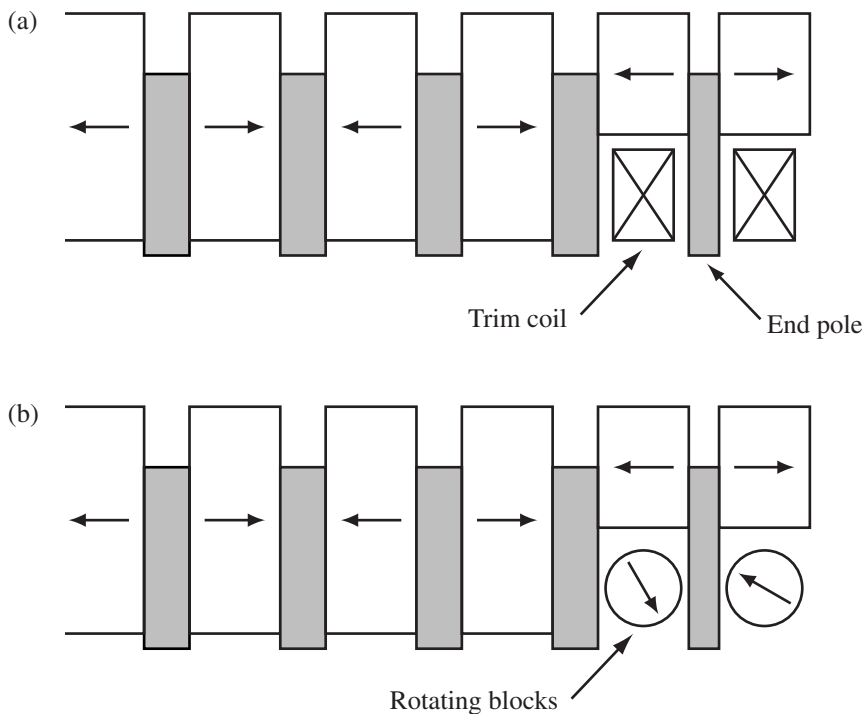
FIG. 7.19. Two example active end termination solutions for hybrid magnets; (a) active coils and (b) rotating permanent magnet blocks.
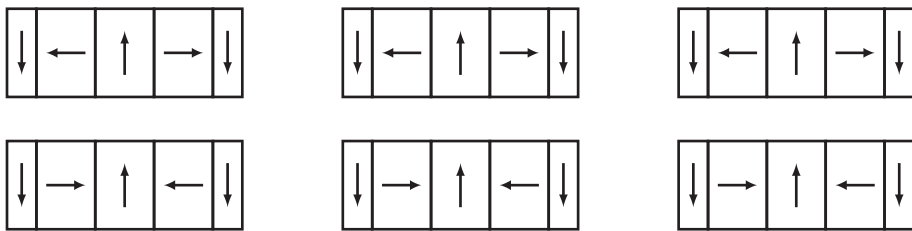
FIG. 7.20. A simple PPM asymmetric multipole wiggler design.

More recent versions of elliptical MPWs have employed electromagnetic coils to generate the horizontal field to enable fast switching of the polarization states. Magnets of this type will be studied in Chapter 8.

7.6.2   *Helical Undulators*

Helical magnetic fields can be generated with permanent magnets that are arranged with either a circular, rectangular, or planar geometry. Naturally the
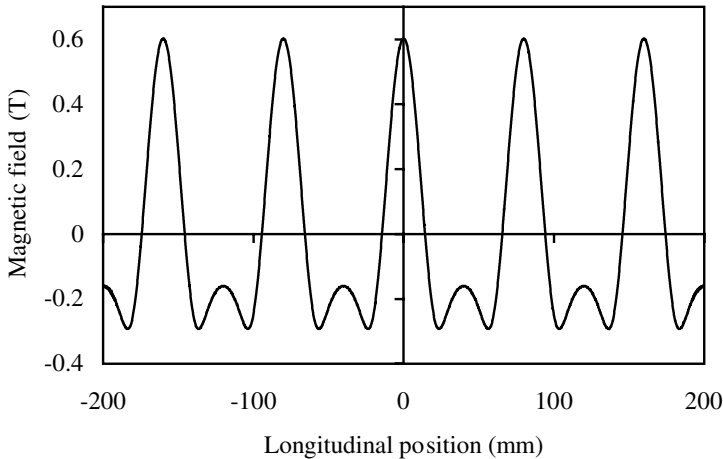
FIG. 7.21. Magnetic field for a PPM asymmetric multipole wiggler with a period of 80 mm, an air space of 30 mm, and a magnet gap of 20 mm.
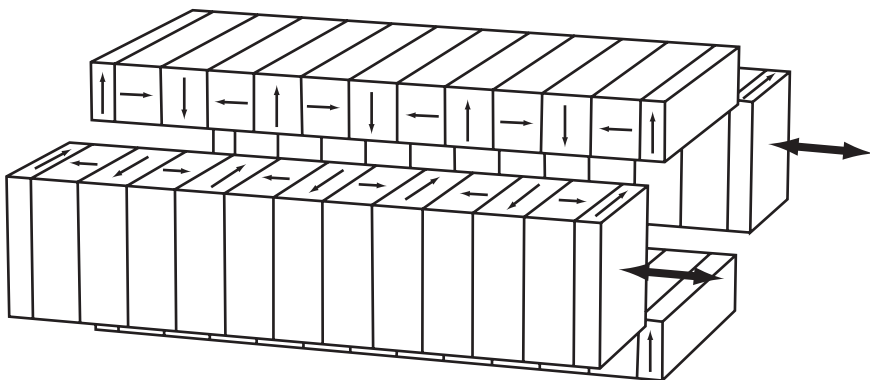
FIG. 7.22. Sketch of a PPM elliptical multipole wiggler design.

circular geometry lends itself more readily to generating purely helical fields $(B_{x_0} = B_{y_0})$ but the ability to independently vary the two transverse fields (and also the phase between them) that is required to tune the polarization (see Section 6.6) is more readily achieved with a rectangular or planar geometry. The rectangular geometry is simply two conventional undulators mounted perpendicular to each other, as for the elliptical MPW (Fig. 7.22). As such, the magnetic design offers no new challenges and will not be discussed further here. The planar helical undulator has the additional benefit that storage rings are well suited to planar magnets rather than rectangular or circular as the electron requires a far larger aperture in the horizontal plane than in the vertical. However, circular

(a)

(b)
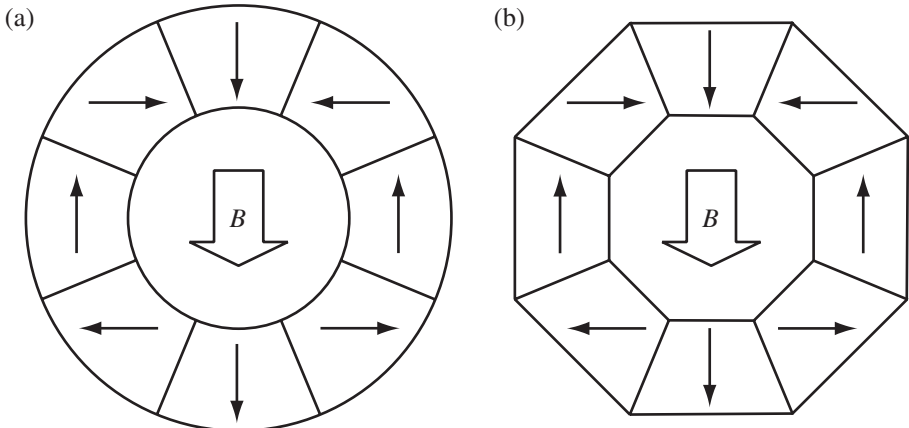
FIG. 7.23. (a) A simple circular permanent magnet geometry for generating a dipole field and (b) an economical trapezoidal approximation to (a).

helical undulators are still worth consideration as in general they produce larger on-axis fields and are well suited to some applications (e.g. free electron lasers).

7.6.2.1 *Circular Geometries* A dipole field can be generated by a ring made of permanent magnet blocks whose axes of magnetization rotates around the circle [91] (Fig. 7.23(a)). A helical field can then be produced by stacking together many such dipole rings with each ring rotated with respect to its neighbour. The quality of the overall magnet is determined first by the number of blocks per ring and second by the number of rings per undulator period. The production of the curved blocks required for the circular geometry clearly requires significant machining. A more economical solution is to create an approximation to the circular design by using trapezoidal blocks (Fig. 7.23(b)) [77].

If each dipole ring is made of M permanent magnet blocks and each period of the helical undulator is made of N dipole rings then the transverse field on-axis, B_0, is given by [77]

$$B_0 = B_r \left(\frac{\sin(\pi/N)}{(\pi/N)} \right) \left(\frac{\sin(2\pi/M)}{(2\pi/M)} \right) (T(2\pi r_1/\lambda_u) - T(2\pi r_2/\lambda_u)) \ ,$$

where

$$T(x) = K_0(x) + \frac{x}{2}K_1(x) \ .$$

The remanent field of the material is B_r and r_1 and r_2 are the inner and outer radii respectively. Note that K_0 and K_1 are modified Bessel functions. Strictly speaking this equation only holds for the circular geometry case but it is a good approximation for the trapezoidal geometry, especially at large M. An example of how the field strength increases with M is given in Fig. 7.24.
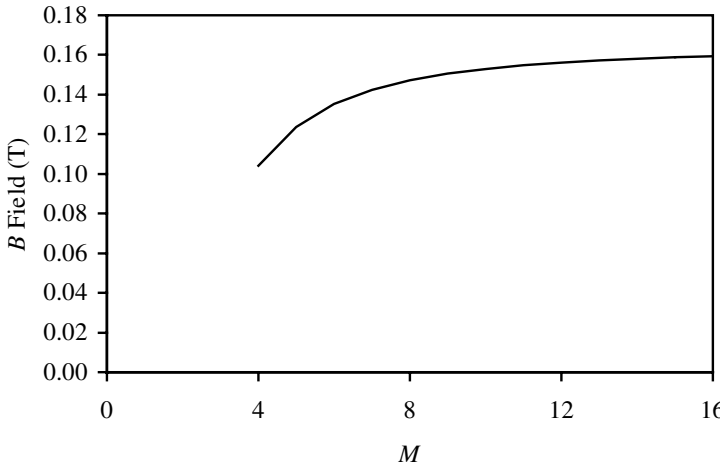
FIG. 7.24. Graph showing how the transverse field on-axis increases for the circular geometry helical undulator as the number of blocks per ring increases. The undulator period is 50 mm, the inner radius is 20 mm, the outer radius is 50 mm and the remanent field is 1.1 T.

7.6.2.2 *Planar Geometries* To generate independently variable horizontal and vertical magnetic fields using only permanent magnets mounted above and below the beam axis is not easy. However, several ingenious designs have been put forward with many practical examples being successfully demonstrated. One key difference between these magnets and conventional planar undulators (see Section 7.3) is that two degrees of freedom are needed to control the two field levels independently (three if the phase is also to be controlled). This can be achieved by adding longitudinal array movement on top of the normal vertical gap adjustment or by adjusting the vertical position of the top and bottom arrays independently.

The first magnet of this kind was the Helios undulator (Fig. 7.25) [63]. In this case the top array is used to generate the horizontal field and the bottom array generates the vertical field. Each array can be adjusted vertically independently and also a longitudinal motion of one of the arrays gives control of the phase as well.

Other designs quickly built upon this planar concept [92,93] but moved away from the two independent arrays above and below the axis to a more complex four-array scheme (one pair above and one pair below) with longitudinal movement of individual arrays necessary to control the polarization. One design, the APPLE-2 (Advanced Planar Polarized Light Emitter - 2) [94], has attracted significant attention since it has the highest peak fields for the circular mode, is relatively simple, and is able to generate all of the desired polarization states required. There are now several APPLE-2 undulators installed in storage rings
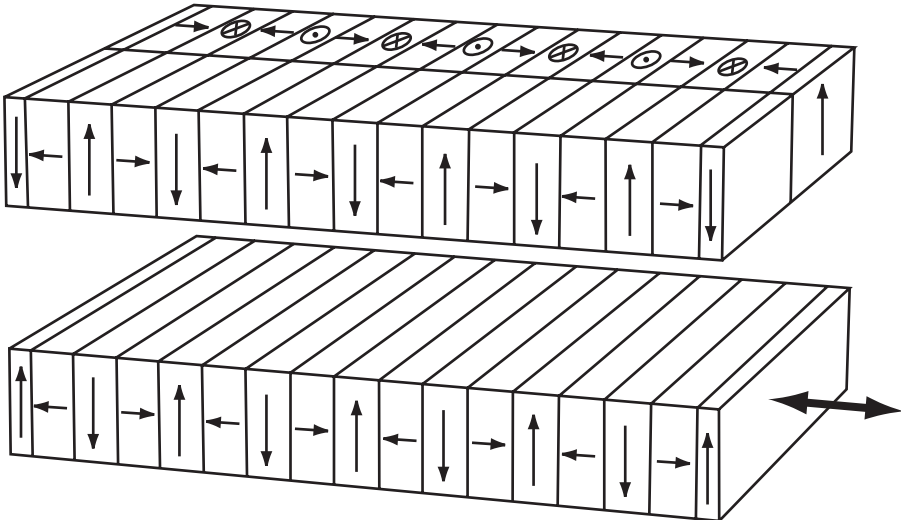
FIG. 7.25. Sketch of the Helios design.

around the world [95–98] and it is by far the most popular helical undulator design at present. We will study this particular design in some detail to better understand some of the features of this type of magnet. The basic design consists of two pairs of conventional arrays (see Section 7.3) mounted as shown in Fig. 7.26. The bottom right and top left arrays can both move longitudinally as well as both pairs being able to move vertically like a conventional undulator so as to adjust the magnet gap.

If the longitudinal shift between the two sets of arrays is equal to D then we can say that the phase difference, ϕ, is $2\pi D/\lambda_u$. We will denote the bottom left and top right array pair as Undulator a and the other diagonal pair as Undulator b. The horizontal and vertical magnetic fields generated on-axis by Undulator a can be written as

$$B_{a_x} = B_{x_0} \sin\left(\frac{2\pi s}{\lambda_u}\right)$$

$$B_{a_y} = B_{y_0} \sin\left(\frac{2\pi s}{\lambda_u}\right) \ ,$$

where B_{x_0} and B_{y_0} are the peak horizontal and vertical fields from this array pair. Similarly we can write down the fields for Undulator b as

$$B_{b_x} = -B_{x_0} \sin\left(\frac{2\pi s}{\lambda_u} + \phi\right)$$
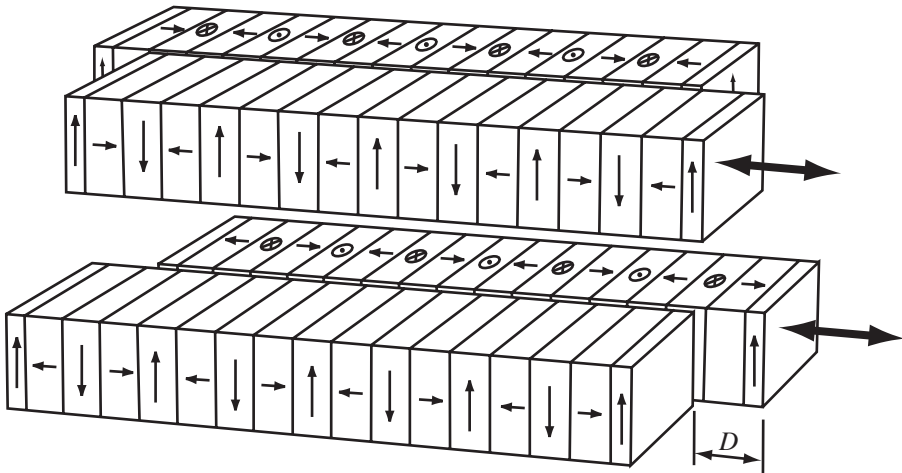
FIG. 7.26. Sketch of the APPLE-2 design.

$$B_{b_y} = B_{y_0} \sin\left(\frac{2\pi s}{\lambda_u} + \phi\right) \ .$$

The minus sign is present for B_{b_x} since the standard planar undulator ($\phi = 0$ in this case) has no horizontal fields on axis.

The total horizontal and vertical fields generated by the four arrays are found by simply adding together the two contributions (using the principle of superposition for permanent magnets described earlier in Section 7.1).

$$B_x = B_{a_x} + B_{b_x} = B_{x_0}\left(\sin\left(\frac{2\pi s}{\lambda_u}\right) - \sin\left(\frac{2\pi s}{\lambda_u} + \phi\right)\right) \ .$$

Using the three identities $\sin(A + B) = \sin A \cos B + \sin B \cos A$, $\cos 2A = 1 - 2\sin^2 A$ and $\cos(A + B) = \cos A \cos B - \sin A \sin B$ this simplifies to

$$B_x = -2B_{x_0} \sin\left(\frac{\phi}{2}\right) \cos\left(\frac{2\pi s}{\lambda_u} + \frac{\phi}{2}\right) \ .$$

Similarly the vertical field is given by

$$B_y = B_{a_y} + B_{b_y} = B_{y_0}\left(\sin\left(\frac{2\pi s}{\lambda_u}\right) + \sin\left(\frac{2\pi s}{\lambda_u} + \phi\right)\right)$$

$$= 2B_{y_0} \cos\left(\frac{\phi}{2}\right) \sin\left(\frac{2\pi s}{\lambda_u} + \frac{\phi}{2}\right) \ .$$

Examination of the two equations for B_x and B_y shows that there is always a fixed phase difference between the two fields of $\pi/2$ implying that the polarization

ellipse is always upright. In other words, as ϕ increases from zero (vertical field only, linear horizontal polarization) an observer viewing the electron head on will see the electron travel around an ellipse that always has a principle axis coincident with the vertical axis of the undulator. The ellipse will become a circle when $B_x = B_y$ (circular polarization condition) and in the limit, when $\phi = \pi$, the electron will appear to oscillate in a vertical line (horizontal field only, linear vertical polarization). Note that by taking ϕ beyond π (or below zero) the same elliptically shaped trajectories are produced but with the electron now tracing the path out in the opposite direction of rotation. This will then produce polarization with the opposite left or right handedness. Some example electron trajectories for a practical APPLE-2 example are given in Fig. 7.27. The horizontal and vertical magnetic fields for the same undulator in the circular polarization mode are shown in Fig. 7.28. The circular polarization mode occurs when the peak horizontal field equals the peak vertical field. It is easy to show that this occurs when

$$B_{x_0} \sin\left(\frac{\phi}{2}\right) = B_{y_0} \cos\left(\frac{\phi}{2}\right)$$

or when

$$\phi = 2\tan^{-1}\left(\frac{B_{y_0}}{B_{x_0}}\right) \quad .$$

It is not surprising that helical undulators can have a more significant (usually detrimental) effect on the electron beam than the standard planar undulator. These effects will be studied in more detail in Chapter 10. For now it is worth looking at the transverse horizontal and vertical field profiles for the circular polarization case of our example APPLE-2 undulator. These fields are graphed in Fig. 7.29, note that the two fields are shown for different longitudinal positions to account for the $\pi/2$ phase difference. It is clear from the graph that the electron beam will be sensitive to relatively small horizontal misalignments, especially for the horizontal fields. One consequence of a poor electron beam alignment with the magnetic axis would be a degradation in the circular polarization content as the electron trajectory will no longer be circular but elliptical.

There is one further feature of the APPLE-2 undulator, which has not always been exploited but is certainly of interest to experimentalists. If, instead of moving the diagonally opposite pair of arrays together in the same direction to adjust the polarization state they are moved equal distances in opposite directions then something very different occurs. Now with one array with a phase of ϕ and the other with $-\phi$ it turns out that the horizontal and vertical magnetic fields remain in phase at all times rather than with the fixed $\pi/2$ difference found earlier. The consequence of this is that the electron viewed head on appears to trace out a straight line, much like in a standard undulator, except that the inclination of the line can be adjusted to any angle between 0° and 90° by changing the relative amplitude of the two transverse fields. This means that by adjusting the arrays
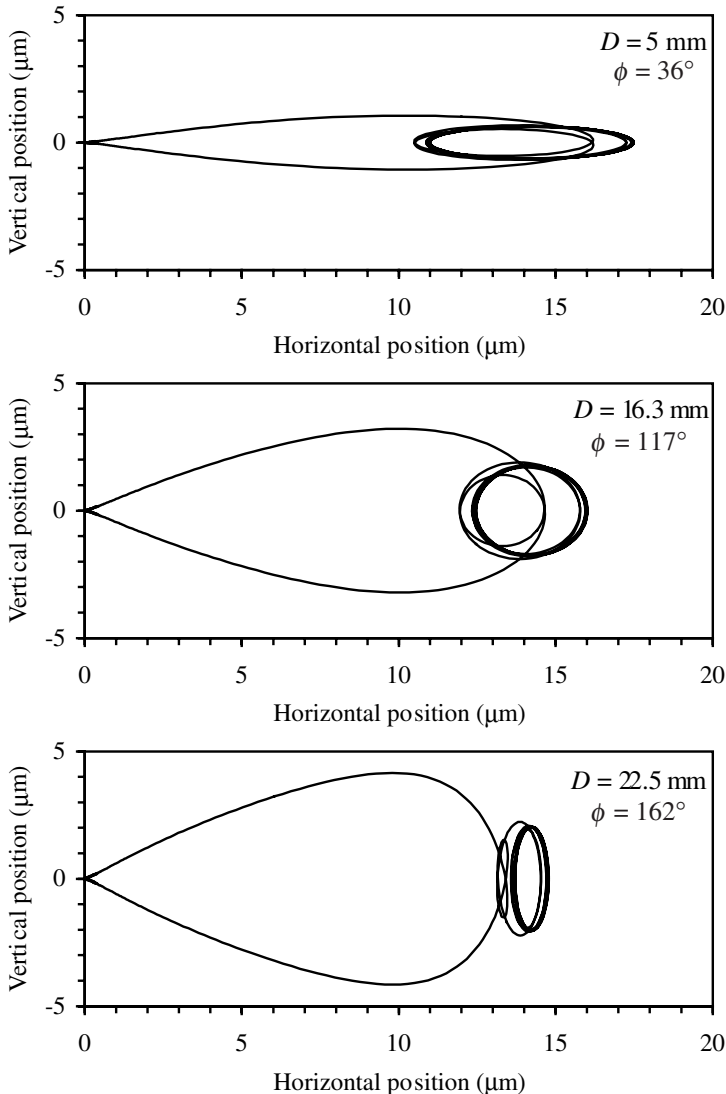
FIG. 7.27. Three example trajectories of a 3 GeV electron viewed head on passing through an APPLE-2 undulator with different phase settings. The undulator has a period of 50 mm and a magnet gap of 20 mm.

in this *opposing* mode of operation any of these angles of linear polarization can be generated [99]. To obtain full control of the angle of inclination of the linear polarization then all four arrays must be moveable [100]. With one pair fixed the range $0°$ – $90°$ is accessible and then with the other pair fixed the range
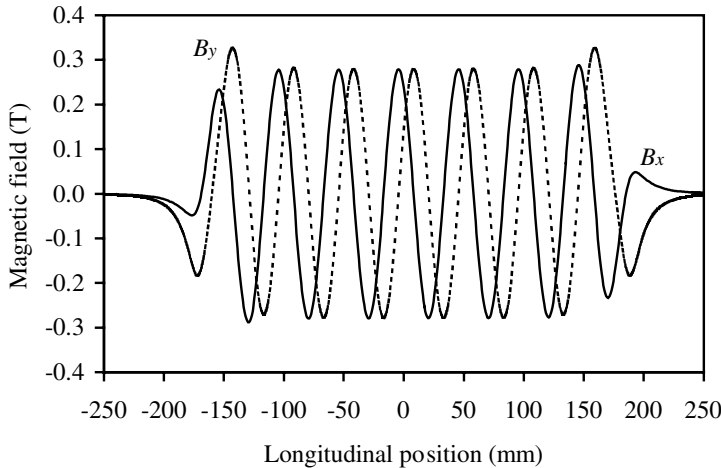
FIG. 7.28. Magnetic fields for an APPLE-2 undulator in the circular polarization mode with a period of 50 mm and a magnet gap of 20 mm assuming a remanent field of 1.1 T.

$90° – 180°$ is available. Clearly this is mechanically more demanding but still quite feasible. Example field levels and the corresponding electron trajectory are plotted in Figs. 7.30 and 7.31.

As explained earlier, the APPLE-2 helical undulator is presently the most popular planar helical undulator and this is why we have studied the features of it in some detail. However, other designs have continued to be put forward, which claim to have superior qualities in some areas. One design has proposed making each array of the APPLE-2 out of two rows of PM blocks (Fig. 7.32) in an effort to enhance the on-axis field level [101]. An increase of $\sim 20\%$ in the transverse field was predicted for the example quoted.

In another scheme, two variations on a six-array undulator (three above and three below) have been built and installed on UVSOR [102] and SPring-8 [103]. In these devices the central arrays produce the vertical field and the outer four arrays produce the horizontal field. Some efforts have been made to improve the transverse field quality by shaping of the magnet blocks [103] and so reduce the impact of the undulator on the electron beam.

7.7   Engineering Issues

The engineering design of permanent magnet-based insertion devices is in itself a highly skilled task. The design engineer is charged with assembling long magnet arrays that must be highly periodic and flat using materials that are often experiencing very large forces during the assembly process. Furthermore they must mount the two arrays parallel to each other and maintain this parallelism
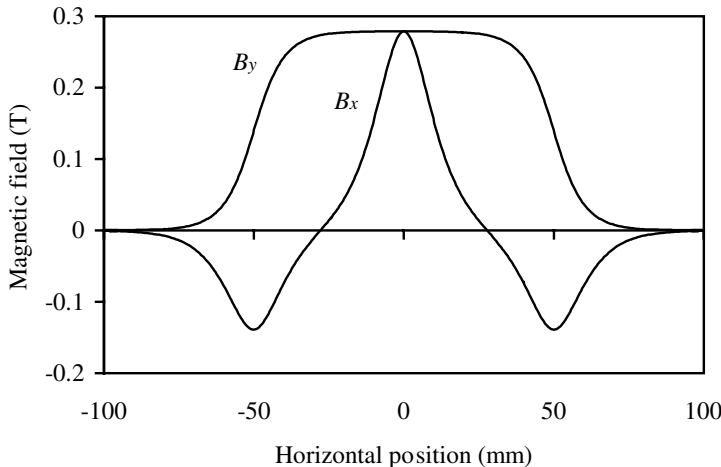
Fig. 7.29. Magnetic fields across the horizontal axis for an APPLE-2 undulator in the circular polarization mode with a period of 50 mm and a magnet gap of 20 mm assuming a remanent field of 1.1 T. Note that the two fields are generated at different longitudinal positions to account for the $\pi/2$ phase difference between the two fields.

while the magnet gap is adjusted with μm resolution. At large gaps the magnetic forces between arrays is negligible while at small gaps it can be several tonnes!

Although virtually all insertion devices are built by independent groups and laboratories a number of common themes are evident in the engineering solutions employed. Of course not all insertion devices use these solutions but the majority do and so it is worth examining why particular themes have emerged. First, the magnet blocks are held in individual non-magnetic holders as this allows each block to be safely manipulated during the assembly process. The blocks are either glued or, more commonly, clamped into the holders (or occasionally both!). These holders are then bolted to some sort of backing beam to create a single array. This then allows a complete magnetic half of an insertion device to be manipulated as a single item. The arrays are then secured onto a support structure that is strong enough and stiff enough to withstand the high forces between the arrays. The structure also provides the mechanical movement required to adjust the magnetic fields on the electron beam axis. In general the structures only support the arrays on one side in a C shaped frame (Fig. 7.33). The advantage of this shape is that it is easy to access the arrays for magnet measurements or to mount the device around a pre-installed vacuum chamber. The clear disadvantage is that the structure is not balanced and under high forces it will have a tendency to close up leading to a magnet with a tapering gap in the horizontally transverse direction. This is easily overcome with an alternative structure that supports on either side in an H frame style but then other solutions need to be found to the
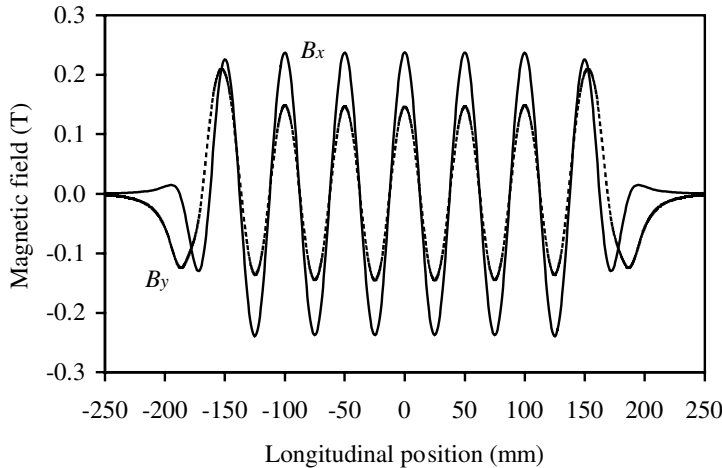
FIG. 7.30. Magnetic field for an APPLE-2 undulator in the opposing mode of operation. Note that the horizontal and vertical fields are now in phase.
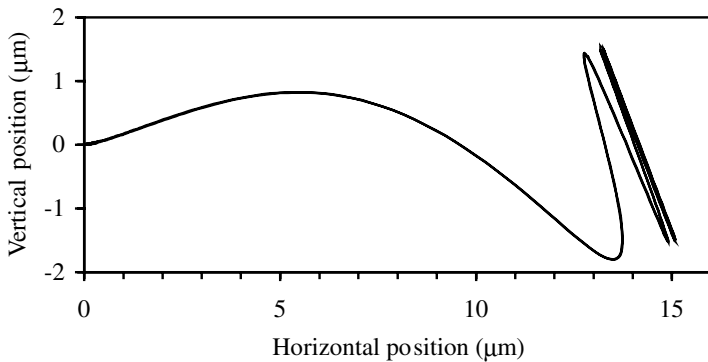
FIG. 7.31. Trajectory of a 3 GeV electron viewed head on passing through an APPLE-2 undulator with the field levels given by Fig. 7.30.

access problem. Incidentally, a number of design teams have used finite element analysis to accurately predict and reduce the deformations in a support structure under high load [85].

Another feature of support structures is that when very long insertion devices ($> \sim 3$ m) are required they are sometimes built in shorter separate modules (typically $1.5 - 2.5$ m). This has the benefit of generating much more easily manageable items in terms of transportation, installation, magnet measurement, and so on but the designers must ensure that magnetically it operates as a single device. Some groups have made a virtue of the module concept by terminating
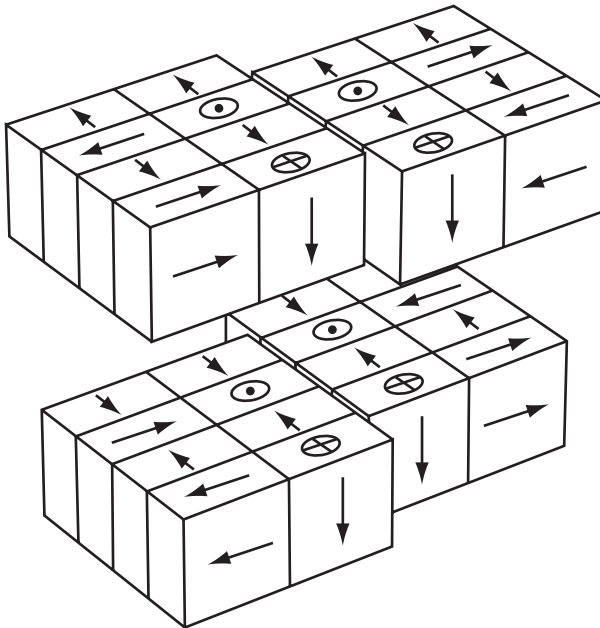
FIG. 7.32. Variation on the APPLE-2 design that enhances the on-axis fields.

each one individually so that they can each be used as separate devices or as one complete device. The advantage here is that the beamline users can adjust the number of segments in use for different beam current conditions to match the power limitations of the beamline optical components [87].

One key area that has been glossed over so far is that of how the ability to move the arrays is included. They are generally mounted to a pair of linear slides, which restrict the allowed movement to the vertical direction only. The longitudinal separation of these slides is important and if chosen correctly it can minimize the longitudinal deflections of the arrays under the magnetic forces. They should be mounted close to the Airy points for each array if possible [104]. Next a motorized leadscrew mechanism is used to move the arrays up and down. The actual magnet gap is measured with a position encoder (usually optical) with linear encoders being preferred because they can measure the gap at the point of interest directly (the gap between the arrays), although rotary encoders are also used extensively.

An interesting point here is the question of how many encoders and motors should be used? In the simplest system a single motor mechanically linked to both leadscrews with a single encoder is sufficient. However, any backlash or slack in the motion system must be tolerated as it cannot be actively corrected and hence the magnet gap is likely to be different at the two leadscrews. This longitudinal gap taper can be minimized with the correct selection of precision components
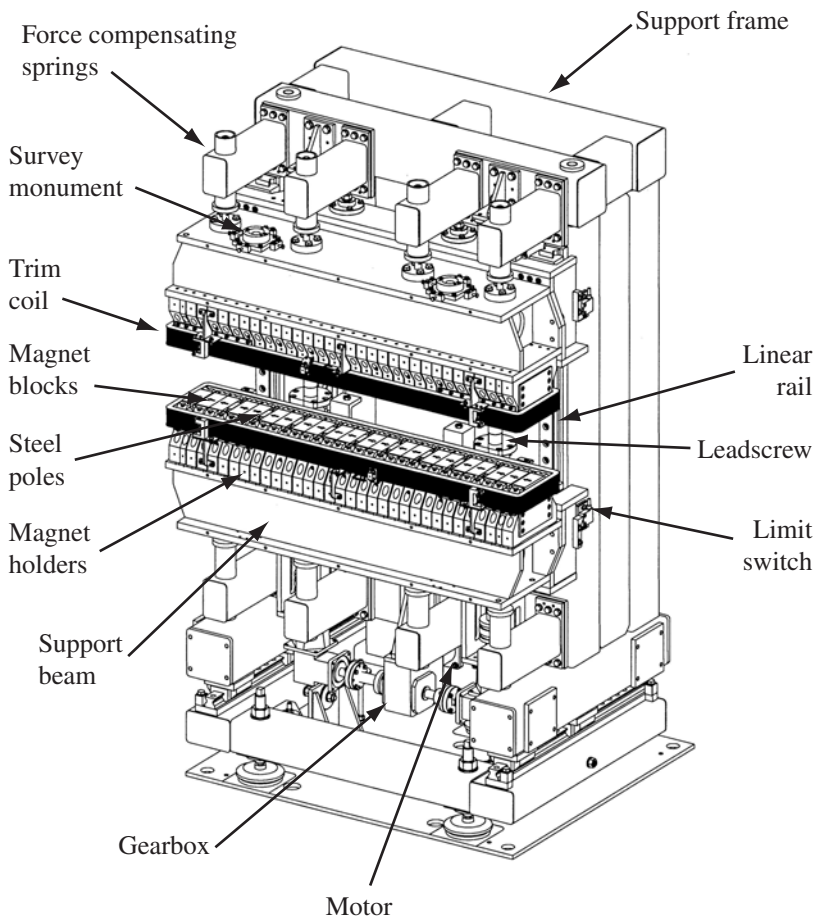
FIG. 7.33. Drawing of a typical insertion device with the key engineering features labelled.

but it will be difficult to keep it below the order of 20 μm. A way of preventing this is to use two motors and two encoders, one pair per leadscrew. Now, the gap is measured at each leadscrew and it is possible to maintain identical readings to within a few steps of the encoder (typically ± 1 μm) with a well designed system. The complication with a two motor system is that the link between the leadscrews is now electrical rather than mechanical. If the motion control system software were to only turn one leadscrew then the magnet gap would become longitudinally tapered, potentially causing damage to the linear slides, leadscrews etc. Of course there is no necessity for the pair of arrays to be mechanically linked either. A valid solution is to not use common leadscrews for both arrays but rather a pair for each. In this case four motors in total are required, two

per array, enabling each array to move independently. This can be helpful in setting the arrays parallel to each other during the mechanical commissioning of the device. It also provides a more satisfactory solution to the requirement of setting deliberate longitudinal gap tapering to alter the output characteristics of an insertion device (see Section 11.1).

Clearly two and four motor systems do carry a higher level of risk. However, potential hazards such as unwanted gap taper or closing the gap and striking the vacuum vessel can be dealt with by hard wired protection systems. These consist of a variety of limit switches, proximity detectors, and tilt sensors that automatically prevent the motors from turning if they are triggered.

7.7.1 In-Vacuum Insertion Devices

Since insertion devices are essentially dominated by their peak magnetic field and period any measure that can be taken to influence these parameters is worth pursuing. The magnet designer is always striving to reduce the gap between the arrays to enhance the magnetic field. This magnet gap is set ultimately by the needs of the electron but in practice is set by the vacuum vessel that the electron beam is travelling through. A typical situation would be that an electron beam requires a full vertical space of 15 mm, say, to maintain a long lifetime. A vacuum vessel will have wall thickness of about 2 mm to support the differential pressure and so allowing a total of 1 mm for clearances would give an actual minimum magnet gap for the insertion device of about 20 mm. An obvious method of reducing the magnet gap is to mount the magnet arrays *inside* the electron beam vacuum vessel (Fig. 7.34), which would save about 5 mm in our example.

There are many increased engineering complications (and costs!) associated with mounting the magnet arrays inside the storage ring vacuum envelope but if the benefits are perceived to be worthwhile they can certainly be overcome. The most crucial requirement is that the storage ring vacuum should not suffer, because if it is poor then the stored beam lifetime will be dramatically reduced. To create and maintain an ultra high vacuum only materials with low outgassing rates can be used. Fortunately, both samarium-cobalt and neodymium-iron-boron have been found to be suitable if they are first covered with a thin coating. Titanium nitride [105] and nickel [106] coatings have both been used successfully in an ultra high vacuum environment.

To reach a good vacuum all materials need to be baked at high temperature (at least $120 - 140°C$). This causes problems in the use of NdFeB as it can suffer from irreversible loss of magnetization at these temperatures. Nevertheless, this material has been used in in-vacuum devices with the designers accepting a loss in magnetization strength of $\sim 2\%$ due to the high temperature baking [107]. The alternative material, SmCo, can be baked to higher temperature with no loss in magnetization (although it is still lower in absolute terms than the baked NdFeB) and also has a greater resistance to radiation damage, which could be an advantage when it is mounted so close to the electron beam. Interestingly however, there is recent evidence that NdFeB magnets that are baked at high
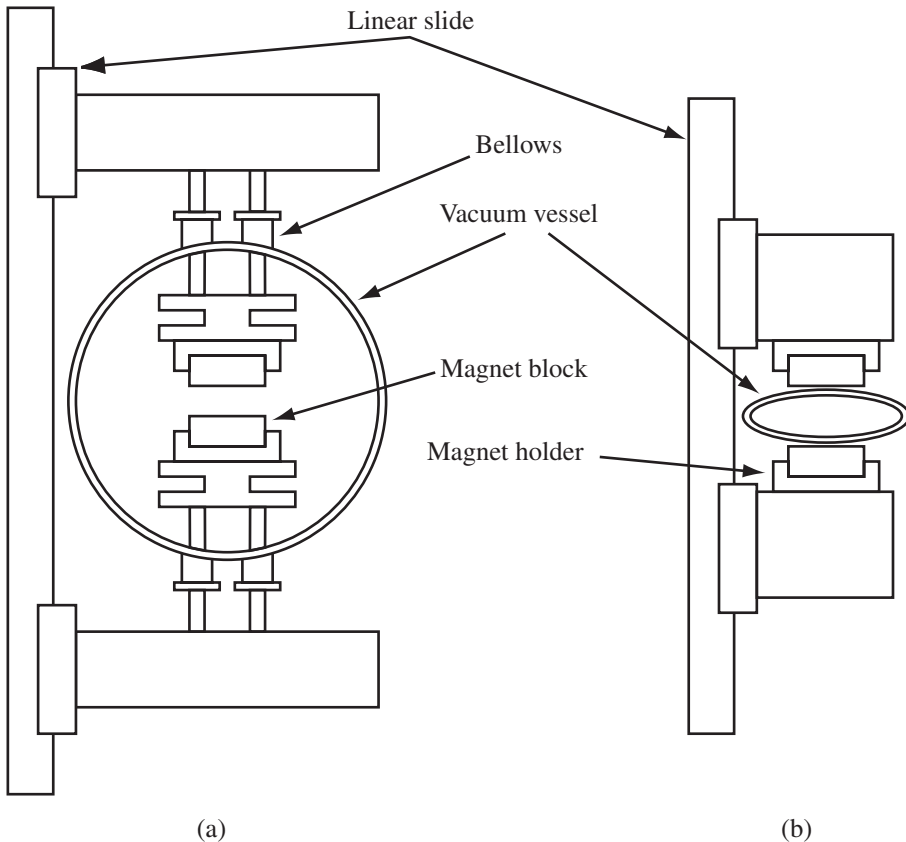
FIG. 7.34. Sketch of (a) the in-vacuum insertion device concept and (b) a conventional insertion device. The electron beam will travel into the paper at the centre of the vacuum vessels. Note that the linear slides mount to the main support structure which is not shown.

temperature have improved radiation resistance over unbaked magnets [108].

One further complication for the in-vacuum insertion device is that the array of permanent magnets provides a high resistance surface close to the electron beam. This will cause the image currents of the electron beam to dump energy into the arrays and cause heating and possibly damage to the magnets [109]. It will also enhance the so-called *resistive wall instability*, which can degrade the quality of the electron beam. To overcome these problems a high conductivity sheet of copper is fixed directly onto the surface of each array to provide a low resistance conducting path. The method of attachment is a thin nickel coating on the copper sheet, which is magnetically attracted to the arrays. Clearly these sheets do slightly alter the magnet gap but as they are usually $\sim 50~\mu$m thick it

is not overly significant.

Another issue for in-vacuum devices is that the magnet measurements have to take place *before* the vacuum vessel is in place due to access restrictions. The engineers must ensure that after the measurements are complete, and any adjustments made, the arrays will be remounted in exactly the same location once the vessel is in place.

Despite all the extra complications introduced by putting the arrays in vacuum this type of insertion device is gaining popularity. Several in-vacuum devices are in operation, most notably at SPring-8 in Japan (which boasts a 25 m long example!) [106, 110] and more recently at the ESRF in France [107, 111]. Also, several recently designed storage rings are relying on this technology to push the spectral coverage of their undulators to shorter wavelengths by the use of short period devices that are not feasible out of vacuum [112–114].

An alternative way of avoiding the limitations set by fixed vacuum vessels is to have a flexible vacuum vessel surrounded by a conventional ID. As the jaws of the ID are closed they squeeze the vacuum vessel, which allows small magnet gaps to be achieved. At times when a larger aperture is needed, during injection, for example, the jaws are opened and the vessel grows accordingly. This option has the advantage of being able to set an appropriate gap to suit the needs of the electron beam and also has all of the complicated ID engineering outside of the vacuum system. Unfortunately the engineering solution for the squeezable vacuum chamber has proven to be difficult to realize in practice, though some short examples have been built successfully [115].

7.7.2 *Forces*

One of the features of permanent magnet insertion devices is coping with the rapidly increasing attractive forces as the arrays are brought together. Naturally it is essential that the design takes account of the forces on the arrays and also, in a detailed level, of the forces experienced by individual blocks.

When we bring two magnets together that have the same poles facing each other we feel a strong repulsive force. To bring them closer and closer we have to use more and more energy. Where is the energy we exert going? The answer is that it is being stored by the combined magnetic field of the two magnets. If opposite poles face each other then the force between them will be attractive and energy will be removed from the magnetic field and do work on the system. To calculate the force we have to compute how the energy stored by the magnetic field changes with distance.

By considering the energy stored in a solenoid, for example, it is relatively easy to show that the magnetic energy density (energy per unit volume, dE/dV) in vacuum and non-magnetic materials is given by [116]

$$\frac{dE}{dV} = \frac{d^3 E}{dxdyds} = \frac{B^2}{2\mu_0} \ ,$$

where μ_0 is the permeability of free space. Then, using the standard result that

force can be expressed as energy (or work done) per unit distance [117], $F = dE/dy$, we can express the force between two magnets as

$$F = \int \int \frac{dE}{dV} dx ds = \int \int \frac{B^2}{2\mu_0} dx ds \ .$$

So, in a region of constant magnetic field over an area in the xs-plane equal to A the force would be

$$F = \frac{B^2 A}{2\mu_0} \ .$$

This situation is a fair approximation to a simple dipole magnet with pole area A.

If we look at the case of a standard planar insertion device of length, L, with a sinusoidal magnetic field in the s direction and peak field on-axis of B_{y_0}, then using the result that

$$\int_{-L/2}^{L/2} B_y^2 ds = B_{y_0}^2 \int_{-L/2}^{L/2} \sin^2 \left(\frac{2\pi s}{\lambda_u} \right) ds = \frac{B_{y_0}^2 L}{2}$$

we can see that the force between the two magnet arrays is given by

$$F = \frac{\int B_{y_0}^2 L dx}{4\mu_0} \ .$$

Assuming that the peak field is constant in the x direction over a width, W, and zero outside this range then the force between the two magnet arrays becomes

$$F = \frac{B_{y_0}^2 L W}{4\mu_0} \ .$$

For our example PPM undulator that has a 50 mm period and a peak field of 0.54 T (see Fig. 7.9) the vertical field under the pole is plotted as a function of x in Fig. 7.35. We can see that the width of the magnetic field can be approximated to around 60 mm. In this case then the force between the two undulator arrays is about 3500 N/m length of undulator. Of course this force will decrease rapidly as the B field reduces or equivalently as the magnet gap opens. A graph showing how the force will vary with gap for this example is given in Fig. 7.36.
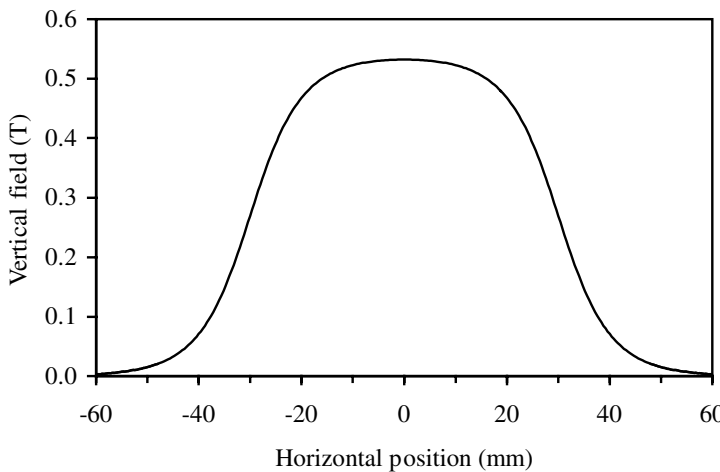
FIG. 7.35. Graph of the vertical field under a pole as a function of horizontal position for a PPM undulator of period 50 mm and magnet block width of 60 mm.
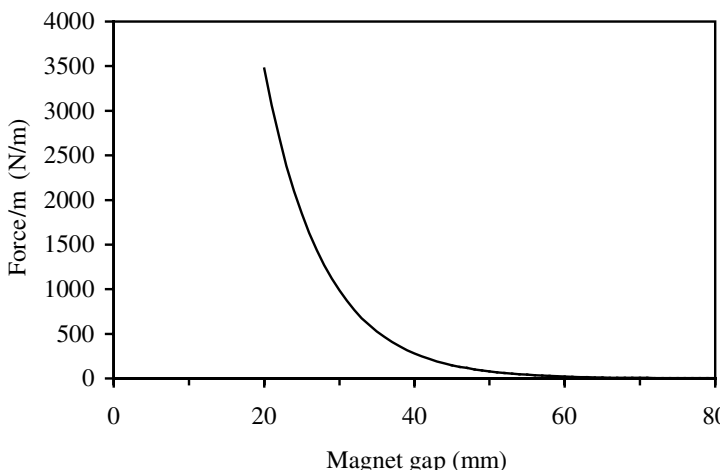
FIG. 7.36. Graph showing how the force per meter length of array reduces as the gap increases for the undulator of Fig. 7.35.

Electromagnet-Based Design of Insertion Devices

Given that particle accelerators are built using many different types of electromagnet (e.g. dipoles, quadrupoles, sextupoles, etc), with permanent magnets very rarely being used, it is perhaps surprising that relatively few electromagnetic (EM) insertion devices (IDs) have been built. In this chapter we will explore the issues surrounding EM ID design and explain why permanent magnets are generally preferred. Despite their limitations EM IDs do have certain advantages and these are the reason why there has been an increased activity in this type of magnet in recent years. One key advantage is the ability to generate a rapidly time varying magnetic field, which is impossible with motor driven (permanent magnet) based systems. This ability has been especially exploited in the field of helical magnets, enabling fast switching between different polarization states (e.g. between left and right circular) that is essential for certain types of experiment. Another advantage of EM devices is that if superconducting coils are used then very high magnetic fields can be generated with relatively short periods. Both of these issues will be covered later in the chapter but first we will look at the basics of planar EM IDs.

8.1 Planar Undulator Design

The basic EM undulator layout is given in Fig. 8.1. Current carrying coils are wrapped around steel poles that are connected by a steel backing beam to carry the return flux. A return yoke between the top and bottom halves is not required. Variation of the magnetic field to tune the undulator is achieved by simply changing the current flowing through all the coils. Mechanically this magnet is much simpler than the permanent magnet type and this is one reason why they generally have a lower capital cost (not including superconducting magnets!). Of course, the running costs are far larger because of the electrical consumption (which can be many tens or even hundreds of kW!).

If we first consider the device to be a series of EM dipoles of length $\lambda_u/2$ then we can get an idea of the field levels that will be achievable. The approximate field produced by a simple dipole with gap, g, being driven by NI Ampere-turns per coil is given by [118]

$$B = \frac{2\mu_0 NI}{g} \quad .$$
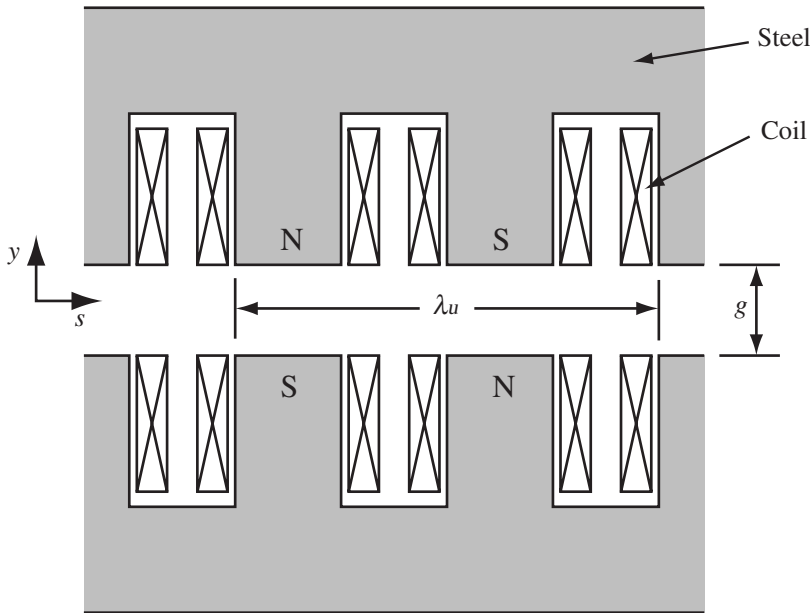
Fɪɢ. 8.1. Sketch of an electromagnetic undulator.

This will give an undulator deflection parameter of

$$K = 2.35 \times 10^{-4} \, NI \frac{\lambda_u}{g} \ .$$

We can immediately see that to generate K values of the order of unity will require typically thousands of Ampere-turns. It is also clear that as the period to gap ratio reduces the number of Ampere-turns has to increase to maintain a particular value for K. In other words, if the gap is fixed and we want to reduce the period, then the coil has to deliver a correspondingly greater value of NI. However, since the period is reducing, the coil will have less space to occupy and so the *current density* will have to increase rapidly to compensate. It is easy to imagine that at some period the current density will have to be so large that the resistive losses can no longer be removed by water cooling circuits. We will now establish what are realistic period to gap ratios for normal conducting EM undulators.

The field in a planar undulator can be expressed, in a two-dimensional approximation, by two infinite sums [119, 120]

$$B_y = \sum_{m \text{ odd}} B_m \sin(mks) \cosh(mky)$$

$$B_s = \sum_{m \text{ odd}} B_m \cos(mks) \sinh(mky) \ ,$$

with the conventional wavenumber definition, $k = 2\pi/\lambda_u$. The solution of B_m can be found by defining a boundary condition along $y = g/2$ and it has been found that a good approximation is that the two field components follow a square wave pattern along this surface [119]. From this we have that

$$B_m = \frac{32\mu_0 NI}{\pi\lambda_u} \frac{\sin(m\pi/4)}{m\sinh(mkg/2)} \ .$$

It has also been shown that the best approximation to the variation of B_y with y when compared with numerically computed values is with the first two terms only from the infinite series [119]. In this case then

$$B_y = \frac{32\mu_0 NI}{\sqrt{2}\pi\lambda_u} \left[\frac{\cosh(ky)}{\sinh(kg/2)} - \frac{\cosh(3ky)}{3\sinh(3kg/2)} \right] \ .$$

We can use the value of B_y when $y = 0$ to find the deflection parameter for this case

$$K = 8.45 \times 10^{-4} \, NI \left[\frac{1}{\sinh(kg/2)} - \frac{1}{3\sinh(3kg/2)} \right] \ .$$

This expression is plotted in Fig. 8.2 with the simple dipole model. At large period to gap ratios the dipole approximation is good (i.e. the poles do act independently) but it breaks down below ratios of about 3.

If we assume that for an EM undulator the coil cross section is $\lambda_u/8 \times \lambda_u/2$ (both these values are somewhat arbitrary but nevertheless reasonable) and that the maximum current density that can be effectively water cooled is 10 A/mm^2 then we can make some realistic estimates for what K values are achievable as a function of period. The results are plotted in Fig. 8.3 for a 20 mm gap. We can see that K does not reach unity until about 55 mm period but at twice this value it reaches a value of about 10. However, even this is optimistic because it takes no account of saturation effects in the steel; in reality the K value would not rise so quickly with the period. From these comments we can see that short period EM undulators are unlikely to be very useful and in fact are easily outperformed by permanent magnet devices (compare with Fig. 7.14 for example).

There are several examples of planar EM IDs around the world. A multipole wiggler was built for the VEPP-4 storage ring [121], which had a peak field of 1.6 T and a period of 22 cm. In this design the poles were carefully shaped to make the field less sinusoidal and so reduce the horizontal angular divergence of the photon beam.

Two EM designs have been produced for the TNK facility [122], an undulator and a wiggler. The undulator uses an unusual method for generating the Ampere-turns needed for each pole by using snake-like windings that wrap around half
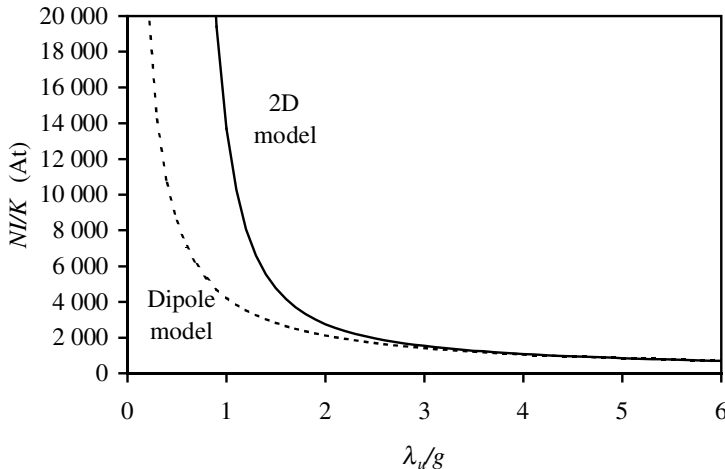
FIG. 8.2. The number of Ampere-turns for a given K value as a function of
the period to gap ratio for a two-dimensional model and also a simple dipole
approximation.
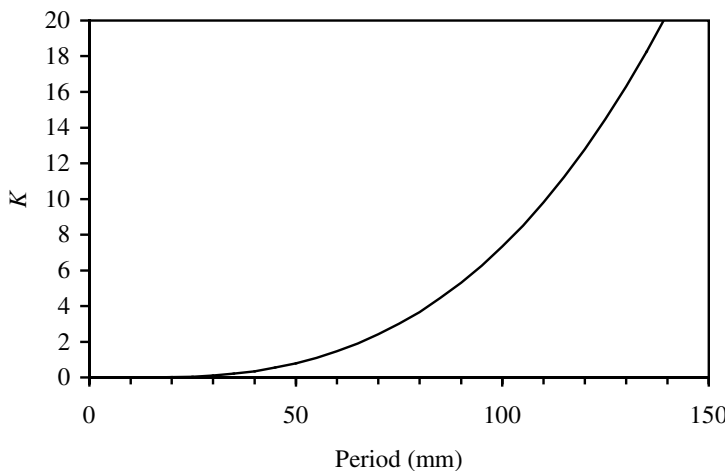
FIG. 8.3. K as a function of period for an EM undulator with a magnet gap of
20 mm and realistic coil cross section and current density.

of each pole along the full length of the device. A similar winding wraps around
the other half of each pole to complete the Ampere-turns. This technique was
said to simplify manufacture, connections and cooling of the windings.

One of the limitations with an EM ID is that the steel poles saturate and
limit the on-axis fields that can be achieved. In a standard EM design the region

that saturates first is where the pole joins to the yoke (the pole root). Some designs have tried to suppress this saturation by using permanent magnets, not to generate field on-axis, but to effectively *reverse-bias* the flux in the steel. Devices that use this technique are called *laced* electromagnets [123, 124].

The first example of this kind was used for the Paladin Free Electron Laser (FEL) [125], which successfully demonstrated higher on-axis fields than would otherwise have been possible. One disadvantage to this biasing is that it is not possible to operate properly with the opposite polarity on the poles. In this case the steel saturates very rapidly with increasing excitation current and only low fields are achievable on-axis.

8.2   Helical Magnets

There are two main families of electromagnets that are used to generate helical or elliptical fields. The first is called the *bifilar helix*, which is a very simple coil winding with a circular geometry that generates a pure helical field on-axis and the other is the elliptical wiggler that uses EMs to generate the (weak) horizontal field; the vertical field can either be produced by EM or permanent magnet technology. This latter type of ID usually takes advantage of the EM technology by switching the horizontal field rapidly (~ 1 to ~ 100 Hz) so as to flip the polarization state from left to right circular, say.

8.2.1   *Bifilar Helical Magnets*

The bifilar helix has a very simple geometry that is made of two helical windings with currents flowing in opposite directions (Fig. 8.4). The transverse field on-axis generated by wires of zero cross section carrying a current, I, is given by [126]

$$B = \frac{2\mu_0 I}{\lambda_u} \left(\frac{\pi g}{\lambda_u} K_0 \left(\frac{\pi g}{\lambda_u} \right) + K_1 \left(\frac{\pi g}{\lambda_u} \right) \right) \quad ,$$

where K_0 and K_1 are modified Bessel functions and g is the coil diameter (equivalent to the magnet gap). The undulator deflection parameter for this device is then

$$K_x = K_y = 2.35 \times 10^{-4} \, I \left(\frac{\pi g}{\lambda_u} K_0 \left(\frac{\pi g}{\lambda_u} \right) + K_1 \left(\frac{\pi g}{\lambda_u} \right) \right) \quad .$$

This expression is plotted in Fig. 8.5 in a similar manner as for Fig. 8.2. We can see that the current demand rises more sharply in the helical magnet than the planar magnet at the low period to gap ratios. This is not surprising considering that this magnet does not benefit from any iron pole pieces. If we assume a current of 10 kA and a magnet diameter of 20 mm then we can plot the K value as a function of period (Fig. 8.6). Here we can see that reasonable K values can be reached for periods of about twice the gap and greater. However, the assumption of a current of 10 kA is optimistic for a normal conductor given that current densities beyond 50 A/mm^2 are difficult to water cool. This would imply
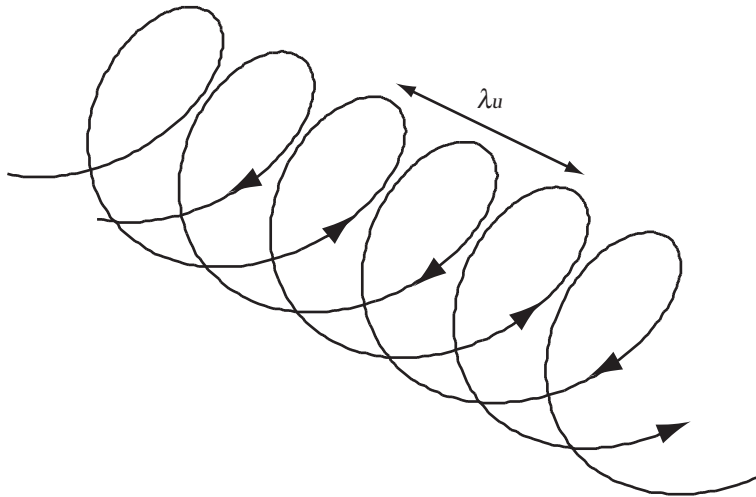
FIG. 8.4. Sketch of the bifilar helix concept.
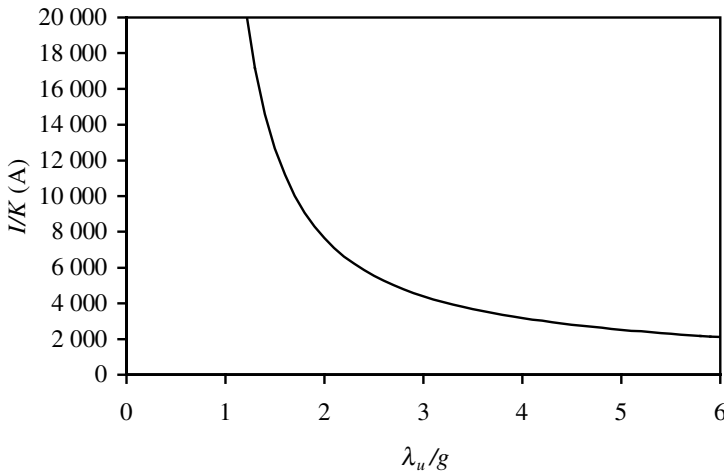
FIG. 8.5. The current I for a given K value as a function of the period to gap ratio for a simple bifilar helix.

a conductor cross section of 200 mm^2, which would be difficult to fit into a magnet with a period of less than 50 mm say. This explains why almost all examples of this simple magnet geometry have resorted to superconducting technology.

The first terms of the expansion of the three-dimensional magnetic fields, expressed in cylindrical polar coordinates (ρ, ϕ, and s), for a helical winding with a finite (cosinusoidal in both ϕ and s) current distribution have been found
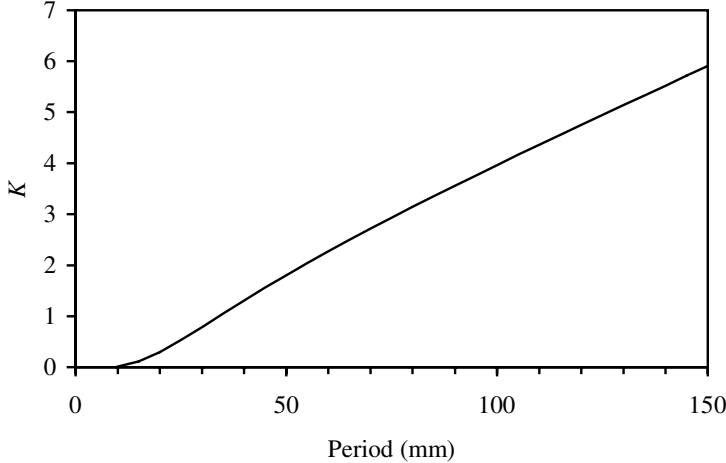
FIG. 8.6. K as a function of period for a bifilar helix undulator with a magnet
     diameter of 20 mm and a current of 10 kA.

to be [127]

$$B_\rho = 2B_0 \left(I_0(k\rho) - \frac{I_1(k\rho)}{k\rho} \right) \cos(\phi - ks)$$

$$B_\phi = -2B_0 \left(\frac{I_1(k\rho)}{k\rho} \right) \sin(\phi - ks)$$

$$B_s = 2B_0 I_1(k\rho) \sin(\phi - ks) \ ,$$

where B_0 is the magnitude of the on-axis field, I_0 and I_1 are modified Bessel
functions and $k = 2\pi/\lambda_u$ is the wavenumber. These have also been expressed in
terms of cartesian coordinates, though this is less useful [78].

Efforts have been made to improve the field quality due to the conventional
two-wire system by including additional wires. In one case [128] two pairs of wires
were used to improve the field homogeneity with the phase separation between
the pairs of wires being set by optimization with a two-dimensional magnet code.

The end terminations for the bifilar helix can cause problems as the current
carrying wires have to be taken away from the beam axis carefully to connect to
the power supply. A number of options have been studied to minimize the effect
of the termination on the electron beam [129].

The first FEL experiment used a superconducting bifilar helical magnet that
was capable of reaching 1.3 T with a bore diameter of 10 mm and period length
of 32 mm [130]. A normal conducting version was installed in the VEPP2 ring
at Novosibirsk, interestingly this was later upgraded by including a helical iron
arrangement to enhance the field levels [131]. The full device was later replaced
by a superconducting version [121].
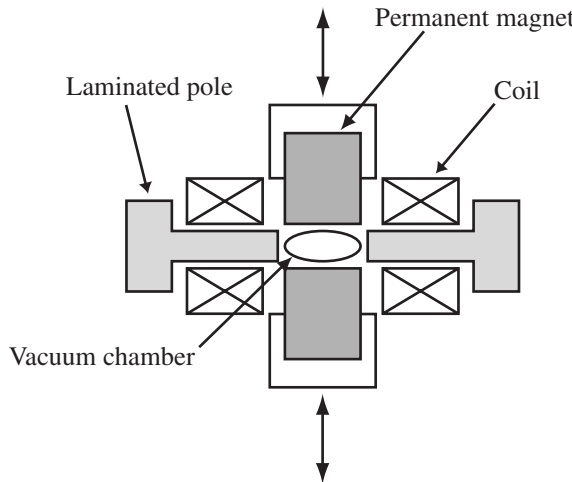
FIG. 8.7. Sketch of an elliptical multipole wiggler with the vertical field gener-
ated by a permanent magnet hybrid structure and the horizontal field gen-
erated by an EM system. The horizontal and vertical poles are offset longi-
tudinally by $\lambda_u/4$.

8.2.2 *Elliptical Wigglers and Undulators*

We have already seen in Section 6.5 that the requirements for an elliptical wiggler
are a strong vertical field to generate the broad synchrotron radiation spectrum
and a relatively weak horizontal field that puts a sufficient angular deviation on
the electron beam so that the observer sees the same polarization state from
each pole rather than opposite helicities that would otherwise cancel out. If the
horizontal field polarity is reversed then the observer will see radiation of opposite
helicity. The vertical field does not need to vary. Therefore, in order to provide
fast switching of the polarization state (~ 1 to ~ 100 Hz) it is only necessary to
use an EM system for the horizontal field component. The vertical field can be
generated with either a permanent magnet or EM based system.

An example of an elliptical wiggler with a permanent magnet structure to
provide the vertical field is installed in the NSLS X-ray ring [59, 132]. The peak
vertical field in this case is 0.8 T with a period of 16 cm. The peak horizontal
field is 0.22 T. The horizontal poles have to be laminated to reduce the Eddy
current losses at high frequency (up to 100 Hz). In fact there are higher losses in
the hybrid magnet induced by the time varying horizontal fields than there are
in the laminated horizontal poles.

One problem with this design is that access to the vacuum chamber is highly
restricted as it is surrounded by the poles of the magnets (see Fig. 8.7). This
also makes accurate magnet measurements extremely difficult.
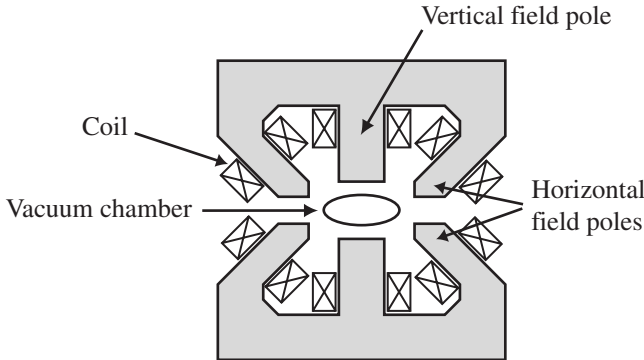
FIG. 8.8. Sketch of an elliptical multipole wiggler with the vertical and horizontal fields generated by an EM system. The horizontal and vertical poles are offset longitudinally by $\lambda_u/4$.

The alternative approach, of an all EM device, has been pursued by a collaboration led by ELETTRA [58, 133]. The motivation for generating the vertical field by an EM was so that the device could also run in undulator mode with low vertical field but still high field quality. This also meant that no vertical gap movement was required, which removed some other engineering constraints. In particular, a simple method for generating the horizontal field with four poles rather than two was used, which gave free access to the vacuum chamber region for maintenance and also magnet measurements (see Fig. 8.8).

This device has a longer period (21.2 cm) but lower peak fields (0.5 T vertical and 0.1 T horizontal). The vertical field is DC but the horizontal can switch at up to 100 Hz. Surprisingly the effect of changing one transverse field on the other is quite small ($< 1\%$) because the flux paths generated by the two sets of coils are to a large extent independent. A similar device has also been built for the APS though this is only designed to operate in the undulator mode [49].

Another device that operates as a helical undulator has been built for the ESRF [134, 135]. This one is unusual because the vertical field is generated by EM coils but the horizontal field is generated by permanent magnets. The permanent magnets are mounted above and below the horizontal plane in a similar manner to the planar helical undulators of Section 7.6 so that access for magnet measurements is still possible.

One final helical device that is worth mentioning is the helical crossed undulator that was built for Super-ACO [60, 136]. This is based upon a pair of identical planar EM undulators mounted orthogonally to each other so that one provides a vertical field and the other a horizontal. Full polarization control is obtained by also including a longitudinal translation motion on the vertical undulator. This magnet is ideally suited to EM technology because the requirements were for a long period, weak field to reduce the total power produced and thus the

thermal load on the optics. This device is optimized for a low energy beamline, which uses near-normal incidence of the photon beam on the optics, rather than grazing incidence, and so power levels were of considerable concern.

8.3 Superconducting Magnets

Using superconducting materials in insertion devices opens up new possibilities that would otherwise not have been achievable. Superconducting wires have zero electrical resistance and so do not suffer from Ohmic losses and heating. As a consequence they can carry much higher current densities than normal conducting cable and that allows magnetic fields of several Tesla to be generated relatively easily.

There are three distinct classes of superconducting ID; high field wavelength shifters, medium field multipole wigglers, and short period undulators. Of these the high field wavelength shifters are by far the most common with numerous operational examples around the world. However, the medium field multipole wigglers are presently growing in popularity and there are now a few examples of these either in construction or in use. Superconducting short period undulators are generating a lot of interest but they have several technological challenges still to overcome and at present there are none of these installed in any storage ring light source though they have been used successfully in FEL experiments.

8.3.1 *Superconducting Magnet Basics*

Of course the subject of superconductivity is far too large as to be covered here to any depth, fortunately there are several excellent texts available for those who would like a more detailed explanation of the phenomenon (e.g. [137] and [138]). Here I will just give a brief overview of the main features that are relevant to ID design.

There are only really two materials that are used for superconducting IDs at present, these are the alloys Niobium-Titanium (NbTi) and Niobium-Tin (Nb_3Sn). These are both so-called 'Type II' superconductors that are characterised by a *critical surface* in temperature, magnetic field, and current density space (see Fig. 8.9). If the material is operated below the surface then it will be superconducting, if it is taken above the surface then it will be normal conducting. Type I superconductors (such as Mercury, Lead, or Tin) are not useful for IDs because they are only superconducting at low fields (typically < 0.1 T).

NbTi is the preferred material to use because it is ductile and easy to form into coils. It will remain superconducting up to ~ 6.5 T at 4.2 K or ~ 9 T at 2 K. In a field of 5 T and temperature of 4.2 K (the boiling point of liquid helium under atmospheric pressure) it can conduct at current densities in excess of 3000 A/mm^2 [138]. Superconducting wires of NbTi consist of many individual filaments (typically 20 μm diameter) held together in a copper matrix that provides mechanical stability, an electrical bypass when a filament goes normal conducting, and also a heat sink. A 1 mm diameter wire can contain hundreds
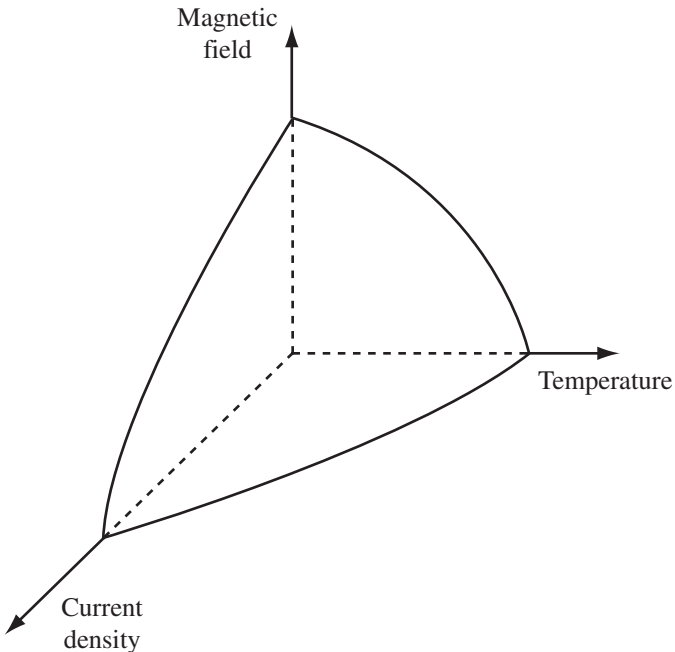
FIG. 8.9. Sketch of the critical surface for a Type II superconductor, below the surface the material will be superconducting and above it it will be normal conducting.

or even thousands of filaments. Typically 20 – 40 wires are wound together to form cables.

The alternative material, Nb_3Sn, is able to operate at higher fields (up to 20 T at 4.2 K) but it is very brittle and difficult to work with and should be avoided if at all possible. The recent generation of high critical temperature ceramic-copper oxide superconductors has made little impact on superconducting magnet coils as yet though they are now used for the current leads.

One important feature of superconducting magnets that is different to normal conducting ones is that with such high current densities and strong field levels the field quality is set by the position of the conductors rather than the (saturated) iron poles and this makes the coil geometry and accurate positioning very important. Also, the forces on the coils can be enormous, which is especially important because the frictional heating caused by minor coil movement can be enough to make the coil normal conducting, which is called a *quench*. Quenches are important because a sudden increase in resistance in a coil that has very large current densities flowing within it can easily damage or even destroy that coil. Protection systems must be included with the power supply so that in the event of a quench the current is rapidly (< 1 s) reduced to zero.

The reason that such apparently small effects, such as the frictional energy associated with coil motion, can cause significant temperature increases is due to the specific heat capacity of materials in general at cryogenic temperatures being so small. They are typically 0.1% of their room temperature values [137] and so much less energy is required to raise the temperature of the coils.

One final feature that is related to the quench problem is that of *magnet training*. Often when a magnet is first energized it will quench at a certain field level, the second time it will quench at a slightly larger field level, and so on until, after a number of quenches, the field level reached each time no longer improves. This process is called *training* and is generally ascribed to small movements within the coils that need to be 'ironed out'. Some magnets reach their design specification without quenching while others might need to be trained with several energization cycles before reaching the desired level.

8.3.2 *High Field Wavelength Shifters*

These magnets usually consist of a single (or occasionally a few) high field pole (typically around 6 T) surrounded by two weaker, approximately half strength, side poles to ensure the electron path returns to the nominal beam orbit. There are 5 T [22] and 6 T [139] examples installed in the SRS (both about 1 m long, including the cryostat). The 7 T BESSY II magnet [24] is designed to run in persistent current mode where, by closing a switch within the cryostat, the current flows around a purely superconducting circuit and the power supply can be mechanically disconnected. This has the advantage of reducing the running costs, reducing the consumption of liquid helium, and also removing the magnet power supply noise as a possible cause of unwanted electron beam motion. This magnet is similar to that installed at CAMD [23] in that it has an extra pole at either end so that the electron beam trajectory can be adjusted so that the source point at the centre, high-field, pole is always on the nominal beam axis for all field levels.

Another interesting example is the 5 T magnet that was installed on the Photon Factory [140]. This magnet was designed to produce a horizontal field so that the electron motion was in the vertical plane to produce vertically polarized light. To accommodate injection into the storage ring the whole magnet had to be translated vertically so that the 'T' shaped vacuum chamber presented a larger horizontal aperture to the electron beam. This magnet was later replaced [141] by a version, which had a wide horizontal aperture between the magnet poles and so no vertical movement was then required. This second version also employed persistent current switches so that the magnet could run for several weeks with the power supply disconnected. The current in the coils gradually decreased with time due to the finite resistance at the junction between the coils and the switches. The consumption of liquid helium was found to reduce from 4 l/h for the first magnet to about 0.1 l/h for the second when it was run in persistent mode.

One final example of note is the wavelength shifter at SPring-8 that has

achieved 10.3 T [142,143]. This is a rare example of the use of Nb_3Sn conductor (by necessity) as all of the other examples mentioned above have used only NbTi.

8.3.3 *Medium Field Multipole Wigglers*

The first wiggler of this type was installed on VEPP-3 in 1979 [144]. It had 20 poles of field strength 3.3 T with a period of 90 mm. After this magnet was produced there was relatively little activity in this area for about 15 years. An interesting device with three modes of operation was developed for the NSLS in the mid-1990s [145]. This device could operate as either an 11 pole, 3 T device, a 5 pole, 4.7 T device, or a single pole wavelength shifter at 5.5 T. Switching between the different modes involved changing the connections of the magnet leads to the power supply.

More recently MAX-lab have built a multipole wiggler with 47 poles of 3.5 T with a period of only 61 mm [146, 147]. An interesting feature of this device is that the magnet is 'cold bore', that is, the vacuum chamber for the electron beam is cooled down to close to 4.2 K. This is unusual because there is then little insulation between the potential heat sources associated with the electron beam (e.g. synchrotron radiation, resistive wall heating, and wakefield effects) and the superconducting coils. Also, in the event of a vacuum leak within the storage ring water vapour would freeze onto the surface and could cause problems with attaining a good vacuum in the future. A very similar magnet has been installed into the ELETTRA ring [148], although interestingly this has a slightly warmer bore of 20 K. Future light sources are also planning to use magnets with similar parameters [112].

8.3.4 *Short Period Undulators*

It would be very difficult to wind individual coils for short period (< 25 mm) undulators so designs have been developed for winding them continuously over many tens of periods. In general, wires are wound onto ferromagnetic formers that have grooves precisely machined into them to set the periodicity of the undulator. A pair of energized formers are brought close together to generate the transverse field required.

An 8.8 mm period device that operated at a 4.4 mm gap was built for an FEL experiment [149]. With 70 periods the complete device was about 0.6 m long and generated a peak field of 0.51 T (a permanent magnet-based device would have generated about 0.4 T). To keep the field errors small ($< 0.5\%$) the solid low carbon steel former had to be machined to a tolerance of 15 μm. A similar design for a storage ring has been built and tested successfully on a microtron [150]. This had a period of only 3.8 mm and was designed to operate with a gap of between 1 and 2 mm. The experience gained with this second device has been used to refine the design and to match it more closely to the requirements of a storage ring. In particular a larger gap of 5 mm has been adopted and a correspondingly longer period of 14 mm used [151]. A 10-period prototype has demonstrated peak field levels of about 1.3 T, in comparison a permanent magnet-based device would

reach about 0.7 T.

There are many problems with operating this type of undulator in a storage ring. Again it will be cold bore and similar comments apply to those above. For the short periods designed, a small gap is also required and even if this can be tolerated in terms of the electron beam lifetime, it is certain that the heat sources associated with the electron beam will be difficult to cope with. Also, although magnet measurements at low temperatures are still possible with Hall sensors it is difficult to maintain a high accuracy either in terms of the measured field level or the exact probe location within the magnet. The difficulties associated with making precise magnetic field maps may limit the final quality of these devices as any field shimming will by necessity be limited. However, this type of device does show much promise in terms of extending the wavelength coverage of undulators by generating useful field levels at shorter periods than are presently possible with permanent magnet-based devices. If the technological challenges can be met then superconducting undulators will surely play a significant part in any future light sources.

9

Measurement and Correction of Insertion Devices

In the past the process of magnet design was often limited to the use of analytical techniques and simple numerical codes. Prototype magnets would frequently be built and undergo comprehensive magnetic tests to verify the final magnet design. Now that we have a suite of three-dimensional magnet codes at our fingertips that accurately predict electromagnet and permanent magnet designs, it is worth reconsidering our motivation for magnet measurements. If we look at graphs comparing predicted magnetic fields against measured ones it is often difficult to tell them apart, the agreement appears to be so good. However, looks can be deceiving! The fact is that the magnetic field requirements for insertion devices, especially undulators, are so demanding that comprehensive magnet measurements are *essential*. First, of course, it would be unwise to solely rely upon idealistic computer models as they will not show the effects of the real materials on the magnet (e.g. the inhomogeneities in the permanent magnets or the actual permeability curve of the steel) nor would they show if a magnet block had been inserted with the wrong magnetization direction! Second, it is only with the knowledge gained from magnet measurements that the insertion device can be adjusted or tweaked to give the best possible performance. This process of improvement, often based upon shimming techniques, can make very impressive differences to the quality of the radiation emitted by undulators in particular. In fact, it is an almost universal practice to not only measure the complete insertion device but to measure every single individual magnet block prior to assembly. The results of the block tests are then used to specify where each individual block should be fitted within the magnet (so-called block sorting) to produce the best possible performance in terms of electron beam trajectory and spectral output.

In this chapter, we will first examine the different measurement techniques available that have been applied to the characterization of complete insertion devices or individual permanent magnet blocks. In the second part of this chapter we will examine how the magnet measurement results can be used to first build the best possible ID and second to improve the final device to give the best possible performance.

9.1 Magnet Measurement Techniques

There are a very wide variety of methods available for measuring magnetic fields so only the common ones that are relevant to IDs will be described here. The choice of which method to use depends upon the requirements; point measurements, field integrals, speed, accuracy, geometric constraints, etc. A good ID laboratory would have most, if not all, of these techniques available since each of these offer some advantage in the correct circumstances.

9.1.1 *Nuclear Magnetic Resonance*

This technique is the most precise one readily available and so is used as the primary standard in the laboratory for calibration of other methods. It relies upon a fundamental property of particles that have spin and a magnetic moment such as the proton or the deuteron. When they are exposed to an external magnetic field this magnetic moment precesses about the external field direction (like a gyroscope) [152, 153]. The precession frequencies of these particles are well known and vary linearly with the external field level. Measurement of the frequency, which is independent of both temperature and field direction, can be carried out very precisely using resonant techniques.

In practice a sample, such as heavy water or rubber, is placed inside an excitation coil that oscillates at high frequency. The sample size is typically a cylinder of diameter 5 mm and length 5 mm. The measurement range for each probe is essentially limited by the high frequency electronics and so different probes must be used to cover a wide field range. The frequency response for protons is 42.58 MHz/T and for deuterons is 6.54 MHz/T, hence protons are used to cover the lower magnetic field range of about 0.04 – 2 T and deuterons the higher field range of about 1.5 – 13.7 T. If required, very low field levels (0.5 to 3 mT) can be covered using the related technique of electron spin resonance. These field ranges quoted are for commercially available instruments that also claim absolute accuracy of 5 ppm (parts per million).

This type of measurement is relatively slow (the order of seconds per reading) and requires a stable homogeneous field. Sophisticated techniques are available for measuring in magnet field gradients and also time-varying fields [152] but these are best avoided if at all possible!

9.1.2 *Hall Generators*

Edwin Hall discovered in 1879 that a thin metal strip carrying a current in an external field perpendicular to the plane of the strip developed a voltage, orthogonal to the current and the field, that opposed the Lorentz force on the electrons (Fig. 9.1). Since this phenomena is directly related to the force on the electrons due to an external magnetic field it is not surprising that the Hall voltage varies monotonically with the field and can be used as a method for measuring the field level. The most sensitive Hall generators should have high carrier mobility and low conductivity [154] and so metals are not well suited. The best materials to use are semiconductors, particularly InSb and InAs [155],
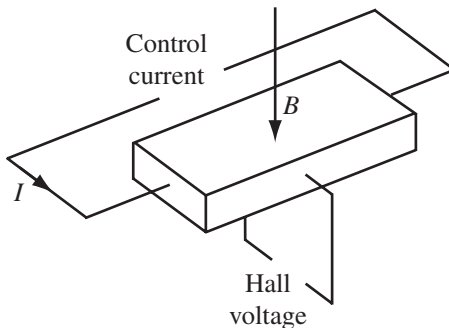
FIG. 9.1. Sketch of a Hall generator.

and these types of sensor are now widely available from industry.

The variation of the Hall voltage with field is approximately linear but for precise measurements the sensor must be carefully calibrated over the full field range of interest, usually using a homogeneous dipole magnet and an NMR system (see Section 9.1.1). Of more serious concern is the fact that the response of the sensors also varies with temperature and so this must also be accounted for. Some probes are kept at a fixed temperature (typically 40°C) using a thermostat and small heater fitted to the sensor, while others have integral thermocouples that record the temperature and compensate for it. Of course they can only account for a variable temperature if they have previously been calibrated as a function of temperature which is a rather long-winded process. However, the temperature stabilized probes with thermostats are naturally more bulky and can be too large for some ID applications. Calibrated Hall sensors, including the electronics, are available commercially with accuracies of about 100 ppm over field ranges of up to 3 T. The Hall generators themselves typically have a sensitive area of about 3 mm by 1 mm though much smaller dimensions are available if required. Regular calibration is recommended because the semiconductors and electrical contacts can suffer from ageing processes.

Clearly Hall generators are very sensitive to the direction of the magnetic field as well as its polarity. Care must be taken when aligning the probe so that the required orientation is set and also that the location of the sensitive area (which is generally hidden by the protective packaging, similar to other semiconductor devices) is well known. Different sensor packages are available that have two or sometimes three Hall generators mounted orthogonally to each other so that magnetic fields can be measured simultaneously in more than one plane. Some groups have also mounted several generators equally spaced apart in the same plane so that the magnetic field in one direction can be measured simultaneously at several points. This has the advantage of greatly speeding up field mapping of large magnets. Hall generators respond relatively quickly to field changes and so measurements 'on the fly' are possible (i.e., the probe is scanned continuously

and smoothly through the magnet without actually stopping to take readings) to speed up data taking. However, for more accurate results a slower step by step method may be needed, though this does not guarantee accuracy as probe vibration can then occur and introduce errors.

One significant cause of error in Hall generators is the so-called *planar Hall effect*. This is a magnetoresistive effect caused by having a magnetic field in the *plane* of the Hall generator that creates an error voltage on top of the Hall voltage. It arises from the difference between the magnetoresistance of the material in the transverse and longitudinal directions. Fortunately it is proportional to B^2 rather than B and so it always has the same sign, unlike the Hall voltage. A simple technique for accounting for this error then is to take one set of measurements with the Hall generator in the plane of interest and then to take a second set with the generator flipped over by 180°. Simple subtraction (and dividing by 2) of the two data sets will cancel out the planar term. A more attractive proposition is to have two Hall generators mounted one on top of the other but with one rotated by 180° so that it reads the Hall voltage of opposite sign. Again taking the difference between the two signals will cancel the planar Hall voltage error.

Hall generators will also work at cryogenic temperatures though in this case another error is present due to the so-called *Shubnikov - de Haas effect* [154]. This effect produces a field-dependent oscillation in the Hall voltage of the order of 1%. The effect can be calibrated out, though of course this requires a calibration to be performed at cryogenic temperatures.

All ID labs have some form of Hall probe measurement bench. One or more Hall generators are mounted onto a motorized carriage that can be remotely manipulated in all three orthogonal axes (Fig. 9.2). They are designed to scan along the length of a typical ID so the longitudinal motion will generally be at least 2 m and often 5 m. The horizontal and vertical motions only need to map out the area between the arrays of the ID so these only need a small range of motion, typically 20 – 30 cm in both planes. The complete motion system is generally mounted onto a massive synthetic granite slab that is selected to damp any vibrations. The position of the carriage must be known accurately as this determines the position of the Hall sensor within the magnet. Fortunately linear encoders that can measure position with resolutions of better than 1 μm are readily available and this is more than adequate given the typical undulator period lengths of 10s of mm.

As mentioned earlier, the favoured method for using such a bench is to continuously move the probe along the longitudinal axis (with the horizontal and vertical position fixed) and to take measurements quickly enough so that of the order of 50 data points per period are recorded. Although the probe speed and data taking frequency are adjusted to suit each ID under test, typical values quoted are speeds of around 20 – 30 mm/s and measurement frequencies of 20 – 30 Hz.
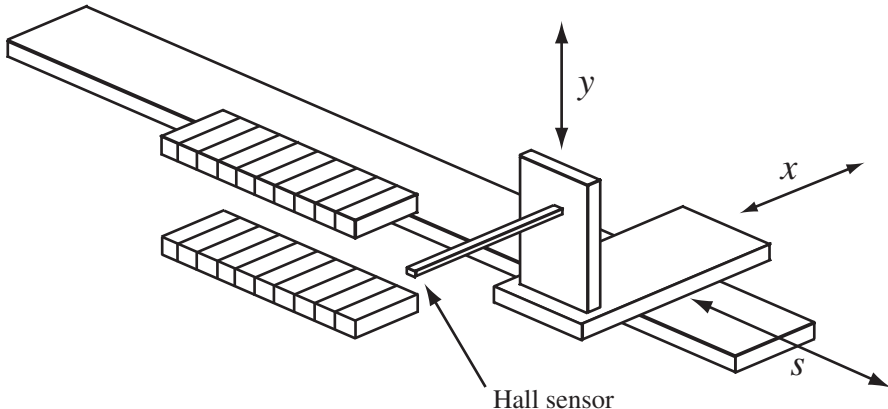
FIG. 9.2. Sketch of a Hall probe bench.

9.1.3   *Coils*

This is a very old technique based upon measuring the voltage induced in a coil as it moves through a region of field or equivalently the voltage induced in a stationary coil by a time varying field. Given the simplicity of the technique it is surprising how precise it can be if enough care is taken. Since IDs are usually static fields it is more common for the coil to either be translated or rotated. Long coils are well suited to precise measurements of field integral along the electron trajectory, though one of the benefits of this technique is that the coil geometry can be matched to the measurement required. For instance, one sensitive technique is to use a coil exactly the length of one undulator period since as it moves through the main body of the device it should ideally induce zero output [156]. Another benefit of using coils is that it is easily adapted for measurements at cryogenic temperatures.

A very common method for measuring conventional accelerator magnets with circular cylindrical geometry, such as quadrupoles and sextupoles, is to use the *harmonic coil method* [157, 158]. In this case a long coil is continuously rotated inside the magnet with one side of the coil coincident with the rotation axis, which is positioned along the magnet axis. The induced integrated voltage is measured as a function of rotation angle and Fourier analysed to determine the coefficients of all of the multipoles present. The radial field, B_r, can be expressed as a sum of multipole components with coefficients a_n and b_n [159]

$$B_r = \sum_{n=1}^{\infty} [a_n \cos(n\theta) + b_n \sin(n\theta)] r^{n-1} \ ,$$

where r is the radius of the circle mapped out (the coil width), and θ is the angle of the coil to the horizontal. This can then be inserted into the equation for the integrated voltage induced in the coil

$$\int V\,dt = -N\Delta\Phi \ , \tag{9.1}$$

where N is the number of turns in the coil and $\Delta\Phi$ is the change in the magnetic flux. The Fourier analysed integrated voltage is of the form

$$\int V\,dt = \sum_{n=1}^{\infty} V_{n_c}\cos(n\theta) + V_{n_s}\sin(n\theta)$$

and the *integrated* (along the length of the coil) multipole coefficients are given by [159]

$$A_n = \frac{nV_{n_c}}{2Nr^n\sin(n\Delta\theta/2)}$$
$$B_n = \frac{nV_{n_s}}{2Nr^n\sin(n\Delta\theta/2)} \ ,$$

where $\Delta\theta$ is the angular step size per integrated voltage. The A_n terms refer to *skew* fields and the B_n terms refer to *normal* fields. So A_1 is the skew dipole (i.e. horizontal field), B_1 is the normal dipole (i.e. vertical field), A_2 is the skew quadrupole and so on.

Unfortunately the ID geometry of a narrow vertical aperture and a wide horizontal one is not well suited to this technique and so it is rarely used. Only small width coils can be used (unless the ID gap is opened) and these will be less sensitive to the higher order multipoles. However, the advent of the *stretched wire technique* has made implementation of this harmonic method straightforward and so it is likely to become more popular in ID measurement than it has been up to now.

The most common coil system used with IDs is the *flipping coil*, which is used to measure the field integrals along the full length of the magnet. It is more precise than numerically integrating Hall probe data and also a far quicker measurement.

9.1.3.1 *Flipping Coils* In this method a long coil (typically 1 m longer than the ID length) is rotated in $90°$ steps within the ID and the integrated voltage recorded (Fig. 9.3). To avoid complicated electrical contacts the coil only completes one revolution and then reverses its direction to return to its starting position (again taking data in steps on the return journey). The coil generally moves relatively slowly, a few seconds per data point. The integrated vertical field can be deduced from the rotation between $0°$ and $180°$ and the integrated horizontal field from the result between $90°$ and $270°$. If the data is recorded in $90°$ steps then both integrals can be readily calculated from the one data set and it also allows for some redundancy in the data to check for reproducibility.

Rewriting (9.1), for the vertical field case, for a coil of length L and width W gives
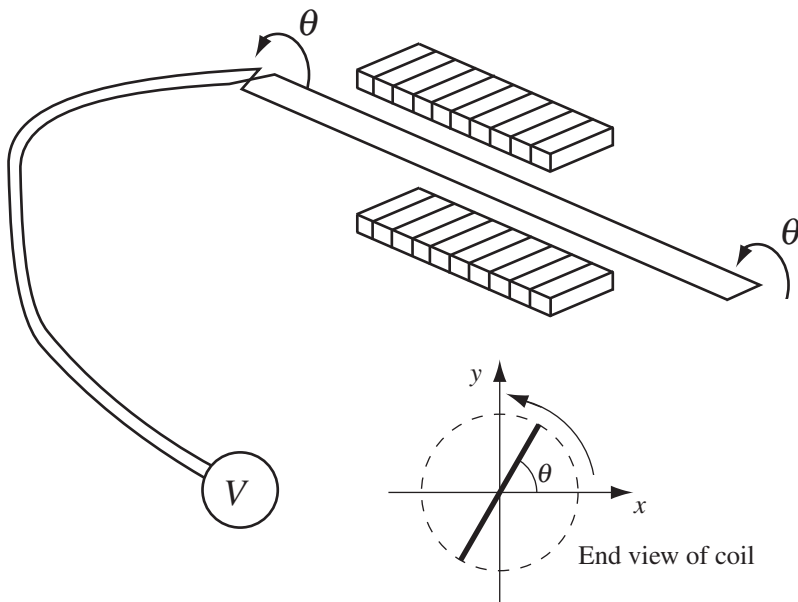
FIG. 9.3. Sketch of a flipping coil system.

$$\int V dt = -N \int_{-L/2}^{L/2} \int_{-W/2}^{W/2} B_y dx ds \approx -NW \int_{-L/2}^{L/2} B_y ds$$

assuming that B_y does not depend upon x (i.e. W is small). Then, the first vertical field integral is given by (see Section 7.5)

$$I_y = -\frac{\int V dt}{NW} \ .$$

Values for the integrated multipoles mentioned earlier can also be found by measuring the field integrals as a function of x. In this case the skew components are found from horizontal field integrals and normal components from vertical field integrals,

$$I_x(x) = \sum_{n=1}^{\infty} A_n x^{n-1}$$

$$I_y(x) = \sum_{n=1}^{\infty} B_n x^{n-1} \ .$$

In practice, the field integral data is measured as a function of x by simply translating the coil centre to the required setting. It is then fitted to a polynomial function with coefficients corresponding to the dipole, quadrupole, sextupole etc.

The coil itself is simply stretched between two formers that define the coil width (typically 10 mm). The alternative of mounting the coil to a long, solid former is not used because the coil geometry would then be less well known. Even so, the error introduced due to the width of the coil being difficult to measure accurately could easily be of the order of 1%. Fortunately, since the requirement is usually to set the integrals to zero, this is not a significant drawback for this technique. To make the coil it is usual to use a single turn of Litz wire, which is itself made of many thin strands ($\sim 40 \ \mu$m diameter) of conductor. The individual strands are then connected together in series to form a coil of typically 20 or 30 turns.

The system performance of flipping coils measuring complete IDs is very impressive. Reproducibilities of 3 μTm have been achieved [160], which is about an order of magnitude better than what a scanning Hall probe can manage. When field integrals can be resolved to this level it is necessary to take into account the Earth's magnetic field. A typical value for this field is 50 μT, so over 1 m it will generate about 50 μTm.

Often a flipping coil system is combined with a Hall probe bench so that both point by point and fast integral measurements can be made on the same ID without the need to move it to a new location and resurvey the magnet. The coil is mounted at each end onto a remotely operated xyz stage that has an additional rotation table mounted onto it. Again μm resolution position encoders are used for the translation motion and for the rotation table angular encoders that can resolve 0.001° are readily available. These motion stages are again generally mounted onto synthetic granite blocks to reduce vibrations.

9.1.3.2 *Stretched Wires* This technique is based upon the concept of not moving a complete coil within a magnetic field but only part of a coil. One side of a coil is stretched straight between two supports and held within the magnetic field (Fig. 9.4). The return path of the coil is taken well away from the magnetic field and is kept stationary throughout. The stretched section is then translated within the magnetic field, cutting the flux and so inducing a voltage within the coil. This idea was first applied to quadrupoles [161] but was later implemented for ID measurements [159, 162].

If the stretched wire, of length L, is translated horizontally by a distance, Δx, (Fig. 9.5(a)) then the change in the magnetic flux is

$$\Delta\Phi = \int_{-L/2}^{L/2} \int_{a}^{a+\Delta x} B_y dx ds \sim \Delta x \int_{-L/2}^{L/2} B_y ds \ .$$

Clearly the above assumes that the magnetic field is not varying with the horizontal position. The first field integral is then given by
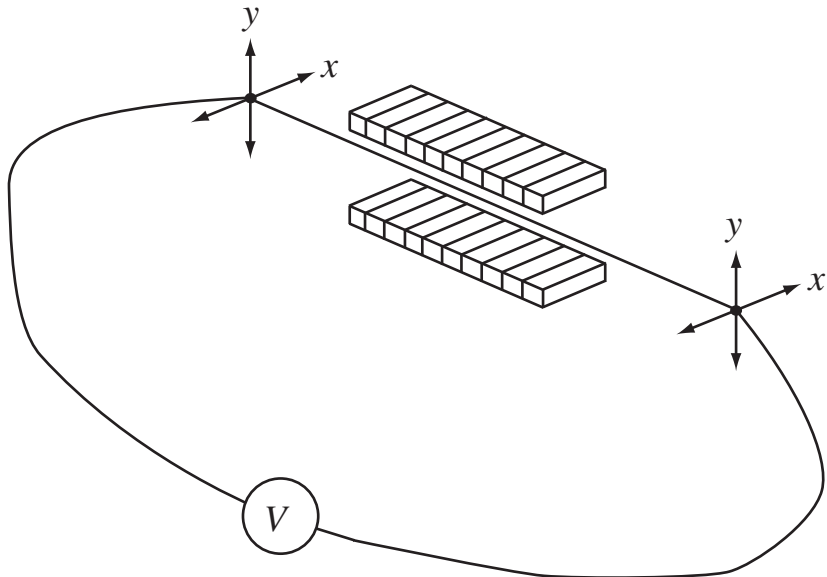
FIG. 9.4. Sketch of a stretched wire system.

$$I_y = -\frac{\int V\,dt}{N\Delta x} \ .$$

A similar equation can be generated for I_x that depends upon a vertical translation Δy. The advantages of this technique over the flipping coil are that the translations, Δx or Δy, are not set by any fixed coil dimension but can be selected for each case as a compromise between signal levels and spatial resolution for the integral measurements. Also, with modern motors and encoders, it is relatively simple to translate the wire with μm accuracy *over the full length of the wire*. The systematic error term in the flipping coil system due to the width of the coil not being well known over its length has effectively been removed. One further point, that also applies to the flipping coil system, is that precise synchronization between the translation stages at each end of the wire is not necessary. It is enough to set the start and end points accurately.

Another feature of the stretched wire system is the ability to measure the second field integral. In this case the two ends of the wire are translated in opposite directions (Fig. 9.5(b)). In this case then the change in the magnetic flux is given by

$$\Delta\Phi = \int_{-L/2}^{L/2}\int_{-s\Delta x/L}^{s\Delta x/L} B_y\,dx\,ds \sim \frac{2N\Delta x}{L}\int_{-L/2}^{L/2} sB_y\,ds \ .$$
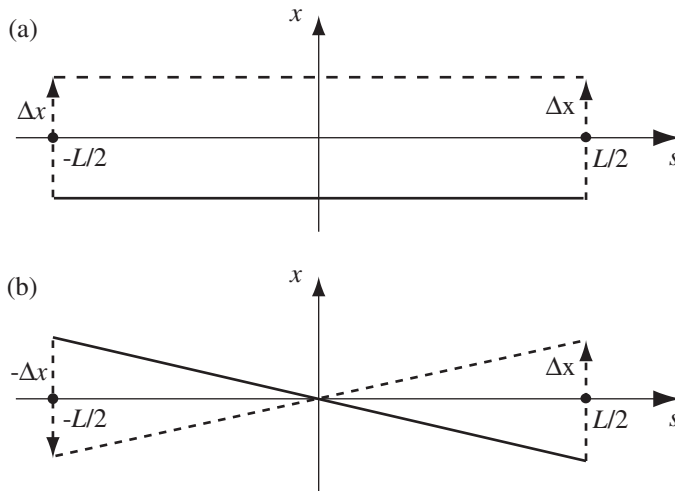
FIG. 9.5. Wire translations used in the stretched wire system to measure (a) first field integral and (b) second field integral.

Again assuming that the vertical field does not depend on x. This integral term is proportional to the (negative) position of the electron beam back projected to the centre plane of the magnet (eqn (7.4)) and is related to the second field integral using a simple geometrical argument by

$$II_y = \frac{LI_y}{2} - \int_{-L/2}^{L/2} sB_y ds \ .$$

Therefore the second field integral is given by

$$II_y = \frac{LI_y}{2} + \frac{L}{2N\Delta x} \int V dt \ .$$

In practical terms, it is usual to make a coil with $20 - 30$ turns again using Litz wire. The tension in the wire can have a significant effect on the repeatability of measurements and it must be adjusted empirically until good reproducibility is achieved. Typical values quoted for the standard deviation in a series of repeat measurements are $1.5 - 2 \ \mu$Tm for the first field integral and $0.7 - 1 \ \mu$Tm^2 for the second field integral [159, 162]. The wire is usually translated by up to 10 mm in a few seconds. The hardware involved in setting up a stretched wire system is identical to that used for the flipping coil bench, except it does not require any rotation stage. Therefore, both techniques can be available with the same bench by simply changing the coil arrangement. However, experience seems to show that once a particular system is up and running successfully it is not tampered with without a very good reason!
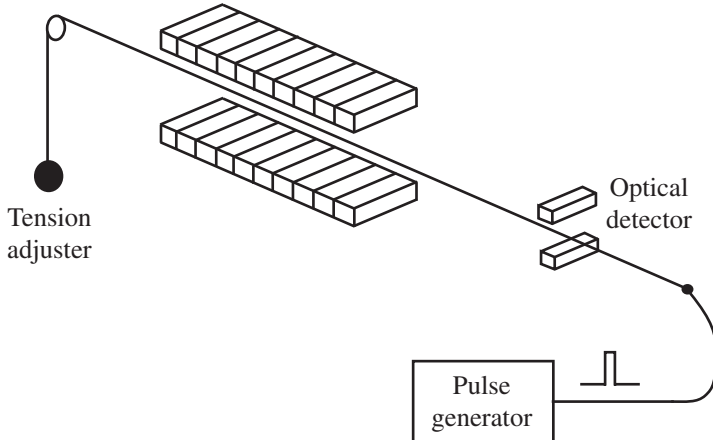
FIG. 9.6. Sketch of a pulsed wire system.

One interesting benefit of this technique is that the harmonic coil method can be easily implemented by simply programming a circular path into the wire translation stages. As a consequence the harmonic method is now used to measure IDs at some laboratories [159, 162]. It is also worth noting that the technique described for measuring the second field integral can also be equally applied to a flipping coil system that has one end rotated by 180° with respect to the other end at the start of the measurement so that the coil is twisted and maps out a similar shape as that of the stretched wire (Fig. 9.5(b)).

9.1.4 *Pulsed Wires*

This is another technique that is based upon a simple concept that requires care in setting up to get the best performance. A wire is stretched through the magnet and a short current pulse (a delta function) is passed through it (Fig. 9.6). The current impulse passing through the magnetic field causes a wave to travel along the wire. An optical sensor that can detect the motion of the wire is placed outside the magnetic field region and this measures the position of the wire as a function of time. It can be shown that the amplitude of the wire at the sensor, $x(t)$, for a current pulse, Idt, is proportional to the integral of the field versus position along the wire [163]

$$x(t) = \frac{Idt}{2vP} \int_0^{vt} B_y ds \ ,$$

where $v = \sqrt{T/P}$ is the velocity of the acoustic wave, P is the linear density of the wire, and T is the wire tension. In other words, the measured wire amplitude with time is directly proportional to $I_y(s)$ or the angular deflection experienced by an electron as it travels through the magnet.

Furthermore, if a current step is applied to the wire (the integral of a delta function), rather than a pulse then the measured wire amplitude is now proportional to the second field integral $II_y(s)$ [163]

$$x(t) = \frac{I}{2v^2P} \int_0^{vt} \int_0^{s'} B_y ds' ds \ .$$

So this technique can either provide a measure of the electron beam displacement or angle through the magnet depending upon the current pulse shape selected. Of course, it is possible to detect either horizontal or vertical field integrals by simply changing the orientation of the detector. Typical values for the current pulse are a few Amps over some 10's of μs (for the first integral measurement). The peak deflection in the wire is of the order of 100 μm and the wave velocity is typically 300 m/s though of course these values vary with the wire selected. Beryllium-Copper alloy wire seems to be favoured due to its high tensile strength (and so less sag) and also good conductivity [164, 165].

The wire length has to be quite a bit longer than the magnet under test so that reflections from the wire mounts do not interfere with the first pass data from the magnet. Wire sag can then be quite an issue since the wire will not be perfectly aligned along the electron beam axis. Even BeCu wire can sag by $\sim 10~\mu$m over 1 m or $\sim$1 mm over 10 m [163]. This particular issue is not limited to this technique alone, it is common to all suspended coil and wire systems. Another effect that is worsened with wires of longer length is that of dispersion. The velocity of the waves in the wire is a function of their wavelength and so even the ideal signal will degrade with distance travelled, as the different Fourier components in the signal will arrive at slightly different times. The effect of this dispersion has been negligible in some experiments [164] but significant in others [165], although it has been demonstrated that increasing the tension in the wire can reduce this problem. Other effects caused by imperfections in the wire have been alleviated by choosing a thicker wire (250 μm) [165].

Even though this technique does not provide a calibrated measurement of the electron trajectory or angle through the ID it does still possess some very definite advantages over the other techniques described. First, by its nature it is a very fast method and it is easy to record hundreds of signals for averaging purposes. Second, it is able to be implemented in magnets that have very restricted apertures (sub mm gaps) and with no side access. Third, it will highlight local trajectory errors and can be used to accurately determine the magnetic axis for survey and alignment purposes [166].

Again, the pulsed wire method requires much of the hardware that the flipping coil system also uses, in particular the remotely operated xyz tables mounted on stable plinths. Of course, it additionally requires the pulsed current source and the optical detector but in principle it could be implemented on the same basic bench as the flipping coil or stretched wire system.

9.1.5   *Helmholtz Coils*

This technique is not used for measuring complete magnet assemblies but rather individual permanent magnet blocks prior to assembly. This is important as the measured magnetic information for each block is often used to decide the exact location of each individual block in the complete magnet arrays. This idea of *block sorting* will be treated in more detail later in this chapter.

Helmholtz coils consist of a pair of circular coils of radius, R, made up of N turns that are separated by a distance, S (Fig. 9.7). If this separation distance is close to the value for the radius then the magnetic field, B, near the centre of the coil pair, generated by a current I in each coil, is uniform and parallel to the coil axis [167].

$$B = \frac{\mu_0 N I}{R G} \qquad (9.2)$$

where G is a geometric constant for the coil pair, given by [168]

$$G = \left(1 + \left(\frac{S}{2R}\right)^2\right)^{3/2} \quad .$$

So in the ideal case, where $S = R$, we have that $G = (5/4)^{3/2} = 1.3975$.

To measure the magnetization along one axis of a magnet block the block is placed in the central region of the (unpowered!) coils with the desired magnetization direction parallel to the coil axis and so pointing at one coil. Then the integrated voltage induced in the coils is measured as the block is rotated (sometimes by hand) by 180° so that it is again parallel to the coil axis but pointing at the opposite coil. All three magnetization direction strengths can be obtained by performing three measurements each starting with different block orientation. Of course repeated measurements, with different block alignments can be used to improve the accuracy of the data and also to eliminate systematic effects due to imperfect alignment of the block with the coil axis.

The integrated voltage due to a block of magnetization, M, and volume, U, being rotated by 180° is given by [169]

$$\int V \, dt = \frac{2 N M U}{R G} \quad .$$

The selection of the coil radius is related to the anticipated block dimensions to be measured. A larger radius will ensure that the field homogeneity range covers the entire block but will give a smaller signal to detect. For blocks with longest dimension of around $50 - 100$ mm, the coil radius selected is typically $30 - 60$ cm. The number of turns is usually of the order of $500 - 1000$ using insulated copper wire of diameter $0.1 - 0.3$ mm. Clearly the finite dimensions of the manufactured coil will place some uncertainty as to the correct values to use for the radius and separation in the calibration constant, G. Mean values for S
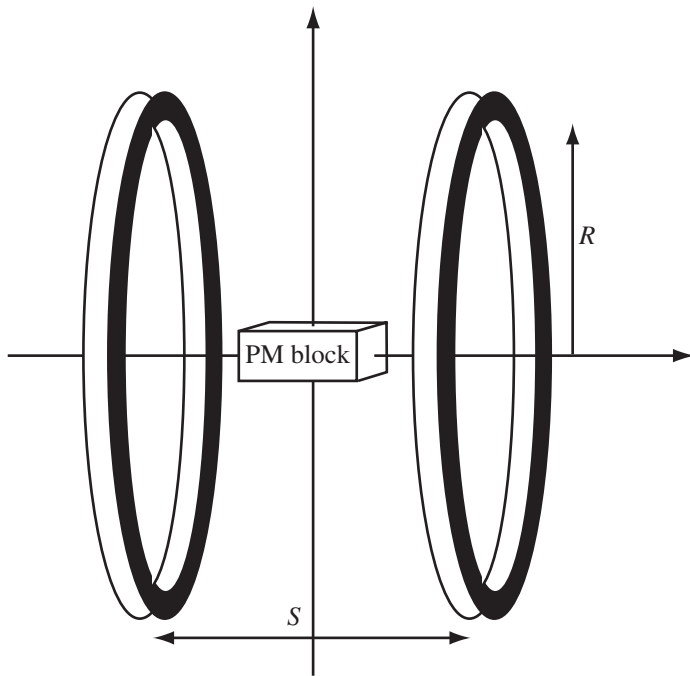
FIG. 9.7. Sketch of a pair of Helmholtz coils.

and R can be measured but an alternative method is to pass a known current through the coils and to record the magnetic field produced at the centre of the coil pair. The constant, RG, can then be found using (9.2). However, the actual magnetic field is very small to measure (a few mT) and so the accuracy of this measurement may give a larger error in the geometric constant than relying upon the measured dimensions.

9.2   Improving Insertion Device Performance

The motivation for making detailed magnet measurements of insertion devices is not just to confirm the magnet design but also to detect and correct minor imperfections. The ID will then give the best possible performance in terms of minimizing the disruptive effect on the electron beam and providing the optimum spectral output. Before we can make corrections to the magnetic field we have to have some means of assessing the magnetic quality of an ID. First we can say that the first and second field integrals should be zero along the beam axis so that there is no net effect on the electron beam orbit. Second, since undulator radiation is a constructive interference effect the phase advance between successive poles should be equal to π in an ideal magnet (2π per period). Calculating the deviation of the radiation phase from this ideal along the length of the magnet is a good measure of the radiation quality that will be produced by

the undulator and this is now a common technique for comparing the magnetic quality of undulators.

9.2.1   *Phase Error*

Traditionally undulator quality was measured in terms of the magnetic field deviation from the ideal value, in particular the rms peak field error was often used as a figure of merit. However, since the electron trajectory is strongly dependent upon the *order* in which it encounters the field errors and not just the spread in the errors, this quantity is poorly correlated with the spectral performance of an undulator [170, 171]. A quantity that has been shown to be well correlated with the spectral output is the rms phase error, σ_Φ [172, 173].

The radiation phase, Φ, is given by

$$\Phi(s_1) = \frac{\pi}{\lambda} \left(\frac{s_1}{\gamma^2} + \int_{-\infty}^{s_1} \dot{x}^2(s) ds \right) \ ,$$

where λ is the radiated wavelength and $\dot{x}$ is the electron angle (dx/ds) from (7.2). The evolution of the phase for an ideal undulator is shown in Fig. 9.8. The phase errors are defined as the deviations from the ideal values at the points where the tangent to the trajectory are parallel to the longitudinal axis $(\dot{x} = 0)$. However, since the phase varies slowly around the poles, the phase errors can instead be evaluated at the nominal pole positions as this is an adequate measure of the phase error for each emission point [172]. The underlying linear variation with position in the phase can be subtracted as this corresponds exactly to the $2\pi/$period phase advance, indeed this gradient effectively *defines* the output wavelength of the undulator. The phase errors will then be scattered randomly about zero and the rms value of these errors, σ_Φ, is able to be used as a figure of merit for the undulator quality. The phase errors at the poles of an undulator with random field errors included is shown in Fig. 9.9 and the corresponding electron trajectory is shown in Fig. 9.10. The field model has been constructed from a series of alternating half sine waves with a 0.5% rms random amplitude variation and then the trajectory has been corrected so that the electron exits the undulator on-axis by applying a static magnetic field along the full length of the device. In practice the phase errors at the ends of the magnet can be disproportionately large, even for ideal magnets, and for this reason it is conventional to ignore the first and last two or three periods when calculating σ_Φ [173]. In the example of Fig. 9.9, σ_Φ is 8.0 degrees.

The relevance of the rms phase error is that it is well correlated with the intensity of the output radiation, larger values mean lower intensity at the harmonics (because the photon energy width of the harmonics widens and not because the electrons are no longer emitting radiation). The phase error we have calculated has been for the first harmonic and so it is three times larger for the third harmonic and so on. For this reason the effect of this error increases with each harmonic. This is why it was felt that during the design of the first third generation light sources that undulators would not be useful beyond about the
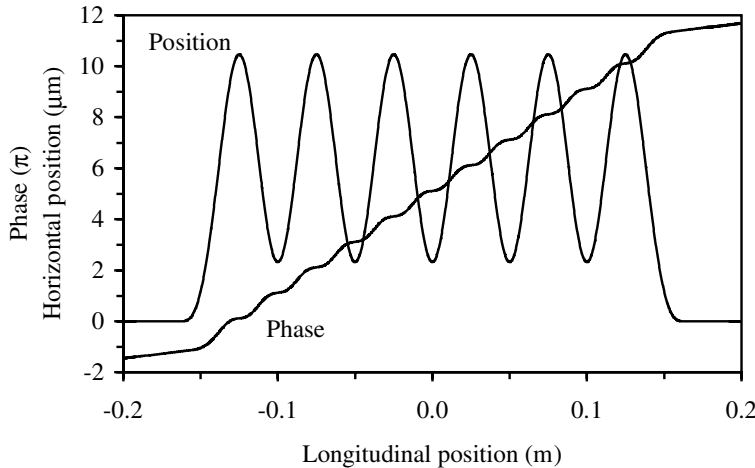
FIG. 9.8. Graph showing the radiation phase as a function of position in an ideal undulator with 5 periods. The undulator period is 50 mm, its K value is 3 and the phase has been evaluated for a 3 GeV electron trajectory that is also shown. Note that the phase is given in units of π.

fifth harmonic. It is to the credit of the undulator experts that, by implementing clever magnet sorting and shimming techniques, they have been able to reduce the phase errors to such an extent that operation of up to at least the 15th harmonic is now relied upon by the latest synchrotron light sources.

The ratio of the peak intensity for the odd harmonics on-axis to the ideal undulator, R, is given by [172]

$$R = \frac{(1 - e^{-n^2\sigma_\Phi^2})N + e^{-n^2\sigma_\Phi^2}N^2}{N^2} \sim e^{-n^2\sigma_\Phi^2} \ ,$$

where n is the harmonic number and N is the number of periods. This function is plotted for the first harmonics in Fig. 9.11.

The process by which an ID with low phase error is produced is usually carried out in two stages, especially for pure permanent magnet devices where linear superposition of the fields simplifies modelling. The first stage is to measure each magnet block individually, either in terms of magnetization strengths, field integrals, or by taking point by point field measurements. Then, this data is used to select the exact location of each block so as to optimize the quality of the final device, this stage is called *sorting*. The second stage is to measure the field of the full device and then to improve it by tweaking it, either by swapping magnet blocks around, making small changes to block positions (e.g. raising a block slightly) or by placing thin ferromagnetic strips or shims onto the magnet array surfaces. This second stage is generally referred to as *shimming* though strictly this term only applies to the use of shims of course.
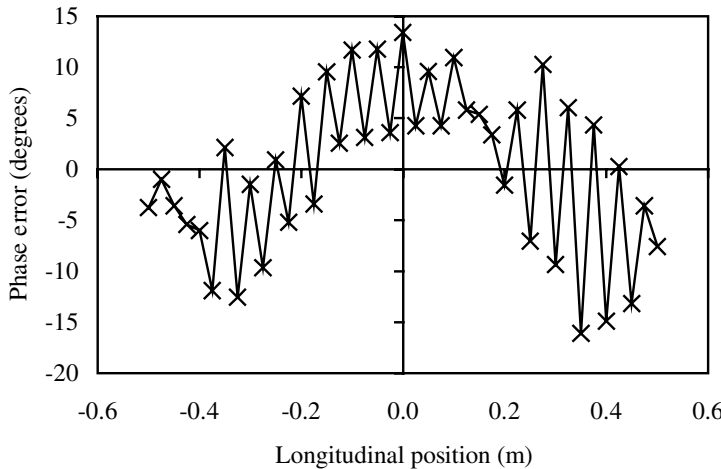
FIG. 9.9. Graph showing the phase error in degrees at the poles of a 20 period undulator with random 0.5% normal distribution field errors included. The undulator period is 50 mm, its K value is 3 and the phase has been evaluated for a 3 GeV electron whose trajectory is shown in Fig. 9.10.
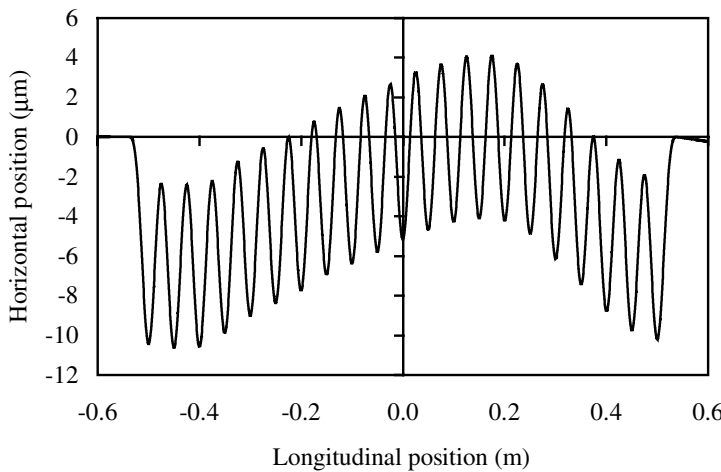
FIG. 9.10. Graph showing the trajectory of a 3 GeV electron through the 20 period undulator with field errors included as for Fig. 9.9.

9.2.2 *Block Sorting*

The problem of block sorting belongs to the class of problem called *combinatorial minimization* where we want to minimize some function for which there is a finite set of possible combinations. In our case we want to minimize the phase
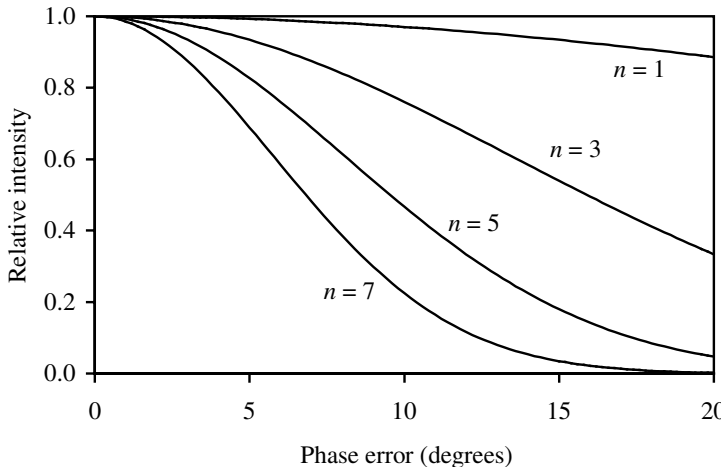
Fig. 9.11. Graph showing the ratio of the on-axis intensity to the ideal as a function of rms phase error for the first four odd harmonics.

and trajectory errors by choosing the best arrangement of magnet blocks. Given enough time we could simply try every possible combination and choose the best one (the global minimum). Of course the snag is that there are so many combinations that there is no way that all of them could be evaluated. We need some method then of finding a good solution in a reasonable time. It is important to realize that whatever algorithm we adopt to find our solution it will find a *good* solution (a local minimum in the function) but it will not necessarily find the *best* solution. Given that this sort of problem is not one that is unique to IDs it is no surprise that standard mathematical routines have been adopted and applied to magnet sorting. The most common technique adopted is that of *simulated annealing* or variations of it [174–176] though others have successfully demonstrated the use of *genetic algorithms* as well [177, 178].

9.2.2.1 *Simulated Annealing* As its name suggests, simulated annealing [179, 180] is analogous to the physical process of annealing or slow cooling that allows atoms the opportunity to find a low energy state such as when liquids crystallize or metals anneal. The alternative of fast cooling or quenching will leave materials in a higher energy state because the atoms will not have had the chance to 'explore' their neighbourhood to find the low energy positions.

So, simulated annealing is an algorithm which has a parameter that corresponds to a 'temperature', T, and this parameter reduces slowly with time and the number of iterations. The algorithm uses a similar concept to the Boltzmann distribution, where the probability of a particular particle having a certain energy, E, depends upon $e^{-E/kT}$ where k is the Boltzmann constant. The algorithm starts with a random configuration (of blocks, in our case) and a high temper-

ature and the aim is to minimize the 'energy' (our undulator quality factor). Random block position changes are then tried and if they give a lower energy they are *always* kept, if not they are *sometimes* kept. The decision as to whether or not to retain a new configuration that gives a higher energy is taken by comparing a random number with a form of the Boltzmann probability. So, at high temperatures the probability of retaining these higher energy configurations is high but as the system cools the probability reduces, although it is still finite. The algorithm naturally explores a wide range of the configuration space at high temperature and tends to make the 'big' decisions that have the greatest effect upon the energy. As the system cools, smaller refinements occur that cause the algorithm to home in on a particular local minimum.

One crucial input to the simulated annealing (or any other) algorithm is the definition of the energy or cost function. This defines what should be minimized and also gives the relative importance of different contributors to the function. It is not enough to simply minimize the rms phase error because the electron trajectory may then not be acceptable. It is better to make the function a sum of all the terms that are important and then to give each term a particular weighting factor. For instance, the sum is likely to include as a minimum the rms phase error and the first field integrals on-axis in both planes. However, it could also include the first and second field integrals at different transverse positions, the trajectory straightness, and also the rms peak field variation.

9.2.3 *Magnet Shimming*

Shimming is a general term applied to the final stage of tweaking the assembled insertion device so as to optimize the magnet performance. Sometimes magnet blocks are replaced or their orientation flipped [181], sometimes a block is raised by a tenth of a mm or so to slightly adjust the field strength locally or, more commonly, thin ferromagnetic shims are attached to the top surface of the magnet arrays in a few key positions. As this last technique is the most common, that is the one that shall be described in some detail though the principles associated with the other two methods are broadly similar.

There is quite a bit of freedom available with the use of shims. The thickness of each shim can be selected (in a few discrete steps) to be between 0.05 and 0.5 mm typically. The width and length of the shims are also free parameters, as well as the exact location on the array and of course the number of shims to use. Given all this freedom it might sound like an almost impossible task to choose these parameters for an unspecified number of shims. In fact, it is not so daunting as it might appear. The first step is to generate a 'signature' for each shim option, usually by using a magnet simulation code but also sometimes by direct measurement [175]. The signature is simply the change in the magnetic fields due to placing a particular sized shim in a specific location. A number of signatures are generated for the possible shim options in certain discrete steps in dimension, for example, as well as different possible positions on the array. Figure 9.12 is a sketch of an array with shims attached. These show the standard shim
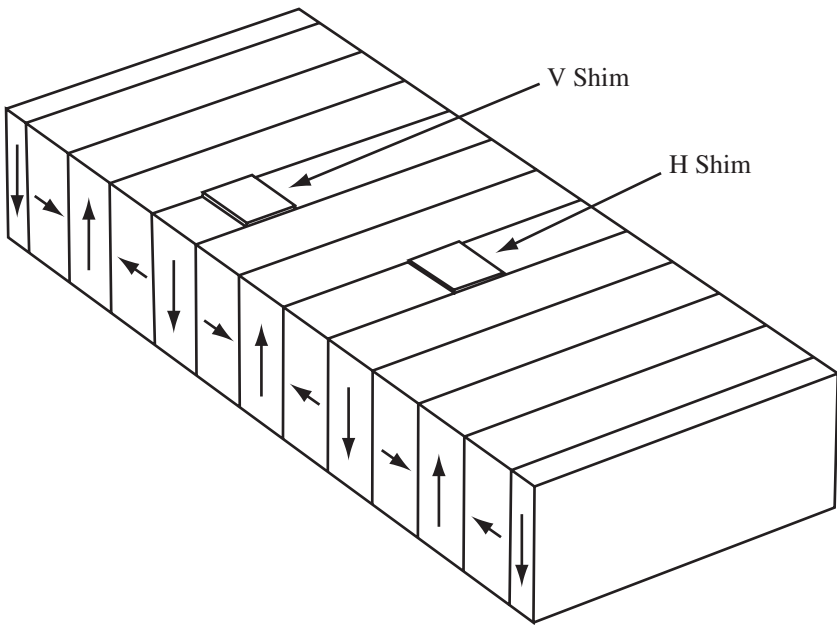
FIG. 9.12. Sketch of an undulator array with shims attached.

locations; either placed centrally (in the longitudinal direction) on a vertically magnetized block (a V shim) or a horizontally magnetized block (an H shim). The transverse position is still a free parameter. The V shim is an obvious choice as this will enhance the field locally under the pole, the H shim is more subtle. The effect of the two shims on the vertical magnetic field as a function of the longitudinal position is shown in Fig. 9.13. As expected the V shim increases the field locally and it also has a small integrated field effect $(\Delta \int B_y ds)$, in this case of about 80 μTm. The H shim has an antisymmetric signature so that it has an integrated field change of zero. However, by slightly adjusting the path length taken by the electron it will affect the phase without changing the first and second field integrals or the trajectory straightness. So, the V shims will adjust all the quality factors of interest, such as the first and second field integrals, the phase, the local peak field, and the trajectory straightness whereas the H shims can adjust the phase independently. A similar approach can be applied to the hybrid case [182].

Shim signatures for the transverse direction are shown in Figs. 9.14 and 9.15. Here we can see that both the horizontal and vertical fields are adjusted simultaneously and that this adjustment varies with the transverse position of the shim. This transverse information is needed to correct the field integrals so that they are flat as a function of transverse position to minimize the higher order multipoles that could affect the electron beam dynamics (see Section 9.1.3.1).
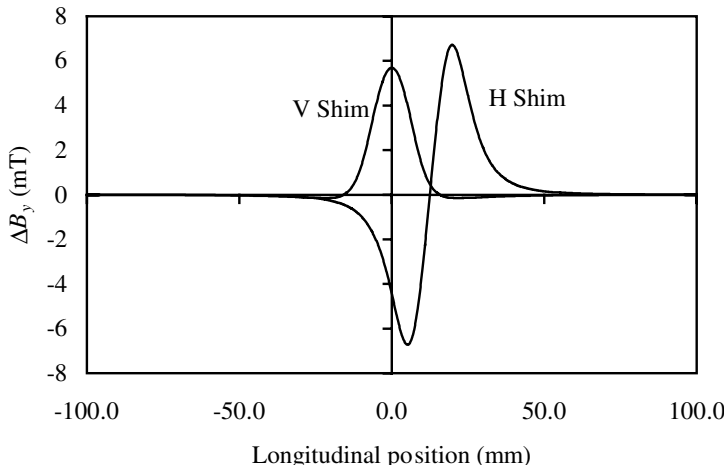
Fig. 9.13. Graph showing the effect of a shim placed on top of either a vertically magnetized block (centre at 0 mm) or a horizontally magnetized block (centre at 12.5 mm). The undulator period is 50 mm and the magnet gap is 20 mm. The shim is 0.5 mm thick, 10 mm wide and is the length of a single magnet block (12.5 mm).

Once the shim signatures have been generated then the next step is to again use an optimization algorithm, often simulated annealing as for the block sorting, to select the optimum shim sizes and locations. This optimization may be split into two stages, the first being to optimize the V shim locations, which affects all of the parameters in the cost function. The second is then to optimize the H shim locations so as to fine tune the phase error only. An interesting point to note is that since the H shim shunts a small amount of flux from the H block it reduces the field level at both poles. As a consequence this final stage of applying just H shims will always reduce the average peak field level of the undulator. One added complication that has not been mentioned yet is that everything changes as a function of gap! So, the signatures and the optimization should also try to take this into account.

Excellent results have been obtained through the application of shims. Field integrals and multipoles can be controlled [183], phase errors below 1° have been achieved [184], though a more typical target value would be 2 or 3°. The fact that the phase error can now be adjusted to these low levels ensures that its effect on the intensity of the undulator harmonics is no longer the dominating factor. The effect of the electron beam emittance and energy spread is now more detrimental at the high harmonics. For example, an undulator with a phase error of between 0.8° and 2.1° over a gap range of 20 – 50 mm was predicted to emit intensities of about 80% of the ideal theoretical result even up to the 21st harmonic [184]. However, the electron beam emittance and energy spread are far more harmful
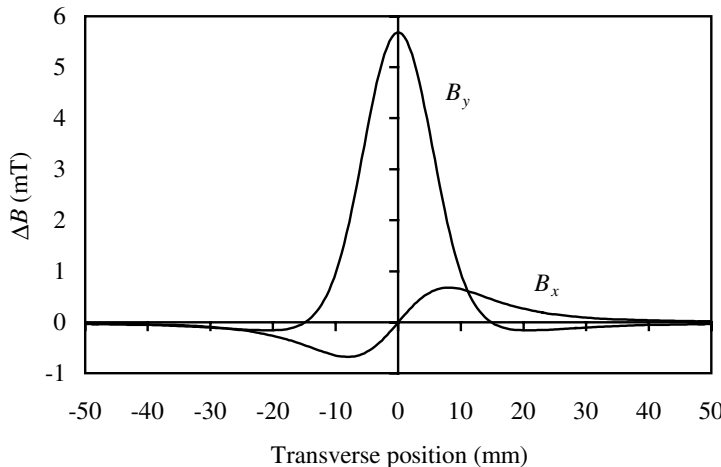
FIG. 9.14. Graph showing the effect of a shim placed on top of a vertically magnetized block on both the horizontal and vertical magnetic fields in the transverse plane. The undulator and shim parameters are as for Fig. 9.13 and the magnet block width is 60 mm.
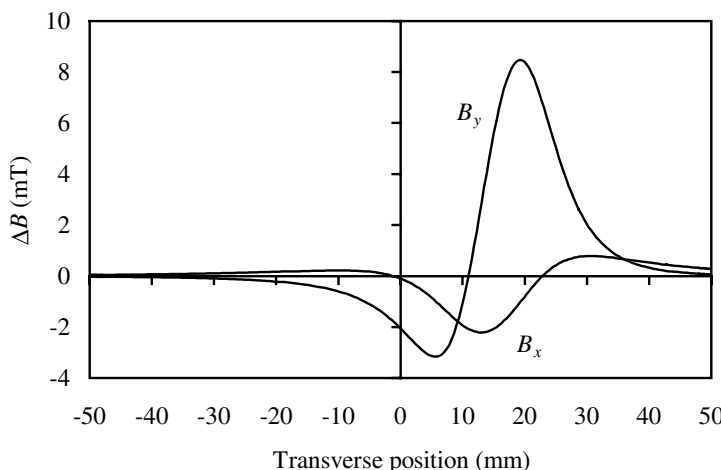
FIG. 9.15. As for Fig. 9.14 except the shim is displaced 15 mm in the transverse direction.

than this, in this example, having roughly equal effects upon the ideal intensity in this case, and they reduce the predicted intensity to only 4% of the ideal at the 21st harmonic.

The Effect of Insertion Devices on the Electron Beam

It is no surprise that the electrons that emit synchrotron radiation (SR) by interacting with insertion devices (IDs) suffer some consequences. Of course they will lose some fraction of their energy, which needs to be replaced in a storage ring by an accelerating cavity, but there are more subtle effects also at work. In this chapter, we will try to look at how the periodic fields of an ID can disrupt a beam of electrons, sometimes with positive results and sometimes with negative results.

This chapter assumes a certain knowledge of electron beam dynamics, especially in regard to storage rings, since it is too big a subject to possibly cover here. There are several texts available that cover this subject at the introductory level [18] and also to some depth [185, 186] for the reader who has a particular interest in this area.

10.1 The Effect on the Synchrotron Radiation Integrals

There are a number of well known electron beam parameters, such as the emittance, bunch length, and the energy spread, that are determined by equilibrium processes in a storage ring that involve the emission of synchrotron radiation. The balance between damping by longitudinal acceleration in the cavities and excitation by the quantum emission of synchrotron radiation is all important for electron storage rings. The fundamental electron beam properties are thus determined to some extent by the bending magnets where SR is always emitted. Since IDs will increase the amount of SR power emitted it is clear that they must disrupt the equilibrium and therefore change these electron beam parameters.

Five simple equations are used by accelerator physicists to determine these radiation dependent beam properties and these are called the *synchrotron radiation integrals* [185]. We can look at how much an ID will change these integrals and hence how much the electron beam parameters will change when the ID is introduced into the storage ring. First, we will assume the standard planar ID with a sinusoidal field variation.

$$B = B_0 \sin\left(\frac{2\pi s}{\lambda_u}\right) \quad .$$

Expressing this in terms of bending radius, ρ, instead of magnetic field (since the synchrotron radiation integrals are generally expressed with $1/\rho$ terms), we get

$$\frac{1}{\rho} = \frac{1}{\rho_0} \sin\left(\frac{2\pi s}{\lambda_u}\right) \quad .$$

The integrals also refer to a quantity called *dispersion*, η, which is a measure of the trajectory that will be taken by electrons that are not at the correct energy. This is most easily understood by considering the path taken by electrons of different energy in a dipole magnet. It is clear that electrons with a higher than nominal energy will take a circular path with a larger radius and those with a lower energy will follow a tighter radius. In other words the electron beam becomes *dispersed* in transverse position to an extent determined exactly by the electrons energy and the dipole field. This effect is of course used in spectrometer magnets to measure electron beam energy. The trajectory deviation from the nominal value is simply given by the product of the dispersion and the relative electron energy deviation, $\eta \Delta E/E$.

Since electrons travelling through IDs will take different trajectories depending upon their energy these magnets will themselves 'generate' dispersion, which is the so-called *self dispersion*. The trajectory taken has a simple dependence upon the electron energy (3.3) and the dispersion generated by the ID is simply $-x$. Similarly the rate of change of dispersion, $\dot{\eta} = d\eta/ds$, is given by $-\dot{x}$. This can be combined with the dispersion that is present without the ID installed, η_0 and $\dot{\eta}_0$ to give the general result for a straight section that contains an ID,

$$\eta(s) = \eta_0 + \dot{\eta}_0 s + \frac{\lambda_u^2}{4\pi^2 \rho_0} \sin\left(\frac{2\pi s}{\lambda_u}\right)$$

$$\dot{\eta}(s) = \dot{\eta}_0 + \frac{\lambda_u}{2\pi \rho_0} \cos\left(\frac{2\pi s}{\lambda_u}\right) \quad .$$

The first three synchrotron radiation integrals are defined as

$$I_1 = \int_0^C \frac{\eta}{\rho} ds$$

$$I_2 = \int_0^C \frac{1}{\rho^2} ds$$

$$I_3 = \int_0^C \frac{1}{|\rho^3|} ds \quad ,$$

where C is the circumference of the ring, and so the changes in these integrals due to the introduction of the ID of length L can now be calculated:

$$\Delta I_1 = \int_{-L/2}^{L/2} \frac{\eta}{\rho} ds = \frac{L\lambda_u^2}{8\pi^2 \rho_0^2}$$

$$\Delta I_2 = \int_{-L/2}^{L/2} \frac{1}{\rho^2} ds = \frac{L}{2\rho_0^2}$$

$$\Delta I_3 = \int_{-L/2}^{L/2} \frac{1}{|\rho^3|} ds = \frac{4L}{3\pi\rho_0^3} \quad.$$

For the last two integrals we have to do a little more work. The I_4 integral contains a focussing term, k, which is given by [25]

$$k = -\frac{e}{\gamma m_0 c} \frac{dB_y}{ds} \dot{x} = \frac{1}{\rho_0^2} \cos^2\left(\frac{2\pi s}{\lambda_u}\right) \quad.$$

The fourth integral is defined as

$$I_4 = \int_0^C \left(\frac{\eta}{\rho^3} - \frac{2k\eta}{\rho}\right) ds$$

and so the change in I_4 is

$$\Delta I_4 = \int_{-L/2}^{L/2} \left(\frac{\eta}{\rho^3} - \frac{2k\eta}{\rho}\right) ds = \frac{3L\lambda_u^2}{32\pi^2 \rho_0^4} - \frac{2L\lambda_u^2}{32\pi^2 \rho_0^4} = \frac{L\lambda_u^2}{32\pi^2 \rho_0^4} \quad.$$

The fifth integral, I_5, contains a quantity that is called the dispersion H function that depends upon the so-called Twiss parameters of the storage ring (α, β, and γ). These parameters are set by the arrangement and strength of the dipole and quadrupole magnets (often referred to as the magnet lattice) and define the transverse motion of the electron beam around the ring. Note that they are not related to the β and γ parameters that are used throughout this book for the relative velocity and energy of the electron, though unfortunately, by convention, they share the same symbols. The H function is defined as

$$H = \gamma_x \eta^2 + 2\alpha_x \eta\dot{\eta} + \beta_x \dot{\eta}^2$$

and the fifth synchrotron radiation integral as

$$I_5 = \int \frac{H}{|\rho^3|} ds$$

There is no general solution for the change in I_5 due to an ID but we can derive an approximate result for the case where the dispersion without the ID installed in the straight is zero. This is actually a common situation for all third generation storage rings; the dispersion is deliberately set to zero or close to zero in the straight sections. In this case then the $\beta_x \dot{\eta}^2$ term dominates and

$$\Delta I_5 \simeq \int_{-L/2}^{L/2} \frac{\beta_x \dot{\eta}^2}{|\rho^3|} ds \simeq \hat{\beta}_x \int_{-L/2}^{L/2} \frac{\dot{\eta}^2}{|\rho^3|} ds$$

$$= \frac{\hat{\beta}_x L \lambda_u^2}{15\pi^3 \rho_0^5}$$

where $\hat{\beta}_x$ is the average value of β_x along the length of the ID.

10.1.1   Beam Emittance

The electron beam emittance is given by

$$\epsilon = C_q \gamma^2 \frac{I_5}{I_2 - I_4} \quad,$$

where C_q is a constant (3.83×10^{-13} m). So the fractional change in emittance due to the ID is given by

$$\frac{\epsilon_{ID}}{\epsilon} = \frac{(I_5 + \Delta I_5)/((I_2 + \Delta I_2) - (I_4 + \Delta I_4))}{I_5/(I_2 - I_4)} = \frac{1 + \Delta I_5/I_5}{1 + (\Delta I_2 - \Delta I_4)/(I_2 - I_4)}$$

A typical bending radius for a storage ring bending magnet (ρ_{BM}) and also for an ID (ρ_0) would be of the order of 5 – 20 m. So we can see by inspection of the equations that $\Delta I_2 >> \Delta I_4$. It is generally the case that $I_2 >> I_4$ as well since the focussing term in I_4 is usually zero or close to zero. In this case then the I_4 terms can be neglected in the emittance change equation.

Fig. 10.1 shows how the emittance can change as a function of ID peak field strength for a typical third generation light source. We can see that for this case, where the natural dispersion in the straight is assumed to be zero, all of the examples presented actually *reduce* the emittance. If the natural dispersion in the straight is finite then the effect on the emittance can be quite dramatic. For example, an emittance increase of 50% is observed in the second generation SRS with the 6 T wavelength shifter [21]. It is because of the need to minimize the effect of the IDs on the emittance that third generation rings were *designed* to have zero natural dispersion in the straight sections.

Since IDs can have quite dramatic effects upon the natural emittance of a ring it is not surprising that they have been used to deliberately reduce the emittance of some rings. These particular IDs are called *damping wigglers* and they have been used successfully in colliding beam storage rings, such as LEP [187]. The next generation of electron and positron linear colliders rely very heavily on the use of *damping rings* to condition the beam at relatively low energy before it is accelerated to high energy and collided. These rings are extremely technologically challenging and to achieve the damping required in the short time available large numbers of damping wigglers are required. For example, the TESLA proposal envisages the use of damping wigglers of total length $\sim$ 475 m with a period of 400 mm and a peak field of 1.67 T [188, 189].
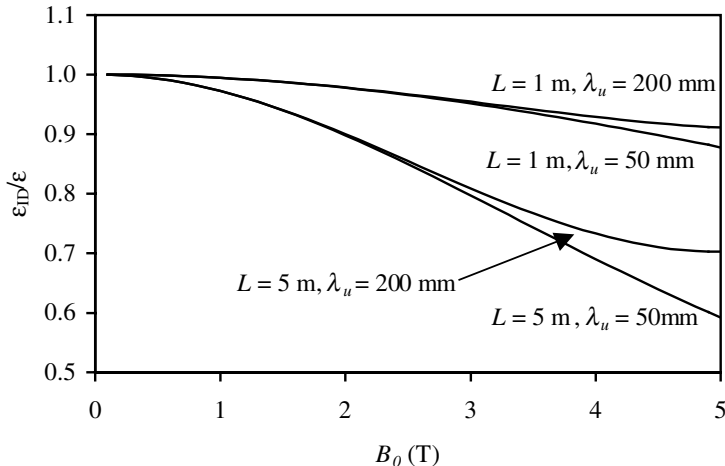
FIG. 10.1. Graph showing the fractional change in the emittance as a function of ID peak field strength in a ring with zero natural dispersion in the straight section. The storage ring energy is 3 GeV, the bending radius is 7.14 m, the natural emittance is 5 nmrad, and the average beta value is 5 m.

10.1.2   *Energy Spread*

The electron beam energy spread is given by

$$\left(\frac{\sigma_E}{E}\right)^2 = C_q \gamma^2 \frac{I_3}{2I_2 + I_4} \ .$$

So, in a similar way as for the emittance, we can say that the fractional change in the energy spread due to an ID is

$$\left(\frac{\sigma_{E_{\text{ID}}}}{\sigma_E}\right)^2 = \frac{1 + \Delta I_3/I_3}{1 + (2\Delta I_2 + \Delta I_4)/(2I_2 + I_4)} \ .$$

Again we can neglect I_4 and this then gives

$$\left(\frac{\sigma_{E_{\text{ID}}}}{\sigma_E}\right)^2 = \frac{1 + 2L\rho_{\text{BM}}^2/3\pi^2\rho_0^3}{1 + L\rho_{\text{BM}}/4\pi\rho_0^2} \ .$$

Fig. 10.2 shows how the energy spread varies as a function of ID peak field strength for a typical storage ring. In this case there is no dependence upon the period of the ID and it is much easier to increase the energy spread rather than decrease it.

10.1.3   *Damping Times*

All perturbations to the electron beam in a storage ring have natural damping terms that help to maintain stability of the motion. The damping that is due to
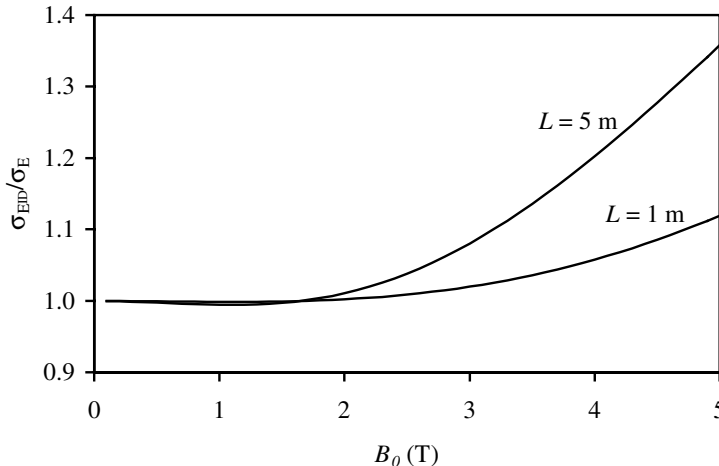
FIG. 10.2. Graph showing the fractional change in the energy spread as a function of ID peak field strength in a storage ring. The storage ring energy is 3 GeV and the bending radius is 7.14 m.

the emission of synchrotron radiation has a characteristic damping time that is different, though of the same order, in every degree of freedom [190],

$$\tau_i = \frac{2ET_0}{U_0 J_i} \ ,$$

where $i = x$, y, or s, T_0 is the revolution time of the ring and U_0 is the energy radiated by each electron per turn (from eqn (2.42)). Also, J_i are the damping partition numbers, which are given by

$$J_x = 1 - \frac{I_4}{I_2}$$
$$J_y = 1$$
$$J_s = 2 + \frac{I_4}{I_2} \ .$$

Using the same arguments as above, the I_4 terms are much smaller than the I_2 ones and so the partition numbers are essentially constant and are also not changed by the introduction of an ID.

Inserting the value for U_0 the damping times reduce to

$$\tau_i = \frac{12\pi\epsilon_0 ET_0}{e^2\gamma^4 I_2 J_i}$$
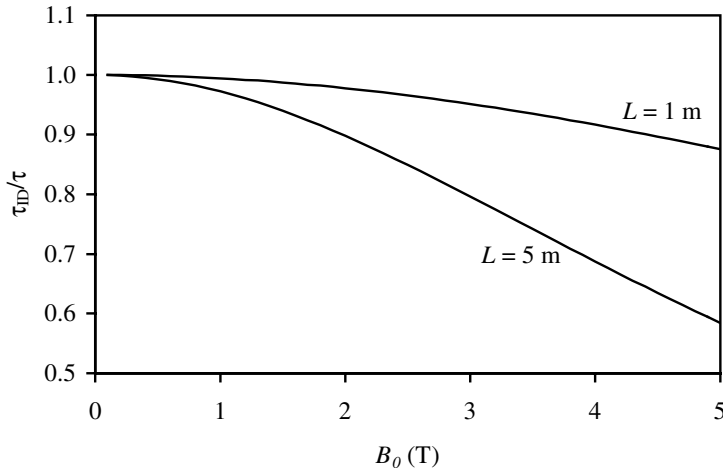
FIG. 10.3. Graph showing the fractional change in the damping times as a function of ID peak field strength in a storage ring. The storage ring energy is 3 GeV and the bending radius is 7.14 m.

$$= \frac{3T_0}{r_e \gamma^3 I_2 J_i} \ ,$$

where r_e is the classical electron radius. The damping times are all dependent upon I_2, which always increases when an ID is introduced. Therefore all of the damping times will reduce when an ID is added to a storage ring. The fractional change in the damping times is plotted in Fig. 10.3 as a function of peak ID field strength.

10.2   Focussing Effects

We know that an electron travelling through a standard planar ID will oscillate in the horizontal plane and, provided that the first and second field integrals are zero (Section 7.5), the electron will exit the magnet travelling along the axis. However, as yet we have not considered what would happen to an electron that entered the ID with either a horizontal or vertical displacement from the axis. In fact, provided the magnet poles are wide enough, the electron that enters with a horizontal displacement follows exactly the same trajectory as the on-axis electron but with a fixed horizontal offset to it. The overall net effect on the electron is therefore basically zero. However, an electron that enters the ID with a vertical offset is bent back towards the horizontal plane, even in an ideal magnet, and so planar IDs are considered to be *vertically focussing* elements. An example of the trajectory taken by an electron at various starting positions outside of an ID is given in Fig. 10.4. It is clear that the different electron trajectories are being focussed together and that the particles that start with larger offsets are bent by more than those with smaller offsets. Since the deflection is proportional
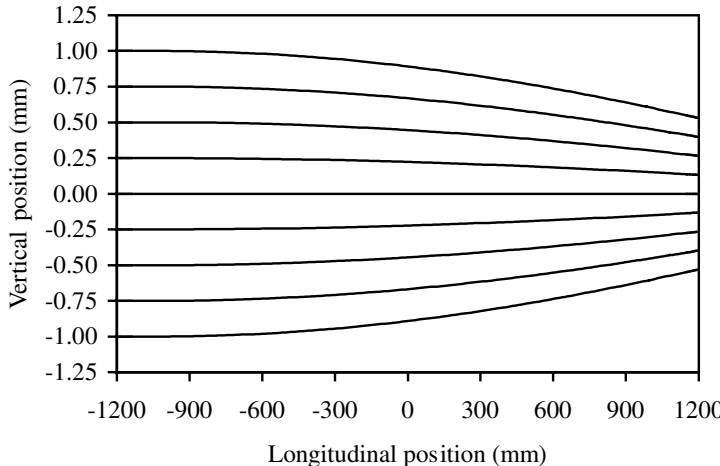
FIG. 10.4. Graph showing the path taken by a 1 GeV electron at different initial vertical positions through a 2 m long, 2 T device with a 100 mm period.

to y this is said to be a *linear* effect. Effects that depend upon higher orders (e.g. y^3) are termed *non-linear* and these can also have important consequences as we shall see later.

The origin of this focussing term is actually the *longitudinal* magnetic field that is generated between two successive poles (it is often called 'edge focussing' for this reason). This is illustrated in Fig. 10.5 where it can be seen that a strong longitudinal field is present halfway between the successive north and south poles. This is the same region as where the electron has its greatest transverse velocity and so a component of the electron motion is travelling orthogonal to this longitudinal field and therefore experiences a force towards the vertical midplane. Since the longitudinal field switches polarity below the axis the force is always towards this midplane. An example of how the longitudinal field varies with vertical position is plotted in Fig. 10.6. It is just possible to see that the field variation does not follow a perfect straight line but does have some curve on it (this is evidence of the presence of higher order terms).

To quantify the focussing term we need to start with the equations of motion for the electron (Section 3.1)

$$\ddot{x} = \frac{d^2x}{ds^2} = \frac{e}{\gamma m_0 c}(B_y - \dot{y}B_s)$$

$$\ddot{y} = \frac{d^2y}{ds^2} = \frac{e}{\gamma m_0 c}(\dot{x}B_s - B_x) \ .$$

Close to the axis the component B_s can be approximated by [191]
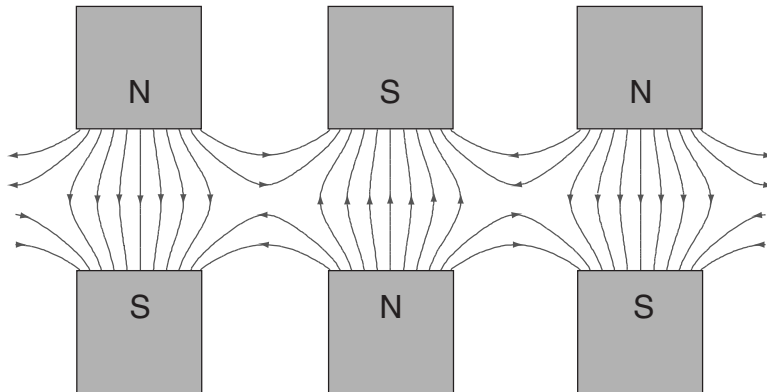
FIG. 10.5. Sketch of the flux lines present in an ID showing the origin of the longitudinal field term.
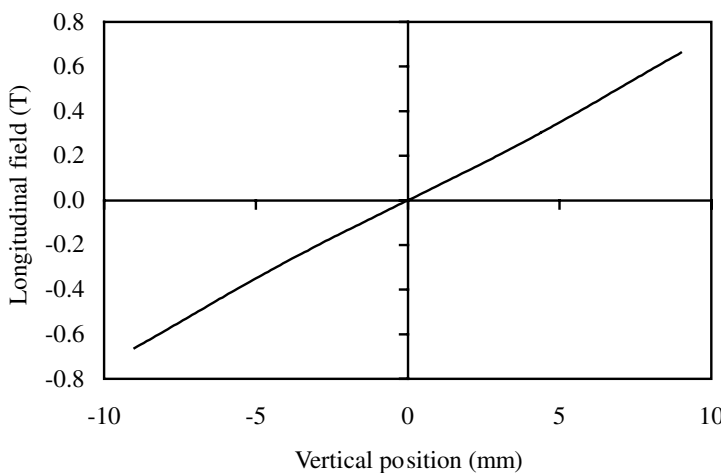
FIG. 10.6. Graph showing the variation of longitudinal field vs vertical position midway (longitudinally) between two poles for a PPM undulator with a period of 50 mm and magnet gap of 20 mm. The peak on-axis vertical field is 0.54 T.

$$B_s \simeq \frac{dB_s}{dy}y = \frac{dB_y}{ds}y \ .$$

Inserting this into the equation of motion with the general result for $\dot{x}$ (7.2) gives

$$\frac{d^2y}{ds^2} \simeq \left(\frac{e}{\gamma m_0 c}\right)^2 \left(\int B_y ds \frac{dB_y}{ds}\right) y \ .$$

This can be compared with the general equation for vertical motion in an accelerator

$$\frac{d^2y}{ds^2} + k_y(s)y = 0 \ ,$$

where $k_y(s)$ is the vertical focussing term. In our case then the instantaneous focussing provided by an ID is

$$k_y(s) = -\left(\frac{e}{\gamma m_0 c}\right)^2 \int B_y ds \frac{dB_y}{ds} \ .$$

This function can be averaged over the full length of the device, using integration by parts, to give an average focussing parameter [25]

$$\hat{k}_y = \left(\frac{e}{\gamma m_0 c}\right)^2 \frac{\int B_y^2 ds}{L} \ ,$$

which for the usual sinusoidal field variation gives

$$\hat{k}_y = \left(\frac{e}{\gamma m_0 c}\right)^2 \frac{B_0^2}{2} ds = \frac{1}{2\rho_0^2} \ .$$

For magnets with a more complicated field distribution a more rigorous approach needs to be followed [192].

The effect of the additional focussing provided by an ID on a ring is to disturb the electron 'optics'. One way to measure the effect is to calculate the change in the 'betatron tune' of the machine. The betatron tune is defined as the number of transverse oscillations that are made per revolution of the lattice and it must be a non-integer (there are many other restrictions as well!) to avoid harmful resonant effects. There is both a horizontal and a vertical betatron tune and it is one of the most important parameters for a storage ring since it is a key factor in determining whether the electron is stable within the ring. If the wrong tune is selected all of the electrons will be lost! Similarly, if the addition of an ID to a ring is enough to move the tune to a poor setting, the results can be equally disastrous. Since the ID adds focussing to the vertical plane it is to be expected that there will be more oscillations per revolution and hence the vertical tune will increase. This is indeed the case and it has been shown that, for the majority of devices that have $L\sqrt{\hat{k}_y} < 0.5$, the tune change induced by the ID, ΔQ_y, is given by [25]

$$\Delta Q_y = \frac{\hat{k}_y L \hat{\beta}_y}{4\pi} \left(1 + \frac{L^2}{12\hat{\beta}_y^2}\right) \ .$$

The tune change varies with $1/\rho_0^2$ and so is a larger value with stronger magnets in lower energy storage rings. Typically the tune change induced by an ID would be less than 0.1 though even this level can be difficult to cope with and would certainly need compensating. The tune is compensated by changing other focussing elements (quadrupoles) in the lattice, ideally close to the ID [21, 193, 194].

10.3   Non-Linear Effects

The magnetic field produced by an ID is complicated and varies rapidly in all three dimensions. The result from the equation of motion showed that $\ddot{y}$ varies with y (a linear dependence) but, as was hinted at earlier, a more exact treatment shows that many terms of higher order should also be included [193, 195, 196]. The effect of these non-linear terms can be serious and a great effort has been made to carefully simulate the influence they can have on the electron beam behaviour.

The overall effect of these terms can be to reduce the 'dynamic aperture'. The dynamic aperture defines a boundary in the transverse directions such that if an electron travels beyond this limit then its motion is no longer stable and the electron will be lost. In this sense it is analogous to the physical aperture (set by the vacuum chamber), where clearly an electron will be lost if it strays beyond this limit. The size of the dynamic aperture is set by the magnet lattice itself and in particular is strongly dependent upon the non-linear fields that are present.

The dynamic aperture of a lattice can be reduced significantly by the addition of an ID in any case simply because the additional focussing in one section of the machine immediately removes all of the periodicity that is initially present. The non-linear terms of the ID exacerbate this effect. The addition of further IDs has generally less impact on the dynamic aperture simply because the periodicity has already been destroyed. The first third generation storage rings were highly symmetric, containing a large number of identical cells. When IDs were modelled in these lattices with simulation codes, significant reductions were observed causing great concern. In the later storage rings there has been a trend to more complex lattices with less periodicity and although in general they start with a smaller dynamic aperture the addition of the IDs is less dramatic since there is less symmetry to destroy in the first place.

Many simulations of the influence of IDs on the dynamic aperture have been carried out [81, 197, 198] and comparisons with experimental measurements show good agreement in general [199–201]. A good example of the problems that can be caused by an ID were seen at SPEAR when a 2 T multipole wiggler was installed into the ring [202]. First it was found that it was not possible to inject at 2.3 GeV with the magnet gap closed, then it was found that the lifetime reduced from 48 to 33 h when the gap was closed at the operating energy of 3 GeV. It was also shown that if the horizontal trajectory in the wiggler was offset by a few mm the lifetime would collapse to a few minutes. This behaviour was caused by a reduction in the dynamic aperture of the lattice due to the intrinsic non-linear fields of the wiggler. The problem was traced to the narrow horizontal pole width, which caused the vertical field to change too rapidly as a function of x near to the longitudinal axis. This meant that the first field integral measured along the oscillating electron trajectory was non-zero and strongly x dependent, even though the field integrals were zero when measured along a straight path parallel to the axis. Small additional magnets were placed at either

end of the magnet to counter-balance this problem. As a result the lifetime is now constant with magnet gap at 3 GeV and injection with the gap closed is also possible.

Insertion Devices for Free Electron Lasers

A Free Electron Laser (FEL) is a device that produces tuneable, coherent radiation through the interaction between a relativistic electron beam and a co-propagating optical beam within an undulator. The interaction is such that there is a transfer of energy between the electron beam and the optical beam, which causes microbunching of the electron beam on the scale of the radiation wavelength (set by the undulator equation) and hence, coherent emission. The properties of the light emitted by the FEL are significantly enhanced when compared with that emitted spontaneously by an electron beam travelling through an undulator, such that these devices are now considered to be the main components of the future fourth generation light sources. There are several texts available that explain the full details of the FEL [203–205].

There are two main types of FEL. The first type, known as an *Oscillator FEL*, traps the spontaneous light emitted by the electrons, travelling through the undulator, between two mirrors that surround the undulator and so creating an 'optical cavity'. This trapped light then interacts with successive electron bunches to create the required bunching effect. The second type, known as a *High Gain FEL*, uses a longer undulator and no mirrors. In this type the light emitted by the electrons in the early part of the undulator starts to interact with the electron beam. As the beam passes through the device the interaction between the light and the electron beam becomes strong enough to cause microbunching to begin. This then causes the electrons to emit with even higher intensity and so produce even more bunching. If the undulator is long enough fully coherent emission will be produced. The IDs that are required for X-ray high gain FELs are the longest that have ever been proposed (up to 100 m). The mechanical engineering design, alignment tolerances, and cost optimization of these segmented devices pose some particularly interesting challenges [206–208]!

Furthermore, there are two ways of using the electron beam. If the FEL is installed into a storage ring then the electrons are continuously circulating and the same electrons are used again and again within the FEL. An alternative is to use the electrons once only in a *single-pass* method where the electrons are accelerated, usually in a linac, sent through the FEL and then deliberately dumped. This second method has many advantages, one of which being that electron beam lifetime is of no concern and so smaller magnet gaps can be used within the undulator.

The undulators used for storage ring based FELs are the same as those used
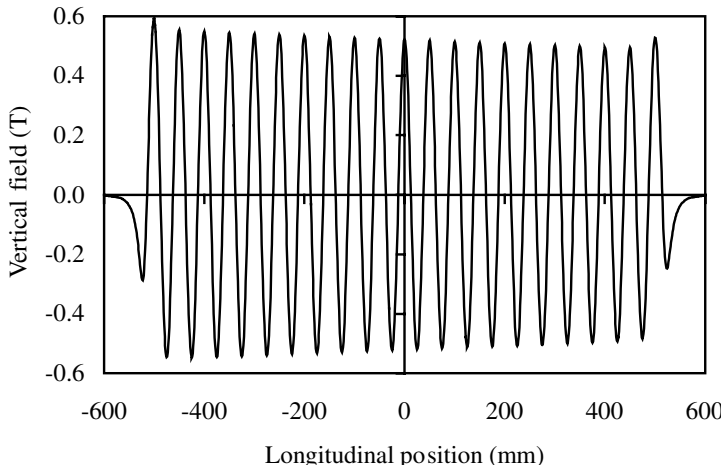
FIG. 11.1. Graph showing the vertical field variation along the length of a 20-period tapered undulator. The undulator period is 50 mm and the magnet gap is 20 mm at the entrance and 21 mm at the exit.

for spontaneous radiation. Most use planar devices [90, 209, 210] but more recent examples have switched to planar helical devices since these generate lower power on-axis and therefore cause less heating of the cavity mirrors [211, 212]. An additional advantage is the higher optical amplification or gain associated with a helical undulator due to the constant longitudinal velocity of the electron beam leading to a better interaction with the co-propogating optical beam.

Undulators for single-pass FELs have incorporated both tapering and horizontal focussing to enhance the FEL interaction. There has also been much activity in this area to generate small gap undulators (less than 5 mm) with short periods.

11.1   Tapered Undulators

When the electrons interact within the FEL they are giving energy to the optical beam as they pass through the undulator. If they give too much energy they will no longer meet the resonance condition set by the undulator equation. If the undulator period or field strength is altered along its length to counteract the electron energy loss then a more efficient FEL can be generated. Such an undulator is quite feasible and is called a *tapered undulator* [213, 214]. It is relatively simple to taper the field in an undulator by simply setting a different magnet gap at the entrance and exit of the device. An example of how the field can vary in such an undulator is shown in Fig. 11.1.

Tapered undulators are also used as spontaneous sources of radiation in storage rings since it is useful to broaden the harmonic width for certain types of

experiment [215, 216]. Naturally the beam intensity is reduced at the peak of the harmonic! The engineering support structure for a permanent magnet device can be quite readily adapted so as to allow some small amount of tapering to be selected when required.

11.2   Horizontal Focussing

We have seen in Chapter 10 that standard planar IDs focus in the vertical plane but not in the horizontal one. This focussing is useful in FELs since it can help to maximize the interaction if the electron beam optics are 'matched' to the ID at the entrance to the undulator. Further enhancement in the FEL performance can be gained if there is focussing in the horizontal plane as well. Also, the very long undulators that are designed for the high gain FELs have to include focussing as well just to maintain reasonable electron beam parameters over the full length of the device. Although some of these achieve this by inserting conventional quadrupoles between undulator segments others include focussing explicitly in the ID magnet design. For these reasons several horizontal focussing schemes have been designed for IDs and some of them will be briefly described here.

11.2.1   *Canted Poles*

One of the simplest methods of introducing a focussing term on top of the standard planar undulator fields is to slightly alter the geometry of a standard 4 block/period pure permanent magnet undulator. By tilting (or canting) the blocks with magnetization axis perpendicular to the beam direction in alternate directions a transverse field gradient can be introduced [217]. Figure 11.2 shows an (exaggerated view of an) example device. The required cant angle to provide equal two-plane focussing is only a few degrees (taking into account the intrinsic vertical focussing) and there is no degradation of the on-axis field strength.

This idea has been further developed with hybrid undulators having the steel pole pieces angled [218]. It is claimed that a much smaller cant angle is required in the hybrid case for the same field gradient and that the field quality is improved. To provide equal two-plane focussing only a subset of the total number of poles is canted. In the case of NISUS [219] only 6 out of 32 poles in each section were canted so that the cant angle (10.8 mrad) was larger and it could be reproduced more readily in manufacture.

11.2.2   *Curved Poles*

It has been noted [220] that additional quadrupole focussing in an FEL affects the phase of the electron motion with respect to the optical electric field, which could decrease the gain of the laser. An alternative focussing scheme was devised that used 'sextupole focussing', which preserved the FEL resonance. The sextupole term was introduced by shaping of the pole faces with a near-parabolic curvature (Fig. 11.3). Sextupole focussing can be understood by considering the field shape within the device. Although the field varies quadratically, the os-
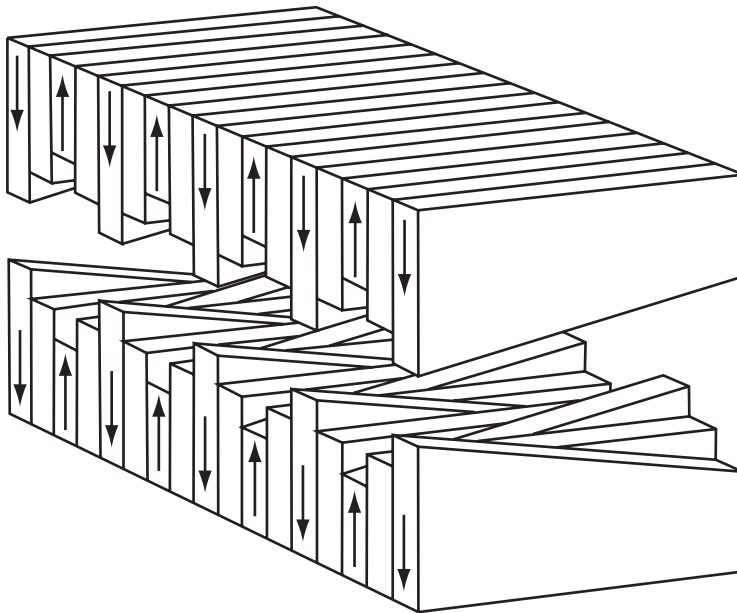
FIG. 11.2. Sketch of a PPM canted undulator.

cillating electron experiences an effective quadrupole-like field. One example of curved pole focussing is the undulator for the Paladin FEL [125].

Concern has been raised over the maximum field that can be attained on-axis while still maintaining adequate focussing. One study has shown [221] that only curving the central third of the permanent magnets still provides adequate focussing with larger on-axis fields. A much simpler and inexpensive solution has been used by one group [222]. A rectangular slot is machined out of each magnet block as a first order approximation to the ideal curved pole design.

11.2.3 *Side Magnets*

If a standard planar undulator has additional side magnets fitted (Fig. 11.4), which have their direction of magnetization opposite to the on-axis field, then they will increase the on-axis fields and also provide a field profile similar to that given by the parabolic-shaped poles above [223]. One obvious disadvantage of this design is that access to the region of interest is not possible while the side pieces are in place. This will make magnetic measurements rather difficult. If the side pieces have their direction of magnetization opposite to each other but still parallel with the main field then a quadrupolar field can be produced on-axis [224].

A natural development of the straightforward side magnet focussing undulator is to split the side magnets along the horizontal x-s plane and separate the two halves vertically. The side magnets can in effect become part of the main
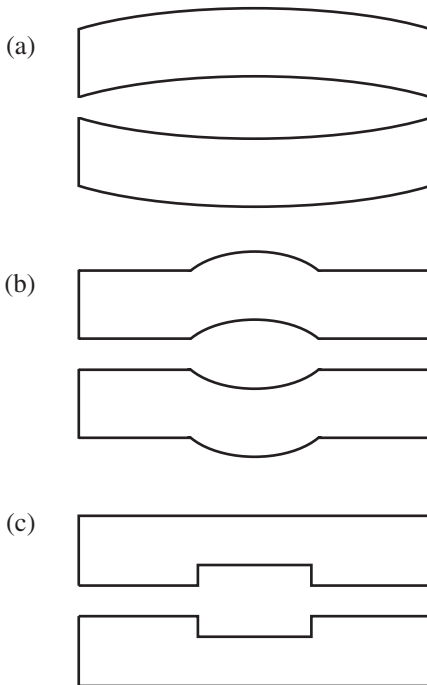
FIG. 11.3. Sketch showing three possible curved pole focussing schemes viewed
end on, (a) shows the ideal solution, (b) a variation which provides higher
on-axis fields, and (c) a rectangular slot approximation to (b).

arrays. This has the distinct advantage of allowing easy access to the electron
beam path from the side for magnet measurements and other interventions. An
example of this is shown in Fig. 11.5. Analysis of this particular scheme high-
lighted the fact that the gradient is very dependent upon horizontal position [225]
and so an alternative solution has been put forward, which has a much reduced
sensitivity to the horizontal position.

11.2.4 *Staggered Poles*

If a hybrid design has the poles staggered alternately to the left and right then
the vertical field will vary with horizontal position. Fig. 11.6 shows an example
of this type of design. In a planar undulator the vertical field is horizontally
symmetric for both positive and negative poles. However, in the staggered design
the symmetry is broken and only electrons on-axis see no net vertical field. It
has been shown that to obtain an appreciable focussing the stagger has to be
about half the pole width and this can cause a significant decrease of the on-axis
field [226].
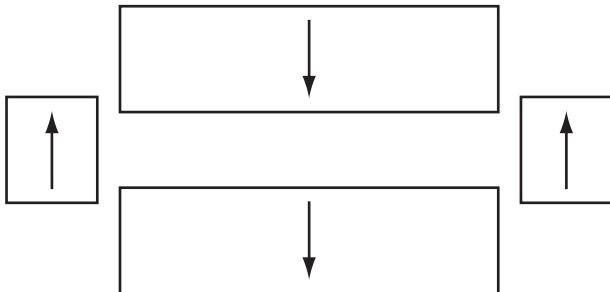
FIG. 11.4. Sketch of side magnet focussing undulator for producing sextupolar fields.
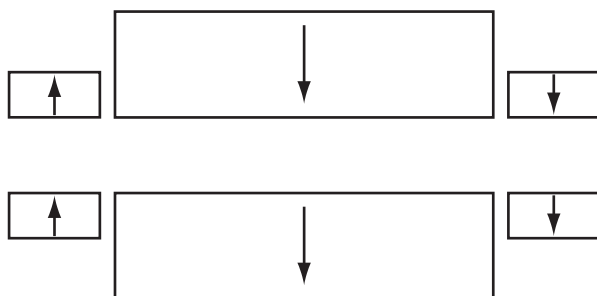
FIG. 11.5. Sketch of a side magnet (quadrupole) focussing undulator, which allows access from the side for magnet measurements.
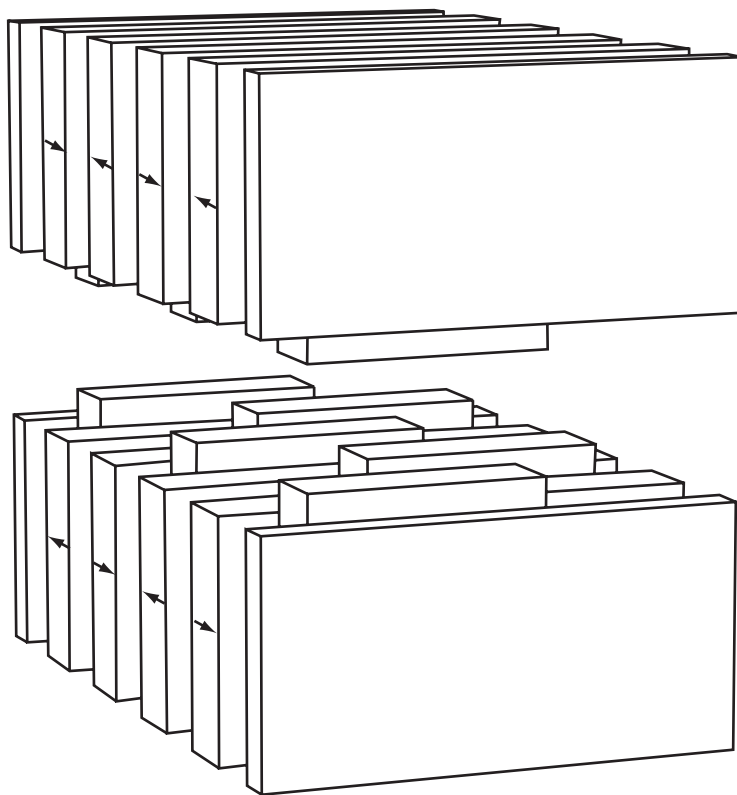
FIG. 11.6. Sketch of the staggered pole undulator design.

Novel and Exotic Insertion Devices

So far we have examined the most common insertion devices (IDs) that are in use today. In particular, planar periodic undulators as well as several helical schemes for generating variable polarization. There are many other types of ID that have been proposed to provide some advantage over the 'standard' types. For instance, suppression of the higher harmonic radiation, lower on-axis power densities and simultaneous production of alternative polarization states on different harmonics have all been addressed.

In addition to these magnets which try to improve the output parameters to suit some particular experimental need there is another family of IDs altogether that tries to exploit different types of interaction with the electron rather than using the standard periodic static magnetic field. For instance, electrostatic devices, electromagnetic waves, and single crystals have all been investigated to see if they offer some advantage over the more conventional approach.

In this chapter, we will first look at the devices that rely on magnets directly but that try to offer some advantage over the standard IDs. Then, later in the chapter, we will examine the alternative approaches that have been put forward for creating a periodic interaction with a relativistic electron.

12.1   Quasiperiodic Undulators

One problem with undulator radiation is that the higher harmonics are integer multiples of the fundamental and hence these harmonics are not always completely removed by optical monochromator systems. Although there are techniques that can be used to remove or reduce this contamination in the optical beamline it would be more satisfactory to not generate the higher harmonics in the first place. This is the motivation for the *quasiperiodic undulator*.

The concept for the device was generated by analogy with X-ray diffraction from a quasicrystal [227, 228]. A quasiperiodic magnetic structure can be formed by placing the magnet poles at locations defined by a so-called Fibonacci sequence. The normalized position of the nth pole, S_n, is given by

$$S_n = n + \left(\frac{1}{\eta} - 1 \right) \left[\frac{n}{\eta + 1} + 1 \right] \ ,$$

where η is an irrational number and the operator $[a]$ gives the largest integer less than a. This sequence produces a list of numbers that increases in steps of either d
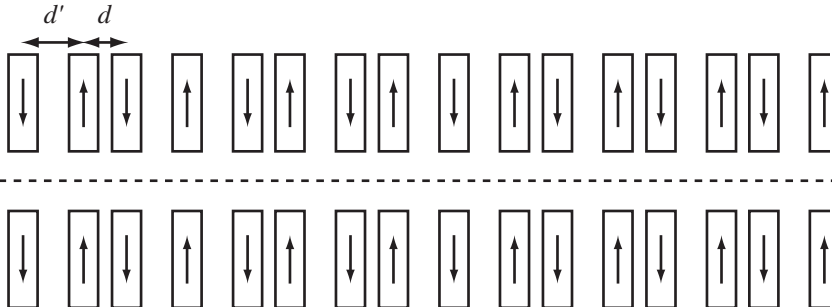
FIG. 12.1. An example quasiperiodic magnet structure created using $\eta = \sqrt{2}$.

or d' and that also has the feature that $d'/d = \eta$. An example magnetic structure is shown in Fig. 12.1. Although this type of undulator still produces radiation at higher harmonics the harmonics are now *irrational* multiples of the fundamental rather than integer and so the contamination through the monochromator is extremely well suppressed.

The quasiperiodic undulator principle was first demonstrated on NIJI-IV [229, 230] using a magnet array that had spacing determined by the Fibonacci sequence. A more compact version, that gives greater flux density per unit length, simply displaces the relevant blocks vertically away from the beam axis to achieve the correct longitudinal field profile [231]. A hybrid version using this idea has also been built [232]. An electromagnet that can either operate in quasiperiodic or standard mode has also been constructed [114].

A further extension of the idea has been developed that uses a slightly modified sequence [233]. This has been applied to an APPLE-2 type helical undulator and is implemented by simply leaving out horizontally magnetized blocks in a standard periodic array structure [95].

An alternative method for suppressing the higher harmonics has also been put forward [234]. In this scheme a standard undulator is broken down into short segments and small phase adjusters (a magnet that can change the path length taken by the electron) inserted in-between. If the phase is set correctly between the segments then particular harmonics can be suppressed. For example, if the phase change between segments is set to $4\pi/3$ then a 100 period undulator split into four segments can reduce the peak flux in the next highest harmonic to 2.4% of the fundamental whereas a non-segmented device would have a level of 36%.

12.2 Figure-8 Undulators

An issue for many beamline designs is the on-axis power density. Often the *useful* power (i.e. at the wavelength of interest) that is generated by an undulator is a fraction of the total power produced. All this power has to be handled by the beamline front-end and the first optical element and this can often limit the overall performance of a beamline. We saw earlier (Chapter 6) that a helical

Figure-8 Undulators 201
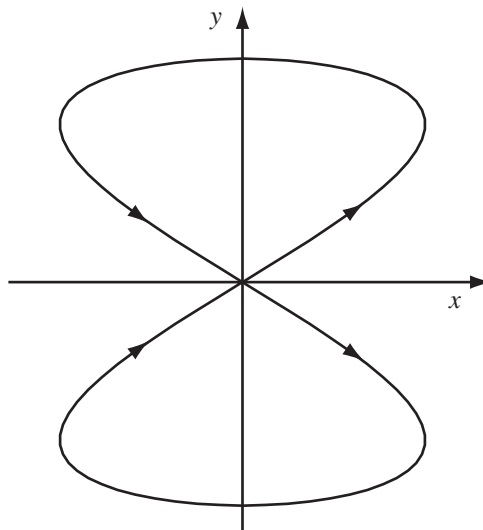
FIG. 12.2. Trajectory of an electron in the transverse plane in a figure-8 undulator.

undulator has low on-axis power because only the single circular harmonic is present on-axis. The *Figure-8* undulator is a device that has low on-axis power density but produces linear polarization on-axis instead [235].

The principle of the device is to cause the electron trajectory to trace out a figure-8 pattern in projection onto the transverse plane (Fig. 12.2). Any circular polarization components on-axis cancel out because of the opposite helicity of the electron motion above and below the axis. The figure-8 pattern is relatively easy to produce by using two orthogonal sinusoidal motions with the vertical motion having twice the wavelength of the horizontal one. The magnetic fields required are given by

$$B_x = -B_{x_0} \sin\left(\frac{\pi s}{\lambda_u}\right)$$
$$B_y = B_{y_0} \sin\left(\frac{2\pi s}{\lambda_u}\right) \ .$$

An unusual consequence of this factor of 2 between the magnet period lengths is that *half* odd integer harmonics are now present in the spectrum also (e.g. 1/2, 3/2, 5/2, ...). These half harmonics have vertical polarization and the usual integer harmonics have horizontal polarization. So at any particular undulator setting the spectrum on-axis contains both horizontal and vertical polarization though at different photon energies of course.

An example of the on-axis power density reduction with this device has been calculated for an 8 GeV ring [235]. For the case of $K \sim 5$ it was shown that for $K_x/K_y = 1$ for the Figure-8 undulator the on-axis flux density in the first harmonic was about two-thirds that of a conventional planar undulator tuned to give the same photon energy. However, the on-axis power density was only 1.5% of that produced by the conventional device. Another example that had $K \sim 1$ demonstrated that with the correct choice of ratio between K_x and K_y the higher harmonic content was suppressed, which could be useful for reducing the harmonic contamination that can pass through monochromators.

The permanent magnet structure of a Figure-8 undulator is similar to that used for generating variable polarization though in the Figure-8 device the phase between the magnet arrays is fixed (Fig. 12.3). An in-vacuum version has been built to take advantage of the simultaneous horizontal and vertical polarization feature [236]. Also, an out of vacuum device has been constructed to take advantage of the reduced on-axis power levels [237]. An interesting feature of this device is that it has been built in two segments (each about 2.3 m long) and that the phase in the horizontal field is switched between the two [238]. This has the consequence of making the power density pattern away from the axis symmetric, which was thought to be advantageous for photon beam alignment purposes and also reduced the peak power load on some mechanical components.

An asymmetric Figure-8 undulator has also been proposed [239] that introduces an additional vertical field with the same period as the horizontal one though 90° out of phase. This has the effect of distorting the Figure-8 shape so that it is no longer symmetrical and one loop of the 8 is much larger than the other. In this way the simple arguments about circular polarization modes cancelling are no longer true. In fact the polarization is found to be vertical on the 0.5th harmonic, horizontal on the first and circular on the second. So this device can produce the three most useful polarization states in the same spectrum without any need for varying the longitudinal phase of the magnets. This could be of particular benefit to in-vacuum undulators since including longitudinal motion in these devices is extremely difficult. The additional vertical field contribution required can be provided by setting a fixed longitudinal offset (phase difference) between the two outer arrays shown in Fig. 12.3. Other variations on the Figure-8 scheme have also been proposed [233, 240].

12.3   Adjustable Phase IDs

Conventional permanent magnet IDs rely on a magnet gap change to alter the on-axis magnetic fields. In the adjustable phase device the gap is fixed but the longitudinal phase is altered between the top and bottom arrays to vary the on-axis field [241]. If the phase is altered between zero and $\lambda_u/2$ then the peak vertical field will change between a maximum and zero (Fig. 12.4). Note that as a consequence of this the longitudinal field on-axis is finite unlike in a conventional device. An additional difference is that B_y varies exponentially with gap but sinusoidally with phase, so the motion control resolution required can be reduced.
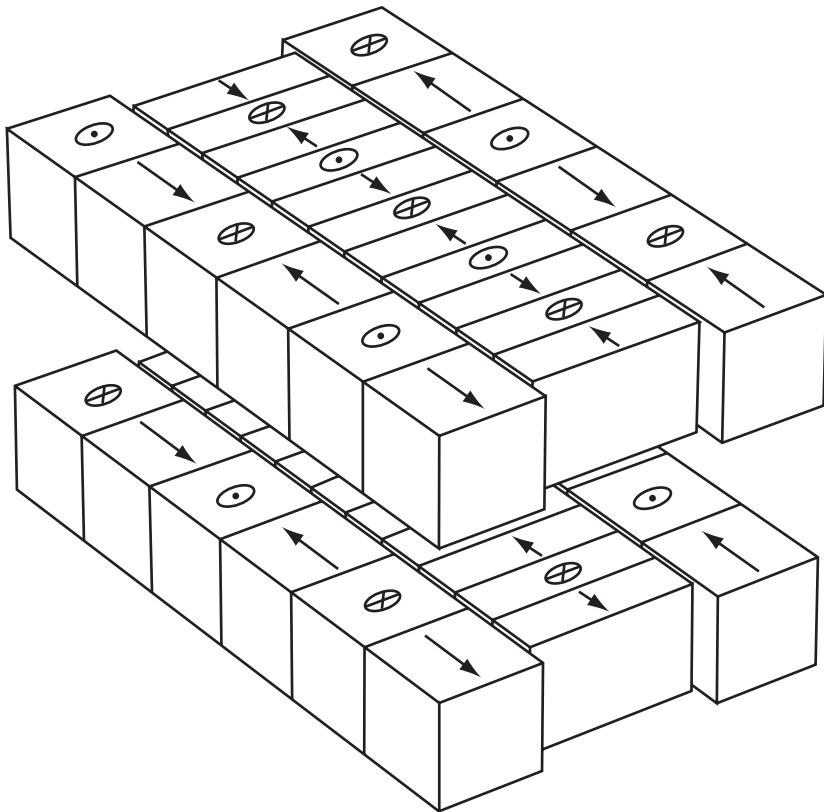
FIG. 12.3. Magnet design for a Figure-8 undulator. The central arrays produce the vertical field and the outer arrays (of twice the period) produce the horizontal field.

Since the gap is fixed, the longitudinal field integrals should be almost constant with phase and furthermore the focussing effect of the device on the electron beam should also be constant. So, as the device is tuned by varying the phase the overall effect on the electron beam should be minimal. The spectral properties of an adjustable phase undulator are very similar to those produced by a conventional device though some concerns have been raised over the spectral sensitivity to vertical position and the stricter requirements on the electron beam properties that are needed to maintain high quality radiation [242]. Nevertheless a successful test has been carried out on the SPEAR ring, which showed very little effect on the electron beam properties as it was adjusted [243].

A hybrid version has also been built and tested [244, 245]. Since it contains iron poles it would be expected to show greater variation of the field integrals with phase and this was indeed the case. However, the tests suggested that the
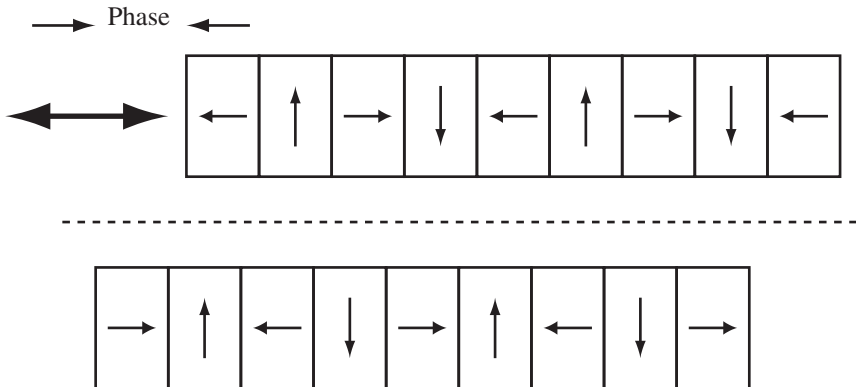
FIG. 12.4. Principal of the adjustable phase insertion device.
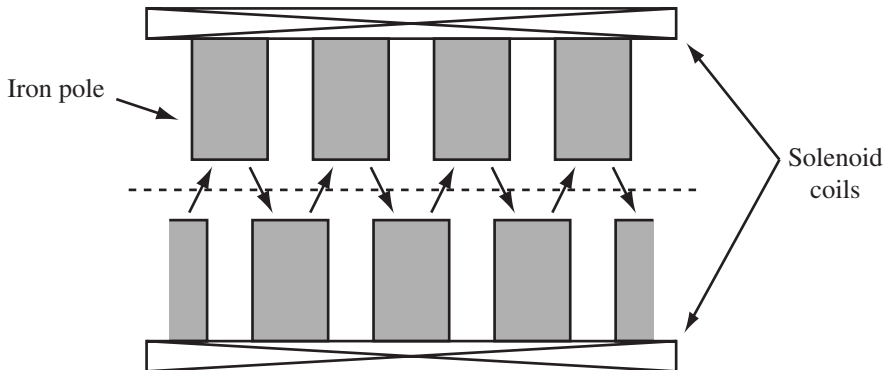
FIG. 12.5. Sketch of a staggered array insertion device. The arrows indicate the magnetic field directions produced.

variation was still less than would be expected for a conventional hybrid device. Also, the focussing effects observed were less than those for a variable gap device. Another advantage highlighted was the simpler mechanical system required.

12.4   Staggered Array IDs

The staggered array magnet is a simple method of generating relatively strong magnetic fields at small periods and gaps [246]. Two planar arrays of iron poles are placed opposite each other with a fixed 180° 'stagger' between them. These are then placed within a solenoid and the longitudinal fields of the solenoid are modified by the high permeability poles to generate a transverse field across the pole gaps (Fig. 12.5). The longitudinal field is also beneficial at low electron energies as it helps to confine the beam as it travels through the device.

The first example built used a 0.7 T superconducting solenoid to generate a 1.08 T transverse field in a device with a 10 mm period and 2 mm gap [246]. Shaping of the iron poles has been suggested as a means of including horizontal focussing in this type of device, which would be beneficial for low energy FEL operation [247].

A version that combines a permanent magnet hybrid device with a solenoid has also been suggested [248]. The inclusion of the permanent magnets enhanced the transverse field by 16% in their example. A proposal has since been put forward to use two such staggered hybrid arrays to form an in-vacuum crossed undulator pair (see Section 6.7) for generating variable polarization [249].

It is possible to generate a helical magnetic field by mounting two pairs of arrays orthogonal to each other and shifted longitudinally by $\lambda_u/4$ [250]. Ideas have also been put forward for mounting several independent staggered arrays within the same solenoid. In one design a 200 mm diameter solenoid contained four independent undulators [250].

Adjusting the magnetic field of an ID to change the spectral output is so common that it is sometimes forgotten that it is not the only method available. Changing the electron energy is also an option in an FEL since they are in general single-user facilities and so no other beamlines are affected. This method is not possible in a synchrotron light source because the energy change would alter the output of all the synchrotron radiation sources installed. The third option of varying the magnet period is rarely implemented. This is because it is mechanically more difficult to adjust the period with the accuracy required when compared with changing the magnetic field. However, it does have some advantage over gap tuning in terms of the photon range available and also the power generated can be kept lower than for a conventional device [251]. A recent design has been generated for a variable period length staggered array undulator that uses a scissor type action to alter the separation between the pole pieces [252]. Some interesting modes of operation are available in principle, such as constant flux output or constant power output.

12.5 Revolvers and Multiundulators

An obvious method for changing the period of an undulator to increase the tuning range available is to simply swap it for another one. This is not so crazy as it sounds and has in fact been implemented in a few storage rings. The idea is to have a number of pairs of magnet arrays of different period lengths available and to select the best array for the wavelength range required. The magnet gap is then adjusted as for a conventional device to tune the wavelength. The problem of swapping arrays remotely in a support structure is a mechanical design issue, magnetically the arrays are conventional.

Two solutions have been used so far. The first, termed a *multiundulator*, had four pairs of arrays mounted side by side in a mechanical support structure that varied the gap of all the arrays simultaneously [253]. To swap arrays the system was slid horizontally until another pair of arrays was positioned over the

electron vacuum vessel. The main drawback of this approach is that it needs quite a bit of space horizontally, which is often not available because of neighbouring components such as photon beamlines from upstream IDs or bending magnets. The second solution adopted has been to mount up to four arrays on a single square cross-section beam and to rotate the beam to swap between arrays, hence the name *revolver*. Two identical beams are needed of course and again, when the magnet gap is adjusted, all of the arrays are moved. Early examples of these had four [254] or three arrays [255]. A more recent version could only have two different arrays because they chose to support the beam in several places down its 4.5 m length [256]. Excellent reproducibility has been measured in terms of gap and angle when the beams are rotated and on-line switching between arrays has little observable effect upon the stored electron beam and is carried out routinely.

12.6   Micro-Undulators

Undulators with periods below about 1 mm are (loosely) defined as *micro-undulators*. The motivation for producing such short periods is the ability to produce short wavelengths from lower energy (and so more economical) electrons and also the ability to have a large number of periods in a physically short space. Of course these short period devices have to have a similarly short gap and so they are not well suited to storage rings but could be very useful for single pass devices such as linacs. Even so, the small magnet gap will be difficult to pump to achieve a good vacuum pressure and there would be a strong electromagnetic interaction with the electron beam and the surface of the undulator that could cause instabilities in the electron beam itself [257].

Several methods have been tried for generating a periodic magnetic field with periods below 1 mm. One idea started with a larger unmagnetized permanent magnet block. This then had periodic grooves machined into the surface and was then magnetized. Both horizontally and vertically magnetized blocks can be used to create a periodic magnetic field, two schemes are shown in Fig. 12.6. A pair of vertically magnetized blocks has been used to demonstrate an undulator with a period of 4.1 mm and a peak on-axis field of about 0.1 T [258]. Of course with the period being so small the K parameter is also very small, in this case being about 0.04.

An alternative scheme is to periodically magnetize a magnetic tape and to then mount two such tapes opposite each other [259]. In this way very short periods could indeed be created but as yet no satisfactory demonstration of this method has been achieved.

12.7   Future Possibilities

In this section we will review some of the alternative methods for generating a periodic interaction with an electron beam to generate undulator radiation.
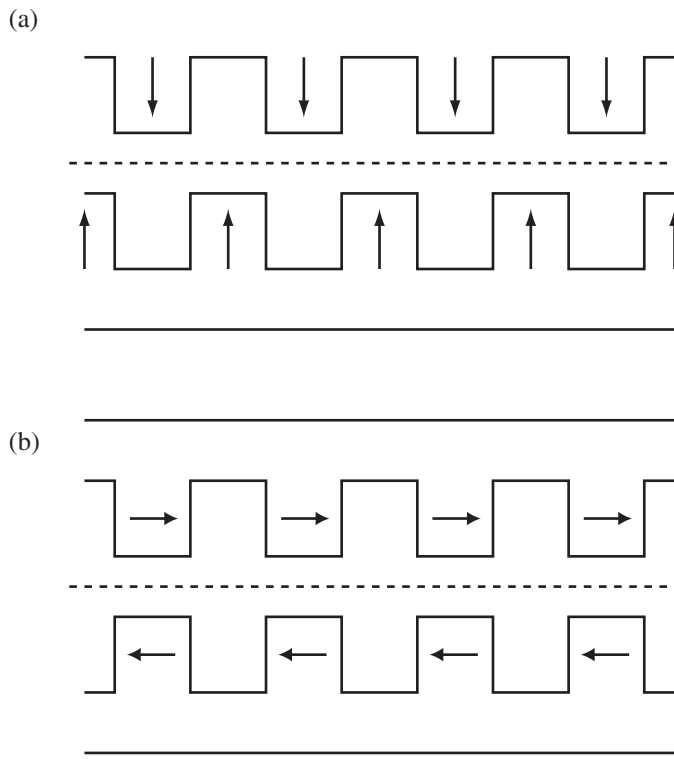
FIG. 12.6. Two possible micro-undulator schemes made from permanent magnets.

12.7.1 *Electrostatic Devices*

Rather than using a magnetic field an electrostatic field could be used instead. In particular, variable period transverse and helical designs have been proposed [260]. Also, electrostatic micro-undulators with periods of less than 0.1 mm have been suggested [261]. Electric field strengths of $\sim 3 \times 10^7$ V/m are thought to be possible with a 1 mm period device (equivalent to 0.1 T). The main advantage of electrostatic devices appears to be the simple design and low cost but they could also have a field strength advantage over magnetostatic devices at submillimeter periods.

12.7.2 *Image Charge Undulator*

An electron beam passing near a conducting surface produces an image current, which can act back on the beam. These so-called *wakefields* can cause instabilities in electron beams but have also been proposed to produce an undulating motion in the beam [262]. The metal surface needs to be shaped with a longitudinally periodic profile (similar to a diffraction grating) to have the desired effect. This

idea is similar to Smith-Purcell radiation [263, 264].

12.7.3   *Microwave Devices*

High frequency microwaves can be used to interact with an electron beam to cause periodic oscillations. Transverse kicks are applied to electron beams in special radio-frequency cavities in many accelerator applications and this is a simple extension of this idea. A test system that operated at ∼3 GHz, which is equivalent to a 55 mm magnet period, was built in Japan [265]. The undulator cavity was pulsed at 10 Hz with 300 kW of microwave power and undulator radiation was observed. The device had a K value of 0.24. The use of superconducting cavities would reduce the total power requirements and therefore would allow continuous operation. A very high frequency design has been proposed (120 GHz), which has a period length of only 1.45 mm and an electric field of 20 MV/m, which is equivalent to 0.066 T [266].

12.7.4   *Crystalline Undulator*

In a crystalline undulator the planes of a single crystal are bent so that they form a periodic profile. If an electron is passed through this structure then it will experience strong forces due to the nearby atomic nuclei and oscillate with the period of the crystal planes and thus emit undulator radiation. This concept was first proposed in 1979 [267] but undulator radiation from a crystal has not yet been observed. The problem with this idea appears to be the fabrication of a suitable crystal. However, several approaches are being pursued and progress has been made over the past few years [268–270].

The benefits of such a device could be very great as they seem to be well suited to producing submillimeter periods and also electromagnetic fields of up to 1000 T are possible. Interestingly, this is the only undulator where there is a benefit of using a positron rather than an electron in the interaction.

References

[1] J. P. Blewett. Radiation losses in the induction electron accelerator. *Phys. Rev.*, 69:87–95, 1946.

[2] J. P. Blewett. Synchrotron radiation — early history. *J. Synchrotron Rad.*, 5:135–139, 1998.

[3] F. R. Elder *et al.* Radiation from electrons in a synchrotron. *Phys. Rev.*, 71:829–830, 1947.

[4] F. R. Elder *et al.* Radiation from electrons accelerated in a synchrotron. *Phys. Rev.*, 74:52–56, 1948.

[5] J. Schwinger. Electron radiation in high energy accelerators. *Phys. Rev.*, 70:798–799, 1946.

[6] J. Schwinger. On the classical radiation of accelerated electrons. *Phys. Rev.*, 75(12):1912–1925, 1949.

[7] H. Motz. Applications of the radiation from fast electron beams. *J. Appl. Phys.*, 22(5):527–535, 1951.

[8] H. Motz *et al.* Experiments on radiation by fast electron beams. *J. Appl. Phys.*, 24(7):826–833, 1953.

[9] D. Ivanenko and I. Pomeranchuk. On the maximal energy attainable in a betatron. *Phys. Rev.*, 65:343, 1944.

[10] D. F. Alferov *et al.* Undulator radiation. *Sov. Phys. Tech. Phys.*, 18(10):1336–1339, 1974.

[11] G. Stephenson and C. W. Kilmister. *Special relativity for physicists*. Longmans, London, 1958.

[12] J. D. Jackson. *Classical Electrodynamics*. Wiley, New York, 3rd edition, 1999.

[13] A. V. Durrant. *Vectors in Physics and Engineering*. Chapman and Hall, 1996.

[14] A. Hofmann. Characteristics of synchrotron radiation. In *Proceedings of the CERN Accelerator School, 98–04*, pages 1–44, 1998.

[15] K. Hubner. Synchrotron radiation. In *Proceedings of the CERN Accelerator School, 90–03*, pages 24–36, 1990.

[16] K-J. Kim. Characteristics of synchrotron radiation. In *AIP Conference Proceedings 184: Physics of Particle Accelerators*, pages 567–632, 1989.

[17] M. Abramowitz and I. A. Stegun, editors. *Handbook of Mathematical Functions*. Dover Publications, Inc, 1965.

[18] P. J. Duke. *Synchrotron Radiation: Production and Properties*. Oxford University Press, Oxford, 2000.

[19] D. Zwillinger, editor. *CRC Standard Mathematical Tables and Formulae*. CRC Press, 1996.

[20] H. Wollnik. *Optics of Charged Particles*. Academic Press, Orlando, 1987.

[21] J. A. Clarke *et al.* Update on commissioning and operations with the second superconducting wiggler at Daresbury. In *Proceedings of the European Particle Accelerator Conference, London*, pages 648–650, 1994.

[22] N. Marks *et al.* Initial operation of a 5 T superconducting wiggler magnet in the SRS. *Nucl. Instrum. Methods*, 208:97–103, 1983.

[23] V. M. Borovikov *et al.* Superconducting 7T wiggler for LSU CAMD. *J. Synchrotron Rad.*, 5:440–442, 1998.

[24] V. M. Borovikov *et al.* Superconducting 7T wavelength shifter for BESSY–II. *Nucl. Instrum. Methods*, A467–468:181–184, 2001.

[25] R. P. Walker. Wigglers. In *Proceedings of the CERN Accelerator School, 95–06*, pages 807–835, 1995.

[26] R. P. Walker. Multipole wiggler brilliance and effective source size. *Sincrotrone Trieste Internal Report*, ST/M-TN-89/24, 1989.

[27] K-J. Kim. Angular distribution of undulator power for an arbitrary deflection parameter K. *Nucl. Instrum. Methods*, A246:67–70, 1986.

[28] R. J. Dejus and A. Luccio. Program UR: General purpose code for synchrotron radiation calculations. *Nucl. Instrum. Methods*, A347:61–66, 1994.

[29] R. P. Walker. Insertion devices: undulators and wigglers. In *Proceedings of the CERN Accelerator School, 98–04*, pages 129–190, 1998.

[30] F. A. Jenkins and H. E. White. *Fundamentals of Optics.* McGraw-Hill, New York, 4th edition, 1976.

[31] H. Kitamura. Polarization of undulator radiation. *Jpn. J. Appl. Phys.*, 19(4):L185–L188, 1980.

[32] K-J. Kim. Brightness, coherence and propagation characteristics of synchrotron radiation. *Nucl. Instrum. Methods*, A246:71–76, 1986.

[33] W. Joho. Radiation properties of an undulator (a simple primer). *Swiss Light Source Internal Report*, SLS-Note 4/95, April 1996.

[34] R. Coisson. Effective phase space widths of undulator radiation. *Opt. Eng.*, 27(3):250–252, 1988.

[35] Y. Hirai *et al.* Study of the radiation from an undulator: near field formulation. *J. Appl. Phys.*, 55(1):25–32, 1984.

[36] R. P. Walker. Near field effects in off-axis undulator radiation. *Nucl. Instrum. Methods*, A267:537–546, 1988.

[37] D. A. Mossessian and P. A. Heimann. Characterization of ALS undulator radiation — high K, taper, and the near field effect. *Rev. Sci. Instrum.*, 66(11):5153–5161, 1995.

[38] C. P. Neuman *et al.* Coherent off-axis undulator radiation from short electron bunches. *Phys. Rev. ST-AB*, 3:030701, 2000.

[39] M. Takao and Y. Miyahara. Expected radiation spectra of a 30 m long undulator in SPring-8. In *Proceedings of the Particle Accelerator Conference, Dallas*, pages 1435–1437, 1995.

[40] O. Chubar and P. Elleaume. Accurate and efficient computation of synchrotron radiation in the near field region. In *Proceedings of the European Particle Accelerator Conference, Stockholm*, pages 1177–1179, 1998.

[41] T. Tanaka and H. Kitamura. SPECTRA: a synchrotron radiation calculation code. *J. Synchrotron Rad.*, 8:1221–1228, 2001.

[42] H. Burkhardt. Monte carlo generator for synchrotron radiation. *CERN Internal Report*, LEP Note 632, 1990.

[43] R. Coisson *et al.* Multipole wigglers as sources of synchrotron radiation. *Nucl. Instrum. Methods*, 201:3–12, 1982.

[44] F. Cerrina *et al. SHADOW primer 2.0.* University of Wisconsin, 1994.

[45] R. P. Walker and B. Diviacco. URGENT — A computer program for calculating undulator radiation spectral, angular, polarization, and power density properties. *Rev. Sci. Instrum.*, 63(1):392–395, 1992.

[46] A. Geisler *et al.* SpontLight — A package for synchrotron radiation calculations. *DELTA Internal Report*, 94–7, 1994.

[47] C. Wang *et al.* Calculation of undulator radiation from measured magnetic fields and comparison with measured spectra. In *Proceedings of the European Particle Accelerator Conference, Berlin*, pages 928–930, 1992.

[48] S. D. Shastri *et al.* Experimental characterisation of APS undulator A at high photon energies (50–200 keV). *J. Synchrotron Rad.*, 5:67–71, 1998.

[49] E. Gluskin. APS insertion devices: Recent developments and results. *J. Synchrotron Rad.*, 5:189–195, 1998.

[50] W. Lavender *et al.* Observation of x-ray undulator radiation on PEP. *Rev. Sci. Instrum.*, 60(7):1414–1418, 1989.

[51] T. Mitsuhashi *et al.* An investigation of synchrotron X–radiation from the Photon Factory vertical wiggler. *Nucl. Instrum. Methods*, A246:54–57, 1986.

[52] M. Born and E. Wolf. *Principles of Optics.* Cambridge University Press, Cambridge, 7th edition, 1999.

[53] M. A. Green. Activity on sources of variable polarization for users. *Nucl. Instrum. Methods*, A319:83–88, 1992.

[54] J. Pfluger and G. Heintze. The asymmetric wiggler at HaSYLAB. *Nucl. Instrum. Methods*, A289:300–306, 1990.

[55] J. Chavanne *et al.* A 3 T asymmetric permanent magnet wiggler. *Nucl. Instrum. Methods*, A421:352–360, 1999.

[56] D. Schirmer *et al.* First experience with the superconducting asymmetric wiggler of the DELTA facility. In *Proceedings of the European Particle Accelerator Conference, Vienna*, pages 2337–2339, 2000.

[57] S. Yamamoto *et al.* Construction of insertion devices for elliptically polarized synchrotron radiation. *Rev. Sci. Instrum.*, 60(7):1834–1837, 1989.

[58] R. P. Walker *et al.* Construction and testing of an electromagnetic elliptical wiggler for ELETTRA. In *Proceedings of the European Particle Accelerator Conference, Stockholm*, pages 2255–2257, 1998.

[59] E. Gluskin *et al.* The elliptical multipole wiggler project. In *Proceedings of the Particle Accelerator Conference, Dallas*, pages 1426–1428, 1995.

[60] L. Nahon *et al.* OPHELIE: a variable polarization electromagnetic undulator optimised for a VUV beamline at super-ACO. *J. Synchrotron Rad.*,

5:428–430, 1998.

[61] S. Sasaki *et al.* First observation of undulator radiation from APPLE-1. *Nucl. Instrum. Methods*, A347:87–91, 1994.

[62] R. Carr *et al.* Performance of the elliptically polarizing undulator on SPEAR. *Rev. Sci. Instrum.*, 66(2):1862–1864, 1995.

[63] P. Elleaume and J. Chavanne. A new powerful flexible linear/helical undulator for soft X-rays. *Nucl. Instrum. Methods*, A304:719–724, 1991.

[64] K-J. Kim. A synchrotron radiation source with arbitrarily adjustable elliptical polarization. *Nucl. Instrum. Methods*, 219:425–429, 1984.

[65] R. P. Walker and B. Diviacco. Studies of insertion devices for producing circularly polarized radiation with variable helicity in ELETTRA. *Rev. Sci. Instrum.*, 63(1):332–335, 1992.

[66] P. Elleaume. Special synchrotron radiation sources part II: Exotic insertion devices. *Synchrotron Rad. News*, 1(5):21–27, 1988.

[67] M. A. Green *et al.* Rapidly-modulated variable-polarization crossed-undulator source. In *Proceedings of the Particle Accelerator Conference, San Francisco*, pages 1088–1090, 1991.

[68] J. Bahrdt *et al.* Circularly polarized synchrotron radiation from the crossed undulator at BESSY. *Rev. Sci. Instrum.*, 63(1):339–342, 1992.

[69] J. Bahrdt *et al.* The crossed field undulator at BESSY: First data. *Synchrotron Rad. News*, 5(2):12–14, 1992.

[70] S. Sasaki *et al.* Crossed elliptical polarization undulator. In *Proceedings of the Particle Accelerator Conference, Vancouver*, pages 802–804, 1997.

[71] B. M. Kincaid. A short-period helical wiggler as an improved source of synchrotron radiation. *J. Appl. Phys.*, 48(7):2684–2691, 1977.

[72] P. Campbell. *Permanent Magnet Materials and their Application*. Cambridge University Press, Cambridge, 1994.

[73] H. R. Kirchmayr. Permanent magnets and hard magnetic materials. *J. Phys. D: Appl. Phys.*, 29:2763–2778, 1996.

[74] R. D. Schlueter. Wiggler and undulator insertion devices. In *Synchrotron Radiation Sources — A primer*. World Scientific, Singapore, 1994.

[75] T. Ikeda and S. Okuda. Magnetic flux loss of the permanent magnets used for the wigglers of FELs by the irradiation with high-energy electrons or X-rays. *Nucl. Instrum. Methods*, A407:439–442, 1998.

[76] Y. Ito *et al.* Magnetic flux loss in rare-earth magnets irradiated with 200 MeV protons. *Nucl. Instrum. Methods*, B183:323–328, 2001.

[77] K. Halbach. Physical and optical properties of rare earth cobalt magnets. *Nucl. Instrum. Methods*, 187:109–117, 1981.

[78] M. W. Poole. Design and technology of undulators. In *Proceedings of the CERN Accelerator School, 90–03*, pages 195–217, 1990.

[79] K. Halbach. Permanent magnet undulators. *J. de Phys.*, 44(C1):211–216, 1983.

[80] *7 GeV Advanced Photon Source conceptual design report, ANL-87-15*. ANL, 1987.

[81] *DIAMOND Synchrotron Light Source — Report of the Design Specification.* CLRC, 2002.

[82] J. Chavanne *et al.* End field structures for linear/helical insertion devices. In *Proceedings of the Particle Accelerator Conference, New York*, pages 2665–2667, 1999.

[83] R. P. Walker. Advanced insertion devices. In *Proceedings of the European Particle Accelerator Conference, London*, pages 310–314, 1994.

[84] B. Diviacco and R. P. Walker. Pure permanent magnet end-configurations. *Sincrotrone Trieste Internal Report*, ST/M-TN-92/5, 1992.

[85] J. A. Clarke *et al.* Design of a 2 T multipole wiggler insertion device for the SRS. *J. Synchrotron Rad.*, 5:434–436, 1998.

[86] L. H. Chang *et al.* Passive end pole compensation scheme for a 1.8 Tesla wiggler. In *Proceedings of the Particle Accelerator Conference, Dallas*, pages 1450–1452, 1995.

[87] J. Chavanne *et al.* Segmented high quality undulators. In *Proceedings of the Particle Accelerator Conference, Dallas*, pages 1319–1321, 1995.

[88] J. Goulon *et al.* Special multipole wiggler design producing circularly polarized synchrotron radiation. *Nucl. Instrum. Methods*, A254:192–201, 1987.

[89] J. Pfluger. Insertion devices for DORIS III. *Rev. Sci. Instrum.*, 63(1):295–300, 1992.

[90] M. Barthes *et al.* Magnet developments for the new Orsay synchrotron radiation source Super ACO. *IEEE Trans. Mag.*, 24(2):1233–1236, 1988.

[91] K. Halbach. Design of permanent multipole magnets with oriented rare earth cobalt material. *Nucl. Instrum. Methods*, 169:1–10, 1980.

[92] B. Diviacco and R. P. Walker. Fields and trajectories in some new types of permanent magnet helical undulator. *Nucl. Instrum. Methods*, A292:517–529, 1990.

[93] S. Sasaki *et al.* Design of a new type of planar undulator for generating variably polarized radiation. *Nucl. Instrum. Methods*, A331:763–767, 1993.

[94] S. Sasaki. Analyses for a planar variably-polarizing undulator. *Nucl. Instrum. Methods*, A347:83–86, 1994.

[95] B. Diviacco *et al.* Construction of elliptical undulators for ELETTRA. In *Proceedings of the European Particle Accelerator Conference, Stockholm*, pages 2216–2218, 1998.

[96] H. Kobayashi *et al.* Design of variable polarizing undulator (APPLE-type) for SX beamline in the SPring-8. In *Proceedings of the European Particle Accelerator Conference, Sitges*, pages 2579–2581, 1996.

[97] C. Wang *et al.* Conceptual design for the SRRC elliptically polarizing undulator EPU5.6 part I: Magnetic configuration and merit function optimisation. In *Proceedings of the European Particle Accelerator Conference, Sitges*, pages 2567–2569, 1996.

[98] J. Bahrdt *et al.* Elliptically polarizing insertion devices at BESSY II. *Nucl. Instrum. Methods*, A467–468:21–29, 2001.

[99] A. T. Young *et al.* Variable linear polarization from an X-ray undulator. *J. Synchrotron Rad.*, 9:270–274, 2002.

[100] C. S. Hwang and S. Yeh. Various polarization features of a variably polarized undulator with different phasing modes. *Nucl. Instrum. Methods*, A420:29–38, 1999.

[101] R. D. Schlueter and S. Marks. Three-dimensional pure permanent magnet undulator design theory. *IEEE Trans. Mag.*, 32(4):2710–2713, 1996.

[102] S. Kimura *et al.* Performance of a helical undulator of the UVSOR. *J. Synchrotron Rad.*, 5:453–455, 1998.

[103] T. Hara *et al.* SPring-8 twin helical undulator. *J. Synchrotron Rad.*, 5:426–427, 1998.

[104] G. B. Bowden. Undulator gravitational deflection. *LCLS Internal Report*, LCLS-TN-02-6, 2002.

[105] H. Kitamura. Present status of SPring-8 insertion devices. *J. Synchrotron Rad.*, 5:184–188, 1998.

[106] H. Kitamura. In-vacuum ID technology. In *25th ICFA Advanced Beam Dynamics Workshop: Shanghai Symposium on Intermediate-Energy Light Sources*, pages 206–210, 2002.

[107] J. Chavanne *et al.* Magnetic design considerations for in-vacuum undulators at ESRF. In *Proceedings of the European Particle Accelerator Conference, Paris*, pages 2604–2606, 2002.

[108] T. Bizen *et al.* Baking effect for NdFeB magnets against demagnetization induced by high-energy electrons. *Nucl. Instrum. Methods*, A515:850–852, 2003.

[109] T. Hara *et al.* SPring-8 in-vacuum undulator beam test at the ESRF. *J. Synchrotron Rad.*, 5:406–408, 1998.

[110] H. Kitamura *et al.* Recent developments of insertion devices at SPring-8. *Nucl. Instrum. Methods*, A467–468:110–113, 2001.

[111] J. Chavanne *et al.* Construction of Apple II and in vacuum undulators at ESRF. In *Proceedings of the Particle Accelerator Conference, Chicago*, pages 2459–2461, 2001.

[112] J. A. Clarke *et al.* The initial insertion devices for the DIAMOND light source. In *Proceedings of the European Particle Accelerator Conference, Paris*, pages 2607–2609, 2002.

[113] O. Marcouille *et al.* Preliminary design of the SOLEIL insertion devices. In *Proceedings of the European Particle Accelerator Conference, Paris*, pages 2625–2627, 2002.

[114] T. Schmidt *et al.* Insertion devices at the swiss light source (phase I). *Nucl. Instrum. Methods*, A467–468:126–129, 2001.

[115] P. M. Stefan *et al.* Small-gap undulator research at the NSLS: concepts and results. *Nucl. Instrum. Methods*, A412:161–173, 1998.

[116] H. C. Ohanian. *Physics*. W. W. Norton and Co., New York, 2nd edition, 1989.

[117] R. Resnick *et al.* *Physics*. Wiley, New York, 5th edition, 2002.

[118] N. Marks. Conventional Magnets – I. In *Proceedings of the CERN Accelerator School, 94–01*, pages 867–890, 1994.

[119] M. W. Poole and R. P. Walker. Some limitations on the design of plane periodic electromagnets for undulators and free electron lasers. *Nucl. Instrum. Methods*, 176:487–495, 1980.

[120] M. W. Poole and R. P. Walker. Periodic magnets for undulators and free electron lasers — A review of performance features. *IEEE Trans. Mag.*, 17(5):1978–1981, 1981.

[121] N. A. Vinokurov. Insertion device development at Novosibirsk. *Nucl. Instrum. Methods*, A246:105–108, 1986.

[122] G. I. Erg *et al.* Multipole wiggler and undulator for the TNK SR source. *Nucl. Instrum. Methods*, A308:57–60, 1991.

[123] K. Halbach. Some concepts to improve the performance of dc electromagnetic wigglers. *Nucl. Instrum. Methods*, A250:115–119, 1986.

[124] G. A. Deis *et al.* Electromagnetic wiggler technology development at the Lawrence Livermore National Laboratory. *IEEE Trans. Mag.*, 24(2):986–989, 1988.

[125] G. A. Deis *et al.* A long electromagnetic wiggler for the Paladin free electron laser experiments. *IEEE Trans. Mag.*, 24(2):1090–1093, 1988.

[126] W. R. Smythe. *Static and Dynamic Electricity.* McGraw-Hill, New York, 1950.

[127] J. P. Blewett and R. Chasman. Orbits and fields in the helical wiggler. *J. Appl. Phys.*, 48(7):2692–2698, 1977.

[128] A. K. Kaminsky *et al.* Field distribution investigation in few types of helical undulators. In *Free Electron Lasers 1996*, pages II–109. Elsevier Science, 1996.

[129] D. Craun and W. B. Colson. Undulator fields and electron trajectories at the end of a helical undulator. *Nucl. Instrum. Methods*, A304:714–718, 1991.

[130] L. R. Elias and J. M. Madey. Superconducting helically wound magnet for the free-electron laser. *Rev. Sci. Instrum.*, 50(11):1335–1340, 1979.

[131] E. S. Gluskin *et al.* Experimental study of the circular polarization level soft x-ray radiation from helical undulator installed in the storage ring VEPP-2M. *Novosibirsk INP Preprint*, 83–163, 1983.

[132] P. M. Stefan *et al.* Insertion device development in the X13 straight of the NSLS X-ray ring. In *Proceedings of the Particle Accelerator Conference, Vancouver*, pages 727–729, 1997.

[133] R. P. Walker *et al.* Design of an electromagnet elliptical wiggler for ELETTRA. In *Proceedings of the Particle Accelerator Conference, Vancouver*, pages 3527–3529, 1997.

[134] J. Chavanne *et al.* Recent developments of insertion devices at the ESRF. In *Proceedings of the Particle Accelerator Conference, Vancouver*, pages 3506–3508, 1997.

[135] J. Chavanne *et al.* The ESRF insertion devices. *J. Synchrotron Rad.*,

5:196–201, 1998.

[136] L. Nahon *et al.* A versatile electromagnetic planar/helical crossed undulator optimised for the SU5 low energy/high resolution beamline at super-ACO. *Nucl. Instrum. Methods*, A396:237–250, 1997.

[137] M. N. Wilson. *Superconducting Magnets.* Oxford University Press, Oxford, 1983.

[138] K. H. Mess *et al.* *Superconducting Accelerator Magnets.* World Scientific, Singapore, 1996.

[139] J. Ross and K. Smith. Design and manufacture of a 6 T wiggler magnet for the Daresbury SRS. *Rev. Sci. Instrum.*, 63(1):309–312, 1992.

[140] T. Yamakawa *et al.* The construction of the superconducting vertical wiggler and its operation in the Photon Factory. *Nucl. Instrum. Methods*, A246:32–36, 1986.

[141] K. Ohmi *et al.* Characteristics of the five–pole superconducting vertical wiggler at the Photon Factory. *Rev. Sci. Instrum.*, 63(1):301–304, 1992.

[142] A. Batrakov *et al.* Magnetic measurements of the 10 T superconducting wiggler for the SPring-8 storage ring. *Nucl. Instrum. Methods*, A467–468:190–193, 2001.

[143] A. M. Batrakov *et al.* Superconducting wave length shifters and multipole wigglers developed in Budker INP. In *Proceedings of the Asian Particle Accelerator Conference, Beijing*, pages 251–253, 2001.

[144] G. Kulipanov. Insertion devices at USSR SR sources. *Synchrotron Rad. News*, 4(1):17–21, 1991.

[145] E. B. Blum *et al.* A superconducting wiggler magnet for the NSLS X-ray ring. In *Proceedings of the Particle Accelerator Conference, Vancouver*, pages 3494–3496, 1997.

[146] G. LeBlanc *et al.* The MAX wiggler. In *Proceedings of the European Particle Accelerator Conference, Vienna*, pages 2334–2336, 2000.

[147] E. Wallen *et al.* The MAX-wiggler, a cold bore superconducting wiggler with 47 3.5 T poles. *Nucl. Instrum. Methods*, A467–468:118–121, 2001.

[148] A. Batrakov *et al.* A superconducting 3.5 T multipole wiggler for the ELETTRA storage ring. In *Proceedings of the European Particle Accelerator Conference, Paris*, pages 2634–2636, 2002.

[149] I. Ben-Zvi *et al.* Performance of a superconducting, high field subcentimeter undulator. *Nucl. Instrum. Methods*, A318:781–788, 1992.

[150] T. Hezel *et al.* Experimental results with a novel superconductive in-vacuum mini-undulator test device at the Mainz microtron MAMI. In *Proceedings of the Particle Accelerator Conference, New York*, pages 165–167, 1999.

[151] R. Rossmanith *et al.* Superconductive 14 mm period undulators for single pass accelerators (FELs) and storage rings. In *Proceedings of the European Particle Accelerator Conference, Paris*, pages 2628–2630, 2002.

[152] C. Reymond. Magnetic resonance techniques. In *Proceedings of the CERN Accelerator School, 98–05*, pages 219–231, 1998.

[153] W. G. Clark. Introduction to magnetic resonance and its application to dipole magnet testing. In *Proceedings of the CERN Accelerator School, 92–05*, pages 193–205, 1992.

[154] B. Berkes. Hall generators. In *Proceedings of the CERN Accelerator School, 92–05*, pages 167–192, 1992.

[155] J. Kvitkovic. Hall generators. In *Proceedings of the CERN Accelerator School, 98–05*, pages 233–249, 1998.

[156] D. H. Nelson *et al.* Magnetic measurements for tuning and operating a hybrid wiggler. *J. de Phys.*, 45(C1):957–960, 1984.

[157] L. Walckiers. The harmonic–coil method. In *Proceedings of the CERN Accelerator School, 92–05*, pages 138–166, 1992.

[158] W. G. Davies. The theory of the measurement of magnetic multipole fields with rotating coil magnetometers. *Nucl. Instrum. Methods*, A311:399–436, 1992.

[159] D. Zangrando and R. P. Walker. A stretched wire system for accurate integrated magnetic field measurements in insertion devices. *Nucl. Instrum. Methods*, A376:275–282, 1996.

[160] D. Zangrando and R. P. Walker. Magnetic measurement facility for the ELETTRA insertion devices. In *Proceedings of the European Particle Accelerator Conference, Berlin*, pages 1355–1357, 1992.

[161] P. Schmuser. Magnetic measurements of superconducting magnets and analysis of systematic errors. In *Proceedings of the CERN Accelerator School, 92–05*, pages 240–273, 1992.

[162] C. S. Hwang *et al.* Stretch-wire system for integral magnetic field measurements. *Nucl. Instrum. Methods*, A467–468:194–197, 2001.

[163] R. W. Warren. Limitations on the use of the pulsed-wire field measuring technique. *Nucl. Instrum. Methods*, A272:257–263, 1988.

[164] O. Shahal and R. Rohatgi. Pulsed wire magnetic field measurements on a 4.3 m long wiggler. *Nucl. Instrum. Methods*, A285:299–302, 1989.

[165] T. C. Fan *et al.* Pulsed wire magnetic field measurements on undulator U10P. In *Proceedings of the Particle Accelerator Conference, Chicago*, pages 2775–2777, 2001.

[166] G. Rakowsky *et al.* Measurement and optimization of the VISA undulator. In *Proceedings of the Particle Accelerator Conference, New York*, pages 2698–2700, 1999.

[167] D. W. Carnegie and J. Timpf. Characterizing permanent magnet blocks with helmholtz coils. *Nucl. Instrum. Methods*, A319:97–99, 1992.

[168] C. S. Hwang *et al.* A highly automatic measurement system for three orthogonal magnetic moments of a permanent magnet block. *Rev. Sci. Instrum.*, 67(5):1741–1747, 1996.

[169] D. Zangrando and R. P. Walker. Magnetic measurement systems for the ELETTRA insertion devices. In *Proceedings of the European Particle Accelerator Conference, Nice*, pages 1365–1367, 1990.

[170] B. L. Bobbs *et al.* In search of a meaningful field-error specification for

wigglers. *Nucl. Instrum. Methods*, A296:574–578, 1990.

[171] B. Diviacco and R. P. Walker. The effect of magnetic field errors on the radiation spectrum of ELETTRA undulators. In *Proceedings of the Particle Accelerator Conference, Chicago*, pages 1259–1261, 1989.

[172] R. P. Walker. Interference effects in undulator and wiggler radiation sources. *Nucl. Instrum. Methods*, A335:328–337, 1993.

[173] R. J. Dejus *et al.* Phase errors and predicted spectral performance of a prototype undulator. *Rev. Sci. Instrum.*, 66(2):1875–1877, 1995.

[174] A. D. Cox and B. P. Youngman. Systematic selection of undulator magnets using the techniques of Simulated Annealing. *SPIE*, 582:91–97, 1985.

[175] B. Diviacco. Performance optimization of pure permanent magnet undulators. In *Proceedings of the Particle Accelerator Conference, Washington*, pages 1590–1592, 1993.

[176] S. Lidia and R. Carr. Faster magnet sorting with a threshold acceptance algorithm. *Rev. Sci. Instrum.*, 66(2):1865–1867, 1995.

[177] R. Hajima *et al.* Optimization of wiggler magnets ordering using a genetic algorithm. *Nucl. Instrum. Methods*, A318:822–824, 1992.

[178] G. LeBlanc *et al.* Technical description of the MAX II undulators. In *Proceedings of the European Particle Accelerator Conference, Sitges*, pages 2555–2557, 1996.

[179] S. Kirkpatrick *et al.* Optimization by simulated annealing. *Science*, 220:671–680, 1983.

[180] W. H. Press *et al.* *Numerical Recipes in C++*. Cambridge University Press, Cambridge, 2002.

[181] T. Tanaka *et al.* Undulator field correction by in-situ sorting. *Nucl. Instrum. Methods*, A465:600–605, 2001.

[182] I. Vasserman. A shimming technique for improvement of the spectral performance of APS undulator A. *APS Internal Report*, LS Note 253, 1996.

[183] J. Chavanne *et al.* Recent advances in insertion devices. In *Proceedings of the European Particle Accelerator Conference, Sitges*, pages 220–224, 1996.

[184] B. Diviacco and R. P. Walker. Recent advances in undulator performance optimization. *Nucl. Instrum. Methods*, A368:522–532, 1996.

[185] S. Y. Lee. *Accelerator Physics*. World Scientific, 1999.

[186] H. Winick, editor. *Synchrotron Radiation Sources — A primer*. World Scientific, 1994.

[187] J. M. Jowett and T. M. Taylor. Wigglers for control of beam characteristics in LEP. *IEEE Trans. Nucl. Sci.*, 30(4):2581–2583, 1983.

[188] M. Tischer *et al.* *A permanent magnet wiggler design for the TESLA damping ring*. TESLA Report 2000 – 20, 2000.

[189] *TESLA Technical Design Report*. DESY, 2001.

[190] L. Rivkin. Introduction to dynamics of electrons in rings in the presence of radiation. In *Proceedings of the CERN Accelerator School, 98–04*, pages 45–60, 1998.

[191] R. P. Walker. Electron beam focussing effects and matching conditions in

plane periodic magnets. *Nucl. Instrum. Methods*, 214:497, 1983.

[192] P. Elleaume. A new approach to the electron beam dynamics in undulators and wigglers. In *Proceedings of the European Particle Accelerator Conference, Berlin*, pages 661–663, 1992.

[193] P. Kuske and J. Bahrdt. Influence of the Bessy undulator on the beam dynamics. In *Proceedings of the European Particle Accelerator Conference, Nice*, pages 1417–1419, 1990.

[194] J. A. Clarke and G. S. Dobbing. Commissioning of the new multipole wigglers in the SRS. In *Proceedings of the Particle Accelerator Conference, New York*, pages 2653–2655, 1999.

[195] L. Smith. Effect of wigglers and undulators on beam dynamics. *LBL Internal Report*, ESG Tech Note 24, 1986.

[196] L. Tosi and R. Nagaoka. Effects of helical undulators on beam dynamics. In *Proceedings of the European Particle Accelerator Conference, Nice*, pages 1423–1425, 1990.

[197] A. Jackson *et al.* The effects of insertion devices on beam dynamics in the ALS. In *Proceedings of the Particle Accelerator Conference, Chicago*, pages 1752–1754, 1989.

[198] C. J. Bocchetta *et al.* Studies of the effects of an elliptical wiggler in ELETTRA. In *Proceedings of the European Particle Accelerator Conference, Berlin*, pages 667–669, 1992.

[199] L. Tosi *et al.* Initial operation of the electromagnetic elliptical wiggler in Elettra. In *Proceedings of the European Particle Accelerator Conference, Stockholm*, pages 1353–1355, 1998.

[200] L. Tosi *et al.* Dynamic aperture, comparison of measurements on Elettra with simulations. In *Proceedings of the European Particle Accelerator Conference, Sitges*, pages 989–991, 1996.

[201] W. Decking *et al.* Treatment of wiggler and undulator field errors in tracking codes. In *Proceedings of the Particle Accelerator Conference, Dallas*, pages 2874–2876, 1995.

[202] J. Safranek *et al.* Nonlinear dynamics in a SPEAR wiggler. *Phys. Rev. ST-AB*, 5:010701, 2002.

[203] W. B. Colson *et al.*, editor. *Laser Handbook volume 6: Free Electron Lasers*. Elsevier Science, Amsterdam, 1990.

[204] C. A. Brau. *Free–Electron Lasers*. Academic Press, Boston, 1990.

[205] R. J. Bakker. The storage ring free-electron laser. In *Proceedings of the CERN Accelerator School, 98–04*, pages 337–385, 1998.

[206] J. Pfluger. Insertion devices for 4th generation light sources. In *Proceedings of the Particle Accelerator Conference, New York*, pages 157–161, 1999.

[207] J. Pfluger. Undulators for SASE FELs. *Nucl. Instrum. Methods*, A445:366–372, 2000.

[208] J. Pfluger and M. Tischer. Undulator systems for the TESLA X-FEL. *Nucl. Instrum. Methods*, A483:388–393, 2002.

[209] V. N. Litvinenko *et al.* Operation of the OK-4/Duke storage ring FEL

below 200 nm. *Nucl. Instrum. Methods*, A475:195–204, 2001.

[210] K. Yamada *et al.* Lasing towards the VUV in the NIJI-IV FEL. *Nucl. Instrum. Methods*, A445:173–177, 2000.

[211] R. P. Walker *et al.* European project to develop a UV/VUV free-electron laser facility on the ELETTRA storage ring. *Nucl. Instrum. Methods*, A429:179–184, 1999.

[212] H. Hama. A helical optical klystron for an UV-FEL project at the UVSOR. *Nucl. Instrum. Methods*, A375:57–61, 1996.

[213] K. E. Robinson *et al.* Field certification of a high strength tapered hybrid undulator. *Nucl. Instrum. Methods*, A259:62–72, 1987.

[214] F. Ciocci *et al.* Design of hybrid magnet undulators with non-constant parameters for high gain, high efficiency free electron laser. In *Proceedings of the European Particle Accelerator Conference, Rome*, pages 1027–1029, 1988.

[215] B. Lai *et al.* Spectral properties of a tapered gap hard x-ray undulator. *Rev. Sci. Instrum.*, 64(4):858–863, 1993.

[216] B. I. Boyanov. Numerical modeling of tapered undulators. *Nucl. Instrum. Methods*, A339:596–603, 1994.

[217] D. Quimby and J. Slater. Emittance acceptance in tapered wiggler free electron lasers. *SPIE*, 453:92–99, 1983.

[218] K. E. Robinson *et al.* Hybrid undulator design considerations. *Nucl. Instrum. Methods*, A250:100–109, 1986.

[219] D. C. Quimby *et al.* Development of a 10 meter wedged–pole undulator. *Nucl. Instrum. Methods*, A285:281–289, 1989.

[220] E. T. Scharlemann. Wiggler plane focussing in linear wigglers. *J. Appl. Phys.*, 58(6):2154–2161, 1985.

[221] Y. Tsunawaki *et al.* Focussing permanent magnet undulator. *Nucl. Instrum. Methods*, A304:753–758, 1991.

[222] C. M. Fortgang. A pure permanent magnet – two plane focussing – tapered wiggler for a high average power FEL. *Nucl. Instrum. Methods*, A393:385–388, 1997.

[223] A. A. Varfolomeev *et al.* Performance of the undulator for the FOM–FEM project. *Nucl. Instrum. Methods*, A341:466–469, 1994.

[224] A. A. Varfolomeev *et al.* Mock up of the focussing undulator for the SLAC X–ray FEL project. *Nucl. Instrum. Methods*, A358:70–71, 1995.

[225] Y. M. Nikitina and J. Pfluger. Two novel undulator schemes with quadrupolar focussing for the VUV–FEL at the TESLA test facility. *Nucl. Instrum. Methods*, A375:325–328, 1996.

[226] J. Pfluger and Y. M. Nikitina. Planar undulator schemes with strong focusing properties for the VUV–FEL at the TESLA test facility. *Nucl. Instrum. Methods*, A381:554–559, 1996.

[227] S. Sasaki *et al.* Conceptual design of quasiperiodic undulator. *Rev. Sci. Instrum.*, 66(2):1953–1955, 1995.

[228] M. Takao *et al.* Analytical formulation of a quasi-periodic undulator. In

Proceedings of the Particle Accelerator Conference, Dallas, pages 1438–1440, 1995.

[229] M. Takao *et al.* Design study of quasiperiodic undulator. In *Proceedings of the European Particle Accelerator Conference, Sitges*, pages 2546–2548, 1996.

[230] M. Kawai *et al.* First observation of quasiperiodic undulator radiation. In *Proceedings of the European Particle Accelerator Conference, Sitges*, pages 2549–2551, 1996.

[231] J. Chavanne *et al.* Development of quasiperiodic undulators at the ESRF. In *Proceedings of the European Particle Accelerator Conference, Stockholm*, pages 2213–2215, 1998.

[232] J. Bahrdt *et al.* A quasi-periodic hybrid undulator at BESSY II. *Nucl. Instrum. Methods*, A467–468:130–133, 2001.

[233] S. Sasaki *et al.* Brainstorming on new permanent magnet undulator designs. In *Proceedings of the European Particle Accelerator Conference, Stockholm*, pages 2237–2239, 1998.

[234] T. Tanaka and H. Kitamura. Simple scheme for harmonic suppression by undulator segmentation. *J. Synchrotron Rad.*, 9:266–269, 2002.

[235] T. Tanaka and H. Kitamura. Figure–8 undulator as an insertion device with linear polarization and low on–axis power density. *Nucl. Instrum. Methods*, A364:368–373, 1995.

[236] T. Tanaka *et al.* In–vacuum figure–8 undulator for hard X-rays with both horizontal and vertical polarization. *J. Synchrotron Rad.*, 5:412–413, 1998.

[237] B. Diviacco *et al.* New insertion devices for ELETTRA. In *Proceedings of the Particle Accelerator Conference, Chicago*, pages 2468–2470, 2001.

[238] B. Diviacco *et al.* Design of a figure–8 undulator for ELETTRA. In *Proceedings of the European Particle Accelerator Conference, Paris*, pages 2610–2612, 2002.

[239] T. Tanaka and H. Kitamura. Asymmetric figure–8 undulator as multipolarization light source. *Nucl. Instrum. Methods*, A449:629–637, 2000.

[240] T. Tanaka and H. Kitamura. Parabolic undulator and its application to fast switching of helicity. *Nucl. Instrum. Methods*, A467–468:153–156, 2001.

[241] R. Carr. Adjustable phase insertion devices as X-ray sources. *Nucl. Instrum. Methods*, A306:391–396, 1991.

[242] R. Tatchyn. Off–axis field effects on the output spectra of vertically asymmetric adjustable–phase insertion devices. *Nucl. Instrum. Methods*, A322:126–134, 1992.

[243] R. Carr. Adjustable phase undulator. *Synchrotron Rad. News*, 5(4):10, 1992.

[244] C. S. Hwang *et al.* Field characteristics of a 9–pole adjustable phase hybrid undulator. In *Proceedings of the European Particle Accelerator Conference, Sitges*, pages 2564–2566, 1996.

[245] C. S. Hwang *et al.* Performances and characteristics of a prototype symmetric hybrid adjustable phase undulator. *Nucl. Instrum. Methods*, A399:463–

476, 1997.

[246] Y. C. Huang *et al.* Performance characterization of a far-infrared, staggered wiggler. *Nucl. Instrum. Methods*, A341:431–435, 1994.

[247] M. Ohnishi *et al.* Improvements of a staggered–array undulator by tapered iron disks. *Nucl. Instrum. Methods*, A407:434–438, 1998.

[248] C. H. Chang *et al.* Magnetic design for a staggered hybrid undulator. In *Proceedings of the European Particle Accelerator Conference, Vienna*, pages 2313–2315, 2000.

[249] C. H. Chang *et al.* Circular polarization with rotatable magnetic fields in crossed staggered undulator. *J. Magnetism Mag. Mat.*, 239:363–366, 2002.

[250] C. H. Chang *et al.* Design of a revolving helical staggered undulator. In *Proceedings of the Particle Accelerator Conference, Portland*, pages 1041–1043, 2003.

[251] E. R. Moog. Novel insertion devices. In *Proceedings of the Particle Accelerator Conference, Portland*, pages 156–160, 2003.

[252] G. K. Shenoy *et al.* Variable–period undulators as synchrotron radiation sources. *J. Synchrotron Rad.*, 10:205–213, 2003.

[253] R. Z. Bachrach *et al.* The SSRL insertion device beamline 'Wunder'. *SPIE*, 582:251–267, 1985.

[254] G. Isoyama *et al.* Construction of a multiundulator, Revolver No. 19, at the Photon Factory. *Rev. Sci. Instrum.*, 60(7):1863–1866, 1989.

[255] J. Pfluger and P. Gurtler. Insertion devices for DORIS III. *Nucl. Instrum. Methods*, A287:628–638, 1990.

[256] T. Hara *et al.* Revolver undulator for BL15XU at SPring-8. *Nucl. Instrum. Methods*, A467–468:161–164, 2001.

[257] R. Tatchyn *et al.* Micropole undulators in accelerator and storage ring technology. In *Proceedings of the Particle Accelerator Conference, Washington*, pages 1681–1684, 1987.

[258] G. Ramian *et al.* Micro–undulator FELs. *Nucl. Instrum. Methods*, A250:125–133, 1986.

[259] P. L. Csonka. Insertion devices, future developments, limitations. *SPIE*, 582:298–317, 1985.

[260] R. Tatchyn. Variable–period electrostatic and magnetostatic undulator designs for generating polarized soft x-rays at PEP. *Rev. Sci. Instrum.*, 60(8):2571–2578, 1989.

[261] V. A. Papadichev. An electrostatic undulator with single–polarity feed. *Nucl. Instrum. Methods*, A429:377–385, 1999.

[262] Y. Zhang *et al.* Image charge undulator. *Nucl. Instrum. Methods*, A507:459–463, 2003.

[263] S. J. Smith and E. M. Purcell. Visible light from localized surface charges moving across a grating. *Phys. Rev.*, 92:1069, 1953.

[264] G. Doucas *et al.* Determination of longitudinal bunch shape by means of coherent Smith-Purcell radiation. *Phys. Rev. ST-AB*, 5:072802, 2002.

[265] T. Shintake. Experimental results of microwave undulator. *SPIE*, 582:336–343, 1985.

[266] H. Henke. MM-wave linac and wiggler structures. In *Proceedings of the European Particle Accelerator Conference, London*, pages 322–326, 1994.

[267] V. V. Kaplin *et al.* In *Abstracts of the 10th Conference on the Application of Charged Particle Beams for Studying the Composition and Properties of Materials, Moscow*, page 28, 1979.

[268] R. O. Avakian. Method for preparation of crystalline undulators. *Nucl. Instrum. Methods*, A492:11–13, 2002.

[269] S. Bellucci *et al.* Experimental study for the feasibility of a crystalline undulator. *Phys. Rev. Lett.*, 90(3):034801, 2003.

[270] U. Mikkelsen and E. Uggerhoj. A crystalline undulator based on graded composition strained layers in a superlattice. *Nucl. Instrum. Methods*, B160:435–439, 2000.

This page intentionally left blank

Index